COASTAL PALAEOENVIRONMENTAL CHANGE AND ANCIENT HARBOUR DEVELOPMENT AT LIMAN TEPE – CLAZOMENAE (URLA, TURKEY) AND LECHAION (CORINTH, GREECE): A MULTY-PROXY GEOARCHAEOLOGICAL AND GEOPHYSICAL STUDY

COASTAL PALAEOENVIRONMENTAL CHANGE AND ANCIENT HARBOUR DEVELOPMENT AT LIMAN TEPE – CLAZOMENAE (URLA, TURKEY) AND LECHAION (CORINTH, GREECE): A MULTY-PROXY GEOARCHAEOLOGICAL AND GEOPHYSICAL STUDY

By NICHOLAS L. RIDDICK, M.Sc., B.Sc.

A Thesis Submitted to the School of Graduate Studies in Partial Fulfilment of the Requirements for the Degree Doctor of Philosophy

McMaster University DOCTOR OF PHILOSOPHY (2021) Hamilton, Ontario
(School of Earth, Environment & Society)

TITLE: Coastal palaeoenvironmental change and ancient harbour development at Liman Tepe-Clazomenae (Urla, Turkey) and Lechaion (Corinth, Greece): A multi-proxy geoarchaeological and geophysical study

AUTHOR: Nicholas L. Riddick, M.Sc., B.Sc. (Brock University)

SUPERVISOR: Dr. Joseph Boyce

NUMBER OF PAGES: X, 188

ABSTRACT

Ancient harbour sediment archives can provide long-term records of changes in coastal palaeoenvironments, settlement history, and anthropogenic impacts on coastal systems. In this study, multi-proxy geoarchaeological investigations were conducted at two long-occupied coastal archaeological sites (Liman Tepe-Clazomenae, western Anatolia, Turkey; Lechaion, northeast Peloponnese, Greece) to document coastal palaeoenvironmental change and harbour basin evolution. Multi-proxy core analyses (micropalaeontology, sedimentary facies) were integrated with geophysical mapping and micro-XRF core scanning (chemofacies) to investigate harbour sediment archives and to reconstruct coastal palaeoenvironments.

At Liman Tepe-Clazomenae, the Neolithic to Early Bronze Age (ca. 6700-3000 BCE) coastal palaeogeography was reconstructed using a large subsurface database (>20 cores, ~600-line km geophysical surveys) to determine palaeoshoreline positions and potential locations of prehistoric proto-harbour basins. Geophysical mapping revealed a submerged palaeolandscape with relict river channels and shorelines recording inundation of a middle Neolithic coastal plain. A transgressive systems tract was identified by marine foreshore and shoreface deposits overlying paleosol and lagoonal sediments. Shoreline positions were estimated by back-strip analysis of the de-compacted sediment thickness from the marine transgressive surface. During the middle Neolithic (ca. 6700 BCE) the shoreline was >500 m seaward of the modern shore and transgressed to its maximum extent (~1 km inland) during the Chalcolithic (ca. 4000 BCE). After 4000 BCE, sea level decelerated and the coastline prograded under a high-stand systems tract by barrier accretion. The transition from a Late Bronze Age (LBA) proto-harbour to Iron Age semi-enclosed harbour basin was recorded by shifts in geochemical proxies (Ti/Ca, Si, Br), foraminifera, and sedimentary facies. Shifts in Ti/Ca record potential signals of land clearance and evidence for a 300-year LBA drought period (“Greek Dark Age”). Geophysical mapping of Clazomenae’s Archaic (ca. 7^{th}-6^{th} c. BCE) harbour basin revealed two rubble-constructed breakwater structures and a submerged headland separating east

and west basins. Linear magnetic anomalies within the eastern mole indicate a buried (LBA?) pier or breakwater within the rubble mass.

At Lechaion, a multi-proxy analysis was conducted on seven cores to determine the timing and causes of the Roman harbour decline and abandonment. Coring identified a basin-wide paraconformity surface separating harbour sediments and overlying marl deposits, which records a rapid transition from a marine-estuarine to restricted evaporitic lake environment. Rapid basin restriction was indicated by a decrease in terrigenous elements (Si, Ti, K, Fe), increased Sr and $\delta^{18}O$, and a shift from marine-estuarine to marsh-freshwater taxa. The event records the 6th c. CE tectonic uplift and destruction of the harbour basin, linked with uplift on the nearby Perachora Peninsula (~1.1 m) during destructive earthquakes in 524 and 551/552 CE. No evidence was found for tsunami events proposed in previous work.

This study has documented the development, evolution, and abandonment of harbour basins on two tectonically active coastlines with complex relative sea level histories. Palaeogeographic mapping at Liman Tepe has identified a drowned palaeolandscape with areas of high archaeological potential for submerged prehistoric sites and proto-harbour anchorage areas. At Lechaion, multi-proxy analysis has resolved a long-standing debate, demonstrating that the harbour basin decline in the 6th c. CE was caused by coastal tectonic uplift and rapid basin restriction.

Keywords: Liman Tepe, Clazomenae, Lechaion, ancient harbours, sediment archives, ITRAX, micro-XRF, coastal palaeoenvironmental change, multi-proxy studies, lithochemofacies, proto-harbour basins

ACKNOWLEDGEMENTS

There are a ton of people to thank, whose mentorship, advice, and support propelled me forward. I will start with my Supervisor, Dr. Joe Boyce, who provided me so many opportunities and really went above and beyond. I had a great PhD experience and am completing this degree a more well-rounded and confident researcher…also, I can use some tools now. Special thanks to my committee Dr. Francine McCarthy and Dr. Ed Reinhardt, who provided guidance and advice. Thank you to Dr. James Conolly for being the external on my defense and to Dr. Tristan Carter for being the chair. My time at McMaster University and in the School of Earth, Environment & Society has been wonderful, in no small part of the faculty, staff, and students.

Much of this thesis was made possible by my colleagues and friends at the Ankara University Mustafa V. Koç Center for Maritime Archaeology (ANKÜSAM). Special thanks to Prof. Dr. V. Şahoğlu, Prof. Dr. I. Tuğcu, and Prof. Dr. H. Erkanal who helped organize our field seasons and provided archaeological insight. Yeşim Alkan, Ali Çoban, Kerem Kiyga, and our Captain Şenol Öntülmüş for being members of my awesome coring team.

I would also like to thank contributors who are coauthors on the upcoming papers (those not already named above), Dr. Richard Rothaus, Beverly Goodman-Tchernov, Krista Chomicki, Gillian Krezoski, and Jeremy Gabriel (aka Brenda).

Finally, I would like to thank all my friends and family for their support and, frankly, for putting up with me. Just to name a few people; my partner Jeremy, parents Janet, Ken, Mike, and Sandy, Grandfather Al, siblings Mike, Connor, and Jenn, nephews Carmine and Carter, and friends Shaunna, James, Pierre, Kevin, Tom, Carli, Rebecca M, Rebecca L, Chelsi, Sian, and Yorgan. I probably missed some people and if you are one of them, sorry, thank you, love you!

TABLE OF CONTENTS

LIST OF FIGURES

Chapter 1

Chapter 2

Chapter 3

Chapter 4

LIST OF TABLES

CHAPTER 1: Introduction

In the ancient Mediterranean world, harbours and port settlements were important centres for trade and the interchange of culture and technology (Oleson and Hohlfelder, 2011; Leidwanger et al., 2014; Knapp and Demesticha, 2016). More than 400 ancient harbour sites have been identified in the Mediterranean (Fig. 1.1), and according to Oleson (2015) most known examples date to a period of intensive economic activity between 200 BCE to 200 CE. Ancient harbours are important in geoarchaeological studies as sediment archives, preserving long-term records of palaeoenvironmental change and human activities (Anthony et al., 2014; Marriner et al., 2014). Studies of ancient harbour sediments have yielded long-term records of changes in coastal palaeoenvironments, sea level history and human modification of coastal environments (e.g. Reinhardt et al., 1999, 2006; Le Roux et al., 2005; Marriner et al., 2005, 2006, 2007, 2008, 2010; Goodman et al., 2008, 2009; Hadler et al., 2013; Seeliger et al., 2013; Stock et al., 2013, 2014, 2016, 2019; Goiran et al., 2014; Mourtzas et al., 2014; Shumilovskikh et al., 2016; Delile et al., 2018; Stiros 2020). The study of cultural materials (e.g. pottery) and preserved harbour structures have also led to a better understanding of maritime trade networks, coastal settlement history, and changes in harbouring technology (e.g. Şahoğlu, 2005; Marriner and Morhange, 2007; Oleson and Hohlfelder, 2011; Leidwanger et al., 2014; Knapp and Demesticha, 2016; Erkanal, 2017; Mauro, 2019).

A widely used typology developed by Carayon (2008) and Marriner et al. (2014) for ancient harbour development in the Mediterranean recognizes three harbour types: 1) natural or 'proto-harbour' basins, 2) semi-artificial harbours, and 3) artificial (fully engineered) harbour basins (Fig. 1.2). Prior to the Iron Age (ca. 8^{th}-5^{th} c. BCE in the Aegean), naturally sheltered coastal areas (e.g. bays and lagoons) were commonly used as anchorages (i.e. natural or proto-harbours). In the Levant, researchers have found evidence for human augmentation of proto-harbours in the Middle-Late Bronze Age. For example, ashlar quays at Dor (Israel) have been interpreted as Late Bronze harbour structures (Raban, 1995) and at Sidon (Lebanon) natural sandstone ridges were augmented to improve natural

anchorages during the Late Bronze to Early Iron age (Marriner et al., 2006). Semi-artificial harbours, which employed structures such as breakwaters to augment natural features (Fig. 1.2) and improve harbour function, first appeared in the early Iron Age. For example, at Liman Tepe-Clazomenae (Turkey) breakwater structures were built off headlands (Goodman et al., 2009). The first evidence of a semi-artificial harbour basin in the Aegean dates to the 8th-7th c. BCE at Delos (Greece), while on the Levantine coast they appeared earlier (9th-8th c. BCE) (Flemming 1980; Blackman, 1982; Duchêne et al., 2001; Haggi et al., 2006; Haggi and Artzy, 2007; Mauro, 2019). With advances in technology and building materials, excavated artificial harbour basins were constructed. The Roman discovery of hydraulic concrete (ca. 2nd c. BCE), allowed artificial harbours to be constructed on open coasts (Oleson, 1988; Raban, 1992; Brandon, 1996; Marriner and Morhange, 2007). Cothons are artificial 'inner' basins, often connected to the sea by a man-made channel (Fig. 1.2). This type of harbour is generally associated with the Phoenicians (e.g. Carthage), but can be found in the Greek world as well (Goiran and Morhange, 2003; Carayon, 2005). Lechaion (Greece) is an example of an early Greek cothon that was constructed during the Archaic Period (7th-6th c. BCE) (Rothaus, 1995).

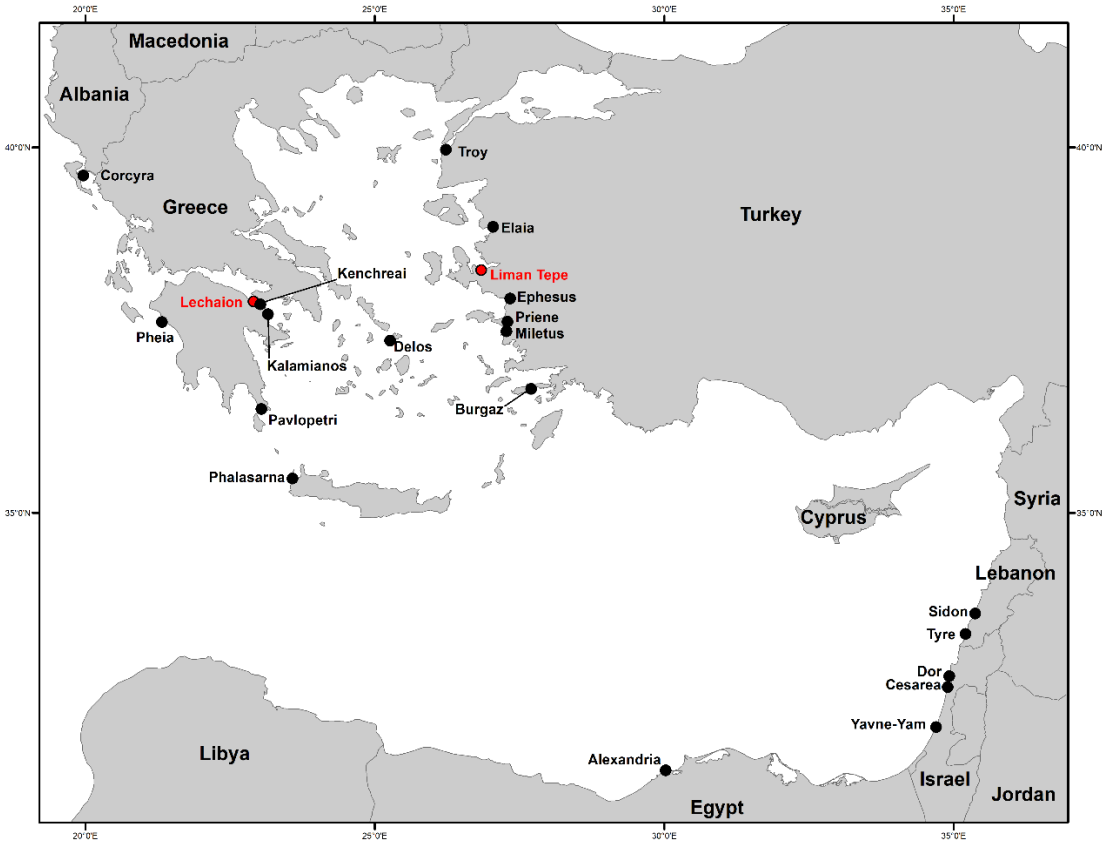

Figure 1.1: Location of study areas and other well-studied ancient harbours in the Eastern Mediterranean and Aegean (GIS data from Natural Earth). Liman Tepe-Clazomenae is situated in the southern Bay of Izmir at the western end of Gediz graben. Lechaion is located in the eastern Gulf of Corinth, within a region of active extension.

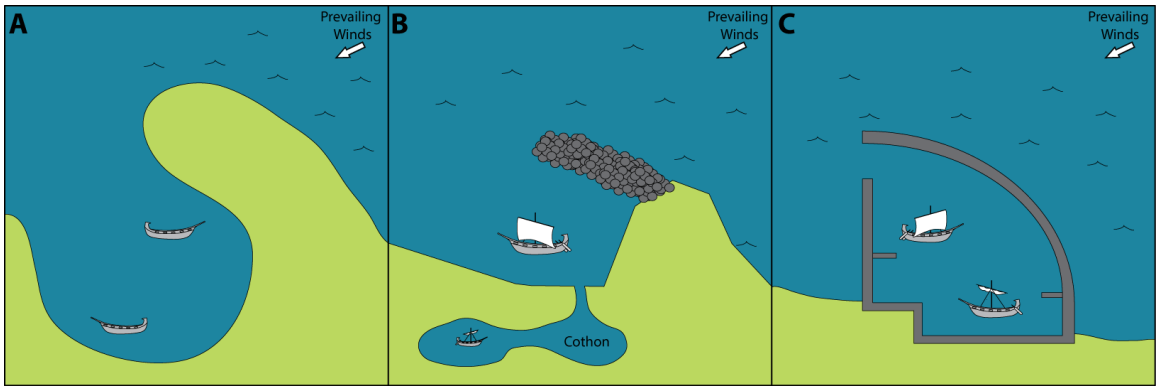

Figure 1.2: A. Proto or natural harbour within a protected natural embayment (e.g. Kalamianos, Greece). B. Semi-artificial harbour with rubble breakwater built off a headland (e.g. Clazomenae, Turkey). On the southern shore of the semi-artificial basin is an artificially excavated inner harbour or cothon (e.g. Lechaion, Greece). C. Artificial harbour excavated/built on an open coast (e.g. Cesarea, Israel).

The introduction of semi-artificial harbour basins in the Aegean coincided with expansion of Greek colonies during the early Iron Age and changes in ship technology. The expansion in trade networks provided the economic impetus for construction of harbours and monumental projects (Blackman, 1982). Steel fitting on ships allowed for much larger hull dimensions and cargo capacity, but also required enhanced deep-water harbours with facilities for lading of goods and ship maintenance (Tartaron, 2013; Marriner et al., 2014). Many proto-harbours were no longer sufficient for the needs of settlements or were inadequate for larger vessels. It is also likely that many natural sheltered anchorage locations gradually deteriorated or were lost due to infilling of river mouths and estuaries by the aggradation coasts or the progradation of deltas following the middle Holocene deceleration in sea level rise (ca. 6-6.5 ka BP) (Marriner and Morhange, 2007; Mauro, 2019). As such, engineering solutions would have been required to better protect larger and deeper harbour basins.

Bronze Age (ca. 3000-1200 BCE in the Aegean) seafaring and trade networks depended on the availability of natural anchorage locations, particularly in the Aegean (Blackman, 1982; Mauro, 2019). However, geoarchaeological records of these proto-harbours is limited, and only a few examples have been identified in the Aegean. For example, at Kalamianos (Greece), proto-harbouring areas were identified by detailed bathymetric mapping and radiocarbon dating submerged beachrocks (Dao, 2011). Identification of former Bronze Age harbour locations is a challenge due to the changes in sea level and the shoreline positions since 6-6.5 ka BP. The best-known examples are from Sidon and Tyre (Lebanon), where the transition from a proto-harbour to engineered harbour was documented (Marriner et al., 2005, 2006). In these examples, the proto-harbour phase underlies the engineered harbour. In other cases, such as at Ephesus (Turkey), harbours were relocated to keep pace with the regressing shorelines, as the delta progradation at the mouth of Kucuk-Menderes River (Brückner, 2005; Stock et al., 2013, 2016, 2019). At Liman Tepe (Turkey), palaeogeographic reconstructions have identified possible pre-Iron Age harbours and settlements both landward and seaward of the modern coast (Goodman et al., 2008, 2009). This highlights the need for palaeogeographic reconstructions to aid in

the discovery and study of early harbours and settlements. This is especially true for submerged sites, which Knapp and Demesticha (2016) noted do not receive the same attention as those found on land, and fewer submerged harbour sites are known comparatively.

1.1 Research Questions and Objectives

Ancient harbour geoarchaeology has emerged as a discipline only in the last three decades, before which the study of shipwrecks and ship architecture dominated maritime archaeology (Marriner et al., 2007, 2010). The founding of harbours, their development, and eventual decline and abandonment are key questions that can be answered through multidisciplinary studies of harbour basin sediment archives (Goiran and Morhange, 2003; Anthony et al., 2014). In tectonically active regions (e.g. the Aegean) co-seismic uplift and subsidence of the coast can complicate relative sea level history and the stratigraphic record within harbour basins. The effects of tectonic uplift and subsidence have been documented at a number of ancient harbour sites, such as Kenchreai, Kalamianos, Lechaion, and Phalasarna (Greece) (Pirazzoli et al., 1992; Rothaus et al., 2008; Nixon et al., 2009; Dao, 2011; Tartaron et al., 2011, 2015; Finkler et al., 2018a; Stiros, 2020). The destruction of harbour facilities by tsunamis have also been inferred in the sedimentary record of a number of harbours, including Corcyra, Pheia, Lechaion (Greece), Caesarea (Israel), and Alexandria (Egypt) (Reinhardt et al., 1999, 2006; Goiran et al., 2005; Vött et al., 2011, Hadler et al., 2013; Finkler et al., 2018b).

This thesis documents multi-proxy geoarchaeological investigations at two long-occupied coastal archaeological sites: Liman Tepe (western Anatolia, Turkey) and Lechaion (Corinth, Greece). The study site locations, research questions and overarching objectives of the research projects are summarized here. A more detailed discussion of the study sites, the research aims, and methodology are provided within the respective papers in Chapters 2-4.

1.1.1 Liman Tepe-Clazomenae (Western Anatolia, Turkey)

Located in the southern Bay of Izmir, near Urla, Turkey (Fig. 1.3), Liman Tepe was an important Early Chalcolithic-Bronze Age site, and contemporary of Troy (Fig. 1.3a). Previous work at Liman Tepe has suggested back-barrier lagoons and coastal embayments may have provided natural proto-harbour and anchorage sites during the Early bronze Age (Goodman et al., 2009). Other work had documented the presence of submerged palaeolandscape features (e.g relict river channels, palaeoshorelines) but their age and relation to the prehistoric coastal settlement were not determined (Krezoski, 2008). Archaeological evidence from land excavation indicates the presence of Neolithic peoples at Liman Tepe, but no settlement from this period had been discovered (Erkanal, 2008), raising questions as to the potential for submerged underwater archaeological sites beyond the present shoreline. Later, during the Iron Age, the Greek city of Clazomenae was founded on the site of Liman Tepe and a semi-artificial harbour basin was constructed on the mainland coast (Fig. 1.3b). The Archaic harbour is one of the best-preserved examples of an Iron Age harbour in the Aegean, but its date of construction, layout and function were not well understood. Archaeological evidence suggests that the harbour was likely constructed during the 7^{th}-6^{th} c. BCE and may represent one of the earliest examples of a semi-enclosed Iron Age harbour basin in the Aegean.

Evaluation of the underwater archaeological potential and the identification of potential anchorage areas at Liman Tepe requires an improved understanding of the prehistoric coastal palaeogeography. The *first objective* at Liman Tepe-Clazomenae was to reconstruct the prehistoric (Neolithic to Bronze Age) coastal palaeogeography and palaeoshoreline positions, with the aim of predicting the location of ancient mooring sites, proto-harbours, and prehistoric underwater archaeological sites (Chapter 2). The *second objective* was to document palaeoenvironmental changes in Liman Tepe's Archaic harbour basin, from the Late Bronze Age proto-harbour phase to the founding of the Iron Age harbour. The sediment archive was also investigated for evidence of land-use changes stemming from the Late Bronze-Iron Age settlement expansion and population growth (Chapter 3).

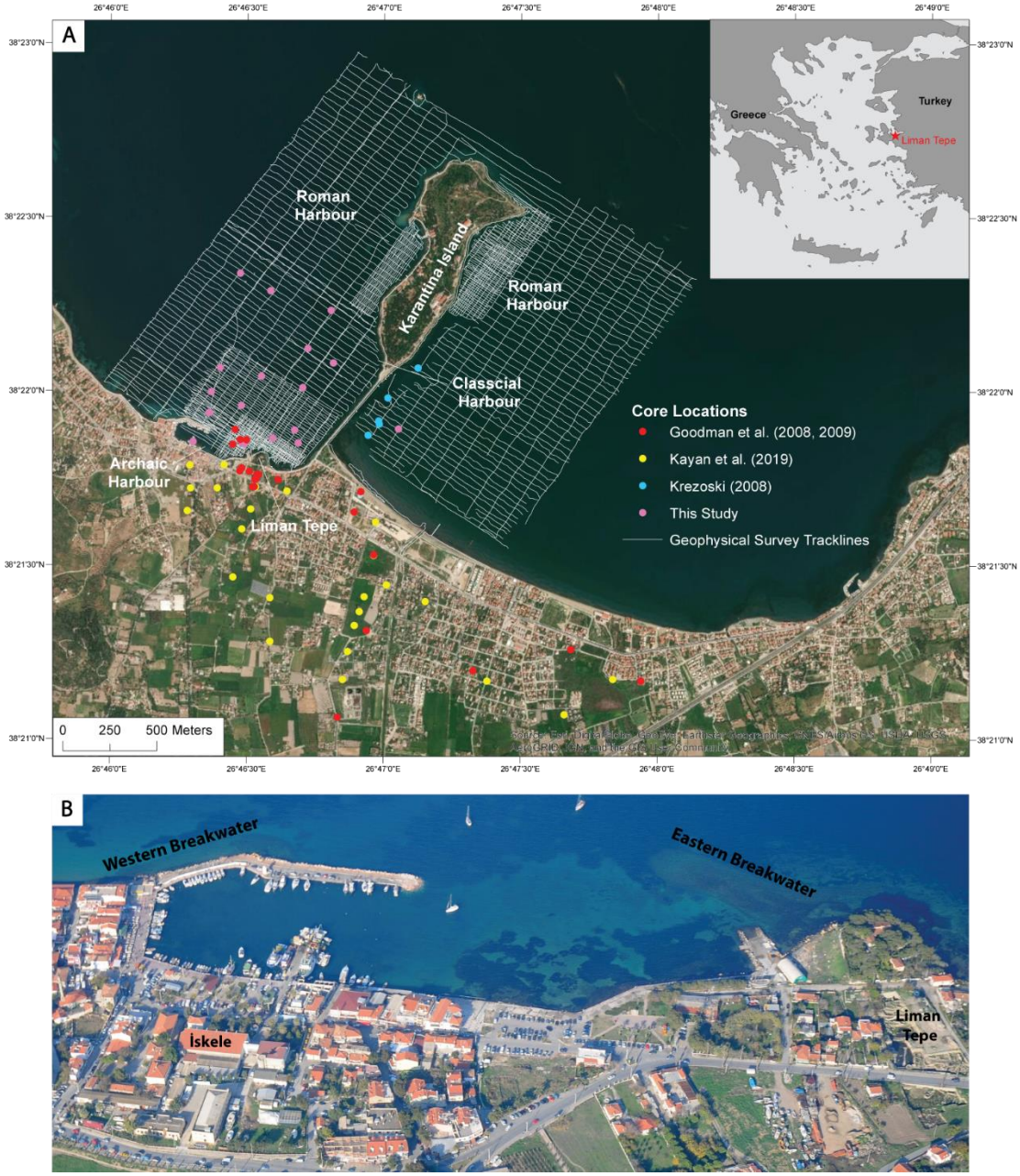

Figure 1.3: A. Liman Tepe-Clazomenae study area with geophysical track lines and core locations shown (Krezoski, 2008; Goodman et al., 2008, 2009; Kayan et al., 2019). B. Aerial photo showing Clazomenae's mainland Archaic Harbour, with submerged breakwaters. Iskele's harbour has been built over the western half of the Archaic harbour.

1.1.2 Lechaion (Corinth, Greece)

Located in the southeastern Gulf of Corinth, Lechaion served as the principal port of ancient Corinth for a millennium (Fig. 1.4). The inner harbour was an artificial, excavated basin (cothon), constructed during the Archaic period (7^{th}-6^{th} c. BCE). The site served as a naval base in the Corinthian War (early 4^{th} c. BCE) and again in 212 BCE as base for the Macedonian fleet (Rothaus, 1995). The site is also known for its Early Christian basilica (ca. 6^{th} c. CE), perhaps the largest structure in the western world at the time (Rothaus, 1995). Over its history, the inner basin was dredged and renovated several times (Kent, 1966; Rothaus, 1995; Vött et al., 2018). The cause of inner harbour decline and abandonment (ca. 6^{th} c. CE) has been the subject of recent debate (Kolaiti et al., 2017; Vott et al., 2018) and attributed variously to uplift and siltation, subsidence, and tsunami impacts (Mourtzas and Marinos, 1994; Rothaus, 1995; Morhange et al., 2012; Mourtzas et al., 2014; Hadler et al., 2013; Kolaiti et al., 2017; Vött et al., 2018).

The objective of geoarchaeological investigations at Lechaion was two-fold. A *first objective* was to determine the timing and cause(s) of the decline and abandonment of the inner harbour. The *second objective* was to evaluate geoarchaeological evidence for tectonic process on the coast (Chapter 4).

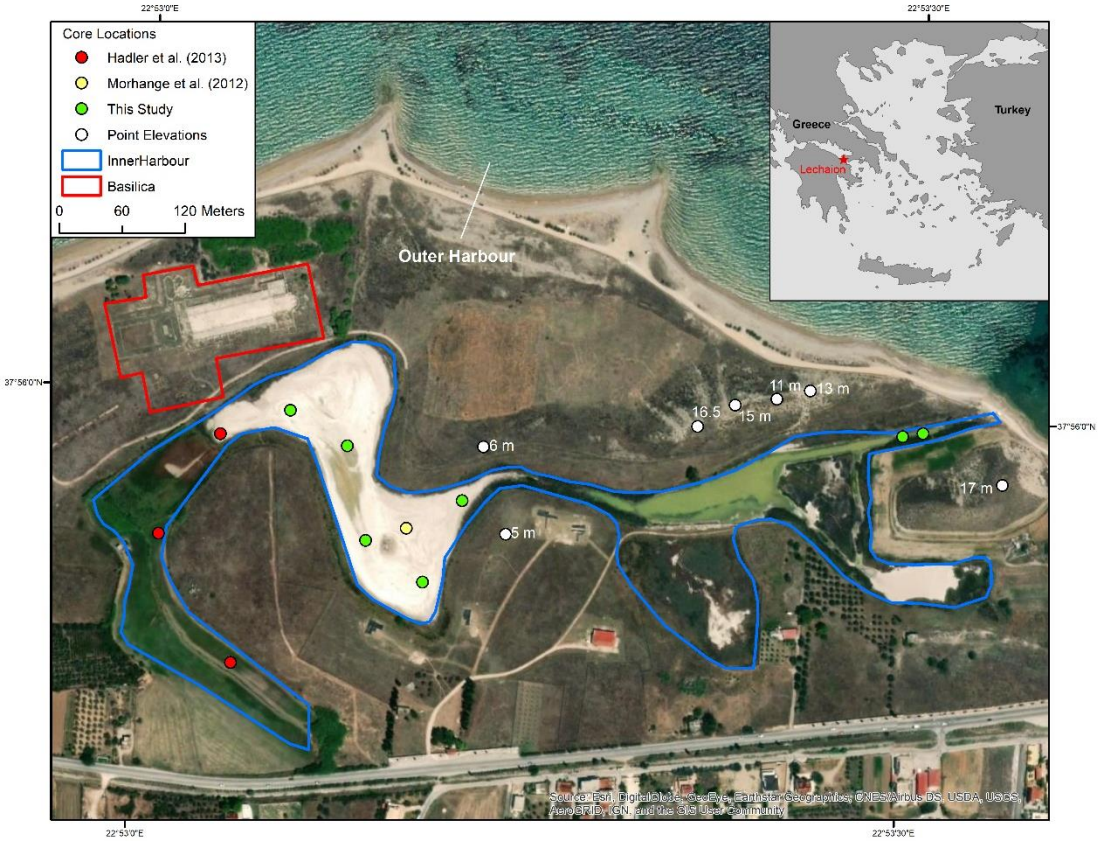

Figure 1.4: Aerial photo showing layout of Lechaion's inner harbour basin and core locations (Morhange et al., 2012; Hadler et al., 2013).

1.1.3 Micro-XRF Elemental Geochemistry

Investigations at Liman Tepe and Lechaion also evaluated micro-XRF elemental geochemistry and chemofacies analysis as a high-resolution tool for geoarchaeological investigation of coastal palaeoenvironmental change (Chapters 2-4). Several recent studies have demonstrated the use of geochemical methods in the investigation of harbour sediment archives (Leroux et al., 2003; Delile et al., 2015). The use of portable hand-held XRF systems (pXRF) has become popular in harbour geoarchaeology (e.g. Vött et al., 2011; Hadler et al., 2013, 2015; Seeliger et al., 2013, 2019; Pint et al., 2015; Finkler et al., 2018a, b) but micro-XRF core scanning techniques have had limited application in ancient harbour studies (e.g. Stock et al., 2013, 2016; Delile et al., 2018). The high-resolution capabilities of core scanners offer the potential for much improved resolution of paleoenvironmental

signals in harbour sediment records with decadal to centennial scales of resolution (Rothwell and Croudace, 2015).

1.2 Author Contributions

This thesis is formatted as a 'sandwich' style thesis, consisting of three full-length papers prepared for journal submission (Chapters 2-4) and a brief introductory and concluding chapters. In accordance with McMaster School of Graduates Studies policy, the contributions of all authors who have contributed to the research is summarized below.

Chapter 2: Palaeoshoreline reconstruction and underwater archaeological potential of Liman Tepe: a long-occupied coastal prehistoric site in western Anatolia, Turkey

Authors: Nicholas L. Riddick, Joseph I. Boyce, Gillian M. Krezoski, Vasıf Şahoğlu, Hayat Erkanal, Irfan Tuğcu, Yeşim Alkan, Jeremy J. Gabriel, Eduard G. Reinhardt, and Beverly N. Goodman-Tchernov.

For submission to Quaternary Science Reviews

NLR collected, described, and sampled cores, analyzed micro-XRF and micropalaeontological data (new marine cores), correlated new marine cores with existing core datasets (largely on land), produced palaeoshoreline estimates, and identified areas of potential archaeological interest. NLR prepared the manuscripts and drafted all figures. JIB supervised the research work, aided in field work and logistics, collected/processed geophysical data, and edited the thesis manuscript. G. Krezoski and J. Gabriel assisted with processing of geophysical datasets and Y. Alkan with core collection and field logistics. Prof. Dr. V. Şahoğlu, Prof. Dr. I. Tuğcu, and Prof. Dr. H. Erkanal assisted with field logistics, and advised on archaeological interpretations. Dr. E.G. Reinhardt and Dr. B. Goodman-Tchernov advised on micropalaeontological methods and interpretation.

Research was supported by the Natural Sciences and Engineering Research Council (NSERC) of Canada grants to JIB, Turkish Ministry of Culture grants to Prof. Dr. V.

Şahoğlu and an NSERC Canada Graduate Scholarship to NLR. Thanks to the students and staff of the Ankara University Mustafa V. Koç Center for Maritime Archaeology (ANKÜSAM) for field and logistical support.

Chapter 3: Multi-proxy palaeoenvironmental record of the Late Bronze to Iron Age transition and harbour development at Clazomenae, western Anatolia, Turkey

Authors: Nicholas L. Riddick, Joseph I. Boyce, Vasıf Şahoğlu, Hayat Erkanal, Irfan Tuğcu, Yeşim Alkan, Eduard G. Reinhardt, and Beverly N. Goodman-Tchernov

For submission to Journal of Archaeological Sciences

NLR collected, described, and sampled cores, analyzed micro-XRF and micropalaeontological data (new marine cores), and correlated and interpreted datasets. NLR prepared the manuscript and drafted all figures. JIB supervised the research work, aided in field work and logistics, collected/processed geophysical data, and edited the thesis manuscript. Y. Alkan assisted with core collection and field logistics. Prof. Dr. V. Şahoğlu, Prof. Dr. I. Tuğcu, and Prof. Dr. H. Erkanal assisted with field logistics, and advised on archaeological interpretations. Dr. E.G. Reinhardt and Dr. B. Goodman-Tchernov advised on micropalaeontological methods and interpretation.

Research was supported by NSERC grants to JIB, Turkish Ministry of Culture grants to Prof. Dr. V. Şahoğlu and an NSERC Canada Graduate Scholarship to NLR.

Chapter 4: Multi-proxy palaeoenvironmental record of coastal tectonic uplift and abandonment (ca. 6th c. CE) of Lechaion's inner harbour, Ancient Corinth (Greece)

Authors: Nicholas L. Riddick, Joseph I. Boyce, Eduard G. Reinhardt, Richard M. Rothaus, Krista Chomicki, and Francine M.G. McCarthy

Submitted to Quaternary Science Reviews

NLR described and correlated cores, compared new data to existing literature, conducted micro-XRF analysis, and interpreted micropalaeontological and isotopic data. NLR prepared the manuscript and created the figures. JIB supervised the research work and edited the thesis manuscripts. Dr. E.G. Reinhardt, K. Chomicki, and Dr. R. Rothaus collected cores, foraminifera, and isotopic data and advised on interpretation of micropalaeontological and archaeological data. Dr. F.M.G. McCarthy conducted the palynological analysis.

This research was supported by NSERC Grants to JIB, Dr. E.G. Reinhardt, and Dr. F.M.G. McCarthy, a Foundation for the Exploration and Research on Cultural Origins Grant to Dr. R.M. Rothaus, and a NSERC Canada Postgraduate Scholarship to NLR.

1.3 References

Anthony, E.J., Marriner, N., Morhange, C., 2014. Human influence and the changing geomorphology of Mediterranean deltas and coasts over the last 6000 years: From progradation to destruction phase? Earth-Science Reviews 139, 336-361.

Blackmann, D.J., (1982). Ancient harbours in the Mediterranean. Part 1. International Journal of Nautical Archaeology 11(2), 79-104.

Brandon, C., 1996. Cements, concrete, and settling barges at Sebastos: comparisons with other Roman harbor examples and the descriptions of Vitruvius. In: Rabbān, A., Holum, K.G. (Eds.), Caesarea Maritima: a retrospective after two millennia (Vol. 21), Brill, pp. 25–40.

Brückner, H., 2005. Holocene shoreline displacements and their consequences for human societies: the example of Ephesus in western Turkey. Zeitschrift fur Geomorphologie 137(Suppl.), 11-22.

Carayon, N., 2005. Le cothon ou port artificiel creusé. Essai de définition. Méditerranée. Revue géographique des pays méditerranéens/Journal of Mediterranean geography (104), 5-13.

Carayon, N., 2008. Les ports phéniciens et puniques. Géomorphologie et infrastructures. Unpublished PhD thesis, Université Marc Bloch-Strasbourg II.

Dao, P., 2011. Marine geophysical and geomorphic survey of submerged Bronze Age shorelines and anchorage sites at Kalamianos (Korphos, Greece). Unpublished PhD thesis, McMaster University, pp. 44, 55.

Delile, H., Goiran, J.P., Blichert-Toft, J., 2018. The contribution of geochemistry to ancient harbor geoarcheology: The example of Ostia Antica. Quaternary Science Reviews 193, 170-187.

Duchêne, H., Fraisse, P., Dalongeville, R., Bernier, P., 2001. Le paysage portuaire de la Délos antique: recherches sur les installations maritimes, commerciales et urbaines, p. 93.

Erkanal, H., 2008. Liman Tepe: New light on prehistoric Aegean cultures. In: Erkanal, H., Hauptmann, H, Şahoğlu, V. (Eds), The Aegean in the Neolithic, Chalcolithic and the Early Bronze Age. Proceedings of the International Symposium, Urla-Izmir, pp. 179-190.

Erkanal, H., 2017. Liman Tepe Kazıları. Kazı Sonuçları Toplantısı, 387-406.

Finkler, C., Baika, K., Rigakou, D., Metallinou, G., Fischer, P., Hadler, H., Fischer, P., Vött, A., 2018a. Geoarchaeological investigations of a prominent quay wall in ancient Corcyra–implications for harbour development, palaeoenvironmental changes and tectonic geomorphology of Corfu island (Ionian Islands, Greece). Quaternary International 473, 91-111.

Finkler, C., Fischer, P., Baika, K., Rigakou, D., Metallinou, G., Hadler, H., Vött, A., 2018. Tracing the Alkinoos Harbor of ancient Kerkyra, Greece, and reconstructing its paleotsunami history. Geoarchaeology 33(1), 24-42.

Flemming, N.C., 1980. Gigantic harbors in the Levant. Archaeology Under Water. In: Muckelroy, K. (Ed), Archaeology under water: an atlas of the world's submerged sites, McGraw-Hill Book Company, p. 168.

Goiran, J.P., Marriner, N., Morhange, C., Abd El-Maguib, M., Espic, K., Bourcier, M., Carbonel, P., 2005. Evolution géomorphologique de la façade maritime d'Alexandrie (Egypte) au cours des six derniers millénaires. Méditerranée. Revue géographique des pays méditerranéens/Journal of Mediterranean geography 104, 61-64.

Goiran, J.P., Morhange, C., 2001. Géoarchéologie des ports antiques de Méditerranée. Problématiques et études de cas. Topoi. Orient-Occident 11(2), 647-669.

Goiran, J.P., Salomon, F., Mazzini, I., Bravard, J.P., Pleuger, E., Vittori, C., Boetto, G., Christiansen, J., Arnaud, P., Pellegrino, A., Pepe, C., Sadori, L., 2014. Geoarchaeology confirms location of the ancient harbour basin of Ostia (Italy). Journal of Archaeological Science 41, 389-398.

Goodman, B.N., Reinhardt, E.G., Dey, H.W., Boyce, J.I., Schwarcz, H.P., Sahoğlu, V., Erkanal, H., Artzy, M., 2008. Evidence for Holocene marine transgression and shoreline progradation due to barrier development in Iskele, Bay of Izmir, Turkey. Journal of Coastal Research 24(5), 1269-1280.

Goodman, B.N., Reinhardt, E.G., Dey, H.W., Boyce, J.I., Schwarcz, H.P., Sahoğlu, V., Erkanal, H., Artzy, M., 2009. Multi-proxy geoarchaeological study redefines understanding of the paleocoastlines and ancient harbours of Liman Tepe (Iskele, Turkey). Terra Nova 21(2), 97-104.

Hadler, H., Vött, A., Koster, B., Mathes-Schmidt, M., Mattern, T., Ntageretzis, K., Reicherter, K., Willershäuser, T., 2013. Multiple late-Holocene tsunami landfall in the eastern Gulf of Corinth recorded in the palaeotsunami geo-archive at

Lechaion, harbour of ancient Corinth (Peloponnese, Greece). Zeitschrift für Geomorphologie 57(4), 139-180.

Hadler, H., Vött, A., Fischer, P., Ludwig, S., Heinzelmann, M., Rohn, C., 2015. Temple-complex post-dates tsunami deposits found in the ancient harbour basin of Ostia (Rome, Italy). Journal of Archaeological Science 61, 78-89.

Haggi, A., 2006. Phoenician Atlit and its newly-excavated harbour: a reassessment. Tel Aviv 33(1), 43-60.

Haggi, A., Artzy, M., 2007. The harbor of Atlit in northern Canaanite/Phoenician context. Near Eastern Archaeology 70(2), 75-84.

Kayan, İ., Öner, E., Doğan, M., İlhan, R., Vardar, S., 2019. Holocene paleogeography and geoarchaeological interpretations on the Urla-İskele coastal plain. Ege Coğrafya Dergisi 28(1): 11-32.

Kent, J.H., 1966. The Inscriptions: 1926 –1950. – Amer. School Classic. Stud. Athens, Athens, pp. 64.

Knapp, A.B., Demesticha S., 2016. Mediterranean connections: maritime transport containers and seaborne trade in the Bronze and Early Iron Ages, Taylor & Francis.

Kolaiti, E., Papadopoulos, G.A., Morhange, C., Vacchi, M., Triantafyllou, I., Mourtzas, N.D., 2017. Palaeoenvironmental evolution of the ancient harbor of Lechaion (Corinth Gulf, Greece): Were changes driven by human impacts and gradual coastal processes or catastrophic tsunamis? Marine Geology 392, 105-121.

Krezoski, G., 2008. Paleoenvironmental reconstruction of prehistoric submerged and coastal environments at Liman Tepe/Klazomenai, Turkey. Unpublished Master's thesis, McMaster University.

Leidwanger, J., Knappett, C., Arnaud, P., Arthur, P., Blake, E., Broodbank, C., Burghmans, T., Evans, T., Graham, S., Greene, E.S., Kowalzig, B., Mills, B., Rivers, R., Tartaron, T.F., Van de Noort, R., 2014. A manifesto for the study of ancient Mediterranean maritime networks Antiquity 342, 1-5.

Le Roux, G., Véron, A., Morhange, C., 2005. Lead pollution in the ancient harbours of Marseilles. Méditerranée. Revue géographique des pays méditerranéens/Journal of Mediterranean geography (104), 31-35.

Marriner, N., Morhange, C., 2007. Geoscience of ancient Mediterranean harbours. Earth-Science Reviews 80(3-4), 137-194.

Marriner, N., Morhange, C., Boudagher-Fadel, M., Bourcier, M., Carbonel, P., 2005. Geoarchaeology of Tyre's ancient northern harbour, Phoenicia. Journal of Archaeological Science 32(9), 1302-1327.

Marriner, N., Morhange, C., Doumet-Serhal, C., 2006. Geoarchaeology of Sidon's ancient harbours, Phoenicia. Journal of Archaeological Science 33(11), 1514-1535.

Marriner, N., Morhange, C., Goiran, J.P., 2010. Coastal and ancient harbour geoarchaeology. Geology Today 26(1), 21-27.

Marriner, N., Morhange, C., Kaniewski, D., Carayon, N., 2014. Ancient harbour infrastructure in the Levant: tracking the birth and rise of new forms of anthropogenic pressure. Scientific Reports 4(1), 1-11.

Marriner, N., Morhange, C., Saghieh-Beydoun, M., 2008. Geoarchaeology of Beirut's ancient harbour, Phoenicia. Journal of Archaeological Science 35(9), 2495-2516.

Mauro, C.M., 2019. Archaic and Classical Harbours of the Greek World: The Aegean and Eastern Ionian Contexts. Archaeopress Publishing Ltd.

Morhange, C., Pirazzoli, P.A., Evelpidou, N., Marriner, N., 2012. Late Holocene Tectonic Uplift and the Silting Up of Lechaion, the Western Harbor of Ancient Corinth, Greece. Geoarchaeology 27(3), 278-283.

Mourtzas, N.D., Kissas, C., Kolaiti, E., 2014. Archaeological and geomorphological indicators of the historical sea level changes and the related palaeogeographical reconstruction of the ancient foreharbour of Lechaion, East Corinth Gulf (Greece). Quaternary International 332, 151-171.

Mourtzas, N.D., Marinos, P.G., 1994. Upper Holocene sea-level changes: Paleogeographic evolution and its impact on coastal archaeological sites and monuments. Environmental Geology 23(1), 1-13.

Nixon, F.C., Reinhardt, E.G., Rothaus, R., 2009. Foraminifera and tidal notches: dating neotectonic events at Korphos, Greece. Marine Geology 257(1-4), 41-53.

Oleson, J.P., 1988. The technology of Roman harbours. International Journal of Nautical Archaeology 17(2), 147-157.

Oleson, J.P., 2015. The evolution of harbour engineering in the ancient Mediterranean world. BYZAS 19, 509-522.

Oleson, J.P., Hohlfelder, R.L., 2011. Ancient harbors in the Mediterranean. In The Oxford Handbook of Maritime Archaeology.

Pint, A., Seeliger, M., Frenzel, P., Feuser, S., Erkul, E., Berndt, C., Klein, C., Pirson, F., Brückner, H., 2015. The environs of Elaia's ancient open harbour–a reconstruction based on microfaunal evidence. Journal of Archaeological Science 54, 340-355.

Pirazzoli, P.A., Ausseil-Badie, J., Giresse, P., Hadjidaki, E., Arnold, M., 1992. Historical environmental changes at Phalasarna harbor, West Crete. Geoarchaeology 7(4), 371-392.

Raban, A., 1992. Sebastos: the royal harbour at Caesarea Maritima—a short-lived giant. International Journal of Nautical Archaeology 21(2), 111-124.

Rabbān, A., 1995. Dor-Yam: maritime and coastal installations at Dor in their geomorphological and stratigraphic context. Excavations at Dor. Final report. Vol. 1., Areas A and C.-A. Introduction and stratigraphy, 285-354.

Reinhardt, E.G., Goodman, B.N., Boyce, J.I., Lopez, G., van Hengstum, P., Rink, W.J., Mart, Y., Raban, A., 2006. The tsunami of 13 December AD 115 and the destruction of Herod the Great's harbor at Caesarea Maritima, Israel. Geology 34(12), 1061-1064.

Reinhardt, E.G., Raban, A., 1999. Destruction of Herod the Great's harbor at Caesarea Maritima, Israel—geoarchaeological evidence. Geology 27(9), 811-814.

Rothaus, R., 1995. Lechaion, western port of Corinth: A preliminary archaeology and history. Oxford Journal of archaeology 14(3), 293-306.

Rothaus, R.M., Reinhardt, E.G., Noller, J.S., 2008. Earthquakes and subsidence at Kenchreai: using recent earthquakes to reconsider the archaeological and literary

evidence. In: Caraher W.R., Hall, L.J., Moore, R.S. (Eds), Archaeology and history in Roman, medieval and post-medieval Greece: studies on method and meaning in honor of Timothy E. Gregory, Ashgate Publishing Ltd., pp. 53-66.

Rothwell, R.G., Croudace, I.W., 2015. Micro-XRF studies of sediment cores: a perspective on capability and application in the environmental sciences. In: Croudace, I.W., Rothwell, R.G. (Eds), Micro-XRF Studies of Sediment Cores, Springer, pp. 1-24

Şahoğlu, V., 2005. The Anatolian trade network and the Izmir region during the Early Bronze Age. Oxford Journal of Archaeology 24(4), 339-361.

Seeliger, M., Bartz, M., Erkul, E., Feuser, S., Kelterbaum, D., Klein, C., Pirson, F., Vött, A., Brückner, H., 2013. Taken from the sea, reclaimed by the sea: The fate of the closed harbour of Elaia, the maritime satellite city of Pergamum (Turkey). Quaternary International 312, 70-83.

Seeliger, M., Pint, A., Feuser, S., Riedesel, S., Marriner, N., Frenzel, P., Pirson F., Bolten A., Brückner, H., 2019. Elaia, Pergamon's maritime satellite: the rise and fall of an ancient harbour city shaped by shoreline migration. Journal of Quaternary Science 34(3), 228-244.

Shumilovskikh, L.S., Seeliger, M., Feuser, S., Novenko, E., Schlütz, F., Pint, A., Brückner, H., 2016. The harbour of Elaia: A palynological archive for human environmental interactions during the last 7500 years. Quaternary Science Reviews 149, 167-187.

Stiros, S.C., 2020. Coastal subsidence, destruction layers and earthquakes from an underwater archaeological excavation: Kenchreai, eastern harbour of Roman Corinth, Greece. Mediterranean Geoscience Reviews, 1-15.

Stock, F., Halder, S., Opitz, S., Pint, A., Seren, S., Ladstätter, S., Brückner, H., 2019. Late Holocene coastline and landscape changes to the west of Ephesus, Turkey. Quaternary International 501, 349-363.

Stock, F., Kerschner, M., Kraft, J.C., Pint, A., Frenzel, P., Brückner, H., 2014. The palaeogeographies of Ephesos (Turkey), its harbours, and the Artemision–a

geoarchaeological reconstruction for the timespan 1500–300 BC. Zeitschrift für Geomorphologie, Supplementary Issues 58, 33-66.

Stock, F., Knipping, M., Pint, A., Ladstätter, S., Delile, H., Heiss, A.G., Laermanns, H., Mitchell, P.D., Ployer, R., Steskal, M., Thanheiser, U., Urz, R., Wennrich, V., Brückner, H., 2016. Human impact on Holocene sediment dynamics in the Eastern Mediterranean–the example of the Roman harbour of Ephesus. Earth Surface Processes and Landforms 41(7), 980-996.

Stock, F., Pint, A., Horejs, B., Ladstätter, S., Brückner, H., 2013. In search of the harbours: New evidence of Late Roman and Byzantine harbours of Ephesus. Quaternary International 312, 57-69.

Tartaron, T.F., 2013. Maritime networks in the Mycenaean world. Cambridge University Press.

Tartaron, T.F., 2015. The Settlement at Kalamianos: Bronze Age Small Worlds and the Saronic Coast of the Southeastern Corinthia. Hesperia Supplements 48, 25-38.

Tartaron, T.F., Pullen, D.J., Dunn, R.K., Tzortzopoulou-Gregory, L., Dill, A., Boyce, J.I., 2011. The Saronic harbors archaeological research project (SHARP): investigations at Mycenaean Kalamianos, 2007-2009. Hesperia 80(4), 559-634.

Vött, A., Bareth, G., Brückner, H., Lang, F., Sakellariou, D., Hadler, H., Ntageretzis, K., Willershäuser, T., 2011. Olympia's harbour site Pheia (Elis, Western Peloponnese, Greece) destroyed by tsunami impact. Die Erde 142(3), 259-288.

Vött, A., Hadler, H., Koster, B., Matthes-Schmidt, M., Röbke, B. R., Willershäuser, T., Reicherter, K., 2018. Returning to the facts: Response to the refusal of tsunami traces in the ancient harbour of Lechaion (Gulf of Corinth, Greece) by 'non-catastrophists'–Reaffirmed evidence of harbour destruction by. Zeitschrift für Geomorphologie, 275-302.

CHAPTER 2: Palaeoshoreline reconstruction and underwater archaeological potential of Liman Tepe: a long-occupied coastal prehistoric site in western Anatolia, Turkey

Abstract

Rising post-glacial sea levels had a major influence on the prehistoric settlement of coastal areas in the Aegean. At Liman Tepe, an important Chalcolithic- Bronze Age coastal site on the southern Bay of Izmir, archaeological evidence indicates a Neolithic (ca. 8000-4800 BCE) presence, but no settlement has been discovered on land. Sea levels during this period were between 4.5->20 m below present and there is high potential for submerged prehistoric sites. To investigate this, marine sediment coring and geophysical investigations (bathymetry, sub-bottom profiling; >600 line-km) were conducted over ~4-km^2 inshore area at Liman Tepe. Multi-proxy analysis (sedimentary facies, micropalaeontology, micro-XRF geochemistry) was conducted on 20 sediment cores to reconstruct relative sea levels (RSL) and the coastal palaeogeography. Palaeoshoreline positions were estimated by back-stripping of the decompacted sediment thickness from a digital bathymetric model.

The inshore stratigraphy consists of shoreface, foreshore and lagoonal deposits overlying terrestrial clay and palaeosols marking a marine transgressive surface (MTS). The MTS records inundation of the coastal plain prior to ca. 4000 BCE (transgressive systems tract; TST) and is marked in cores by increasing Ca/Ti and foraminifera abundance. During the middle Neolithic (ca. 6700 BCE; RSL = -16 m), the coastline was >500 m seaward and present-day Karantina Island was a broad coastal headland with a sheltered western embayment. A submerged palaeoshoreline (ca. 6600 BCE) is defined by low gradient scarp (modern water depth 11-12 m) and is associated with relict palaeochannels recording rivers draining a low-relief coastal plain. By the early Chalcolithic (ca. 4800 BCE), the coastline had transgressed ~800 m inland and Liman Tepe was a coastal headland separated from the mainland by shallow wetlands. The maximum transgression (~1 km at ca. 4000 BCE) was followed by a high-stand systems tract (HST) and rapid coastline progradation by barrier accretion. The palaeogeographic reconstruction

identifies areas with high underwater archaeological potential: 1) palaeoriver channels and lowland riverine habitats formed during the TST prior to 4000 BCE, 2) submerged palaeoshorelines and coastal promontories (water depths 10-14 m) with high potential for Neolithic sites, and 3) sheltered coastal embayments and lagoons, which would have provided favourable Neolithic-Bronze Age anchorage areas. The underwater coring and multi-proxy palaeoshoreline reconstruction methods demonstrated here can be applied more broadly in the exploration of submerged landscapes in shallow shelf areas.

Keywords: Liman Tepe, coastal palaeogeography, palaeoshorelines, submerged Neolithic prehistoric archaeology

2.1 Introduction

Global sea level rise since the last glacial maximum (LGM; ca. 30-20 ka BP) dramatically altered coastlines worldwide and was an important influence on the settlement of prehistoric peoples in coastal areas (Bailey and Flemming, 2008; Clark et al., 2009; Flatman and Evans, 2014; Flemming et al., 2017; Sakellariou and Galanidou, 2017). It has been estimated that worldwide >20 million km^2 of coastal landscapes were inundated as postglacial sea levels recovered from the LGM maximum lowstand (~120-135 m below present) (Clark et al., 2009; Lambeck et al., 2014). These drowned landscapes were former terrestrial and coastal habitats available for prehistoric human migration, settlement, and the procurement of marine resources (Bailey and Flemming, 2008; Fedje et al., 2011; Harff et al., 2016; Benjamin et al., 2017; Braje et al., 2017). The archaeological potential of these drowned landscapes is now widely recognized, and they have become a major focus of underwater archaeological and geoarchaeological research (Flatman and Evans, 2014; Flemming et al., 2017; Bailey et al., 2020; Flemming, 2020).

In the archaeologically rich Aegean, sea-level rise was an important determinant on the location of prehistoric coastal settlements and harbouring sites (Lambeck, 1995; Lambeck and Purcell, 2005; Tartaron et al., 2011; Tartaron, 2013; Harff et al., 2016). During the early post-glacial, sea levels rose rapidly until ca. 6-7 ka BP when ice sheet

volumes stabilized, and sea-level rise decelerated. Glacio-hydrostatic adjustment resulted in a further 4-5 m of relative sea level rise between 6-2 ka BP (Lambeck, 1995). Due to the complex tectonic setting of the Aegean, sites geographically close to each other may have significantly different tectonic and relative sea level (RSL) histories (Vacchi et al., 2014). For example, the well-studied archaeological sites at Kenchreai and Lechaion in Greece, located ~10 km apart, have undergone subsidence and uplift, respectively (Rothaus et al., 2008; Morhange et al., 2012; Stiros, 2020; Chapter 4). Predicting shoreline positions is further complicated because local RSL records often differ significantly from global eustatic and glacio-hydroeustatic models for the Aegean (Vacchi et al., 2014). An important archaeological implication is that the modern shoreline position and geomorphology is often a poor predictor of prehistoric coastal geography and the location of settlements and harbour sites (Tartaron et al., 2011; Tartaron, 2013). For example, the progradation of the Küçük Menderes delta in western Anatolia infilled an estuarine bay where the Neolithic shoreline was at least 2 km inland of its modern position. Successive palaeoshorelines are marked by the now abandoned and buried harbours of Ephesus (Brückner, 1997; Stock et al., 2013, 2014). Similarly, at Troy, shoreline regression over the last ca. 5000 years drastically altered the coastline, which led to difficulties in interpreting the site location based on historical descriptions of the geography (Kraft et al., 2003). Harbours at Miletus, Priene, and Elaia have also become landlocked by aggradation of the coastal plain (Brückner, 1997; Seeliger et al., 2013). At Burgaz, the harbours, while located along the coast, are mostly infilled (Greene et al., 2019).

In this study, we employed marine coring and geophysical surveys to investigate the underwater archaeological potential of Liman Tepe (prehistoric Clazomenae), a long-occupied coastal prehistoric site in western Anatolia, Turkey (Fig. 2.1). Liman Tepe was a major hub for maritime trade during the Early Bronze Age (EBA; ca. 3000-2000 BCE) as part of the Anatolian trade network and was contemporaneous with the city of Troy to the north (Şahoğlu, 2005). The EBA citadel of Liman Tepe was located on a small coastal headland overlooking the Bay of Izmir and was protected by bastioned fortification walls with a monumental entrance gate (Erkanal, 2008; Tuncel and Şahoğlu, 2018). In the early

Iron Age (ca. 9th-7th c. BCE), the city of Clazomenae was founded on the site of Liman Tepe and became an important trading port and olive-producing centre during the Archaic period (ca. 7th-5th c. BCE) (Ersoy, 2004; Aytaçlar, 2004). Since 1992, excavations have uncovered evidence for earlier occupation phases, including Chalcolithic (ca. 4800-3000 BCE) settlement layers and pottery evidence of Neolithic (ca. 8000-4800 BCE) presence (Erkanal, 2008). To date, however, no archaeological evidence for a Neolithic settlement has been discovered on land at Liman Tepe or its environs. Neolithic settlements are known from Izmir (60 km to the west) and in the surrounding region, indicating the broad potential for sites of this age in the Bay of Izmir (Fig. 2.1a) (Koparal et al., 2018).

The absence of Neolithic settlement layers may indicate a lack of settlement on the Liman Tepe headland (Fig. 2.1b) but does not rule out submerged sites, as significant changes in RSL and shoreline position have occurred since the Neolithic (Goodman et al., 2008). The Bay of Izmir has a shallow water depth (max ~90 m; Fig. 2.1a) and was subaerially exposed during the LGM, when global sea levels were >130 m below present. During the maximum lowstand, the gulf was a coastal plain (ria) backed by steep mountain ranges (Kayan, 1988). Drowned river valleys visible in low-resolution bathymetry data record remnants of the lowstand drainage network in the Bay of Izmir (Fig. 2.1a). Due to the low gradient of the former coastal plain, the bay was rapidly inundated by rising post-glacial sea levels until ca. 4000 BCE, when ice volumes stabilized, and the rate of sea-level rise decelerated (Goodman et al., 2008). During this period, most Mediterranean clastic coastlines regressed, and river deltas built seaward as sediment supply outpaced sea-level rise (Giaime et al., 2019). At Liman Tepe, the early-middle Holocene phase of rapid sea-level rise is recorded by submerged landscape features, including relict river channels and palaeoshorelines discovered by bathymetric mapping (Boyce et al., 2007; Krezoski, 2008). The river palaeochannels are up to 2.5 m deep, 10 m in width, and extend >300 m offshore (Figs. 2.2, 2.3), where they terminate at a break in slope that has been interpreted as a Neolithic palaeoshoreline formed during a brief still-stand phase (Krezoski, 2008). Recent sea level reconstructions for the Aegean (Goodman et al., 2009; Vacchi et al., 2014) indicate that during the second half of the Neolithic, water levels in the Bay of Izmir were

between 6-10 m below present. There is therefore a high potential for discovery of prehistoric sites in shallow water coastal areas of the Bay of Izmir (Fig. 2.1a).

The ages of the palaeoshoreline features identified by bathymetric mapping at Liman Tepe were not determined in previous work due to a lack of offshore core data and radiocarbon dates (Krezoski, 2008). The aim of this study was to investigate the submerged landscape features using marine coring and geophysical surveys and to reconstruct the Neolithic-Chalcolithic coastal palaeogeography and stratigraphy. The new core data and palaeoshoreline mapping identify several areas with high archaeological potential, including submerged promontories, river palaeochannels, and sheltered embayments that would have been favourable locations for prehistoric settlement, resource procurement, and harbouring. The maps provide important new baseline data that will guide future underwater exploration for prehistoric sites in the Bay of Izmir.

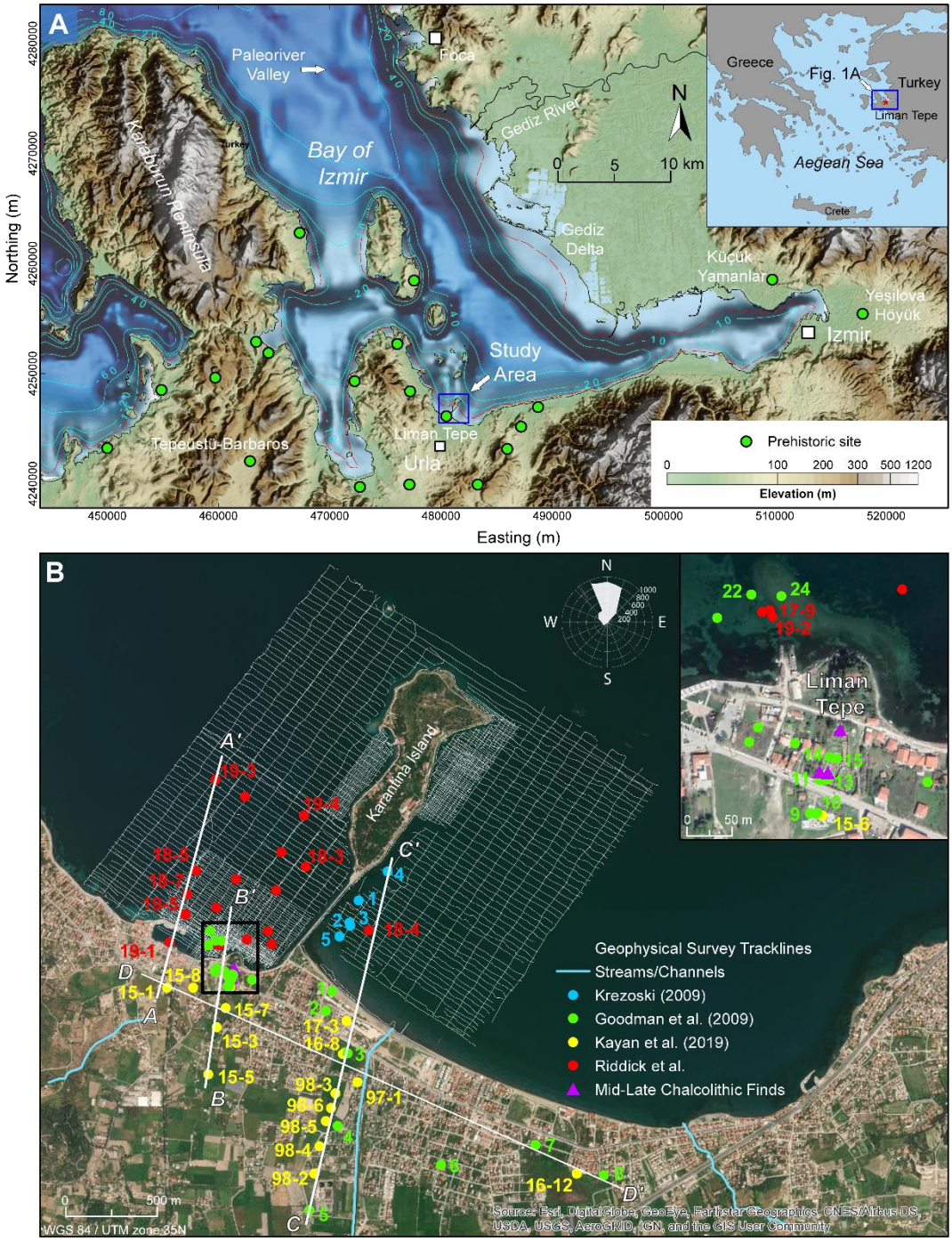

Figure 2.1: A. Digital elevation model (DEM) of Bay of Izmir region with generalized bathymetric contours (10 m interval). Location of study area and prehistoric archaeological sites also shown (adapted from Koparal et al., 2018). Location in western Anatolia shown in inset. B. Study area showing locations of cores, stratigraphic profiles (A-D; Figs. 2.8, 2.9), and geophysical survey tracklines (>400 line-km). Wind rose shows dominant wind direction in Bay of Izmir. Inset shows Liman Tepe headland with locations of cores and archaeological excavations.

2.2 Study Area

2.2.1 Physical Setting and Geology

Liman Tepe is located near Urla on the south shore of the Bay of Izmir, Turkey (Fig. 2.1a). The Bay of Izmir has a maximum water depth of about 90 m and within the study area (4 km^2) water depths are <25 m, within 1 km of the shoreline (Fig. 2.1a). Water circulation and current patterns in the bay are controlled by wind direction and water interchange with the Aegean Sea. The prevailing wind direction during most of the year is from the north (Fig. 2.1b) and wind-driven currents generate cyclonic and anticyclonic gyres. In the eastern Bay of Izmir currents flow clockwise, generating westerly currents along the south shore from Izmir towards Urla (Sayin, 2003; Sayin and Eronat, 2018). The primary sediment input is the Gediz River, on the north shore of the Bay of Izmir (Fig. 2.1a). Due to the dominant westward longshore transport along the south coast, sediment accumulation is greatest on the eastern side of Karantina Island (Figs. 2.1b, 2.2a). Coastal progradation here has been accelerated by a causeway linking the island to the mainland (Goodman et al., 2008), which was constructed by the forces of Alexander the Great in the 4^{th} c. BCE and has undergone several phases of renovation/reconstruction since (Heisserer, 1980, Krezoski et al., 2021). Due to the restriction of longshore flow by the barrier, beaches to the west of the island are sediment starved and prone to coastal erosion. The reduced sediment supply in the west is also evident in the presence of submerged landscape features, which would otherwise have been buried by sediment accumulation (Figs. 2.1b, 2.2, 2.3).

The Bay of Izmir lies at the western end of the Gediz Graben, which was formed by regional extension within the Aegean Extensional Province (Bozkurt and Sozbilir, 2004; Ciftci and Bozkurt, 2011; Jolivet et al., 2013). Extension has been ongoing since the late Oligocene-early Miocene and is associated with active tectonism and destructive earthquakes (Taymaz et al., 2007; Tan et al., 2008). The estimated modern subsidence rate in the Bay of Izmir is ~1 $mmyr^{-1}$ (Aksu et al., 1987). The bedrock in the Urla region comprises Neogene clastic and carbonate sediments, which are intercalated with middle-late Miocene calc-alkaline volcanic rocks (Agostini et al., 2010). The Liman Tepe headland

is formed from Neogene limestones and mudstones (Urla limestone), which are underlain by volcanics (Kayan et al., 2019). The bedrock surface is overlain by a variable thickness of Quaternary alluvial and coastal plain sediments (Aksu et al., 1987; Duman et al., 2004; Goodman et al., 2009; Kayan et al., 2019). Within the study area, Quaternary sediment thickness are >18 m (Kayan et al., 2019). The modern beach and foreshore deposits consist of clastic sediments (silt, sand, gravel) with a variable carbonate component (mainly mollusk shell fragments) (Goodman, 2006). The shoreface sediments are dominantly silt and mud with abundant marine organic matter. *Posidonia* seagrass is the primary component of marine plant organics in sediments and forms extensive meadows in the shallow inshore areas (~2-30 m water depth) (Vortruba et al., 2016).

2.2.2 Previous Work

Goodman et al. (2008, 2009) reconstructed the EBA to Archaic coastal palaeogeography and environments using a multi-proxy geoarchaeological analysis of primarily land core data. They documented a transgressive systems tract (TST), which inundated the coastal plain, reaching 700 m inland at about ca. 4500 BCE. This was followed by a high-stand systems tract (HST) and progradation of the shoreline through the accretion of shore-parallel sandbars (Goodman et al., 2008). Back-barrier lagoons were identified as possible locations of EBA anchorage areas (Goodman et al., 2009) but the shoreline positions and coastal environments during the pre-Bronze period were not established as part of that study.

Krezoski (2008) investigated the coastal sediment record of the Alexander causeway using a multi-proxy study of five marine cores collected on the east side of the barrier (Fig. 2.1b). The onset of causeway construction was identified by a shift in grain size and foraminifera biofacies. The 4th c. BCE date for the barrier construction was also confirmed by radiocarbon dating of the post-barrier sediments. Krezoski (2008) identified submerged river palaeochannels and palaeoshoreline features in the bathymetry to the west of the causeway (Fig. 2.2a). These were inferred to be of Neolithic age based on water

depth and stratigraphic relations, but shoreline ages were not determined due to a lack of core data to the west of the causeway.

Kayan et al. (2019) investigated the Holocene stratigraphy of Liman Tepe using 32 land cores collected between 1998-2018 and correlated using a limited number of radiocarbon dates from Goodman et al. (2008). Using the RSL curve of Kayan (1988), they proposed a marine transgressive limit about 1 km inland of the modern shoreline. Despite the limited core chronology, the available borehole database (Goodman et al., 2008, 2009; Kayan et al., 2019) (Fig. 2.1b) provides a useful framework for correlating offshore sedimentary facies with the land record in this study.

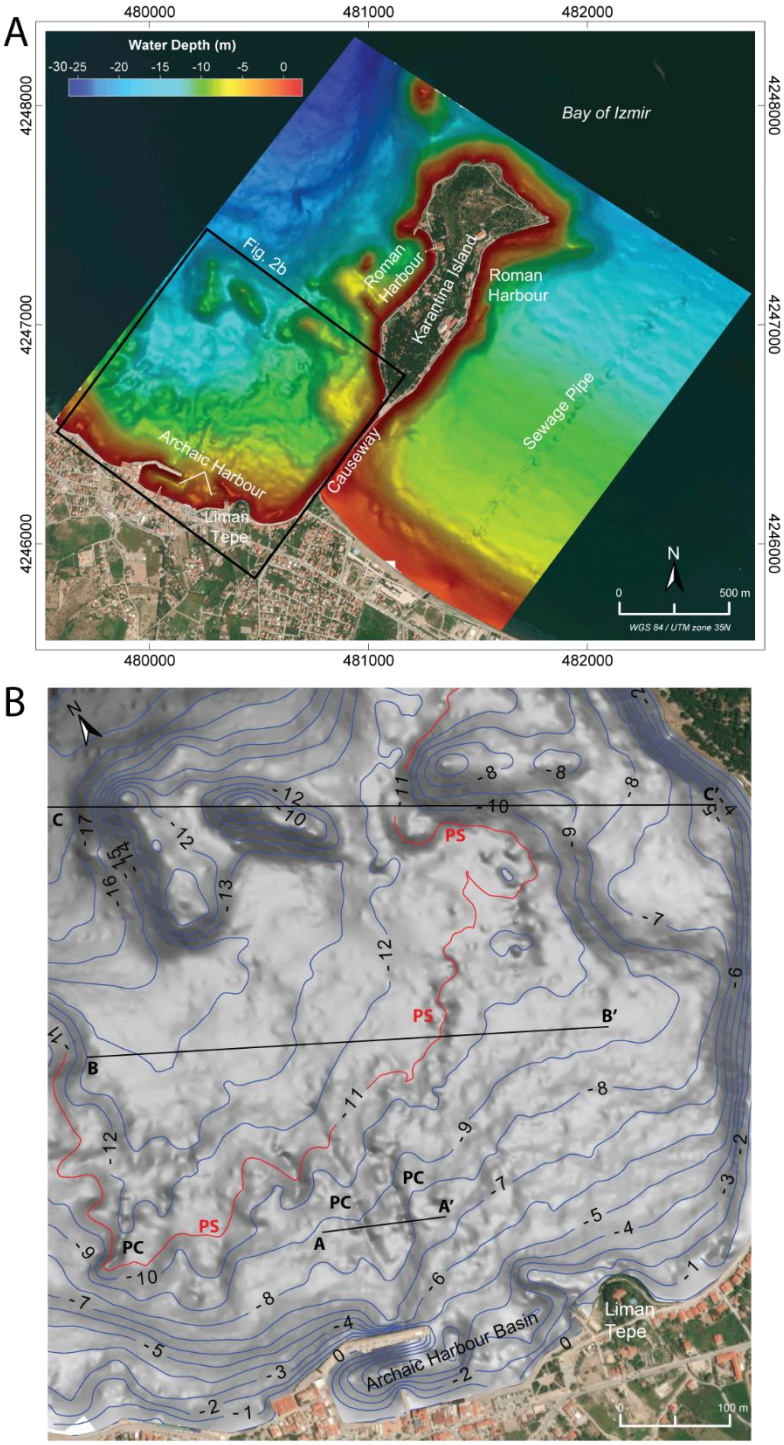

Figure 2.2: A. Colour-shaded digital bathymetric model (DBM) for 1-km^2 inshore area around Liman Tepe. Note smooth, low-relief seabed to east of Karantina Island due to westward longshore sediment transport and shoreline progradation on eastern side of the Alexander causeway. B. Grey-scale bathymetric map showing submerged palaeochannels (PC), palaeoshorelines (PS) and other submerged landscape features on the west side of Karantina Island. Locations of bathymetric profiles (Fig. 2.3) indicated.

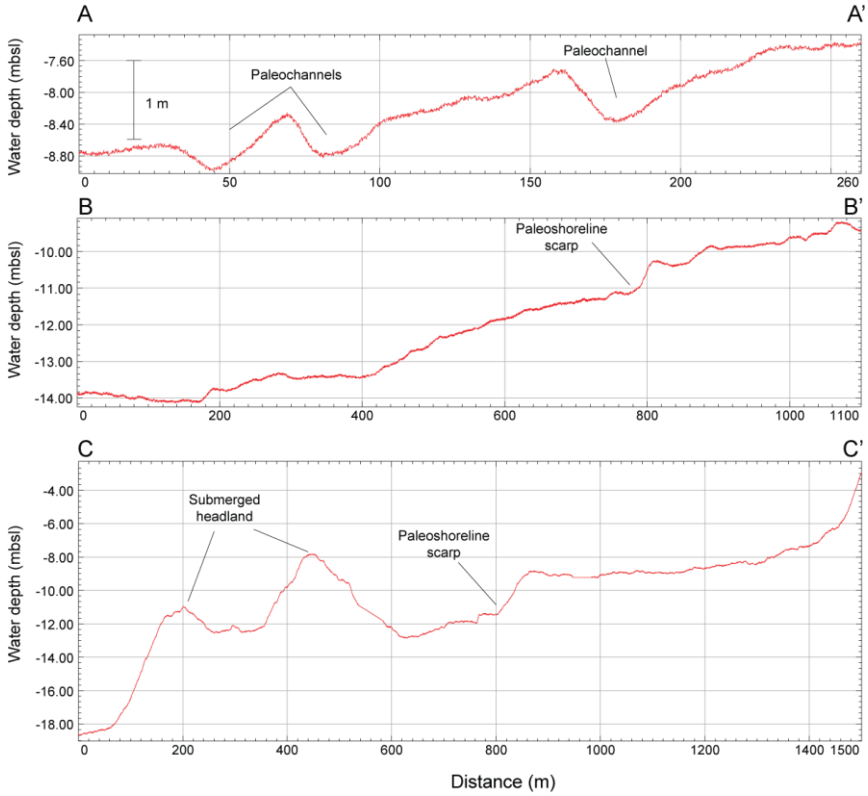

Figure 2.3: Bathymetric profiles showing submerged landscape features. Profile locations in Fig. 2.2b. A. Submerged palaeochannels recording a submerged coastal plain and river system at -8 to -9 mbsl. B. Low-relief scarp indicating a possible palaeoshoreline feature. C. Submerged promontories to west of Karantina Island. The promontories and river floodplain were exposed during the Middle Neolithic when sea levels were >16 m below present sea level.

2.3 Methods

2.3.1 Geophysical Surveys

Detailed bathymetric and sub-bottom seismic surveys were conducted across a 4-km^2 area around Liman Tepe and Karantina Island. More than 600-line-km of single-beam (200 kHz) bathymetry and high-frequency (18-24 kHz) chirp seismic profiles were acquired using a sub-bottom profiling system (Knudsen 320BP) with 5-75 m line spacings (Fig. 2.1b). Processing of bathymetry data included corrections for tides and sensor heave and followed the general processing scheme of Sonnenburg and Boyce (2008). Bathymetric data were gridded using triangular interpolated network (TIN) and sun-shaded to highlight the seabed relief (Fig. 2.2). Processing of seismic profiles included the application of automatic gain control (AGC) to equalize trace amplitudes, band-pass filtering (10-20 kHz)

and depth-conversion of the two-way travel times in the water column and sediment using a velocity of 1550 ms^{-1}. The reflector surfaces were digitized, and calculated depths interpolated to create maps of the reflector surface relief and sediment isochore thickness.

2.3.2 Coring and Sediment Analysis

Twenty sediment cores (2-5 m length) were extracted in water depths of up to 15 m in the inshore area at Liman Tepe using SCUBA equipment (Fig. 2.1b). Cores were collected using a percussion coring system with 75-mm-diameter aluminum tubes and a weighted seabed core platform and extracted using lift bags or a surface winch system, then sealed and refrigerated (4-6 °C) to limit sediment oxidation and bacterial growth prior to analysis. Cores were split and one half sampled for micropalaeontological and petrographic analysis and an archive half retained for micro-XRF core scanning (μ-XRF-CS). Core compaction was determined as the ratio of the recovered core length to total tube penetration and a linear decompaction correction applied to all cores (Morton and White, 1997). The core compaction ranged from 5-47 % and was greatest in long cores containing thick sections of organic-rich muds. Core sedimentary facies and texture were described in detail and genetically related facies were grouped into lithofacies assemblages (Dalrymple and James, 2010).

Petrographic analysis was conducted on eight bedrock and beachrock samples using polarized light microscopy to determine modal compositions (cores 18-3, 18-5, 19-1, 19-4, 19-5). Marine core data were combined with borehole data from previous studies (Goodman et al., 2008, 2009; Kayan et al., 2019; Krezoski et al., 2021) to correlate the offshore and onshore stratigraphy. The assembled core database includes >40 boreholes and is one of the largest assembled in the geoarchaeological study of a coastal archaeological site in the Aegean (Fig. 2.1b).

2.3.2.1 Micropalaeontology

For micropalaeontological analysis (foraminifera), sediment samples (2.5 cc) were collected from four cores (18-5, 19-1, 19-3, 19-4; Fig. 2.1b) at selected intervals. Samples

were taken above and below lithologic contacts with the aim of documenting terrestrial/wetland to marine transitions. Samples were divided into eight aliquots using a settling tube, then wet sieved into 45 µm, 63 µm, 125 µm and 500 µm fractions (Scott and Hermelin, 1993). Where possible, counts were made to at least 100 individuals and identified to the *genus* level, as the goal of the analysis was to determine presence/absence of foraminifera at key lithostratigraphic and sequence boundaries. Identification was assisted by the previous work of Goodman (2006) and Krezoski (2008), which included identification of foraminifera to the species level.

2.3.2.2 Micro-XRF Geochemistry

Micro-XRF elemental analysis was conducted on nine cores extracted to the west of Karantina Island to assist in identification of the marine-terrestrial transition. Split cores were scanned using an Itrax µ-XRF-CS (Cox Analytical Systems) with a Mo anode tube, constant power settings of 30 kV/ 25 mA, and 20 s exposure time (Lowemark et al., 2011). Scans were collected at a 500 µm sampling interval (2000 samples per metre), batch analyzed using QSpec^{TM} software, and a 5-point running average filter was applied to smooth element profiles. The Ca/Ti ratio provides an indicator of relative influence of marine versus terrigenous inputs to the basin was used employed a correlation tool in this study (Piva et al., 2008; Ingram et al., 2010; Koster et al., 2015; Pint et al., 2015; Rothwell and Croudace, 2015).

2.3.2.3 AMS ^{14}C Chronology

AMS ^{14}C dating was conducted on 31 organic samples (A.E. Lalonde AMS Laboratory, University of Ottawa) from 9 cores and combined with 13 additional dates available from previous studies (Goodman, 2006; Krezoski, 2008) (Table 2.1). Radiocarbon ages were calibrated using Calib 7.1 with the IntCal13 and Marine13 calibration curves (Stuiver et al., 2019). A marine reservoir correction was applied to shell samples using a mean ΔR value of 109 +/-27 for the Aegean (Reimer and McCormac, 2002). Samples of plant organic matter were calibrated using IntCal13 as the content of marine versus terrestrial organics was unknown. The terrestrial curve produced age models

which were consistent with archaeological age constraints provided by pottery and harbour architectural features (i.e. mole structures). Bayesian sediment age-depth models were constructed for five cores (17-9, 18-3, 18-5, 19-1, and 19-4; Fig. 2.1b) using BACON (Blaauw and Christen, 2011).

Table 2.1: AMS ^{14}C radiocarbon dates. All dates were calibrated using Calib 7.1 with the IntCal13 and Marine13 calibration curves (Stuiver et al., 2019). Dates from Goodman et al. (2006) (G-#) and Krezoski (2008) (K-#) were recalibrated. Sample elevations corrected (see Section 2.3.3). * Marine reservoir correction ($\Delta R = 109 +/-27$) applied (Reimer and McCormac, 2002). ** Suess Effect.

Sample Code	Core #	Material	Elevation (mbsl)	Corr. Elevation (mbsl)	^{14}C Age (BP)	2σ Max and Min Calibrated Age		
Beta-191877	G-4	Shell*	1.90	1.43	4370 ± 40	2560	2275	BCE
Beta-194731	G-7	Peat	3.26	2.78	2700 ± 40	919	801	BCE
Beta-194730	G-7	Peat	1.85	1.38	4080 ± 40	2706	2548	BCE
Beta-194729	G-8	Peat	4.35	4.27	2770 ± 40	1007	829	BCE
Beta-194732	G-8	Shell*	0.59	0.50	4370 ± 40	2560	2275	BCE
Beta-191881	G-10	Bone	7.66	7.61	3950 ± 40	2504	2336	BCE
Beta-166694	G-11	Peat	8.60	-8.60	4570 ± 40	3376	3103	BCE
Beta-191880	G-22	Shell*	7.60	7.60	6280 ± 40	4781	4527	BCE
Beta-191878	G-23	Shell*	1.60	1.57	3230 ± 40	1088	818	BCE
Beta-191879	G-23	Shell*	2.30	1.95	5420 ± 40	3861	3624	BCE
Beta-243245	K-1	Plant fragments	6.68	6.63	1810 ± 40	122	265	CE
Beta-234186	K-4	Olive pit	5.52	5.48	2360 ± 40	543	369	BCE
Beta-234187	K-4	Plant fragments	6.47	6.44	5090 ± 40	3968	3794	BCE
UOC-7342	17-9	Plant fragments	5.16	5.13	2960 ± 22	1260	1111	BCE
UOC-9339	17-9	Plant fragments	5.54	5.51	3550 ± 25	1960	1868	BCE
UOC-9340	17-9	Plant fragments	5.96	5.93	3966 ± 25	2503	2453	BCE
UOC-7343	17-9	Plant fragments	6.24	6.22	4535 ± 22	3238	3106	BCE
UOC-9341	17-9	Plant fragments	6.38	6.36	4682 ± 25	3474	3371	BCE
UOC-7344	17-9	Plant fragments	6.51	6.50	4996 ± 22	3802	3706	BCE
UOC-10196	18-3	Plant fragments	7.60	7.56	1519 ± 25	529	606	CE
UOC-10197	18-3	Plant fragments	8.12	8.08	2241 ± 29	322	206	BCE
UOC-9342	18-3	Plant fragments	8.93	8.90	4518 ± 25	3241	3103	BCE
UOC-9350	18-3	Shell*	9.39	n/a	7224 ± 28	5716	5559	BCE
UOC-9343	18-4	Plant fragments	7.72	7.67	962 ± 25	1075	1154	BCE

UOC-9344	18-4	Plant fragments	8.56	8.48	2123 ± 25	204	84	BCE
UOC-9345	18-4	Plant fragments	10.73	10.68	3180 ± 25	1500	1416	BCE
UOC-9351	18-4	Shell*	11.68	11.68	4802 ± 25	3076	2879	BCE
UOC-9346	18-5	Plant fragments	11.82	11.77	2322 ± 25	409	345	BCE
UOC-9347	18-5	Plant fragments	13.12	13.05	4655 ± 28	3517	3395	BCE
UOC-9352	18-5	Shell*	14.78	14.71	7355 ± 25	5852	5668	BCE
UOC-9353	18-5	Shell*	14.85	14.80	7523 ± 28	6009	5836	BCE
UOC-12077**	19-1	Plant fragments	5.00	4.97	270 ± 23	1626	1666	CE
UOC-12078	19-1	Plant fragments	5.17	5.13	1330 ± 22	652	695	CE
UOC-12824	19-1	Plant fragments	6.02	5.97	3445 ± 27	1785	1686	BCE
UOC-12103	19-1	Shell*	6.52	6.47	6335 ± 25	4824	4615	BCE
UOC-12825	19-1	Bulk	7.03	6.91	7310 ± 43	6241	6067	BCE
UOC-12220	19-1	Bulk	7.17	6.98	7968 ± 35	7044	6749	BCE
UOC-12079	19-2	Plant fragments	6.98	6.96	6197 ± 29	5229	5048	BCE
UOC-12104	19-3	Shell*	14.93	14.74	8061 ± 27	6560	6386	BCE
UOC-12080	19-4	Plant fragments	8.96	8.90	1603 ± 23	401	477	CE
UOC-12081	19-4	Plant fragments	11.27	11.20	4445 ± 25	3129	3011	BCE
UOC-12105	19-4	Shell*	12.29	12.26	7743 ± 27	6229	6042	BCE
UOC-12106	19-4	Shell*	12.49	12.48	7826 ± 28	6349	6112	BCE
UOC-12107	19-5	Shell*	11.57	11.54	6284 ± 27	4767	4547	BCE

2.3.3 RSL and Palaeoshoreline Reconstructions

Palaeoshoreline positions were estimated for the middle Neolithic to middle Chalcolithic periods (ca. 6700-4000 BCE) using a modification of the sediment back-stripping approach described by Sonnenburg et al. (2012). Back-stripping techniques are employed increasingly in coastal palaeogeographic reconstructions as they provide a more robust estimate of the shoreline positions when compared to modelling based on the modern seabed bathymetry and coastal topography (Bates et al., 2009; Athanassas et al., 2012; Sonnenburg et al., 2012; Westley et al., 2014; Conolly, 2020; Conolly and Obie, 2021). As a first step, a revised RSL curve was constructed for Liman Tepe by combining sea-level indicators from two previous studies (Goodman et al., 2008; Krezoski, 2008) with 10 new RSL indicators from marine sediment cores. The elevations of all RSL indicators were corrected for post-depositional compaction (autocompaction) using the 1-D geotechnical

model of Paul and Barras (1998). Compaction corrections are important in sea-level reconstructions using clay and organic rich sediments, which are susceptible to post-depositional lowering due to autocompaction (Allen, 2000; Bird, 2004; Brain et al., 2015). The elevations of sediment contacts for the marine transgressive surface (MTS) in marine and land cores were also corrected for autocompaction using reported sediment texture to estimate the liquid limit for modelling (25% for lean silty sands and 75% for plastic clays) (Paul and Barras, 1998). The autocompaction correction factor ranged from 0.1-1.13 m and was greatest for long cores containing thick sections of mud and silt. An isopach map of the sediment thickness above the MTS was then constructed using the compaction-corrected values and back-stripped (subtracted) from the modern seabed bathymetry (Fig. 2.2) to produce a surface representing the elevation of MTS relative to modern sea level. In a final step, the shoreline positions were estimated by projecting the RSL elevations onto the back-stripped MTS and plotted as an overlay on the modern bathymetric map.

2.4 Results

2.4.1 Bathymetry and Seismic Data

Bathymetric mapping revealed a low relief sea-bed topography to the west of Karantina Island and a smooth, gradually sloping seabed to the east (Fig. 2.2a). The smooth bottom relief in the east results from the westward longshore transport and trapping sediment by the causeway barrier (Goodman et al., 2008; Krezoski et al., 2021). To the west of the barrier, the reduced sediment accumulation rate has limited coastal progradation and has preserved landscape features of the submerged coastal plain (Fig. 2.2). These features include relict river channels, palaeoshorelines, and submerged coastal promontories (Figs. 2.2b, 2.3). Palaeochannels are up to 20 m in width, 1-2.5 m in depth, and have a linear thalweg. The channels extend >300 m northwest of the modern harbour breakwater where they terminate at a break in slope at -11 to -12 m water depth (Figs. 2.2b, 2.3). The channels are infilled by up to 4 m of marine sediments, which overlie volcanic bedrock and terrestrial mud deposits (see section 2.4.2). The break in slope at -11 m may represent a palaeoshoreline formed during a brief sea level still-stand or a bedrock ridge

underlying the marine sediment cover. Sediment slumps visible at the base of the break in slope indicate that the scarp has been modified to some extent by mass movements (Fig. 2.2b). On the west side of Karantina Island, a submerged ridge and promontories define a former coastal headland that enclosed an embayment to the north of Liman Tepe when sea levels were 12-14 m below present (Figs. 2.2, 2.3).

No submerged landscape features are preserved on the seabed to the east of the causeway, but seismic data provide insights into the buried coastal topography and palaeogeography (Fig. 2.4). Seismic profiling revealed an uppermost package of seismically transparent and crudely stratified seismofacies overlying a continuous high-amplitude reflector at 13-15 ms (Fig. 2.4a). The reflector is a basin-wide seismic horizon which records the top of a compact shoreface sand unit underlying lagoonal mud and silt (Krezoski, 2008). The contoured upper surface of the horizon defines a shallow basin and northwest-trending ridge (BR-1; Fig. 2.4b) that connects the mainland shoreline with the east coast of Karantina Island. The 3-4 m deep central basin is infilled in part with foreshore and lagoonal sediments (Fig. 2.4d). The ridge feature enclosing the depression is interpreted as a beach barrier (BR-1; Fig. 2.4b), which formerly connected Karantina Island with the mainland to the east. Other parallel ridges in the reflector surface (e.g. BR-2) likely record earlier phases of a transgressive barrier-lagoon system (Krezoski, 2008). The bedrock surface below Holocene sediments was not imaged due to the limited penetration depth of the high frequency seismic source (Fig. 2.4a). However, previous low-frequency boomer seismic profiling indicates a total sediment thickness of >8 m over bedrock to the east of the Karantina Island (Mueller et al., 2009).

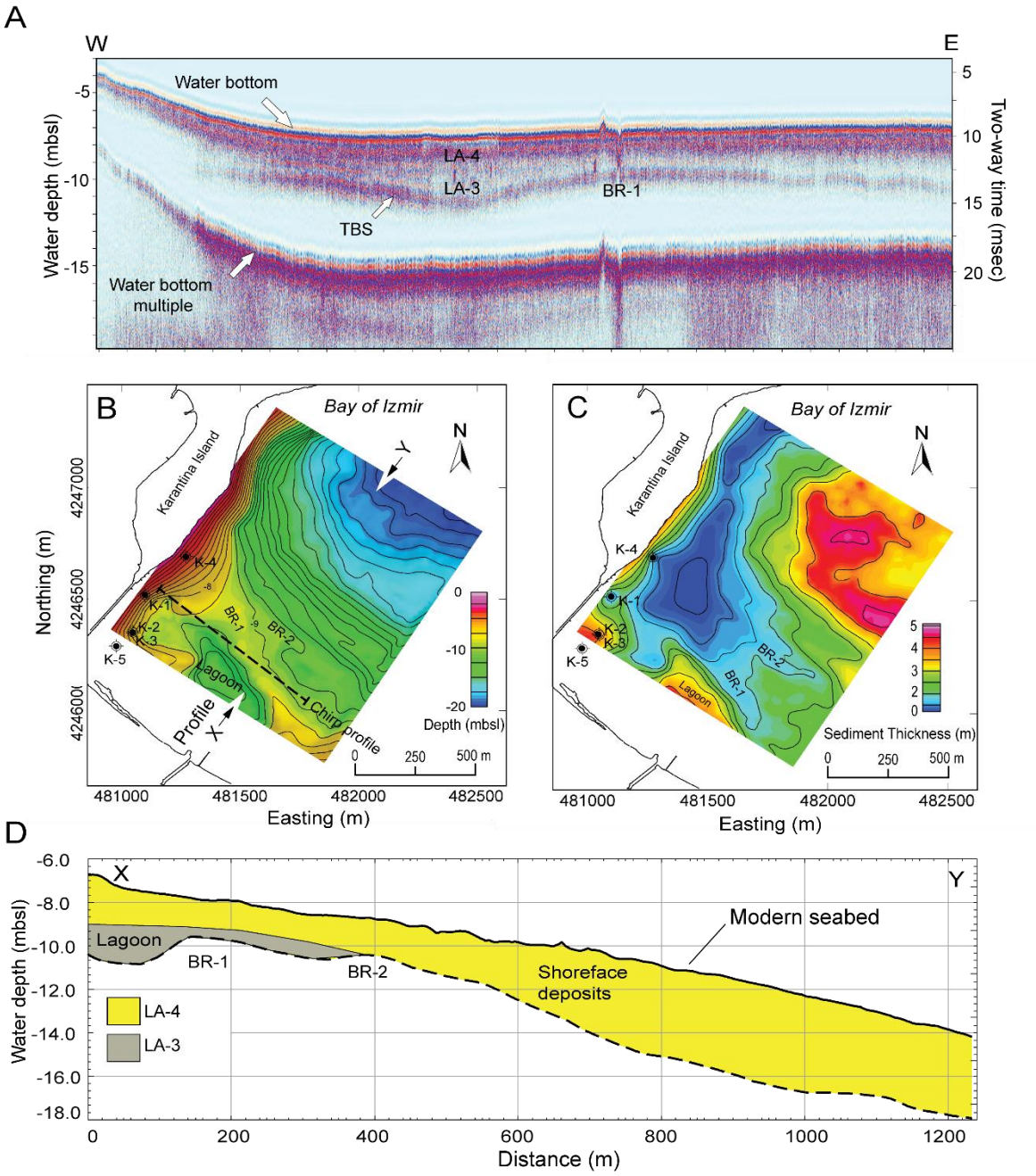

Figure 2.4: A. W-E sub-bottom seismic profile (location in 2.4b) showing high-amplitude reflector at 12-15 ms, inferred to be a buried Neolithic transgressive barrier system (TBS). B. Contoured upper surface of reflector (contour interval 0.5 m) showing two northwest-southeast trending beach ridges (BR-1, BR-2). C. Isochore (sediment thickness) map showing thickening of sediments within interpreted back-barrier lagoon (contour interval 1 m). D. North-south profile (X-Y; 2.4b) showing buried beach ridges and lagoonal deposits. Dashed line indicates interpolated elevation of seismic reflector at top of foreshore sands.

2.4.2 Holocene Stratigraphy

Five distinctive lithofacies assemblages (LA 1-5) were recognized in marine cores (Figs. 2.5-2.7) and correlated with lithofacies identified in land-core data. Lithostratigraphic profiles showing the correlated LA's along west-east and south-north core transects are shown Figures 2.8 and 2.9. The contact between lithofacies assemblages LA-2 and LA-3 is a basin-wide parasequence boundary marking a marine transgressive surface (MTS), which has been identified in land cores (Goodman et al., 2008, 2009; Kayan et al., 2019).

2.4.2.1 LA-1 (Volcanic Bedrock, Regolith)

Bedrock was encountered at a depth of 3.8 m in a single core (19-5) and comprised a thin (~20-30 cm) unit of weathered, angular volcanic rock fragments (Fig. 2.7c). The unit contained no marine fauna and was devoid of organics. The bedrock fragments were an intermediate extrusive composition (trachyte-andesite), consisting of sanidine phenocrysts set in a finer matrix of K-feldspar, plagioclase, minor quartz, biotite, sericite, pyroxene, and hornblende amphibole. LA-1 is identified as the middle Miocene-age Menteş trachyte, which forms local bedrock to the west and south of the site (Kaya, 1979; Göktaş, 2016). The angular shape and weathering of clasts indicates that LA-1 is a regolith (saprolite) formed by chemical weathering of volcanic bedrock.

2.4.2.2 LA-2 (Terrestrial Clays, Palaeosol, Alluvium)

Overlying bedrock, LA-2 was a 10-60 cm thick unit of dark grey to greenish-brown clay containing abundant volcanic (trachyte) clasts up to 1 cm in size and fine organic matter (Figs. 2.5, 2.6c, 2.d, 2.7b). LA-2 contained no shell fragments and foraminifera were absent or in very low abundance (<5/cc) (Fig. 2.5). Difflugid thecamoebians were present in low abundance (<3/cc) in three cores (18-5, 19-1, 19-4). A bulk organic sample from core 19-1 yielded a middle Neolithic age of 7044-6749 cal. BCE (Fig. 2.5). Radiocarbon dates from above LA-2 in cores 18-5, 19-3, 19-4, 19-5 also indicate Neolithic ages, ranging from about 6500 to 6000 BCE (Figs. 2.6c, d, 2.7b, c).

LA-2 is interpreted as a terrestrial mud deposit derived by weathering of the underlying volcanic saprolite (i.e. LA-1). The Ca/Ti values in LA-2 are very low due to the abundance of Ti in the clay and volcanic regolith (Fig. 2.5). The low abundance of difflugids suggests deposition of thecamoebian tests by fluvial inputs to an inland lake or wetland (e.g. palaeochannels; Fig. 2.2). The low abundance of foraminifera may record influx of marine waters during periodic storm run-up and overwash into the wetlands (e.g. Goodman et al., 2009). Goodman et al. (2008) had previously identified freshwater wetland facies in land cores at Liman Tepe, as defined by a high abundance of difflugids (25.5%, ~74.5/cc). Kayan et al. (2019) described a similar dark grey to black mud facies overlying alluvial silt and sand, which we correlate with LA-2 (Figs. 2.8, 2.9). The lowermost terrestrial deposits identified by Goodman et al. (2008, 2009) (cores G-4, G-6, G-7, G-11) are also assigned provisionally to LA-2 based on their stratigraphic position below marine deposits and low foraminifera abundance (<2/cc). Radiocarbon dates from marine sediments in cores G-4, G-7, and G-11 range in age from 3400-2200 BCE (Figs. 2.8, 9), indicating that the lowermost package of LA-2 terrestrial sediments was deposited prior to the maximum marine transgression at ca. 4000 BCE. The contact between the lowermost terrestrial sediments and overlying marine deposits identified by Kayan (2019) and Goodman et al. (2008, 2009) is the onshore extension of MTS identified in marine cores (Figs. 2.8, 2.9). Kayan et al. (2019) and Goodman et al. (2008, 2009) also mapped an uppermost package of alluvial mud, silt, and sand facies (Figs. 2.8, 2.9), which we assign as LA-2 terrestrial deposits. This later sequence of terrestrial sediments records alluvial plain sedimentation from after 4000 BCE (LA-2b).

2.4.2.3 LA-3 (Lagoonal Sediments)

LA-3 consisted of massive to crudely stratified clayey silt facies with mollusk and gastropod shell fragments, overlying LA-2 across a transitional contact (Figs. 2.5, 2.6c, 2.7b). The unit contained disseminated fine organics but *Posidonia* fragments were absent. Foraminifera were in low abundance at the base of LA-3 (5-84/cc) and increased upward in the unit (162-200/cc) (Fig. 2.5). The dominant foraminifera genera were *Elphidium* (25->50%) and *Ammonia* (20->50%). In core 19-1, a few difflugid thecamoebians were present

at the base of LA-3. A bulk organic sample in core 19-1 yielded a middle Neolithic age of 6241-6067 cal. BCE (Fig. 2.5) and shells from core 18-5 ranged in age from 6009-5668 cal. BCE (Fig. 2.6c).

Based on the silty texture and increasing abundance of marine microfossils and shell fragments, LA-3 is interpreted as a lagoon deposit. The LA-2/LA-3 contact marks the MTS and a basin wide parasequence boundary recording marine flooding of the coastal plain (Figs. 2.8, 2.9). The MTS is identified by an increase in Ca/Ti at the base of LA-3 (Figs. 2.5, 2.6c, 2.7b) and correlated throughout the basin (Fig. 2.8). The increase in Ca coincides with the increased abundance of shell fragments and calcareous foraminifera in LA-3. Goodman et al. (2008, 2009) and Kayan et al. (2019) identified two similar packages of foreshore and lagoon silt and mud facies in land cores: one overlying LA-2, the other overlying LA-4 foreshore-shoreface deposits. The land core lithofacies descriptions, however, are not sufficiently detailed for identification of foreshore versus lagoon facies, and so have been grouped together and provisionally correlated with LA-3 (Figs. 2.8, 2.9). Foreshore sands and lagoon silt and mud deposits were also identified by Krezoski (2008) to the east of the Karantina island (Fig. 2.9). These deposits infill a broad basin identified in seismic data (Fig. 2.4), which records an extensive back-barrier lagoon to the west of the island during the late Chalcolithic to EBA periods (Krezoski et al., 2021).

2.4.2.4 LA-4 (Foreshore-Shoreface Deposits)

LA-4 comprised a fining-upwards package of medium to fine sand and *Posidonia*-rich silt and mud facies (Figs. 2.5-2.7). Sand facies (LA-4a) were massive, poorly sorted, and contained sub-rounded to well-rounded mollusk shell fragments and little marine organic matter. The overlying silt and mud facies (LA-4b) were massive to crudely stratified and contained abundant *Posidonia* root fragments and *matte* layers and lenses (0.1-1 cm in thickness). Foraminifera abundance ranged from 258-1000/cc (Fig. 2.5) and the dominant genera were *Elphidium* (20-41%) and *Ammonia* (16-30%). In most cores, LA-4 sediments yielded a wide range of ages from Neolithic to present, as the *Posidonia* muds

extend to the modern seafloor (e.g. core 18-5 <5852-5668 to present and core 19-4 <6229-6042 to present; Fig. 2.6c, d).

The poor sorting and moderate degree of rounding of the sand and absence of *Posidonia* grass in LA-4a indicates high energy conditions and deposition in foreshore to upper shoreface environment. The relatively high abundance of foraminifera and *Posidonia* in the overlying LA-4b indicates deposition in a shallow marine environment. The transition from poorly sorted sand to *Posidonia* silt and mud facies records a shift to a lower energy shoreface environment suitable for the growth of extensive *Posidonia* seagrass meadows. In the modern environment at Liman Tepe, *Posidonia* meadows are extensive in water depths between 2-30 m and favour low water turbidity and low to moderate energy (Vortuba et al., 2016). The Ca/Ti profiles (Figs. 2.5-2.8) reach peak values (>120 peak area units) in LA-4 at about 4000 BCE in all cores, which corresponds with the maximum marine transgression and the end of TST. This is followed by an overall decline in Ca/Ti, possibly signaling increased terrestrial sediment delivery to the marine basin as shorelines began to prograde during the HST after 4000 BCE. Goodman et al. (2008, 2009) and Kayan et al. (2019) described similar shoreface deposits in land cores (Figs. 2.8, 2.9). The shoreface deposits were dominated by *Elphidium-Ammonia* biofacies (defined by >10% *Elphidium*) and the presence of *Ammonia parkinsoniana* (Goodman et al., 2008, 2008).

Shallow water sediments recording a range of foreshore environments were identified at or near the base of several marine cores (18-3, 19-2, 19-4; Fig. 2.1b) and were assigned to LA-4c. In core 19-4, underlying LA-4a, was a thin horizon (~20 cm) of disarticulated oyster shells (*Ostrea edulis*) and shell fragments, overlain by a thin gravel layer, consisting of angular volcanic rock granules and pebble-sized clasts (Fig. 2.6d). The oyster shells and gravel unit contained abundant foraminifera (122-406/cc), dominated by *Elphidium* (25-29%) and *Ammonia* (23-29%). The oyster shell layer was dated to 7th millennium BCE (6349-6112 cal. BCE) and may indicate a storm deposit or possibly a refuse layer, recording human processing of oyster shells. In core 18-3, LA-4b rested on a ~50 cm thick beachrock unit across a sharp erosive contact (Fig. 2.6b). The beachrock

records a shallow intertidal environment (5716-5559 cal. BCE), where groundwater flow permitted the cementation and production of beachrock (Vousdoukas et al., 2007). In core 19-2, LA-4c consisted of thin (~15 cm) basal gravel layer, with rounded carbonate and volcanic rock granules and pebbles (Fig. 2.7a). The gravel layer is lag deposit, recording erosion of underlying sediments and bedrock in a beach or foreshore environment. Overall, erosional lag deposits were not a common feature of the foreshore deposits in LA-4.

2.4.2.5 LA-5 (Harbour Sediments, Archaeological Deposits)

LA-5 comprised an uppermost package of mud and fine silt with abundant marine mollusk shell fragments that is restricted to the Archaic harbour basin (cores 19-1, 17-9, 19-2). The sediments contained minor *Posidonia* lenses and fragments and abundant foraminifera (851-1094/cc). Within the eastern Archaic harbour basin (cores 17-9, 19-2; Figs. 2.1b, 2.6a, 2.7a), LA-5 contained abundant pottery, including Archaic to Classical age vessel fragments and sherds. In core 19-1 (Figs. 2.1b, 2.5), LA-5a silty mud represents a Late Bronze Age to Classical phase of harbour development and LA-5b, which is finer and brown-orange in colour, the Byzantine to Modern harbour deposits.

LA-5 represents harbour basin sediments deposited within a low-energy Archaic harbour basin (ca. 7-6th c. BCE) and a preceding proto-harbour embayment, which existed to the west of the Liman Tepe headland during the Middle-Late Bronze Age (core 17-9 1836-1447 cal. BCE and core 19-1 1442-329 cal. BCE) (Chapter 3). Dredging of the harbour is recorded by an erosional hiatus at a depth of 70 cm in core 19-1 (LA-5a to LA-5b transition; Fig. 2.5). On land, for convenience, we assign the uppermost surficial deposits containing archaeological materials to LA-5 (Fig. 2.8), recognizing that they were deposited in a range of terrestrial environments. Some of these surficial deposits were previously mapped as ‘anthropogenic sediments’ by Kayan et al. (2019) and contain archaeological strata ranging in age from Chalcolithic to present (Saholgu, 2015; Tuncel and Şahoğlu, 2018).

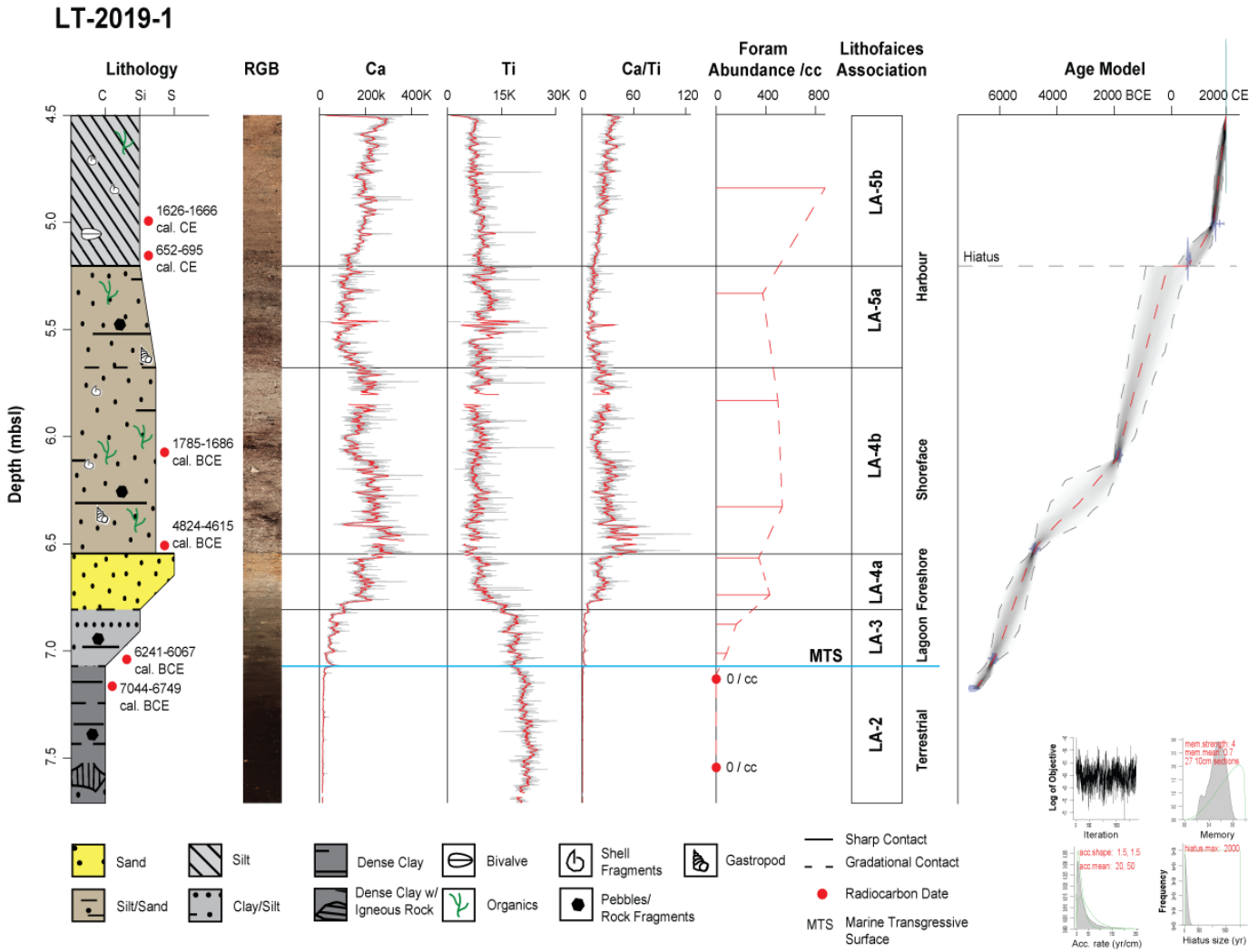

Figure 2.5: Core 19-1 lithofacies log with AMS ^{14}C dates, RGB scan, XRF elemental profiles, foraminifera abundance, and Bayesian age-depth model. Element profiles (Ca, Ti) normalized using the ratio of coherent to incoherent (coh/inc) scatter to minimize matrix effects (Gregory et al., 2019).

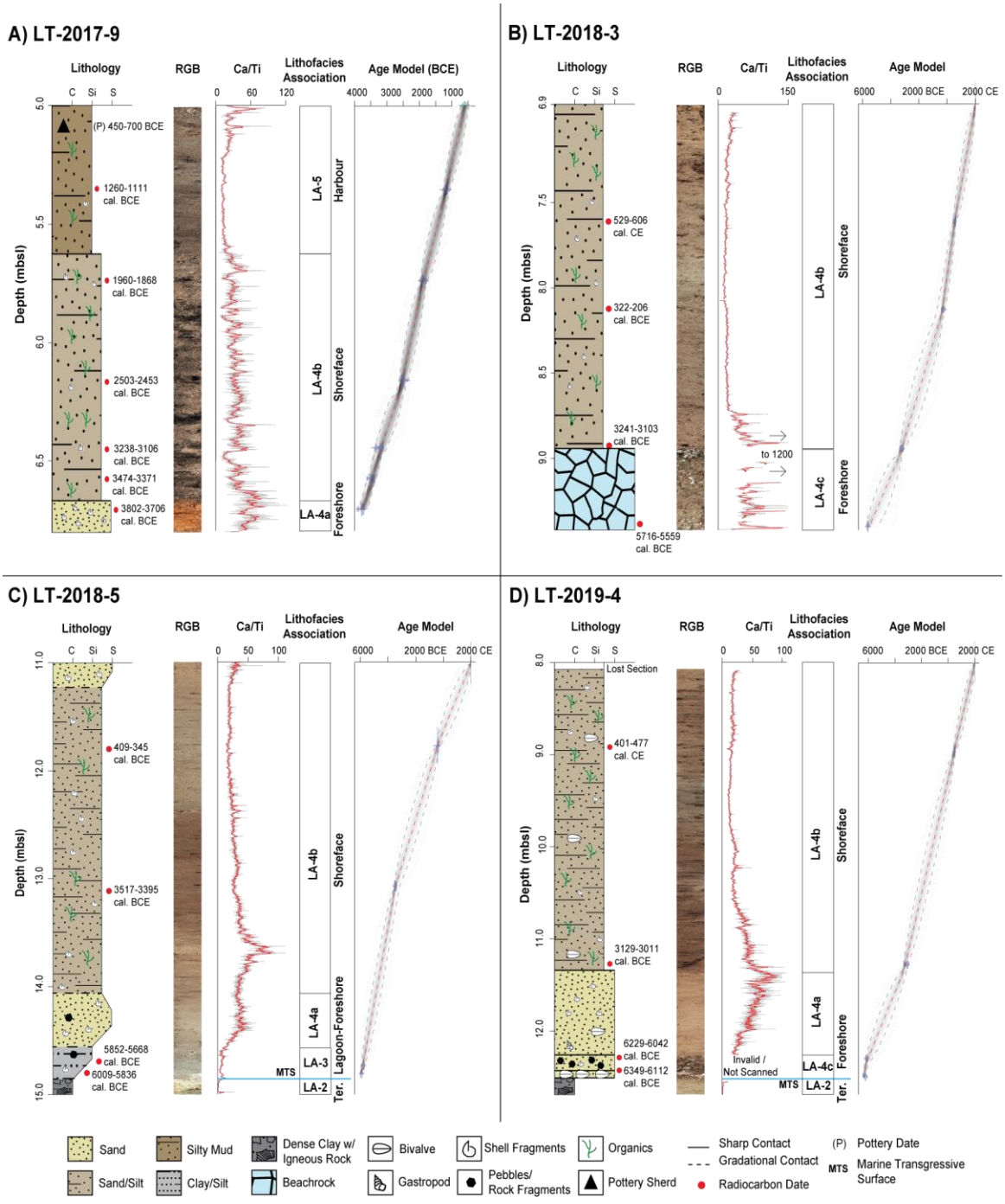

Figure 2.6: Lithofacies logs with AMS ^{14}C dates, RGB scan, Ca/Ti ratio, and Bayesian age-depth model for cores 17-9 (A), 18-3 (B), 18-5 (C), 19-4 (D).

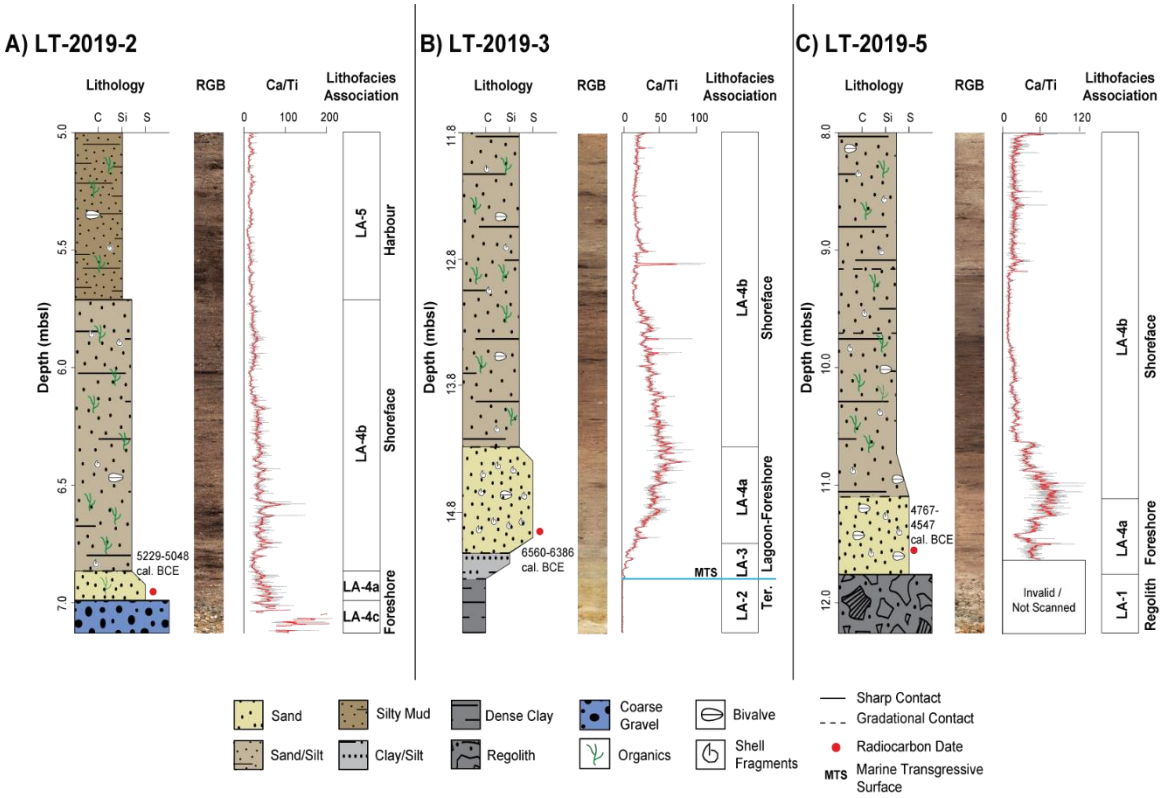

Figure 2.7: Lithofacies logs with AMS ^{14}C dates, RGB scan, and Ca/Ti ratio for cores 19-2 (A), 19-3 (B), 19-5 (C).

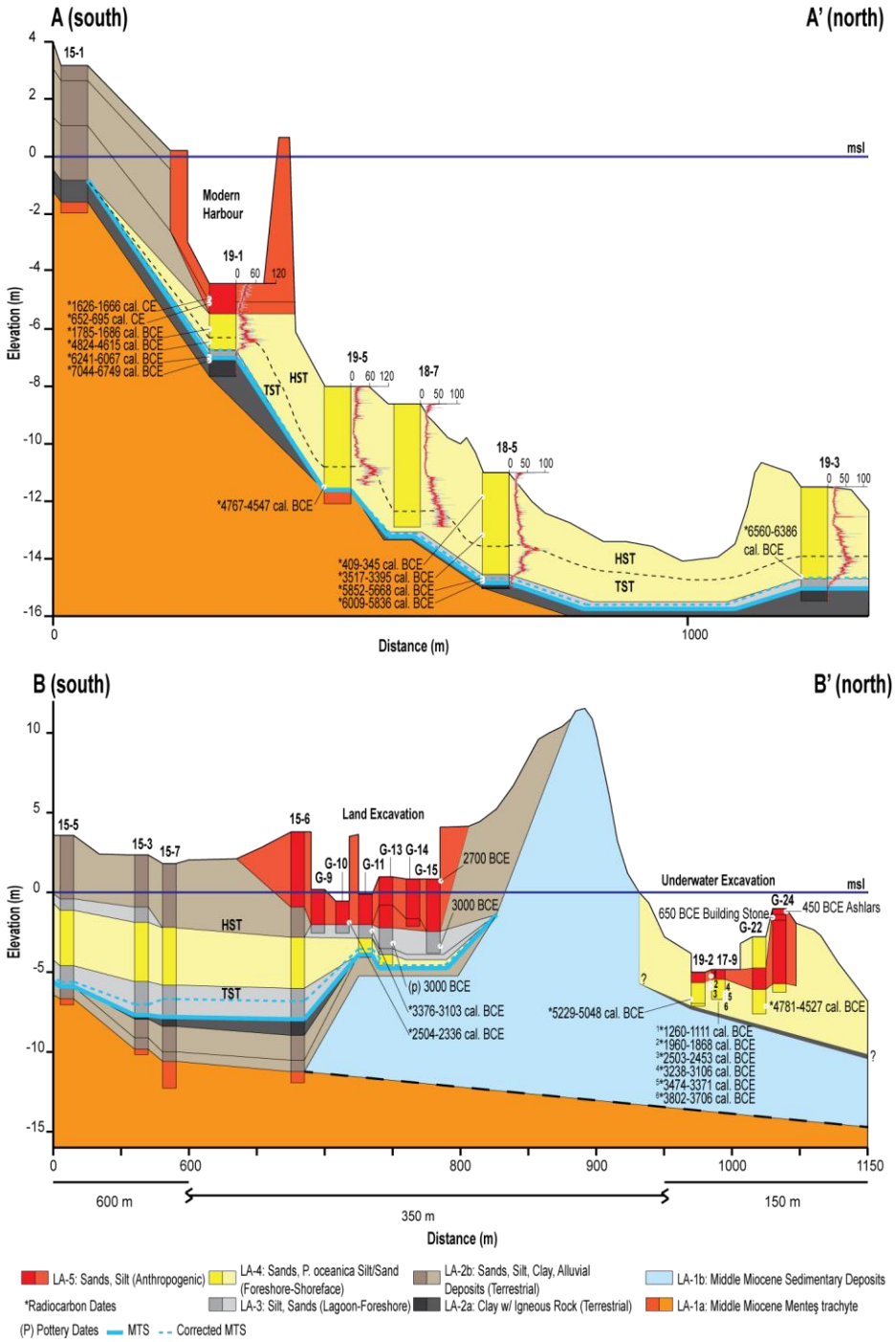

Figure 2.8: Stratigraphic profiles (A-A' and B-B'; location in Fig. 2.1b) showing correlation of marine lithofacies assemblages with onshore core data. In A-A' Ca/Ti profiles are shown and core 15-1 was redrawn from Kayan et al. (2019). In B-B' cores redrawn from Goodman et al. (2008, 2009) and Kayan et al. (2019), and correlated with cores 19-2 and 17-9 (this study). LA-3 includes lagoon and foreshore facies identified by Goodman et al. (2008, 2009) and Kayan et al. (2019). Marine transgressive surface (MTS) corrected for post-depositional compaction indicated by dashed blue line. HST = high-stand systems tract and TST = transgressive systems tract.

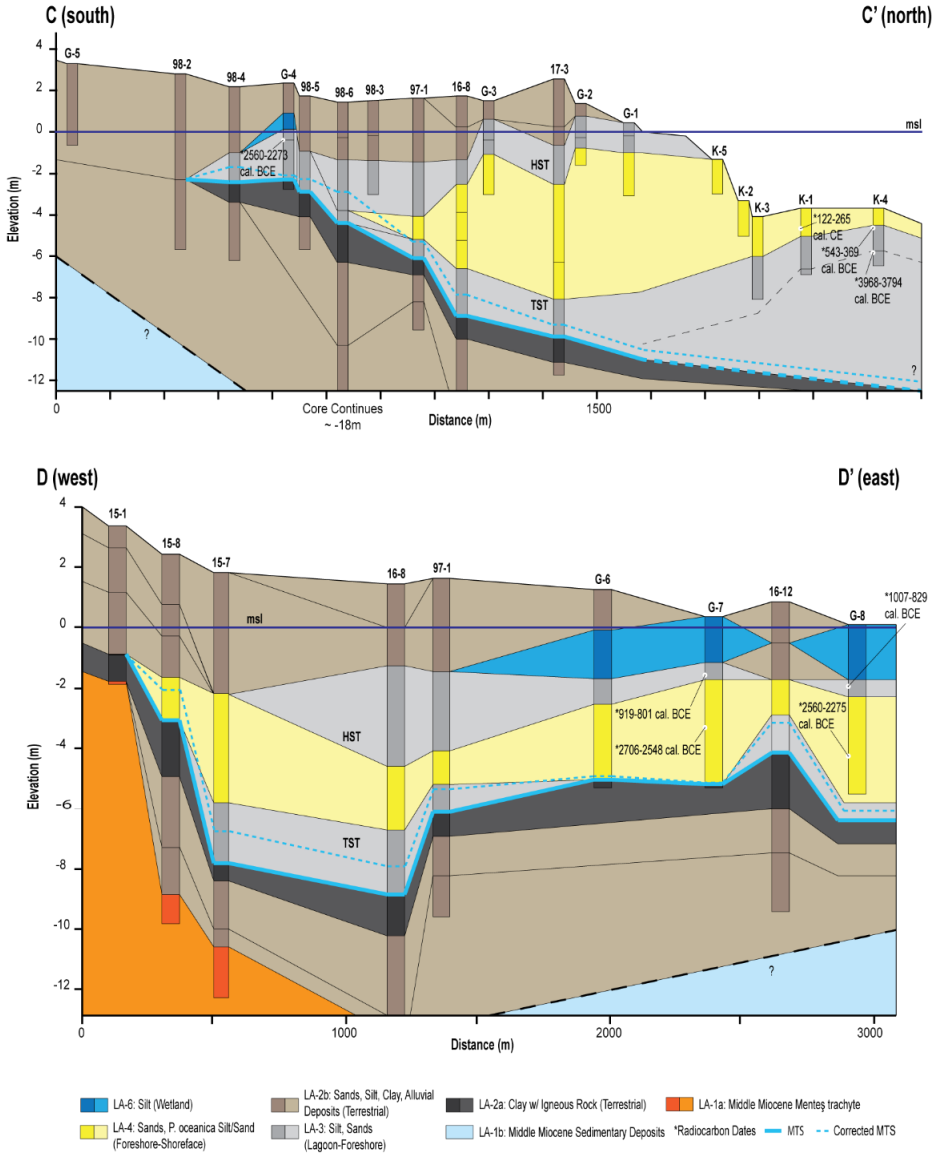

Figure 2.9: Stratigraphic profiles (C-C' and D-D'; location in Fig. 2.1b) showing correlation of marine lithofacies assemblages with lithofacies in onshore core data. The marine transgressive limit is indicated by the maximum shoreward extent of marine deposits. Cores redrawn from Krezoski (2008), Goodman et al. (2008, 2009), and Kayan et al. (2019). LA-3 includes lagoon and foreshore facies identified in previous land coring work. Marine transgressive surface (MTS) corrected for post-depositional compaction indicated by dashed blue line. HST = high-stand systems tract and TST = transgressive systems tract. In C-C' the marine transgressive limit is indicated by the maximum shoreward extent of marine deposits.

2.5 Discussion

2.5.1 RSL Change

The revised RSL curve for Liman Tepe (Fig. 2.10) incorporates 31 new radiocarbon dates (Table 2.1) on terrestrial, intertidal and foreshore sea-level markers (compaction corrected). The glacio-hydro-isostatic sea-level curve of Lambeck (1995) and Aegean (sector "C") curve of Vacchi et al. (2014) are shown for comparison. Kayan's (1988) sea-level curve is also shown, as it was employed in a recent estimate of the marine transgressive limit at Liman Tepe (Kayan et al., 2019). The new RSL curve generally agrees with Lambeck's (1995) regional curve prior to the inflection at ca. 4000 BCE, indicating a rapid middle Holocene rate of sea level rise (~14 $mmyr^{-1}$ until ca. 6300 BCE), followed by a deceleration to ~2 $mmyr^{-1}$, due to a global cooling event (Kendall et al., 2008; Lambeck et al., 2014). During the Neolithic Period (ca. 8000-4800 BCE) RSL's were between -18 and -5 m below present (Fig. 2.10). Given the low gradient of the coastal plain (Figs. 2.2, 2.3) and the rapid rate of RSL rise during this period, the shoreline would have transgressed landward at an estimated rate of about 0.2-0.75 m per year. From ca. 4000 BCE to present, RSL rose at a slower rate of about ~0.5 $mmyr^{-1}$, in parallel with the regional Aegean curve of Vacchi et al. (2014). Both the Liman Tepe RSL curve and that of Vacchi et al. (2014) lie below the global glacio-hydro-isostatic sea-level curve of Lambeck (1995). We also note that a segment of our RSL curve for the period prior to ca. 4000 BCE lies above the Vacchi et al. (2014) curve, as indicated by two subtidal markers (Fig. 2.10). The inflection point at ca. 4000 BCE is generally attributed to the deceleration in post-glacial sea level rise as global ice volumes stabilized (Fleming et al., 1998). The departure in the local RSL from the eustatic curve of Lambeck (1995) (~1.5 m at ca. 4000 BCE) may record ongoing tectonic subsidence in the Bay of Izmir, which was previously estimated at 1 $mmyr^{-1}$ by Aksu et al. (1990). The difference between the local RSL and Lambeck's (1995) eustatic curve at 4000 BCE is about 1.5 m, which suggests a lower rate of subsidence on the order of about 0.25 $mmyr^{-1}$ at Liman Tepe (Fig. 2.10). Some component of subsidence may be due to uncompensated post-depositional sediment compaction in sediments below the base of marine cores (i.e. in cores that do not penetrate fully to bedrock).

The six compaction-corrected radiocarbon dates obtained from *Posidonia* mattes in core 17-9 indicate a linear sediment accumulation rate of ~0.5 mmyr^{-1} following the maximum marine transgression at ca. 4000 BCE (Fig. 2.10). A best-fit line through the dates closely parallels the gradient of the Vacchi et al. (2014) RSL curve obtained for the sector C Aegean microplate. The data from core 17-9 suggests that AMS ^{14}C dates from *Posidonia* matte can provide a useful measure of seabed aggradation and RSL gradient under rising sea levels.

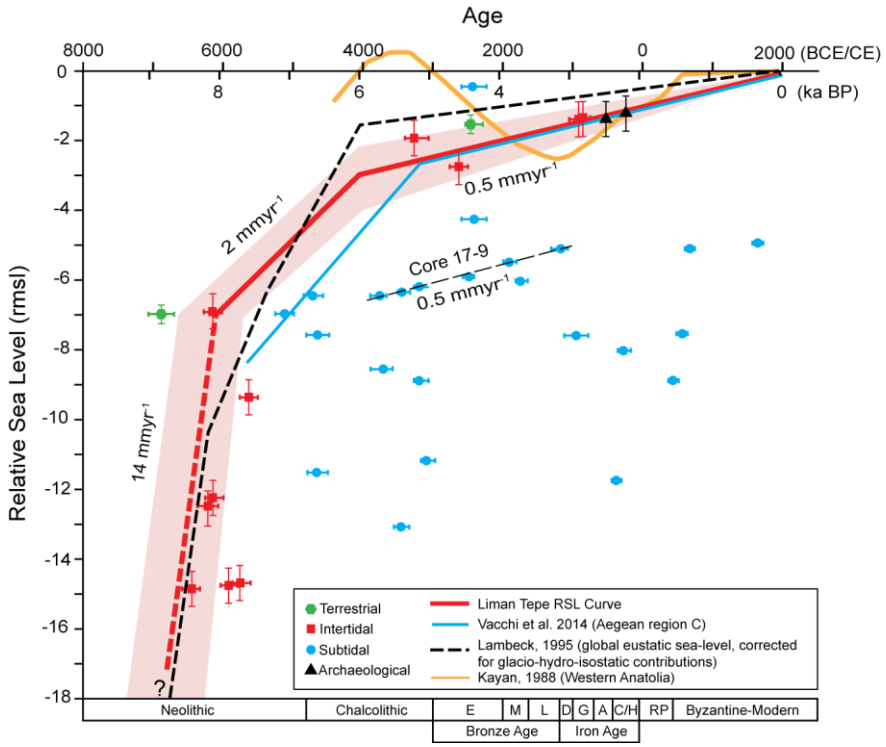

Figure 2.10: Relative sea level (RSL) curve for Liman Tepe (red line) based on new sea level indicators and recalibrated dates from Goodman et al. (2008, 2009) (Table 2.1). All AMS ^{14}C data corrected for core compaction. Glacio-hydro-statically corrected eustatic curve of Lambeck (1995) and RSL curves of Kayan (1988) and Vacchi et al. (2014) also shown for comparison. Kayan's (1988) curve predicts a sea level 0.5 m higher than present during the Chalcolithic period, which is controversial (see Vacchi et al., 2014 for discussion).

Kayan's (1988) RSL curve predicts a middle Holocene high-stand with a RSL ~0.5 m above modern between ca. 4000-3000 BCE and levels below the Lambeck (1995) and Vacchi et al. (2014) models at ca. 1200 BCE (Fig. 2.10). Kayan's model is based on beachrock elevations from two locations on the western Anatolian coast (Datça, Çanakkale)

and has been applied broadly to interpretation of the palaeogeography of coastal sites in western Turkey (Kayan et al., 2019). The high-stand event is not recognized in our observations, which show sea levels below modern after ca. 4000 BCE (Fig. 2.10). A single sub-tidal marker (from Goodman et al., 2008; -1 m at ca. 2400 BCE), lies above the RSL prediction (Fig. 2.10). This radiocarbon sample was a shell fragment in lagoon sediments and may be an outlier. Water levels 0.5 m above modern between 4000-3000 BCE are not supported by our shoreline reconstruction and result in a marine limit that is farther inland than observed in land core data (e.g. Kayan et al., 2019) (Figs. 2.8, 2.9).

Goodman et al. (2008, 2009) employed Lambeck's (1995) glacio-hydro-isostatically corrected sea level curve in their palaeogeographic reconstruction, as it generally conformed to their sea-level indicators. They concluded that while the area is tectonically active, there was no evidence for coastal subsidence or uplift at the resolution of their RSL data. However, their core data were not corrected for compaction effects, which could account for their higher estimates of RSL after 4000 BCE, and also the presence of marine sediments at elevations close to or slightly above modern sea level (e.g. cores G-2, G-4) (Fig. 2.9). The post-depositional compaction corrections resulted in a maximum adjustment of >1 m in cores with thick mud and silt facies. This emphasizes the need for compaction correction of cores prior to RSL modelling, particularly when sea-level indicators are in fine-grained, organic-rich sediments, which are highly susceptible to post-depositional compaction effects (Paul and Barra, 1998; Bird, 2004; Brain et al., 2015).

2.5.2 Holocene Depositional Environments and Palaeogeography

Five distinct lithofacies assemblages have been recognized in marine core data at Liman Tepe and correlated with onshore stratigraphic data from two previous studies. The stacking patterns of lithofacies indicate two major depositional phases (Figs. 2.8, 2.9), which are linked to changes in RSL (Fig. 2.10) and the coastal sediment budget and accommodation space. A TST and rapid phase of sea-level rise obtained until ca. 4000 BCE and was followed by a HST with the deceleration of RSL rise and decrease in accommodation space (Goodman et al., 2008). Changes in the coastal palaeogeography and

environments during these phases at Liman Tepe are shown in Figure 2.11 and discussed in the following sections.

2.5.2.1 Transgressive Systems Tract (TST)

The lowermost sediment package of marine sediments, consisting of a coarsening-upward sequence of marine lagoonal and foreshore facies overlain by upper shoreface deposits (Figs. 2.8, 2.9), represents a TST. At Liman Tepe, the maximum transgression extended approximately 1 km inland from the present shoreline (ca. 4000 BCE; Fig. 2.11e). The marine limit is in general agreement with previous work (Goodman et al., 2008; Kayan et al., 2019) and provides additional details on the configuration of headlands and coastal embayments which formed during the inundation of the coastal plain. The preservation of relict Neolithic palaeoshoreline features and palaeochannels to the west of Karantina Island (Figs. 2.2, 2.3), suggests that the relatively low-relief coastal topography was submerged rapidly.

At 6700 BCE, RSL was about 14 m below present, and the shoreline was >500 m seaward of the modern coast (Figs. 2.10, 2.11a). The shoreline position ca. 6600 BCE was coincident with a break in slope, which is interpreted as a palaeoshoreline feature in the modern bathymetry (-11 to -12 m; Figs. 2.2, 2.11b). The low (1-2 m) scarp defining the palaeoshoreline feature (Fig. 2.3) may record a brief still-stand event or indicate structural control on the shoreline position by underlying bedrock ridge, as the bedrock surface is at a relatively shallow depth on the west side of the study area (Fig. 2.8). The relict river palaeochannels terminate at the palaeoshoreline (Fig. 2.2), which suggests that the preserved floodplain is middle Neolithic in age (ca. 6700-6600 BCE). At this time, Karantina Island was a broad headland with a large western coastal promontory that formed a small, sheltered embayment to the north of Liman Tepe. To the southeast of Karantina Island, an extensive barrier-lagoon system was formed as the coastline stepped landward. The northwest trending ridges identified in seismic data (Fig. 2.4) record relict transgressive barriers which were drowned-in-place by shoreline overstepping (Rampino and Sanders, 1980; Mellett and Plater, 2018).

At 6500-6400 BCE, Karantina Island remained connected to the mainland and a coastal wetland formed to the southeast as a lagoon-barrier complex stepped shoreward during the TST (Krezoski, 2008) (Fig. 2.11b). The western coastal promontory of Karantina Island was progressively inundated after 6600 BCE (locations of cores 19-3, 19-4) forming a series of small islands (Fig. 2.11a, b). The intertidal deposits containing oyster shells and gravel (core 19-4; 6349-6112 cal. BCE), may record Neolithic shell gathering and processing on the western shore of Karantina Island (Fig. 2.11b). The western shore of the island continues to be a habitat for the European flat oyster (*Ostrea edulis*) and fan mussel (*Pinna nobilis*), which are gathered for local consumption (Lok and Acarli, 2006).

By 6000 BCE, the coastline had transgressed close to its modern position and an embayment existed to the southwest of the Liman Tepe headland (Fig. 2.11c). Karantina Island was separated from the mainland and to the west of the headland a coastal lagoon formed as indicated by LA-2 deposits in core 19-1. On the west side of Karantina island, at the location of core 18-3 beachrock formed in an intertidal environment (5716-5559 cal. BCE). *Posidonia* muds do not occur in shallow areas off Karantina Island until the end of the Chalcolithic/beginning of the EBA (3241-3103 cal. BCE in core 18-3 and 3129-3011 cal. BCE in core 19-4; Fig. 2.6b, c), indicating possible shallow, foreshore conditions, not suitable for *Posidonia* growth until the EBA. By 4800 BCE, the coastline had transgressed landward ~800 m and Liman Tepe was a small island or coastal promontory separated from the mainland by shallow wetlands (Fig. 2.11d) (Goodman et al., 2008).

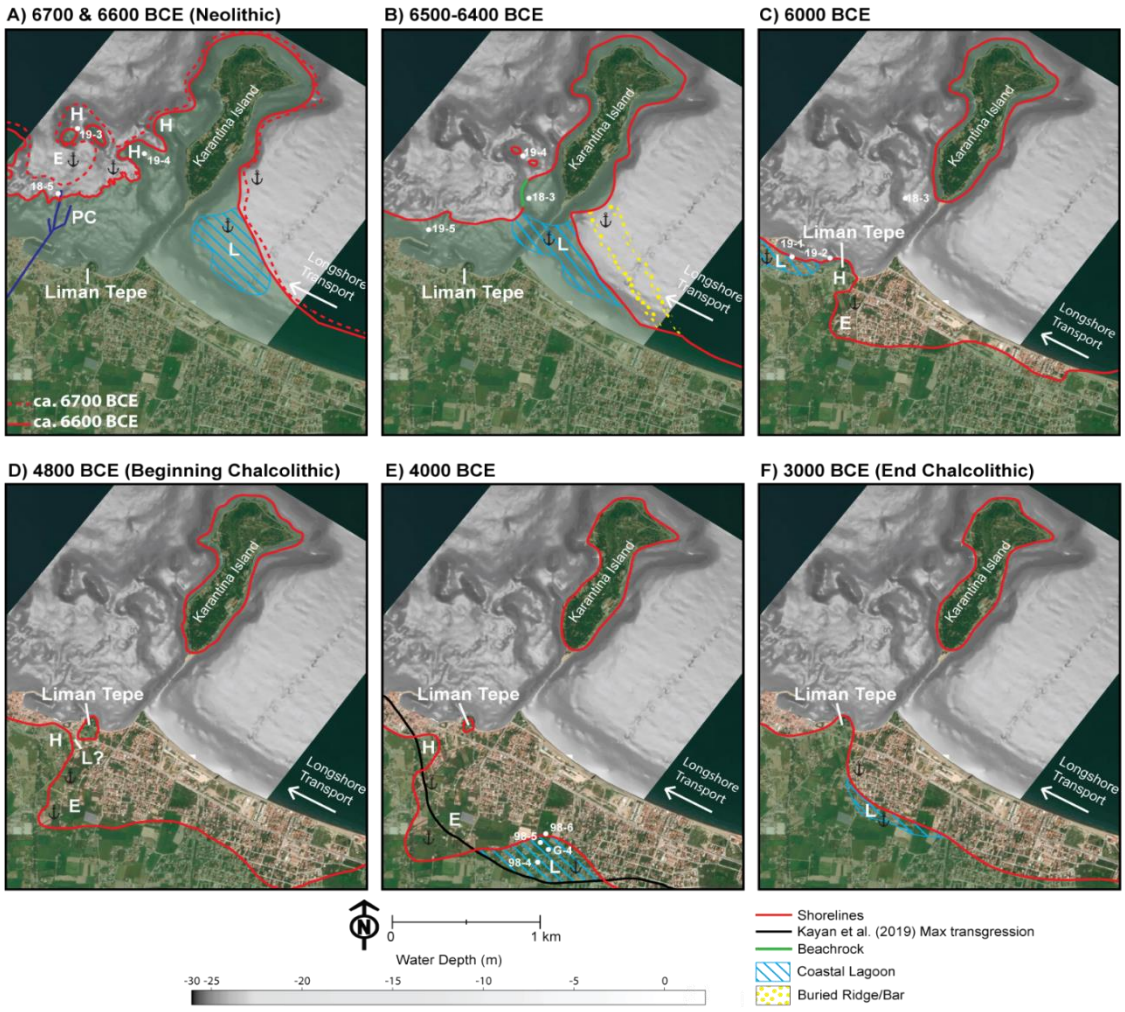

Figure 2.11: Middle Neolithic to Late Chalcolithic palaeogeography and coastal evolution of Liman Tepe. Palaeoshoreline positions estimated by projecting RSL for each period onto back-stripped digital bathymetric model. Areas of archaeological potential include anchorage areas (anchor symbol), headlands/promontories (H), embayments (E), lagoons/wetlands (L), and palaeochannel (PC) features. Previous reconstruction of Kayan et al. (2019) shown for comparison in E.

2.5.2.2 High-Stand Systems Tract (HST)

At ca. 4000 BCE, the rate of sea level rise decreased (Fig. 2.10) and the increase in accommodation space was outpaced by sediment supply on the coast (Fig. 2.8, 2.9). An HST prevailed and the coastline prograded through the accretion of linear beach barriers, which were backed by shallow lagoons (Goodman et al., 2008). The HST is recorded by an upwards fining succession of shoreface sands overlain by lagoonal and wetland facies (Fig. 2.8, 2.9). The Liman Tepe headland was a small island and a large embayment existed

to the southeast at 4000 BCE (Fig. 2.11e). Coastal lagoons were likely present along this embayment, notably at the location of cores 98-4, 98-5, 98-6, and G-4 (Figs. 2.9, 2.11e). Archaeological evidence and the extent of settlement phases at Liman Tepe indicate that the headland was reconnected to the mainland by the late Chalcolithic to EBA period (Fig. 2.11f; modified from Goodman et al., 2008, 2009). By the Archaic (possibly the Middle-Late Bronze Age), the lagoons to the east of Liman Tepe headland were infilled, leaving a coastal embayment to the west, which later became an engineered harbour during the Archaic Period (Chapter 3).

2.5.3 Archaeological Potential

The RSL reconstruction shows that the Neolithic to middle Chalcolithic periods were a time of rapid sea-level rise and marine transgression (Figs. 2.10, 2.11). The changes in shoreline positions and coastal palaeogeography would have strongly influenced coastal settlement patterns. During Neolithic, the shoreline rapidly transgressed across the low-relief coastal plain at an estimated rate of 0.2-0.75 m per year (Fig. 2.11). The landscape was rapidly transformed and the river floodplain that existed at ca. 6700 BCE was completely inundated over a period of 600 years (Fig. 2.11a, b). The rapid changes in the shoreline positions and coastal environments would have been perceptible to people living and gathering resources on the coast and would have required short-term adaptations to rising sea levels. Due to the rapid shoreline advance, high ground areas on Karantina Island and on emergent coastal promontories would have been favourable locations for settlements. Habitations on the coastline would likely have been ephemeral or perhaps seasonally occupied for gathering of food resources.

The palaeogeographic reconstructions identify several areas with high archaeological potential, which we speculate may have been favourable as locations for Neolithic settlements and for procurement of marine resources. During the middle Neolithic (6700-6400 BCE) the coastal headlands on the west side of Karantina may have provided favourable settlement locations (Fig. 2.11a, b). These promontories were much larger in area than the Liman Tepe headland, the locus of the Chalcolithic-Bronze Age

settlement. The use of coastal promontories as settlement locations was common in the prehistoric Aegean, as these locations afforded protected anchorage areas and were defensible positions (Tartaron, 2015). Establishment of the Chalcolithic settlement on the headland at Liman Tepe would have been attractive, as the rocky headland provides an elevated and unobstructed view of the Bay of Izmir. At 6700 BCE, the western headland of Karantina Island was about 4 metres above sea level and formed a small (0.2 km^2) semi-enclosed embayment, which would have provided a well-protected anchorage area and river floodplain to the south (Fig 2.11a). The eastern shoreline of Karantina Island, which is well protected from the northerly winds, would also have provided sheltered mooring areas (Fig. 2.11a, b).

The presence of a large river system and alluvial plain with wetland resources at Liman Tepe (Fig. 2) would have been highly attractive to Neolithic settlers and was also likely a factor in the founding of the Chalcolithic and EBA settlements at Liman Tepe (Goodman et al., 2008). The floodplain and low-lying coastal wetlands would have provided a freshwater source for drinking and agriculture and rich coastal habitats for resource gathering. Evidence from nearby sites in Izmir suggest that marine and riverine shellfish gathering was a major component of Neolithic and Chalcolithic subsistence strategies (Derin, 2007). The presence of oyster shells in core 19-4, representing a possible midden deposit, indicates an important shellfish resource on the coast (Fig. 2.11a, b). The river floodplain would have also provided raw materials for settlement construction. Coring at location 19-1 revealed a thick clay palaeosol developed on the volcanic regolith (Fig. 2.5). These deposits are a potential source of clays used in prehistoric mudbrick/wattle and daub architecture at Liman Tepe.

On the Liman Tepe headland (Fig. 2.1b), the earliest settlement layers date to the Chalcolithic An early settlement phase at ca. 4600-4200 BCE was followed by 600–1000-year hiatus in activity before a final late Chalcolithic re-occupation of the site (Tuncel and Şahoğlu, 2018). Similar hiatuses have been recognized in the Chalcolithic settlement phases of other sites in the region but the reasons for low archaeological visibility during

this period are not well understood (Tuncel and Şahoğlu, 2018). Palaeogeographic mapping indicates that during early Chalcolithic (ca. 4800 BCE), the Liman Tepe headland was connected to the mainland (possibly by a tombolo) and was backed by a shallow water area (<1 m), possibly a coastal wetland or a tidal flat (Fig. 2.11d). During the time of the settlement hiatus, the shoreline advanced about 1 km inland to the maximum marine limit (ca. 4000 BCE) and the northernmost point on the headland became a small island located 300 m offshore (Fig. 2.11e). The inundation of the headland by rising sea levels may have required the migration of Chalcolithic settlement to the mainland and could explain the apparent hiatus in activity at Liman Tepe during this period. The area to the south of Liman Tepe now part of modern town of Iskele, has a high potential as a location for a Chalcolithic settlement.

The archaeological evidence for seafaring activity at Liman Tepe indicates diverse trade connections with wider Aegean and Anatolian hinterlands during the Chalcolithic and EBA periods (Şahoğlu, 2005; Erkanal, 2017). The embayment that existed to the southeast of the headland and the back-barrier lagoon systems which formed as the shoreline prograded during the HST, would have provided favourable anchorage locations during the Chalcolithic and Bronze Age settlement phases (Goodman et al., 2009).

2.6 Summary

Previous geoarchaeological studies at Liman Tepe have focused largely on the land and nearshore sediment record with a limited radiocarbon chronology (Goodman et al., 2008, 2009; Krezoski, 2008; Kayan et al., 2019). In this paper, we have assembled a large marine geoscience database, including 20 cores, 31 radiocarbon dates and geophysical data (>600-line-km) to reconstruct the coastal palaeogeography of Liman Tepe from the middle Neolithic to late Chalcolithic (Fig. 2.11). We have demonstrated an approach to palaeoshoreline mapping that employs back-stripping of estimated sediment thickness above a stratigraphic datum, as opposed to simply using the modern bathymetric data and surface topography (Westley et al., 2014). The modern coastal bathymetry and topography are often poor predictors of prehistoric shoreline geomorphology (Tartaron et al., 2011).

Other approaches have employed seismic profiles to identify surfaces within sediments that can be used as a datum for back-stripping (Westley et al., 2014). In this study, we chose a well-defined marine transgressive surface (MTS) as a datum for calculating the compaction corrected sediment thickness (Figs. 2.6, 2.7), subtracted from a bathymetric relief map (Fig. 2.2). This approach has the advantage that it is tied directly to core measurements of sediment thickness and is not prone to errors in seismic velocities, which are required to convert reflector depths to sediment thicknesses. Sonnenburg et al. (2012) employed a similar approach, using estimates of sediment accumulation rates above a basin-wide erosional hiatus to determine the required thickness for back-stripping. These methods assume that the palaeolandscape surface (e.g. MTS) has undergone burial and that erosion has not been a significant factor. More sophisticated back-stripping approaches are used widely in petroleum geosciences and basin analysis to correct palaeobathymetry for subsidence due to sediment and water loading and tectonics effects (e.g. Kominz and Pekar, 2001; Miall, 2010). To date back-stripping methods have had limited application in geoarchaeological studies (e.g. Sonnenburg et al., 2012; Westley et al., 2014) but the growing availability of high-resolution digital elevation and bathymetric data will likely expand the use of the technique in the future.

The Neolithic to middle Chalcolithic was a period of rapid marine transgression, which submerged a large area of the coastal plain around Liman Tepe. The maximum marine limit extended ~1 km inland and resulted in the submergence of coastal headlands on the west coast of Karantina Island (Fig. 2.11e). At about 4000 BCE, slowing of the global rate of sea level rise resulted in a reduction in accommodation space and a positive sediment budget prevailed. Following 4000 BCE the coastline prograded by the accretion of linear lagoon-barrier systems, which resulted in the infilling of coastal embayment and lagoons that existed to the east of Liman Tepe. Our results are in general agreement with the findings of previous coastal reconstructions (Goodman et al., 2008, 2009; Kayan et al., 2019) but provide important new details of the shoreline positions during the critical Neolithic and Chalcolithic periods of settlement, which were previously undefined. The new RSL curve for Liman Tepe indicates sea levels were below modern during the period

6500 BCE to present and we find no evidence for middle Holocene levels above modern as proposed by Kayan et al. (2019).

The new palaeoshoreline mapping identifies several areas of underwater archaeological interest, including potentially favourable Neolithic settlement locations (i.e. coastal headlands, palaeoshorelines) and better resolves the location of embayments and coastal lagoons, which may have served as anchorage sites (Goodman et al., 2009; Chapter 3). The mapping also identifies relict river channels on a submerged coastal floodplain, which would have been attractive to Neolithic settlers as coastal habitation sites and as a source of fresh water and food resources. Future work at Liman Tepe will investigate the archaeological potential of these submerged landscape features using diver reconnaissance surveys and marine geophysical investigations (e.g. sub-bottom seismic profiling, marine magnetic surveys). The late Holocene sediment thickness (>2-4 m) in the inshore area presents a challenge for exploration but does not preclude future discovery of buried prehistoric sites.

2.7 References

Agostini, S., Tokcaer, M., Savaşçın, M.Y., 2010. Volcanic rocks from Foça-Karaburun and Ayvalik-Lesvos grabens (western Anatolia) and their petrogenetic-geodynamic significance. Turkish Journal of Earth Sciences 19(2), 157-184.

Aksu, A.E., Konuk, T., Ulug, A., Duman, M., Piper, D.J.W., 1990. Quaternary tectonic and sedimentary history eastern Aegean Sea and shelf areas. Jeofizik 4(1), 3-35.

Aksu, A.E., Piper, D.J.W., Konuk, T., 1987. Late Quaternary tectonic and sedimentary history of outer Izmir and Candarli Bays, western Turkey. Marine Geology 76, 89-104.

Allen, J.R.L., 2000. Holocene coastal lowlands in NW Europe: autocompaction and the uncertain ground. Geological Society, London, Special Publications 175(1), 239-252.

Athanassas, C., Bassiakos, Y., Wagner, G.A., Timpson, M.E., 2012. Exploring paleogeographic conditions at two Paleolithic sites in Navarino, Southwest

Greece, dated by optically Stimulated Luminescence. Geoarchaeology 27(3), 237–258.

Aytaçlar, N., 2004. The Early Iron Age at Klazomenai. In: Moustaka, A., Skarlatidou, E., Tzannes, M.C., Ersoy, Y. (Eds.), Klazomenai, Teos and Abdera: Metropoleis and Colony. Proceedings of the International Symposium, Abdera, pp. 17-41.

Bailey, G.N., Flemming, N.C., 2008. Archaeology of the continental shelf: marine resources, submerged landscapes and underwater archaeology. Quaternary Science Reviews 27(23-24), 2153-2165.

Bailey, G.N., Jöns, H., Galanidou, N., Peeters, H., Mennenga, M. (Eds.). (2020). The Archaeology of Europe's Drowned Landscapes (Vol. 35). Springer Nature.

Bakır, G., Ersoy, Y., Fazlıoğlu, I., Ayçatlar, N., Cevizoğlu, H., Hürmüzlü, B., Sezgin, Y., 2000. Klazomenai Kazısı. Kazı Sonuçları Toplantısı 23(2002), 41-55.

Bates, R., Bates, M., Dix, J., 2009. Contiguous palaeo-landscape reconstruction (transition zone mapping for marine-terrestrial archaeological continuity). Marine Aggregates Levy Sustainability Fund Project 4632. Unpublished report prepared for English Heritage. St. Andrews: University of St. Andrews.

Benjamin, J., Rovere, A., Fontana, A., Furlani, S., Vacchi, M., Inglis, R.H., Galili, E., Antonioli, F., Sivan, D., Miko, S., Mourtzas, N., Felja, I., Meredith-Williams, M., Goodman-Tchernov, B., Kolaiti, E., Anzidei, M., Gehrels, R., 2017. Late Quaternary sea-level changes and early human societies in the central and eastern Mediterranean Basin: An interdisciplinary review. Quaternary International 449, 29-57.

Berntsson, A., Rosqvist, G.C., Velle, G., 2014. Late-Holocene temperature and precipitation changes in Vindelfjällen, mid-western Swedish Lapland, inferred from chironomid and geochemical data. The Holocene 24(1), 78-92.

Bird, M.I., Fifield, L.K., Chua, S., Goh B., 2004. Calculating sediment compaction for radiocarbon dating of intertidal sediments. Radiocarbon 46(1), 421-435.

Blaauw, M., Christen J.A., 2011. Flexible paleoclimate age-depth models using an autoregressive gamma process. Bayesian Analysis 6(3), 457-474.

Boyce, J.I., Kresozki, G.M., Erkanal, H., Sahoglu, V., Goodman, B.N., Artzy M., 2007. Shallow water mapping of a submerged Archaic-age harbor at Liman Tepe, Turkey using data-fused magnetic and side-scan data. In 2007 GSA Denver Annual Meeting.

Bozkurt, E., Sozbilir, H., 2004. Tectonic evolution of the Gediz Graben: field evidence for an episodic, two-stage extension in western Turkey. Geological Magazine 141(1), 63-79.

Braje, T.J., Dillehay, T.D., Erlandson, J.M., Klein, R.G., Rick, T.C., 2017. Finding the first Americans. Science 358, 592-594.

Brain, M.J., Kemp, A.C., Horton, B.P., Culver, S.J., Parnell, A.C., Cahill, N., 2015. Quantifying the contribution of sediment compaction to late Holocene salt-marsh sea-level reconstructions, North Carolina, USA. Quaternary Research 83(1), 41-51.

Brückner, H., 1997. Coastal changes in western Turkey; rapid delta progradation in historical times. Bulletin-Insitut Oceanographique Monaco-Numero Special, 63-74.

Çiftçi, N.B., Bozkurt, E., 2009. Pattern of normal faulting in the Gediz Graben, SW Turkey. Tectonophysics 473(1-2), 234-260.

Clark, P.U., Dyke, A.S., Shakun, J.D., Carlson, A.E., Clark, J., Wohlfarth, B., Mitrovica, J.X., Hostetler, S.W., McCabe, M.A., 2009. The last glacial maximum. Science 325(5941), 710-714.

Conolly, J., 2020. Archaeology and paleogeography of a Lake-Wetland complex: Modeling the postglacial evolution of the Kawartha Lakes, Ontario. Geoarchaeology 35(4), 433-450.

Conolly, J., Obie, M., 2021. The archaeology of inundated cultural landscapes in freshwater lake systems: preliminary insights from a multi-methods study in the Kawartha Lakes Region, Ontario. Journal of Maritime Archaeology, 1-18.

Dalrymple, R.W., James, N.P., 2010. Introduction to siliciclastic facies models. Facies models 4, 59-72.

Derin, Z., 2007. Neolithic Shellfish Gathering at Yeşilova: An Ethnoarchaeological View. Ethnoarchaeological Investigations in Rural Anatolia 45.

Duman, M., Avci, M., Duman, S., Demirkurt, E., Duzbastilar, M., 2004. Surficial sediment distribution and net sediment transport pattern in Izmir Bay, western Turkey. Continental Shelf Research 24(9), 965-981.

Erkanal, H., 2008. Liman Tepe: New light on prehistoric Aegean cultures. In: Erkanal, H., Hauptmann, H, Şahoğlu, V. (Eds), The Aegean in the Neolithic, Chalcolithic and the Early Bronze Age. Proceedings of the International Symposium, Urla-Izmir, pp. 179-190.

Erkanal, H., 2017. Liman Tepe Kazıları. Kazı Sonuçları Toplantısı, 387-406.

Ersoy, Y., 2004. Klazomenai: 900-500 B.C. history and settlement evidence. In: Moustaka, A., Skarlatidou, E., Tzannes, M.C., Ersoy, Y. (Eds.), Klazomenai, Teos and Abdera: Metropoleis and Colony. Proceedings of the International Symposium, Abdera, pp. 43-76.

Fedje, D., Mackie, Q., Lacourse, T., McLaren, D., 2011. Younger Dryas environments and archaeology on the Northwest Coast of North America. Quaternary International 242(2), 452-462.

Flatman, J.C., Evans, A.M., 2014. Prehistoric archaeology on the continental shelf: The state of the science in 2013. In: Evans, A.M., Flatman, J., Flemming, N. (Eds), Prehistoric Archaeology on the Continental Shelf, Springer, USA, pp. 1-12.

Fleming, K., Johnston, P., Zwartz, D., Yokoyama, Y., Lambeck, K., Chappell, J., 1998. Refining the eustatic sea-level curve since the Last Glacial Maximum using far- and intermediate-field sites. Earth and Planetary Science Letters 163(1-4), 327-342.

Flemming, N.C., 2020. Global experience in locating submerged prehistoric sites and their relevance to research on the American continental shelves. The Journal of Island and Coastal Archaeology, 1-24.

Flemming, N.C., Harff, J., Moura, D., Burgess, A., Bailey, G.N. (Eds.), 2017. Submerged landscapes of the European continental shelf: Quaternary paleoenvironments (Vol. 1). John Wiley & Sons.

Giaime, M., Marriner, N., Morhange, C., 2019. Evolution of ancient harbours in deltaic contexts: A geoarchaeological typology. Earth-science reviews 191, 141-167.

Göktaş, F., 2016. Neogene stratigraphy of the Izmir-outer-bay islands. Maden Tetkik ve Arama Dergisi 152, 1-24.

Goodman, B.N., 2006. The paleogeography of Liman Tepe, Turkey: A multi-proxy geoarchaeological study. Unpublished PhD thesis, McMaster University.

Goodman, B.N., Reinhardt, E.G., Dey, H.W., Boyce, J.I., Schwarcz, H.P., Sahoğlu, V., Erkanal, H., Artzy, M., 2008. Evidence for Holocene marine transgression and shoreline progradation due to barrier development in Iskele, Bay of Izmir, Turkey. Journal of Coastal Research 24(5), 1269-1280.

Goodman, B.N., Reinhardt, E.G., Dey, H.W., Boyce, J.I., Schwarcz, H.P., Sahoğlu, V., Erkanal, H., Artzy, M., 2009. Multi-proxy geoarchaeological study redefines understanding of the paleocoastlines and ancient harbours of Liman Tepe (Iskele, Turkey). Terra Nova 21(2), 97-104.

Greene, E.S., Leidwanger, J., Tuna, N., 2019. Archaeological Investigations in the Harbours of Burgaz, Turkey: 2011–2015 field seasons. International Journal of Nautical Archaeology 48(1), 103-122.

Gregory, B.R., Patterson, R.T., Reinhardt, E.G., Galloway, J.M., Roe, H.M., 2019. An evaluation of methodologies for calibrating Itrax X-ray fluorescence counts with ICP-MS concentration data for discrete sediment samples. Chemical Geology 521, 12-27.

Harff, J., Bailey, G.N., Lüth, F., 2016. Geology and archaeology: submerged landscapes of the continental shelf: an introduction. Geological Society, London, Special Publications 411(1), 1-8.

Heisserer, A.J., 1980. Alexander the Great and the Greeks. Norman, Oklahoma: University of Oklahoma Press.

Ingram, W.C., Meyers, S.R., Brunner, C.A., Martens, C.S., 2010. Late Pleistocene–Holocene sedimentation surrounding an active seafloor gas-hydrate and cold-seep field on the Northern Gulf of Mexico slope. Marine Geology 278(1-4), 45–53.

Jolivet, L., Faccenna, C., Huet, B., Labrousse, L., Le Pourhiet, L., Lacombe, O., Lecomte, E., Burov, E., Denèle, Y., Brun, J.P., Philippon, M., Paul, A., Salaün, G., Karabulut, H., Piromallo, C., Monié, P., Gueydan, F., Okay, A., Oberhänsli, R., Pourteau, A., Augier, R., Gadenne, L., Driussi, O., 2013. Aegean tectonics: strain localisation, slab tearing and trench retreat. Tectonophysics 597, 1-33.

Kaya, O., 1979. Ortadoğu Ege çöküntüsünün (Neojen) stratigrafisive tektoniği. Türkiye Jeoloji Kurumu Bülteni 22(1), 35-58.

Kayan, İ., 1988. Late Holocene sea-level changes on the western Anatolian coast. Palaeogeography, Palaeoclimatology, Palaeoecology 68(2-4), 205-218.

Kayan, İ., Öner, E., Doğan, M., İlhan, R., Vardar, S., 2019. Holocene paleogeography and geoarchaeological interpretations on the Urla-İskele coastal plain. Ege Coğrafya Dergisi 28(1), 11-32.

Kendall, R.A., Mitrovica, J.X., Milne, G.A., Törnqvist, T.E., Li Y., 2008. The sea-level fingerprint of the 8.2 ka climate event. Geology 36(5), 423-426.

Kominz, M.A., Pekar S.F., 2001. Oligocene eustasy from two-dimensional sequence stratigraphic backstripping. GSA Bulletin 113(3), 291-304.

Koparal, E., Ersoy, Y.E., Massa, M., Demirciler, C., 2018. Sampling the Ionian landscapes: an overview of the archaeological surveys in the Klazomenean and Teian Chorai. In: Steadman, S.R., McMahon, G. (Eds.), The Archaeology of Anatolia Volume II: Recent Discoveries (2015-2016), Cambridge Scholars Publishing, p. 407.

Koster, B., Vött, A., Mathes-Schmidt, M., Reicherter, K., 2015. Geoscientific investigations in search of tsunami deposits in the environs of the Agoulinitsa peatland, Kaiafas Lagoon and Kakovatos (Gulf of Kyparissia, western Peloponnese, Greece). Zeitschrift für Geomorphologie 59, 125-156.

Kouka, O., 2009. Third millennium BC Aegean chronology: old and new data from the perspective of the third millennium AD. In: Manning, S.W., Bruce, M.J (Eds.), Three Rings, Kİngs, and Old World Archaeology and Environment: Papers presented in honor of Peter Ian Kuniholm, Oxbow Books, pp. 133-149.

Kraft, J.C., Kayan, I., Luce, J.V., 2003. Harbor areas at ancient Troy: sedimentology and geomorphology complement Homer's Iliad. Geology 31(2), 163-166.

Krezoski, G., 2008. Paleoenvironmental reconstruction of prehistoric submerged and coastal environments at Liman Tepe/Klazomenai, Turkey. Unpublished Master's thesis, McMaster University.

Krezoski, G.M., Boyce, J.I., Riddick, N.L., Saholgu, V., Erkanal, H., Reinhard, E.G., Goodman-Tchernov, B.N., 2021 (In Prep). Coastal sediment record of the construction of Alexander the Great's causeway at Clazomenae (ca. 4th c. BCE) and its impact on coastal environments (Bay of Izmir, Turkey).

Kylander, M.E., Ampel, L., Wohlfarth, B., Veres, D., 2011. High-resolution X-ray fluorescence core scanning analysis of Les Echets (France) sedimentary sequence: new insights from chemical proxies. Journal of Quaternary Science 26(1), 109-117.

Lambeck, K., 1995. Late Pleistocene and Holocene sea-level change in Greece and south-western Turkey: a separation of eustatic, isostatic and tectonic contributions. Geophysics Journal International 122(3), 1022-1044.

Lambeck, K., Purcell, A., 2005. Sea-level change in the Mediterranean Sea since the LGM: model predictions for tectonically stable areas. Quaternary Science Reviews 24(18-19), 1969-1988.

Lambeck, K., Rouby, H., Purcell, A., Sun, Y., Sambridge, M., 2014. Sea level and global ice volumes from the Last Glacial Maximum to the Holocene. Proceedings of the National Academy of Sciences 111(43), 15296-15303.

Lök, A., Acarlı, S., 2006. Preliminary settlement studies of flat oyster (Ostrea edulis, L.) on oyster and mussel shell collectors in Karantina Island (Turkey). Israeli Journal of Aquaculture-Bamidgeh 58(2), 105-115.

Löwemark, L., Chen, H.F., Yang, T.N., Kylander, M., Yu, E.F., Hsu, Y.W., Lee, T.Q., Song, S.R., Jarvis S., 2011. Normalizing XRF-scanner data: a cautionary note on the interpretation of high-resolution records from organic-rich lakes. Journal of Asian Earth Sciences 40(6), 1250-1256.

Marshall, M.H., Lamb, H.F., Huws, D., Davies, S.J., Bates, R., Bloemendal, J., Boyle, J., Leng, M.J., Umer, M., Bryant, C., 2011. Late Pleistocene and Holocene drought events at Lake Tana, the source of the Blue Nile. Global and Planetary Change 78(3-4), 147-161.

Mellett, C.L., Plater, A.J., 2018. Drowned barriers as archives of coastal response to sea-level rise. In: Moore, L.J., Murray, A.B. (Eds), Barrier dynamics and response to changing climate, Springer, pp. 57-89.

Miall, A.D., 2010. The geology of stratigraphic sequences. 2nd Edition. Springer Science & Business Media, p. 521.

Morhange, C., Pirazzoli, P.A., Evelpidou, N., Marriner, N., 2012. Late Holocene tectonic uplift and the silting up of Lechaion, the western harbor of ancient Corinth, Greece. Geoarchaeology 27(3), 278-283.

Morton, R.A., White, W.A., 1997. Characteristics of and corrections for core shortening in unconsolidated sediments. Journal of Coastal Research, 761-769.

Müller, C., Woelz, S., Ersoy, Y., Boyce, J., Jokisch, T., Wendt, G., Rabbel, W., 2009. Ultra-high-resolution marine 2D–3D seismic investigation of the Liman Tepe/Karantina Island archaeological site (Urla/Turkey). Journal of Applied Geophysics 68(1), 124-134.

Paul, M.A., Barras, B.F., 1998. A geotechnical correction for post-depositional sediment compression: examples from the Forth valley, Scotland. Journal of Quaternary Science: Published for the Quaternary Research Association 13(2), 171-176.

Pint, A., Seeliger, M., Frenzel, P., Feuser, S., Erkul, E., Berndt, C., Klein, C., Pirson, F., Brückner, H., 2015. The environs of Elaia's ancient open harbour–a reconstruction based on microfaunal evidence. Journal of Archaeological Science 54, 340-355.

Piva, A., Asioli, A., Schneider, R.R., Trincardi, F., Andersen, N., Colmenero-Hidalgo, E., Dennielou, B., Flores, J-A., Vigliotti, L., 2008. Climatic cycles as expressed in sediments of the PROMESS1borehole PRAD1-2, central Adriatic, for the last 370 ka: 1. Integrated stratigraphy. Geochemistry, Geophysics, Geosystems 9(1).

Rampino, M.R., Sanders, J.E., 1980. Holocene transgression in south-central Long Island, New York. Journal of Sedimentary Research 50(4), 1063-1079.

Reimer, P.J., McCormac, F.G., 2002. Marine radiocarbon reservoir corrections for the Mediterranean and Aegean Seas. Radiocarbon 44(1), 159-166.

Rothaus, R.M., Reinhardt, E.G., Noller, J.S., 2008. Earthquakes and subsidence at Kenchreai: using recent earthquakes to reconsider the archaeological and literary evidence. In: Caraher W.R., Hall, L.J., Moore, R.S. (Eds), Archaeology and history in Roman, medieval and post-medieval Greece: studies on method and meaning in honor of Timothy E. Gregory, Ashgate Publishing Ltd., pp. 53-66.

Rothwell, R.G., Croudace, I.W., 2015. Micro-XRF studies of sediment cores: a perspective on capability and application in the environmental sciences. In: Croudace, I.W., Rothwell, R.G. (Eds), Micro-XRF Studies of Sediment Cores, Springer, pp. 1-24

Şahoğlu, V., 2005. The Anatolian trade network and the Izmir region during the Early Bronze Age. Oxford Journal of Archaeology 24(4), 339-361.

Sakellariou, D., Galanidou, N., 2017. Aegean pleistocene landscapes above and below sea-level: palaeogeographic reconstruction and hominin dispersals. In: Bailey, G.N., Harff, J., Sakellariou, D. (Eds.), Under the sea: archaeology and palaeolandscapes of the continental shelf, Springer, pp. 335-359.

Sayın. E., 2003. Physical features of the Izmir Bay. Continental Shelf Research 23(10), 957-970.

Sayın, E., Eronat, C., 2018. The dynamics of İzmir Bay under the effects of wind and thermohaline forces. Ocean Science 14(2), 285-292.

Scott, D.B., Hermelin, J.O.R., 1993. A device for precision splitting of micropaleontological samples in liquid suspension. Journal of Paleontology 67(1), 151-154.

Seeliger, M., Bartz, M., Erkul, E., Feuser, S., Kelterbaum, D., Klein, C., Pirson, F., Vött, A., Brückner, H., 2013. Taken from the sea, reclaimed by the sea: The fate of the closed harbour of Elaia, the maritime satellite city of Pergamum (Turkey). Quaternary International 312, 70-83.

Sonnenburg, E.P., Boyce J.I., 2008. Data-fused digital bathymetry and side-scan sonar as a base for archaeological inventory of submerged landscapes in the Rideau Canal, Ontario, Canada. Geoarchaeology 23(5), 654-674.

Sonnenburg, E.P., Boyce, J.I., Suttak, P., 2012. Holocene palaeoshorelines, water levels and submerged prehistoric site potential of Rice Lake (Ontario, Canada). Journal of Archaeological Science 39(12), 3553-3567.

Stiros, S.C., 2020. Coastal subsidence, destruction layers and earthquakes from an underwater archaeological excavation: Kenchreai, eastern harbour of Roman Corinth, Greece. Mediterranean Geoscience Reviews, 1-15.

Stock, F., Kerschner, M., Kraft, J.C., Pint, A., Frenzel, P., Brückner, H., 2014. The palaeogeographies of Ephesos (Turkey), its harbours, and the Artemision–a geoarchaeological reconstruction for the timespan 1500–300 BC. Zeitschrift für Geomorphologie, Supplementary Issues 58, 33-66.

Stock, F., Pint, A., Horejs, B., Ladstätter, S., Brückner, H., 2013. In search of the harbours: New evidence of Late Roman and Byzantine harbours of Ephesus. Quaternary International 312, 57-69.

Stuiver, M., Reimer, P.J., Reimer, R.W., 2019. CALIB 7.1 [WWW program] at http://calib.org

Tan, O., Tapirdamaz, M.C., Yörük, A., 2008. The earthquake catalogues for Turkey. Turkish Journal of Earth Sciences 17(2), 405-418.

Tartaron, T.F., 2013. Maritime networks in the Mycenaean world. Cambridge University Press.

Tartaron, T.F., 2015. The Settlement at Kalamianos: Bronze Age Small Worlds and the Saronic Coast of the Southeastern Corinthia. Hesperia Supplements 48, 25-38.

Tartaron, T.F., Pullen, D.J., Dunn, R.K., Tzortzopoulou-Gregory, L., Dill, A., Boyce, J.I., 2011. The Saronic harbors archaeological research project (SHARP): investigations at Mycenaean Kalamianos, 2007-2009. Hesperia 80(4), 559-634.

Taymaz, T., Yilmaz, Y., Dilek, Y., 2007. The geodynamics of the Aegean and Anatolia: introduction. Geological Society, London, Special Publications 291(1), 1-16.

Tuncel, R., Şahoğlu, V., 2018. The Chalcolithic of coastal western Anatolia: A view from Liman Tepe, Izmir. In: Dietz, S., Mavridis, F., Tabkosic, Z., Takaoglu, T. (Eds), Communities in transition: The circum-Aegean area during the 5th and 4th millennia BC, Oxbow Books Limited.

Vacchi, M., Rovere, A., Chatzipetros, A., Zouros, N., Firpo, M., 2014. An updated database of Holocene relative sea level changes in NE Aegean Sea. Quaternary international 328, 301-310.

Votruba, G.F., Artzy M., Erkanal H. (2016). A set Archaic anchor arm exposed within P. oceanica matte at Klazomenai/Liman Tepe, Turkey: A contribution for understanding marine stratigraphy. Journal of Field Archaeology, 41(6): 671-683

Vousdoukas, M.I., Velegrakis, A.F., Plomaritis, T.A., 2007. Beachrock occurrence, characteristics, formation mechanisms and impacts. Earth-Science Reviews 85(1-2), 23-46.

Westley, K., Plets, R., Quinn, R., 2014. Holocene paleo-geographic reconstructions of the Ramore Head area, Northern Ireland, using geophysical and geotechnical data: Paleo-landscape mapping and archaeological implications. Geoarchaeology 29(6), 411-430.

Wolters, S., Zeller, M., Bungenstock, F., 2010. Early Holocene environmental history of sunken landscapes: pollen, plant macrofossil and geochemical analyses from the Borkum Riffgrund, southern North Sea. International Journal of Earth Sciences 99(8), 1707-1719.

CHAPTER 3: Multi-proxy palaeoenvironmental record of the Late Bronze to Iron Age transition and harbour development at Clazomenae, western Anatolia, Turkey

Abstract

Clazomenae, located in the southern Bay of Izmir, Turkey, was an important Iron Age olive-producing centre and trading port. Clazomenae's mainland harbour basin is one of the best-preserved examples of an Archaic period (ca. 7th c. BCE) semi-enclosed harbour (>5 ha), protected by two broad (>35 m) breakwaters structures, now submerged ~1-2 m below present sea level. A multi-proxy geoarchaeological study was conducted on 6 harbour sediment cores and integrated with geophysical surveys (bathymetry, side-scan sonar, magnetics) to map the harbour structures and to document changes in coastal palaeoenvironments. Anthropogenic signals of land-use impact in harbour basin sediments were evaluated using micro-XRF core scanning (μ-XRF-CS) and chemofacies analysis.

Bathymetry and side-scan mapping delineated two broad rubble-constructed breakwater structures enclosing the harbour, and a submerged headland that divided the harbour into two separate basins. Linear magnetic anomalies within the eastern breakwater indicate a possible Late Bronze buried pier structure, recording augmentation of a proto-harbour embayment. The harbour basin stratigraphy consisted of upper shoreface sands and *Posidonia* muds overlying a Ti-rich terrigenous clay unit. A distinctive silt-rich unit with increased Ti/Ca and decreased Si and Br recorded a transition from a shoreface to sheltered proto-harbour embayment. Increased Ti/Ca records rising terrestrial sediment inputs to the embayment as a result of Middle-Late Bronze Age land clearance and settlement expansion. An abrupt shift to lower Ti/Ca values at ca. 1200 BCE signals a decrease in terrigenous inputs, coinciding with a ~300-year drought phase, possibly linked to the Late Bronze Age collapse. The onset of Iron Age harbour construction (ca. 7th c. BCE) is recorded by a shift to lower Ti/Ca values, an increase in *Rosalina*, and the appearance of Archaic pottery. μ-XRF-CS results show that high-resolution chemofacies analysis can identify subtle geochemical changes in harbour sediments (i.e. terrigenous sediment flux) that would be unresolvable using conventional palaeo-ecological and sedimentological

techniques. This paper represents the first use of µ-XRF-CS geochemical records to document the transition from a proto-harbour to semi-enclosed engineered harbour basin in the Aegean.

Keywords: Clazomenae, Liman Tepe, Archaic harbour, proto-harbour, palaeoenvironments, chemofacies, micro-XRF core scanning, geophysical survey

3.1 Introduction

The Iron Age (ca. 1200-114 BCE) was a period of major cultural and technological change in the Aegean. The expansion of Greek colonies resulted in the broadening of inter-regional trade networks and the establishment of new maritime trade centres (Papadopoulos, 2014). An important technological innovation during this period was the introduction of engineered harbour structures (e.g. breakwaters, piers, and quays) and semi-enclosed harbour basins. During the preceding Bronze Age (ca. 3000-1200 BCE), sheltered embayments, lagoons, and coastal headlands were utilized as natural anchorage sites (Marriner et al., 2005, 2014; Tartaron, 2015; Mauro, 2019). In the Iron Age, many of these 'proto-harbour' basins were augmented with engineered structures to permit harbouring under a wider range of weather conditions and sea states (Shalev et al., 2019). In the Aegean, the transition from natural to 'semi-artificial' engineered harbours began during the Iron Age (Archaic period), with the earliest evidence for man-made breakwaters dating to the 8th-7th c. BCE at Delos. By the late 6th to early 5th c. BCE, breakwaters were built as extensions of city fortification walls (Flemming, 1980; Duchêne et al., 2001; Mauro, 2019). In the eastern Mediterranean, the augmentation of natural proto-harbour basins began earlier, perhaps as early as the Middle-Late Bronze Age (Raban, 1995; Tartaron, 2015). Raban (1995) described ashlar-constructed quays at Dor (Israel) that were built in the Late Bronze and modified during the early Iron Age. At Atlit (Israel), mole and quay structures were built using similar ashlar construction, which were constrained by radiocarbon dating to the 9th-7th c. BCE (Haggi et al., 2006; Haggi and Artzy, 2007). At Sidon (Lebanon) sandstone ridges were augmented with rubble constructions to enhance natural embayments during the Middle-Late Bronze Age (Marriner et al., 2006).

A number of environmental and economic factors played a role in the development of semi-artificial harbours in the Aegean. On clastic coasts, the middle Holocene deceleration in sea level rise at ca. 6-6.5 ka BP rapidly changed coastal sediment budgets and morphodynamics (Marriner and Morhange, 2007; Mauro, 2019). In western Turkey, for example, many large river deltas prograded seaward and coastal plains aggraded rapidly, infilling coastal embayments and river valleys to form rias (Kayan, 1988). Consequently, many naturally sheltered harbouring sites were lost, and engineering interventions were required to create semi-artificial and artificial harbour basins. The expansion of Iron Age maritime trade and the increased size and draft of merchant and naval vessels also necessitated the construction of harbours with built dock structures for lading of goods and for ship maintenance (Marriner et al., 2014). By comparison, Bronze Age merchant ships were smaller vessels built for plying inshore coastal trade routes, and with low-draught hulls designed to be drawn up onto beaches and moored in shallow water (Tartaron, 2013).

Engineered harbour basins are important sediment archives for geoarchaeological studies, as they were low energy depocentres which accumulated and preserved harbour sediments, cultural materials (e.g. pottery), and anthropogenic pollutants (Marriner and Morhange, 2007; Marriner et al., 2010). Consequently, harbour basins have become a major focus of geoarchaeological studies in the Mediterranean, as they can provide important records of seafaring and maritime trade activities and are rich palaeoenvironmental archives of sea level change and coastal evolution (Marriner et al., 2005, 2006, 2008; Reinhardt et al., 1999; Goodman et al., 2008, 2009; Seeliger et al., 2013; Stock et al., 2013, 2014, 2019; Shumilovskikh et al., 2016; Stiros, 2020; Chapters 2, 4). Harbour sediment archives have also yielded long-term records of palaeotsunamis and earthquake impacts on coastlines (Reinhardt et al., 2006; Hadler et al., 2013, 2015; Mourtzas et al., 2014; Stiros, 2020; Chapter 4). Classical and Roman harbours have received the most attention archaeologically, and in the Aegean, few details are available on the critical period of transition from Late Bronze proto-harbours to Iron Age engineered harbour basins (Tartaron et al., 2011; Mauro, 2019).

In this paper, we report on the results of geoarchaeological and geophysical investigations of a well-preserved early Iron Age (Archaic period) harbour basin at Clazomenae, in western Turkey (Fig. 3.1). Located on the southern Bay of Izmir, Clazomenae was an important olive production centre and trading port from its founding in the 11th-9th c. BCE (Aytaçlar, 2004; Ersoy, 2004). The Archaic harbour basin covered an area of >5 ha and was enclosed by two broad (>35 m wide) man-made breakwater structures, which are now submerged ~1.5-2 m below present sea level (Erkanal, 2014a). The eastern breakwater structure is about 120 m in length and is attached to a small coastal headland, which was the location of the Chalcolithic to Bronze Age site of Liman Tepe (prehistoric Clazomenae) (Erkanal, 1997, 2014b). The western breakwater extends from a small rocky headland and is partially covered by the modern harbour installations of the port town of Iskele (Figs. 3.1a, 3.2a). Later in its history, Clazomenae was served by other anchorages, including a large Roman artificial harbour on the west side of Karantina Island (Fig. 3.1a).

Clazomenae's Archaic harbour basin is one of the best-preserved examples of an Iron Age harbour in the eastern Mediterranean, but its date of construction, layout, and function were not well understood. The harbour is significant in a western Anatolian context, as other examples of Iron Age harbours here have been infilled, and in some cases completely buried by the aggradation of alluvial sediments at mouths of major river systems (e.g. Troy - Kraft et al., 2003; Miletus - Brückner, 1997; Ephesus - Brückner, 1997; Stock et al., 2013, 2014, 2019; Elaia - Seeliger et al., 2013; Burgaz - Greene et al., 2019). The state of preservation of Clazomenae's harbour basin provides a unique opportunity to study Iron Age harbour technology, maritime trade, and human/environmental interactions in the Aegean (Erakanal et al., 2017).

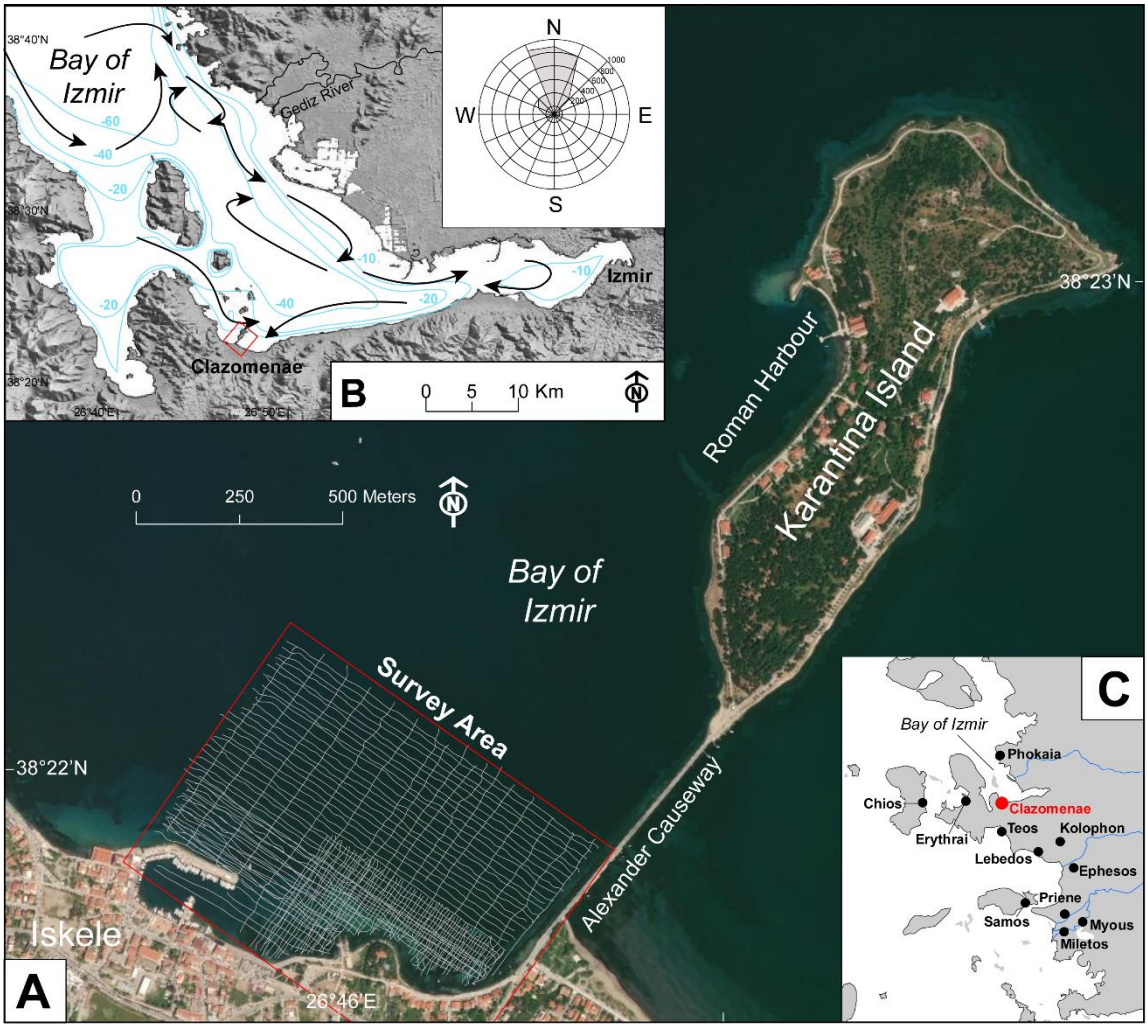

Figure 3.1: A. Satellite image showing location of Clazomenae's mainland Archaic harbour basin and geophysical survey area (0.35 km^2) (aerial image ESRI basemaps). B. Location of study site on the southern Bay of Izmir, with generalized bathymetric contours (interval 10 m). Dominant wind direction and water circulation patterns (arrows) modified from Sayin (2003). C. Location of Clazomenae and other Ionian League cities in western Anatolia, Turkey (GIS data from Natural Earth).

The current study represents the first systematic geoarchaeological investigation of Clazomenae's Archaic harbour basin. We employed a multi-proxy analysis (micro-X-ray-fluorescence geochemistry, micropalaeontology, sedimentary facies, and AMS ^{14}C chronology) of 6 marine sediment cores (Fig. 3.2a) to document changes in the harbour palaeoenvironments stemming from land use changes and harbouring activities. Core data were combined with geophysical mapping of the harbour basin (bathymetry, side-scan sonar, magnetic surveys) to better resolve the harbour layout and construction. We also

evaluated micro-XRF core scanning (µ-XRF-CS) and chemofacies analysis (Craigie, 2018), as an approach for identifying the onset of harbouring and anthropogenic land-use impacts in harbour basin sediments. The results provide important new insights into harbouring activities, from a Late Bronze Age (LBA) proto-harbour phase (ca. 1600 BCE) to the construction of a semi-artificial Archaic harbour basin (ca. 7th c. BCE). Chemofacies analysis (µ-XRF-CS) also identifies changes in terrigenous sediment inputs to the coast that we interpret as a record of prehistoric land disturbance and possible evidence for a 300-year drought period that has been linked to the LBA decline (the so-called Dark Age, ca. 1200-1000 BCE; Drake, 2012).

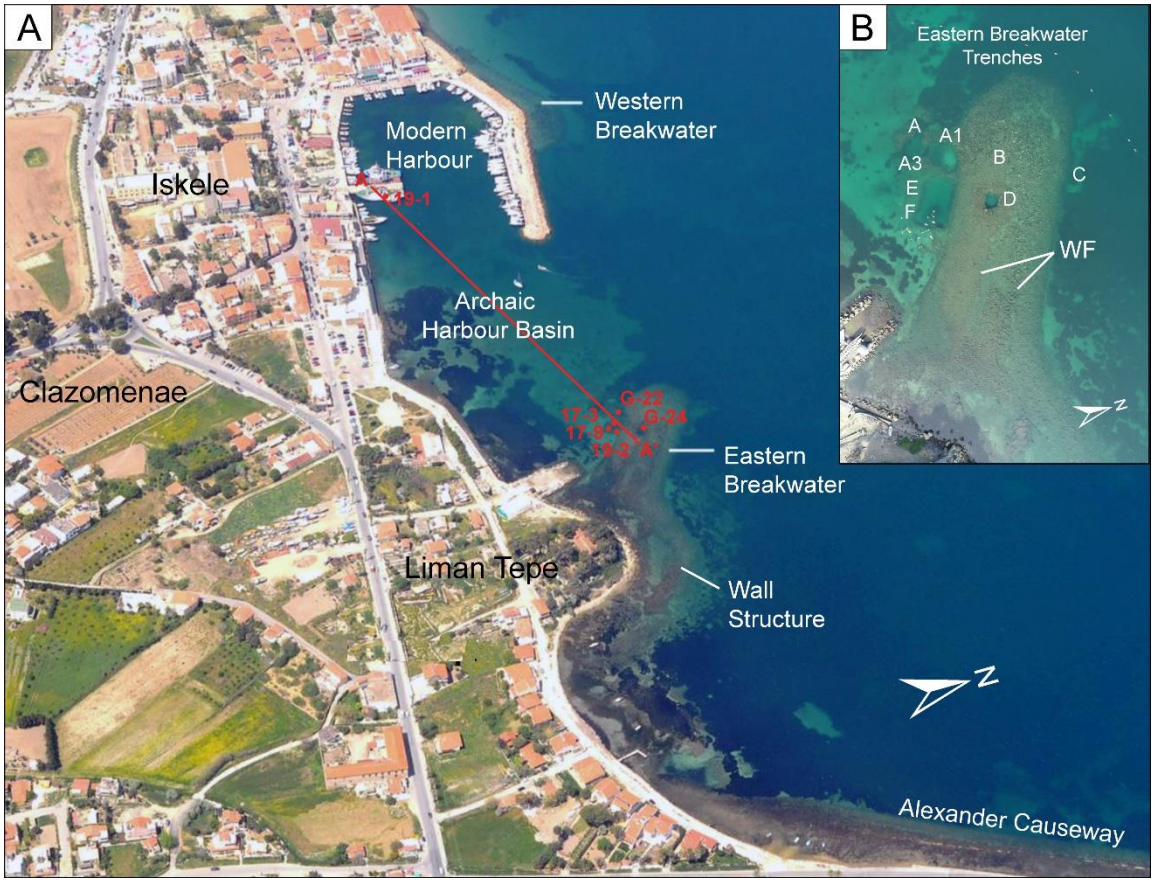

Figure 3.2: A. Aerial photograph showing the submerged remains of Clazomenae's Archaic harbour basin. Location of sediment cores (transect A-A'; Fig. 3.9) also shown. B. Aerial image of eastern breakwater, showing location of excavation trenches. Note rubble construction of breakwater and linear wall features on surface.

3.2 Study Area

3.2.1 Physical Setting and Geology

Clazomenae is located on the south shore of the Bay of Izmir, near Urla, in western Turkey (Fig. 3.1). The Bay of Izmir is microtidal (~20-50 cm) with a maximum water depth of about 100 m (Fig. 3.1b). The dominant wind direction throughout the year is from north and the primary sediment input into the bay is the Gediz River (Fig. 3.1b). The water mass circulation is controlled by inflow of Aegean water and wind-driven currents, which generate cyclonic and anticyclonic gyres (Sayin, 2003; Sayin and Eronat, 2018). In the eastern sector of the Bay, currents are dominantly clockwise, resulting in the transport of sediment eastward along the north shore from the Gediz river and westward along the southern shore towards Urla (Fig. 3.1b). Within the study area, the westward longshore component of sediment transport has resulted in progradation of beaches to the east of Karantina island. This process began following the deceleration in sea level rise at 6 ka BP (ca. 4000 BCE), which caused a shift to a positive sediment budget and aggradation of the coastal plain (Goodman et al., 2008; Kayan et al., 2019; Chapter 2). Progradation was further accelerated by construction of the Alexander causeway (ca. 334 BCE), linking the mainland with Karantina Island (Figs. 3.1a, 3.2a). The barrier has acted as an effective sediment trap resulting in the starvation and erosion of beaches on the west side Karantina island (Goodman et al., 2008; Krezoski et al., 2021). The causeway also acted to limit the siltation of Clazomenae's mainland harbour basin, which would otherwise have undergone burial due to coastal progradation.

Several previous geoarchaeological studies have investigated the coastal palaeogeography and palaeoenvironments at Clazomenae (Goodman et al., 2008, 2009; Krezoski, 2008; Kayan et al., 2019; Chapter 2). Goodman et al. (2009) documented the Archaic harbour basin sediments and identified shifts in foraminifera coinciding with the onset of harbour construction and a shift to eutrophic harbour environments. Goodman et al. (2008) and Kayan et al. (2019) employed land core data to correlate and map the onshore late Holocene stratigraphy. They identified marine sediments recording a transgression

event at ca. 4000 BCE that extended approximately 1 km inland of the modern shoreline. Chapter 2 presents reconstructed palaeoshoreline positions from the middle Neolithic (6700 BCE) to the Early Bronze Age (EBA; ca. 3000), using a large marine and land core dataset. During the middle Neolithic (ca. 6700 BCE), the coastline was about >500 m seaward of the modern shore and Karantina Island was a broad coastal headland. By the beginning of the Chalcolithic (ca. 4800 BCE), the coastline had transgressed inland, forming a large bay to the southeast of the Liman Tepe headland, which was separated from the mainland by coastal wetlands. By ca. 4000 BCE, the embayment had reached its maximum extent (maximum transgression) 1 km inland of the modern shoreline and Liman Tepe was a small offshore island. Following ca. 4000 BCE, a high-stand systems tract obtained, and the shoreline prograded rapidly by the accretion of shore-parallel sandbars (Goodman et al., 2008). The Liman Tepe headland was reconnected with the mainland by the beginning of the EBA and shallow embayments, with back barrier lagoonal environments, existed to the east and west of the headland. The sheltered bays and lagoons would have offered excellent natural anchorages for merchant vessels during the EBA (Goodman et al., 2009; Chapter 2).

3.2.2 Site History and Archaeology

Clazomenae was founded by Ionian and Greek settlers between the 11th and 9th c. BCE and was a member of the Ionian League (Fig. 3.1c). The city was an important olive-producing centre and trading port during the Classical and Roman Periods (Herodotus, 5th c. BCE; Aytaçlar, 2004; Ersoy, 2004). Clazomenae was founded on the prehistoric settlement of Liman Tepe, which was located on the coastal headland to the east of the modern town of Iskele (Figs. 3.1a, 3.2a). Liman Tepe was an important EBA trade centre in the Anatolian Trade Network, which spanned the Aegean and Anatolia (Şahoğlu, 2005; Erkanal, 2017). In the 6th-5th c. BCE Clazomenae's citadel was moved from the mainland to Karantina Island due to conflict with the Persians and in the 4th c. BCE a causeway linking the island to the mainland was constructed by the forces of Alexander the Great (ca. 334 BCE) (Heisserer, 1980; Krezoski et al., 2021).

Land excavations at Liman Tepe/Clazomenae have yielded a broad range of Early to LBA cultural materials, including Minoan and Mycenean finds, indicating a diverse maritime trade network and cultural connections that spanned the Aegean (Erkanal, 2014a, b). The earliest settlement layers on the land site date to the early Chalcolithic (ca. 4600 BCE) (Tuncel and Şahoğlu, 2018) and there is scattered pottery evidence for a possible Neolithic occupation, but to date, no settlement layers from this period have been discovered (Erkanal, 2008; Chapter 2). Bronze Age harbouring locations have not yet been identified, but due to Liman Tepe's importance as a maritime trading port, it has been speculated that natural embayments and coastal lagoons to the east and west of the headland may have provided sheltered mooring areas (Goodman et al., 2009).

Underwater excavations at Clazomenae have been ongoing since 2005 and have focused on the eastern Archaic harbour basin (Fig. 3.2b) (Erkanal et al., 2014). Recent work has yielded a wealth of pottery and other cultural materials that indicate the harbour was an active trading port in 7th-6th c. BCE (Archaic Period), and again in the 4th c. BCE (Classical Period) (Artzy, 2009; Goodman et al., 2009; Şahoğlu, 2010; Erkanal et al., 2015; Votruba et al., 2016; Tuğcu et al., 2017). Coring work conducted by Goodman et al. (2009) in Trench D (Fig. 3.2b) recorded 4.8 m of rubble overlying marine shoreface deposits containing *Posidonia oceanica* (sea grass) mattes. The surface rubble layer included ashlar stones, indicating possible wall structures. Underwater excavations at the same location in 2008 uncovered the remains of a wooden anchor arm, embedded in *Posidonia* mud, which is dated to the 7th or early 6th c. BCE (Votruba et al., 2016). Investigations of the western harbour basin and breakwater have been limited to diver reconnaissance and test trenching. A 1-metre-deep trench excavated inside the modern Iskele harbour, to the south of the western breakwater, did not identify cultural materials, most likely due to modern dredging activities (Tuğcu et al., 2017).

3.3 Methods

3.3.1 Geophysical Surveys

Marine geophysical surveys were conducted at Clazomenae between 2006-2014 as part of a seabed mapping project, to evaluate underwater archaeological potential (Boyce et al., 2007; Müller et al., 2009; Chapter 2). Bathymetric and side-scan sonar surveys were conducted over a 0.35 km^2 inshore area, including the Archaic harbour basin, with a line spacing of 5-20 m (Fig. 3.1a). Sonar data were acquired using a Knudsen 320BP echosounder system with transducers (200-kHz; 0.5 x 50º beam angle) side-mounted to an inflatable boat. Bathymetry processing included corrections for tidal variation, tie-line leveling, and grid interpolation using a triangular interpolated network (TIN) with a 1 m grid cell size (Sonnenburg and Boyce, 2008). Side-scan processing (Sonarview v. 1.0) included application of slant-range and beam angle (radiosity) corrections and mosaicing of swaths using pixel averaging algorithm with 0.1 m cell size (Cervenka and De Moustie, 1993; Anstee, 2001; Young and Anstee, 2001).

Total magnetic intensity (TMI) surveys were acquired over the eastern breakwater area using a marine Overhauser magnetometer (Marine Magnetics Explorer^{TM}) with 3-5 m line spacing and a 4 Hz sample rate (~2 samples m^{-1}). A second base station magnetometer was deployed onshore to record diurnal field variations. Survey positioning by differential GPS receivers (Trimble 132) with a horizontal positional error of <0.5 m. Processing of magnetometer data included diurnal corrections, tie-line leveling, and gridding of the corrected TMI data using minimum curvature with 1-m grid cells. The TMI data were upward continued 10 m and subtracted from the TMI grid to produce a magnetic residual map for detection of shallow magnetic source bodies (Luyendyk, 2007; Boyce et al., 2004).

3.3.2 Coring and Sediment Analysis

A total of four cores (~1.5-3.2 m length) were collected in the Archaic harbour basin using a diver-operated percussion coring system with 70 mm aluminum tubes (Fig. 3.2a). Three cores were collected on the east side of the basin (excavation areas E and F; Fig. 3.2b) and a single long core (3.2 m) in the western harbour basin. Cores were extracted

using a boat mounted winch and lift bags, then sealed and refrigerated at 4-6 °C to prevent microbial growth and oxidation. The cores were split, the sedimentary lithofacies and texture logged, and 13 samples of organics (likely *Posidonia* grass) and shell material were collected for AMS radiocarbon dating (Table 3.1) at the A. E. Lalonde Laboratory (University of Ottawa, Ottawa, Ontario). AMS ^{14}C dates were calibrated with Calib 7.1 software using the IntCal13 and Marine13 calibration curves (Stuiver et al., 2019). Calibration of ages using shell materials included a marine reservoir correction $\Delta R = 109 \pm 37$ (Reimer and McCormac, 2002). Samples of undifferentiated plant matter were calibrated using IntCal13, as the proportion of marine versus terrestrial organics was not determined. The IntCal13 curve produced dates which were consistent with pottery ages in harbour basin sediments and with the archaeological constraints of the age of the breakwater structures. Bayesian sediment age-depth models were constructed for two cores (17-9 and 19-1) using the R-package BACON (Blaauw and Christen, 2011). In core 17-9 a large pottery sherd was present, providing additional sediment age constraints. Interpretation and correlation of core data was aided by comparison with lithofacies and foraminifera data from two previous cores (G-22 and G-24; Fig. 3.2a) collected by Goodman (2006).

Micro-XRF elemental analysis was conducted on four cores using an ITRAX core scanner (Cox Analytical Systems), with a 3-kW molybdenum (Mo) tube. Cores were scanned at 500 µm step size, with an analysis time of 20 s, and 30 kV/25 mA power settings. The micro-XRF spectra were batch analyzed using QSpec^{TM} software and normalized using the ratio of coherent to incoherent (coh/inc) scatter to minimize matrix effects due to changes in sediment water content and porosity (Kylander et al., 2011; Marshall et al., 2011; Berntsson et al., 2014; Gregory et al., 2019). Elemental data were combined with sedimentary facies characteristics to identify and correlate several distinctive chemofacies units within the harbour basin stratigraphy (Ramkumar, 2015; Craigie, 2018). Chemofacies were identified based on downcore changes in the abundance of terrigenous elements (Si, Ti, Fe, Al, K) and elements indicating marine productivity (Ca, Br, Sr). Ca is commonly used as an indicator of biogenic $CaCO_3$ production (aragonite) and Br as an indicator of

marine plant organic matter (Rothwell and Croudace, 2015; Ziegler et al., 2008; Seki et al., 2019). A Pearson correlation matrix (Fig. 3.3) was calculated to determine element relationships and to aid in selecting element ratios. Si and Ti were selected as proxies for terrigenous sediments and Ca and Br as indicators of marine productivity. The metals Cu and Pb were employed as indicators of anthropogenic pollution (Le Roux et al., 2005; Hadler et al., 2013; Stock et al., 2016). The Ti/Ca ratio was used to determine variations in terrestrial runoff in harbour sediments and as a tool for core correlation (Piva et al., 2008; Ingram et al., 2010; Koster et al., 2015; Pint et al., 2015; Rothwell and Croudace, 2015, Chapter 2). Element ratios (e.g. Ca/Fe, Ca/Ti, Ti/Br) have been applied in a number of harbour geoarchaeological studies for determining the relative influence of terrigenous versus marine sediment inputs (Hadler et al., 2013; Stock et al., 2013; Pint et al., 2015; Finkler et al., 2018; Seeliger et al., 2019; Chapter 2, 4). This study is the first to evaluate μ-XRF-CS and the Ti/Ca ratio for identifying signals of land use and palaeoenvironmental change for harbour development and evolution.

Micropalaeontological analysis (foraminifera) was completed on two cores (17-9, 19-1). Samples (2.5 cc) from each core were divided into eight alliquots using a wet splitter and sieved into 45 μm, 63 μm, 125 μm and 500 μm fractions (Scott and Hermelin, 1993). Where possible >100 individual foraminifera were counted and identified to genus level. The identification of foraminifera was assisted by previous work of Goodman (2006) and Krezoski (2008). In addition, foraminifera biofacies from core G-22 of Goodman et al. (2009) were reinterpreted and employed in this study.

Table 3.1: AMS ^{14}C radiocarbon dates. All dates were calibrated using Calib 7.1 with the IntCal13 and Marine13 calibration curves (Stuiver et al., 2019). Date from core G-22 (Goodman, 2006) was recalibrated. * Marine reservoir correction (ΔR = 109 +/-37) applied to shell samples (Reimer and McCormac, 2002). ** Suess Effect.

Sample Code	Core #	Material	Elevation (mbsl)	^{14}C Age (BP)	2σ Max and Min Calibrated Age		
Beta-191880	G-22	Shell*	7.60	6280 ± 40	4781	4527	BCE
Beta-164096	G-24	Plant fragments	5.80	2710 ± 30	910	807	BCE
UOC-7342	17-9	Plant fragments	5.16	2960 ± 22	1260	1111	BCE
UOC-9339	17-9	Plant fragments	5.54	3550 ± 25	1960	1868	BCE
UOC-9340	17-9	Plant fragments	5.96	3966 ± 25	2503	2453	BCE
UOC-7343	17-9	Plant fragments	6.24	4535 ± 22	3238	3106	BCE
UOC-9341	17-9	Plant fragments	6.38	4682 ± 25	3474	3371	BCE
UOC-7344	17-9	Plant fragments	6.51	4996 ± 22	3802	3706	BCE
UOC-12077**	19-1	Plant fragments	5.00	270 ± 23	1626	1666	CE
UOC-12078	19-1	Plant fragments	5.17	1330 ± 22	652	695	CE
UOC-12824	19-1	Plant fragments	6.02	3445 ± 27	1785	1686	BCE
UOC-12103	19-1	Shell*	6.52	6335 ± 25	4824	4615	BCE
UOC-12825	19-1	Bulk	7.03	7310 ± 43	6241	6067	BCE
UOC-12220	19-1	Bulk	7.17	7968 ± 35	7044	6749	BCE
UOC-12079	19-2	Plant fragments	6.98	6197 ± 29	5229	5048	BCE

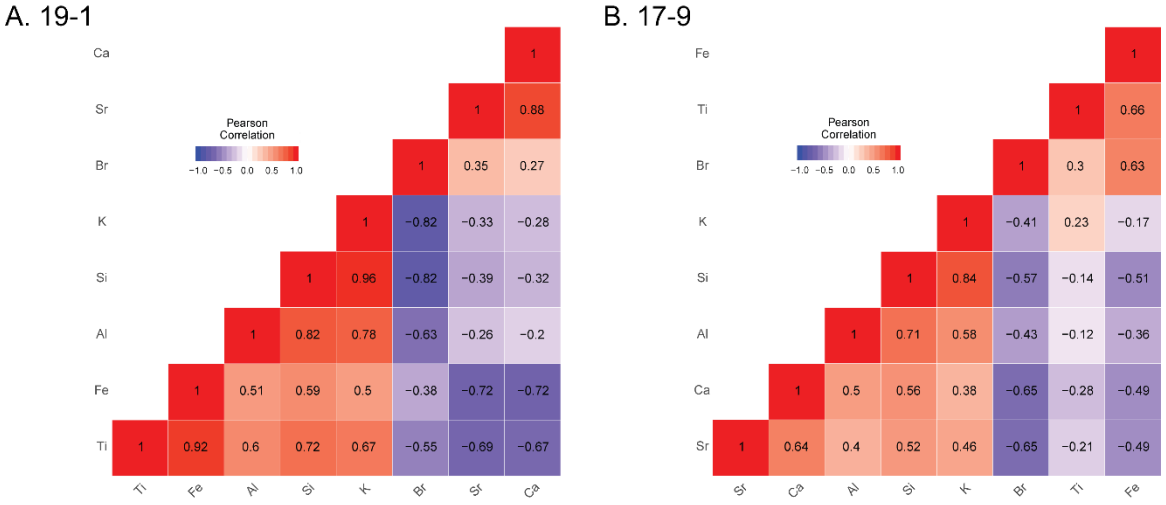

Figure 3.3: Pearson correlation matrix (heat maps) for selected elements. A. core 19-1. B. core 17-9. Note strong correlations between lithogenic terrigenous elements (Ti, K, Fe, Si, Al). Sr and Ca are indicators of biogenic productivity and the abundance of shell fragments ($CaCO_3$; aragonite) in core sediments.

3.4 Results

3.4.1 Geophysics

3.4.1.1 Bathymetry and Side-Scan Sonar

Bathymetric maps of the inshore area and eastern harbour basin are shown in Figure 3.4a. The Archaic harbour breakwaters lie at a depth of 1-4 mbsl and enclose a harbour area of about 5 ha. The inshore area (water depths 5-10 m) beyond the modern harbour preserves a network of relict river channels that were formed during the Neolithic when sea levels were >12 m below present (Chapter 2). The channels record a low-gradient river floodplain with a river mouth located in the western Archaic harbour basin (Fig. 3.4). The river channels were completely submerged by the Chalcolithic period (ca. 4800 BCE), but it is likely that a river system was present at this location on the coast throughout the Bronze Age and possibly during the Iron Age (Chapter 2). The river floodplain would have provided an important source of drinking water for settlements and water for agricultural irrigation. The river system was diverted for agricultural use in the modern period and there is no river inflow into the modern harbour basin.

The side-scan mosaics provide additional details of the seabed sediment texture and surface morphology of the harbour breakwater structures (Figs. 3.4b, 3.5). The eastern breakwater is approximately 120 m in length and 35 m wide, with a surface that is composed dominantly of cobble- to boulder-sized rubble. Within the surface rubble several linear wall structures can be identified, including wall foundations (Fig. 3.5b). The wall features were constructed of 0.25-0.5 m diameter stones which were laid end-to-end, forming the edge of a raised platform on the breakwater surface. A curvilinear wall feature extending eastward from the base of the breakwater and encircling the base of the headland is also clearly visible in side-scan (Fig. 3.5b). This structure appears to be composed of large blocks (ashlars?) and rubble. The 'prong-like' projection (20 m long) on the northwest corner of the breakwater may represent a quay or pier and encloses a small basin at the northwestern end of the mole structure. The circular depression at the north end of the breakwater is a 2-m deep excavation trench (Area D; Figs. 3.2b, 3.5b) that yielded an

Archaic-age wooden anchor (Votruba et al., 2016). The western breakwater is a broad (>50 m), 130-m-long arcuate structure with a rubble construction, similar to the eastern breakwater (Figs. 3.4-3.6). Linear arrangements of large boulders on the breakwater surface indicate architectural foundations or possibly seawalls (Fig. 3.5a). The curved form of the breakwater suggests the presence of a small harbour basin to the south of the mole, but its extent is obscured by the modern harbour installations. Possible architectural features were also identified on a bathymetric high (submerged headland?), dividing the Archaic harbour into two basins (Figs. 3.4, 3.5c).

3.4.1.2 Magnetics

The total magnetic intensity (TMI) across the Archaic harbour basin varies by about 160 nT (Fig. 3.6b). The eastern breakwater structure is clearly defined by a zone of high intensity with two distinct curvilinear magnetic lineaments within the main mass of the eastern breakwater structure. The anomalies extend from the base of the headland and terminate at a magnetic high that underlies the pier at the northwestern end of the breakwater (Fig. 3.6b). The curvilinear shape of the anomalies does not conform with the rectilinear outline of the rubble mass of breakwater structure. This suggests the presence of a pre-existing structure at some depth within the breakwater. The amplitude of the magnetic anomalies (>50 nT) indicates the presence of high magnetic susceptibility materials buried within the rubble mass. Excavations in the breakwater have determined that the rubble materials are dominantly limestone, but also include mafic and intermediate extrusive boulders (i.e. trachyte, andesite) derived from the local volcanic bedrock. Trachyte and andesitic boulders make up a large portion of boulders that were employed to construct the EBA fortification walls and bastions.

The linear stone courses visible in side-scan imagery (Fig. 3.5b) have no apparent magnetic response and appear to be surface constructions that do not extend to depth within the breakwater. The magnetic anomaly pattern is consistent with archaeological excavations, which show the breakwater core was constructed of rubble materials that were laid directly onto the seabed and no ashlar constructions were used in the foundation work.

The magnetic relief across the harbour basin and in the surrounding inshore area is generally low, except for three distinct high magnetic intensity zones to the west and northeast of the breakwater. These zones may indicate the presence of ship refuse (e.g. clay pottery) and ballast materials, (Boyce et al., 2009) or areas where the volcanic bedrock is close to surface. To the west of the breakwater, a 60-70 nT positive magnetic anomaly coincides with harbour basin deposits, which include fragments of large pithoi and ballast stones. Recent underwater excavations in trenches E and F (Fig. 3.2b) have also discovered thick (>3 m) harbour deposits with abundant pottery and ballast (Tuğcu et al., 2017).

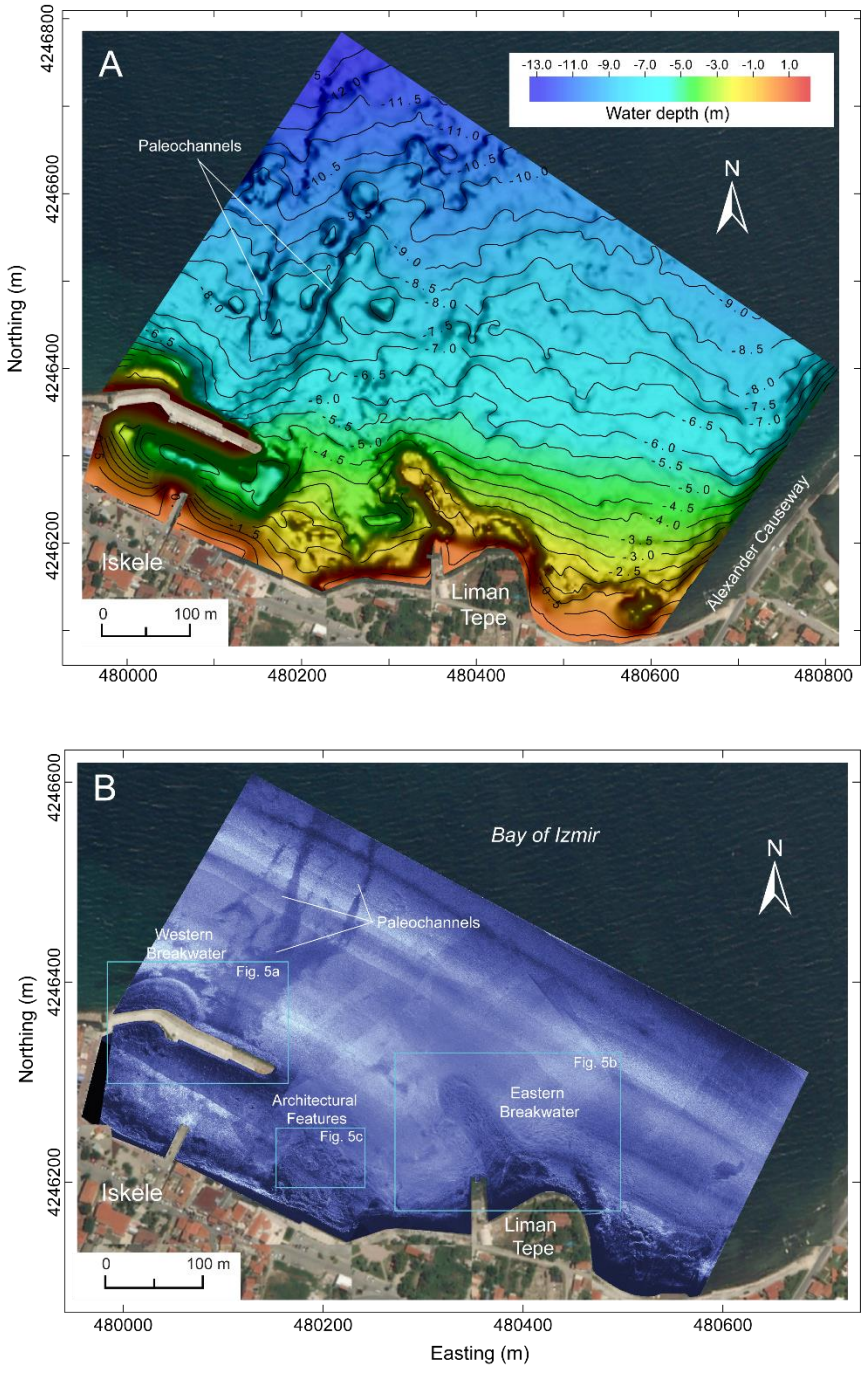

Figure 3.4: A. Bathymetry map of study area (1 m contour interval). Note northwest-trending palaeochannel features, recording a Neolithic drainage network, which existed when sea levels were >8 m below present (Chapter 2). The location of the western breakwater relative to the drowned river channels indicates the likely presence of a river mouth at Liman Tepe/Clazomenae during the Bronze Age and Iron Age settlement phases. B. Side-scan mosaic showing harbour breakwater structures and location of detailed side-scan images in Figure. 3.5. The river palaeochannels features are imaged in the side-scan mosaic as they are infilled with silt and fine sand and are more reflective than surrounding Posidonia seagrass meadows.

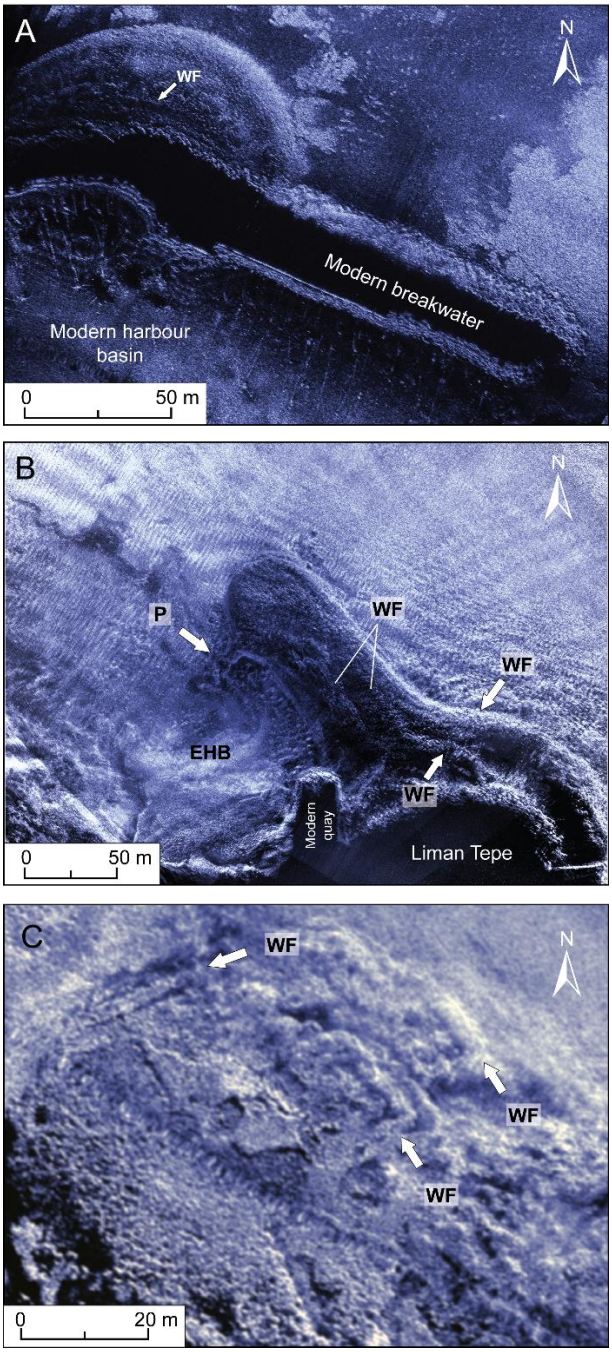

Figure 3.5: A. Side-scan mosaic of exposed northern portion western breakwater showing remains of arcuate wall features (WF) on breakwater surface. B. Side-scan image of eastern breakwater structure. Note linear pier (P) at northwestern tip of breakwater and linear wall features (WF) on breakwater surface. The eastern breakwater is contiguous with a broad (>5 m wide) wall feature at the base of the headland, representing a possible seawall or fortification wall. C. Remains of architectural features indicated by rectilinear patterns of side-scan mosaic on submerged headland to west of eastern breakwater. The headland divides the Archaic harbour into eastern (EHB) and western harbour (WHB) basins.

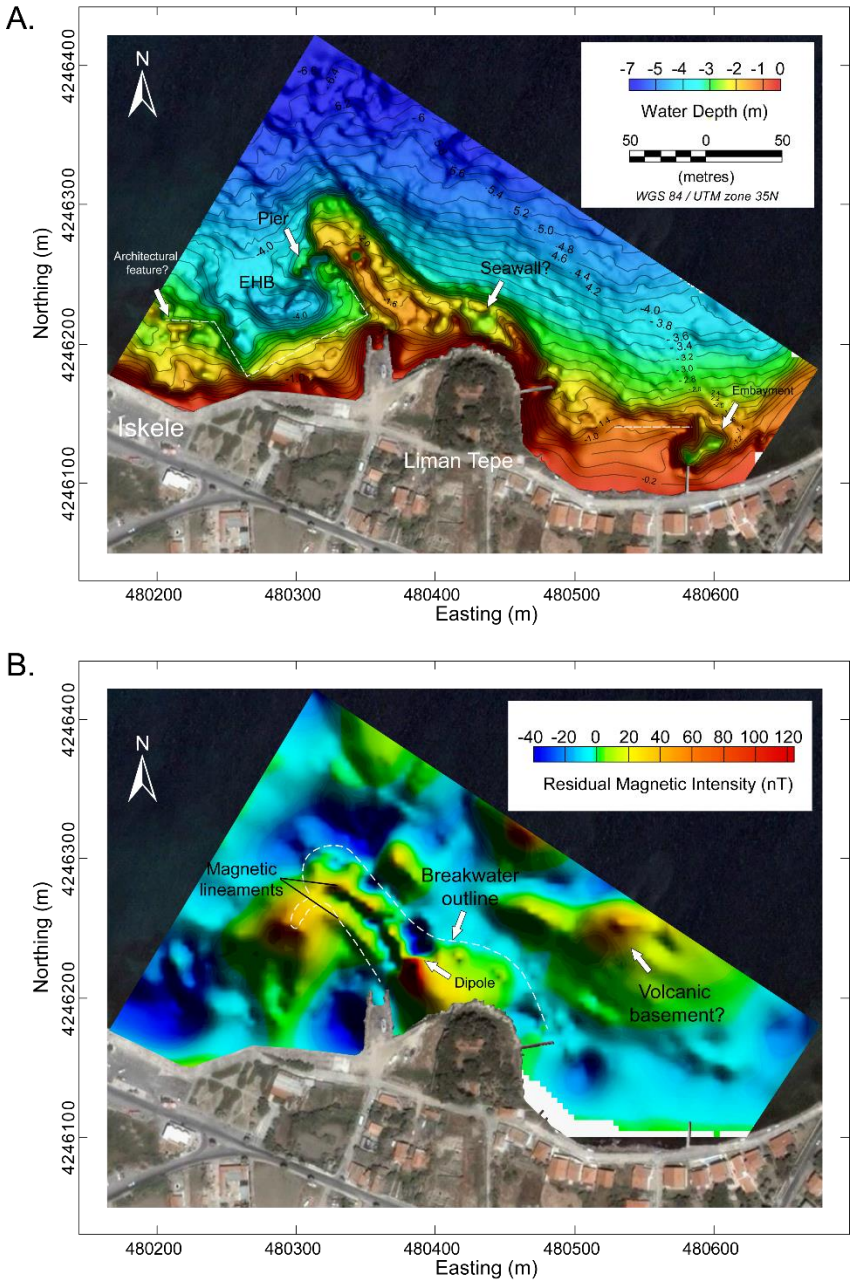

Figure 3.6: A. Bathymetry map of eastern harbour basin (contour interval 0.2 m). Note the rectangular shape of bathymetric contours defining a 70 m wide eastern harbour basin (EHB) between the constructed breakwater and natural headland to the west. Breakwater is contiguous with a semi-circular wall feature to the east, which may present a seawall or fortification. B. Residual magnetic map showing two arcuate northwest-oriented anomalies (20-40 nT) within the breakwater structure. The magnetic anomalies do not conform with the rectilinear outline of Archaic breakwater (white dashed line) and are interpreted as the foundations of an earlier (possible Middle-Late Bronze?) recurved breakwater structure or pier buried within the limestone rubble mass. The isolated magnetic anomalies are interpreted as highs in the Miocene volcanic basement rocks, which are draped by thin Tertiary limestone bedrock. Miocene volcanics are exposed at surface ~1 km to the west of Liman Tepe.

3.4.2 Lithochemofacies

Seven distinct lithochemofacies (LC) were identified based on sediment lithofacies, elemental profiles and foraminifera abundances (Figs. 3.7, 3.8). A west-east transect showing the correlated lithochemical units is shown in Figure 3.9.

3.4.2.1 LC-1 (Terrestrial Clays)

LC-1 was a dark grey dense plastic clay (Fig. 3.7) containing abundant angular rock fragments (up to 50%), derived from the local volcanic bedrock (middle Miocene Menteş trachyte; Kaya, 1979; Göktaş, 2016). The clay was devoid of forams, marine shells, and organics, and contained a low abundance of difflugid thecamoebians. A bulk organics ^{14}C date at the top of the unit yielded a middle Neolithic age, 7044-6749 cal. BCE. Based on the absence of marine fauna and inclusion of bedrock fragments, LC-1 was identified as a terrestrial clay derived by subaerial weathering of the local volcanic bedrock and regolith. Consistent with this interpretation, terrigenous elements Si and Ti were elevated, and marine elements Br and Ca were highly depleted in the clay. Consequently, the Ti/Ca ratio was high and an order of magnitude greater than in overlying marine sediments (Figs. 3.7, 3.9).

3.4.2.2 LC-2 (Lagoonal Sediments)

LC-2 comprised a light grey clayey silt, with low organic content and a foraminifera assemblage dominated by *Ammonia* and *Elphidium.* Foraminifera abundance was low at the base of LC-2 (84 /cc), increased upward (162 /cc). A few difflugid thecamoebians were found at the base of the unit, where a bulk organic sample dated to 6241-6067 cal. BCE (middle Neolithic) (Fig. 3.7). Based on grain size and the increasing abundance of foraminifera, LC-2 was inferred to represent a lagoon environment transitional with foreshore deposits of overlying LC-3.

In core 19-1, Ca showed an upward increase within LC-2, consistent with the increasing foraminifera abundance and Si and Ti were elevated relative to Ca (Fig. 3.7). The increase in Ca and foraminifera abundance at the base of LC-2 and the corresponding

decline in Ti/Ca is interpreted as a transgressive surface (Wolters et al., 2010; Chapter 2), resulting from a middle Holocene rise in sea level. LC-2, defined by increasing Ca and declining Ti/Ca ratio, records increasing marine influence and deposition of silt and mud in a low energy, possibly lagoonal environment.

3.4.2.3 LC-3 (Upper Shoreface Sands and Gravel)

LC-3 comprised a fine to medium sand with moderate to well-rounded shell fragments and abundant forams (342-432 /cc; dominantly *Ammonia* and *Elphidium*). Organics from LC-3 in cores 17-9 and 19-2 dated to 3802-3706 cal. BCE (middle Chalcolithic) and 5229-5048 cal. BCE (late Neolithic), respectively (Figs. 3.7-3.9). LC-3 was defined lithochemically by increasing Ca relative to Si and Ti (decreased in Ti/Ca) (Figs. 3.7, 3.8) and Br was low, indicating low content of marine organic matter.

Based on grain size, the foraminifera assemblage, and the presence of marine shells, LC-3 is interpreted as a high energy foreshore to upper shoreface environment. LC-3 is correlated with the upper shoreface deposits and associated *Elphidium/Ammonia* biofacies identified by Goodman et al. (2009) in core G-22 (Fig. 3.10). The shell materials in the upper shoreface deposits in core G-22 have a comparable early Chalcolithic age (4781-4527 cal. BCE) range to LC-3 (Fig. 3.10).

In core 19-2, underlying foreshore-uppershoreface sands, there was a thin (~15 cm) basal gravel layer, consisting of rounded carbonate and volcanic pebbles (Fig. 3.9). This layer is interpreted as a lag deposit, recording erosion of underlying sediments in a beach or foreshore environment. As such, it has been included with LC-3.

3.4.2.4 LC-4 (Shoreface Muds)

LC-4 was a silty sand with abundant shell fragments and foraminifera (496-675 /cc, dominantly *Ammonia* and *Elphidium*), and frequent organic-rich layers (<1 cm thick), consisting of *Posidonia oceanica* roots and fragments (*Posidonia* mattes). *Posidonia* is common seagrass in the Mediterranean (Béthoux and Copin-Montegut, 1986) and covers much of the inshore around Clazomenae today. Two dates from core 19-1 (shell and

organics) yielded ages of 4824-4615 cal. BCE (early Chalcolithic) and 1785-1686 cal. BCE (Middle Bronze Age). Dates from core 17-9 ranged between 3474-3371 cal. BCE (6.38 mbsl; middle-late Chalcolithic) and 1960-1868 cal. BCE (5.54 mbsl; Middle Bronze Age) (Figs. 3.7, 3.8).

In core 19-1, Si and Ti values were variable in LC-4 and Si generally increased upward through the unit (Fig. 3.7, 3.8). Ca values were high in LC-4 and varied with the content of shell debris. The Ti, Si and Br profiles showed a trend to increasing values upwards in LC-4 and the relative abundances for both terrigenous and marine biogenic elements were similar between cores 19-1 and 17-9 (Figs. 3.7, 3.8). In core 17-9, Br was strongly correlated with the presence of *Posidonia*.

Based on the foraminifera abundance and the presence of marine shells and *Posidonia* mattes, LC-4 was interpreted as a marine shoreface environment. The lithofacies and foraminifera (e.g. core 17-9; Fig. 3.8) in LC-4 correlate with the *Brizalina* biofacies (15-20 % bolivinids) identified in core G-22, which was previously interpreted by Goodman et al. (2009) as a shift to a eutrophic environment in the Archaic harbour (Fig. 3.10). Based on archaeological evidence and new radiocarbon dates for core 17-9, indicating an early Chalcolithic to Middle Bronze Age for LC-4 (Fig. 3.8), we reinterpret the core G-22 *Brizalina* biofacies as eutrophication associated with settlement expansion land use disturbance beginning in the Chalcolithic.

3.4.2.5 LC-5 (Sheltered Embayment and Archaic Harbour)

LC-5 was distinctive laminated, organic rich (increase in Br) silty mud, which was darker in colour than LC-4, with fewer *Posidonia* mattes (Fig. 3.8). The foraminifera abundance was high (374-1094 /cc), however, the dominant taxa varied between cores. In core 19-1, *Ammonia* and *Elphidium* were dominant and in core 17-9, *Ammonia*, *Elphidium*, and *Rosalina*. In core 19-1, LC5 was truncated by LC-6 and a hiatus was included in the age model (Fig. 3.7). Based on elemental geochemistry and sedimentary facies, LC-5 was subdivided into three distinct lithochemofacies (Figs 3.7, 3.8).

LC-5a was marked by basin wide increase in Ti/Ca (Fig. 3.9), suggesting increased terrestrial sediment input to the basin. The shift from mud to silt, a decrease in *Posidonia* mattes, and increase in the Ti/Ca ratio, suggests a transition from an upper shoreface environment (LC-4) to a sheltered embayment with increased terrigenous/fluvial inputs. LC-5a correlates with the *Brizalina* biofacies and eutrophic harbour environment identified in core G-22 (Goodman et al., 2009) (Fig. 3.10). Age models date the transition to LC-5a to the Middle-Late Bronze Age (1442-329 cal. BCE in core 19-1; 1836-1447 cal. BCE in core 17-9) (Figs. 3.7, 3.8).

LC-5b, was defined by a sharp decline in Ti/Ca in all cores and decrease in Si in core 2019-1, indicating a rapid reduction in terrigenous clastic sediment input to the embayment (Figs. 3.7, 3.9). The transition occurred during the Late Bronze-Iron Age transition (1253-1046 cal. BCE; Fig. 3.8). Lithochemofacies LC-5b was correlated with the eutrophic *Brizalina* biofacies identified in core G-22 (Goodman et al., 2009 (Fig. 3.10).

In lithochemofacies LC-5c, Ti/Ca values recovered, then showed a sharp decline in the Archaic period (1074-616 cal. BCE; Fig. 3.8). The lower boundary of LC-5c occurs at a similar depth to the base of Archaic harbour deposits observed in excavation trenches (~4.6 - 5 mbsl). The top of LC-5c in core 19-1 likely dates to the Roman Period, as evidenced by increased Pb (Le Roux et al., 2005; Hadler et al., 2013; Stock et al., 2016), while in other cores the top of LC-5c was truncated by archaeological excavations and is not represented in cores 17-3, 17-9, and 19-2 (Fig. 3.9). LC-5c, in part, correlates with the "final harbour" facies and *Rosalina* biofacies identified in core G-22 (Goodman et al., 2009) (Fig. 3.10), further evidenced by the presence of Archaic pottery in cores 17-9 (Şahoğlu, personal communication, 2019) and G-22. Stock et al. (2016) identified a similar increase in Ca and decrease in Ti, recording a period of intensive harbour use in Ephesus' Roman harbour.

3.4.2.6 LC-6, 7 (Modern Harbour and Shoreface)

The uppermost unit in core 19-1, LC-6 consisted of a brown to orange silty mud, overlying LC-5 across a sharp, erosive contact (Fig. 3.7). LC-6 had abundant forams dominated by *Elphidium* and miliolids (877 /cc) and organics at the basal contact yielded a Byzantine age of 652-695 cal. CE. Elements Si, and Ti decreased upwards in LC-6, while Br, Ca, and metals Pb and Cu were increased upcore.

LC-6 is interpreted as a marine harbour mud recording Byzantine to Ottoman (modern) harbour environment (Fig. 3.7). The major shift in element abundance and 7th c. CE AMS ^{14}C age at the base of LC-6 indicates an erosional hiatus and truncation of underlying LC-5 deposits in core 19-1. The erosional hiatus likely records modern dredging of the harbour basin.

LC-7 was a thin (< 30 cm), coarse gravelly sand at the top of two cores (17-3, G-22), with abundant shell fragments and low Ti/Ca (Fig. 3.9). LC-7 represents upper shoreface deposits, which are accumulating in the open water areas of the modern harbour basin.

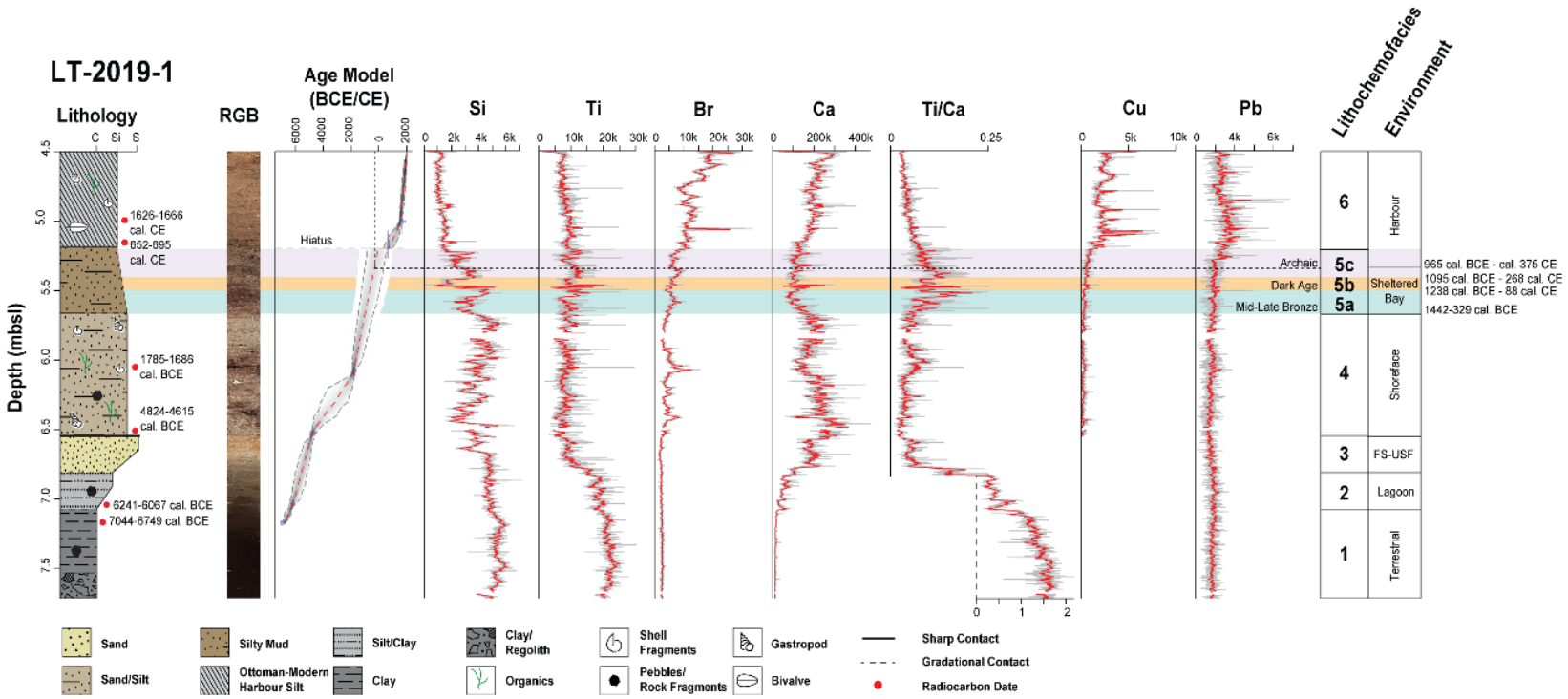

Figure 3.7: Core lithostratigraphy, RGB colour scan, ^{14}C AMS age model and selected micro-XRF element profiles core 19-1. Lithochemofacies and environmental phases also shown. Ages of lithochemofacies transitions were estimated from the age model.

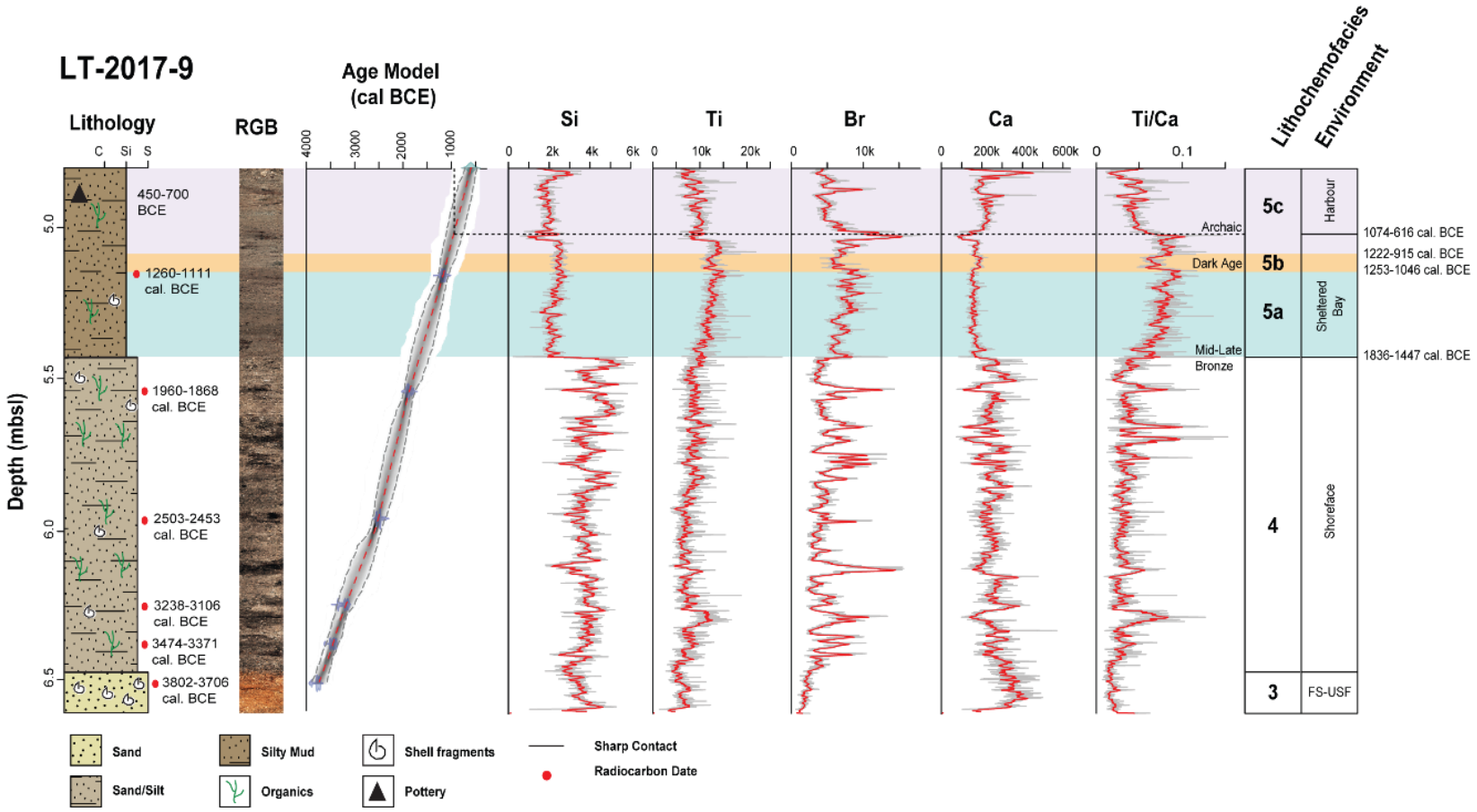

Figure 3.8: Core lithostratigraphy, RGB colour scan, ^{14}C AMS age model, selected micro-XRF element profiles, for core 17-9. Lithochemofacies and environmental phases also shown. Ages of lithochemofacies transitions were estimated from the age model. Note distinct shift in all element profiles at LC-4/5a boundary. The decline in Si and increase in Ti and Ti/Ca in LC-5 is interpreted as a land disturbance signal, recording increased terrigenous detrital sediments, and reduced longshore sand transport during the Middle-Late Bronze Age.

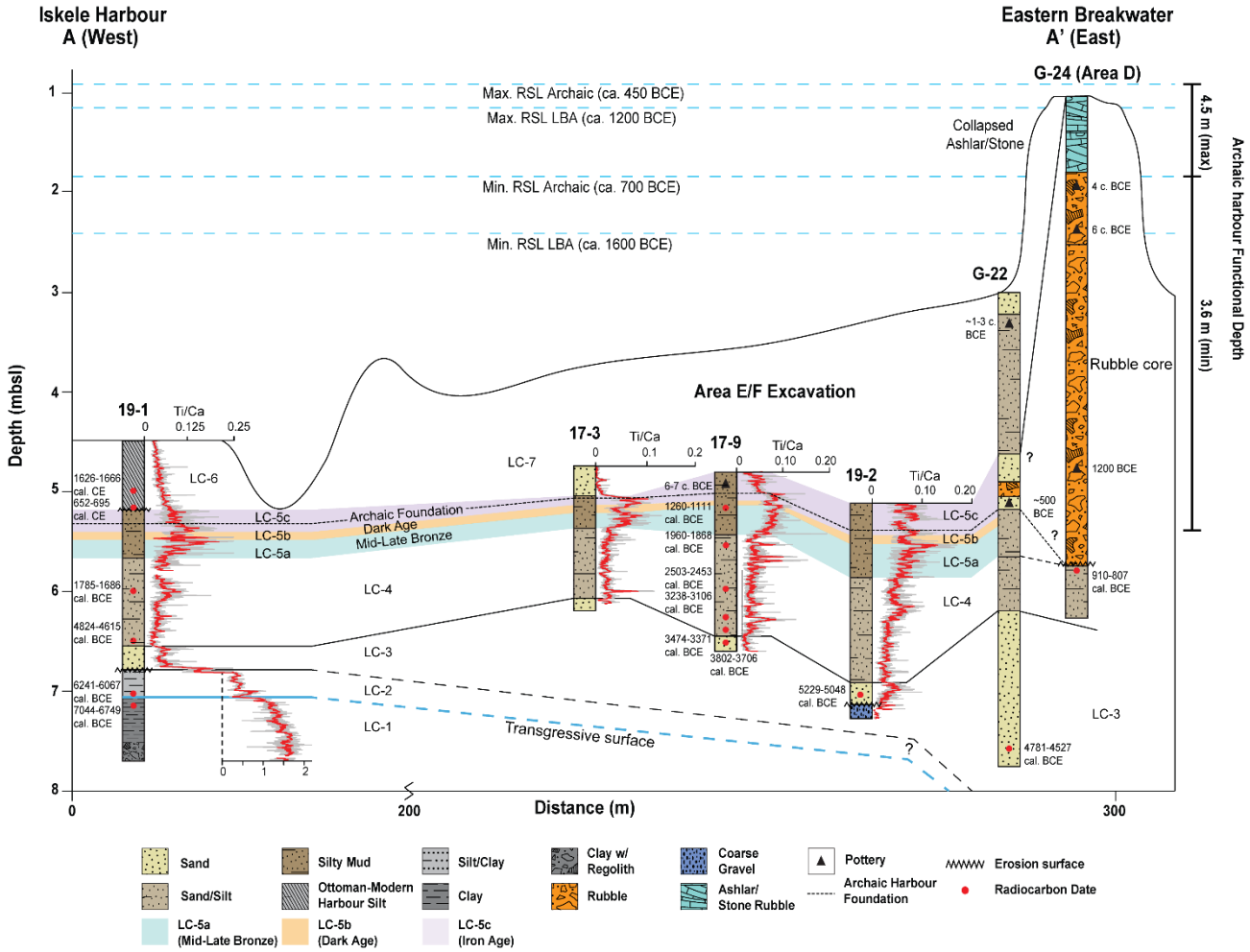

Figure 3.9: West-east transect across the Archaic harbour basin showing correlation of lithofacies and Ti/Ca profiles. Sediment ^{14}C AMS ages and corresponding archaeological periods also shown. The Ti/Ca profiles show a distinct upwards increase within LC-5a, which is interpreted as increased influx of terrigenous sediments due to impacts of Middle-Late Bronze soil erosion and settlement expansion. The decline in Ti/Ca in LC-5b is associated with changes in settlement activity or climate (i.e. Dark Age). The onset of Archaic harbour construction in the 7th c. BCE is indicated by decreased Ti/Ca (LC-5c).

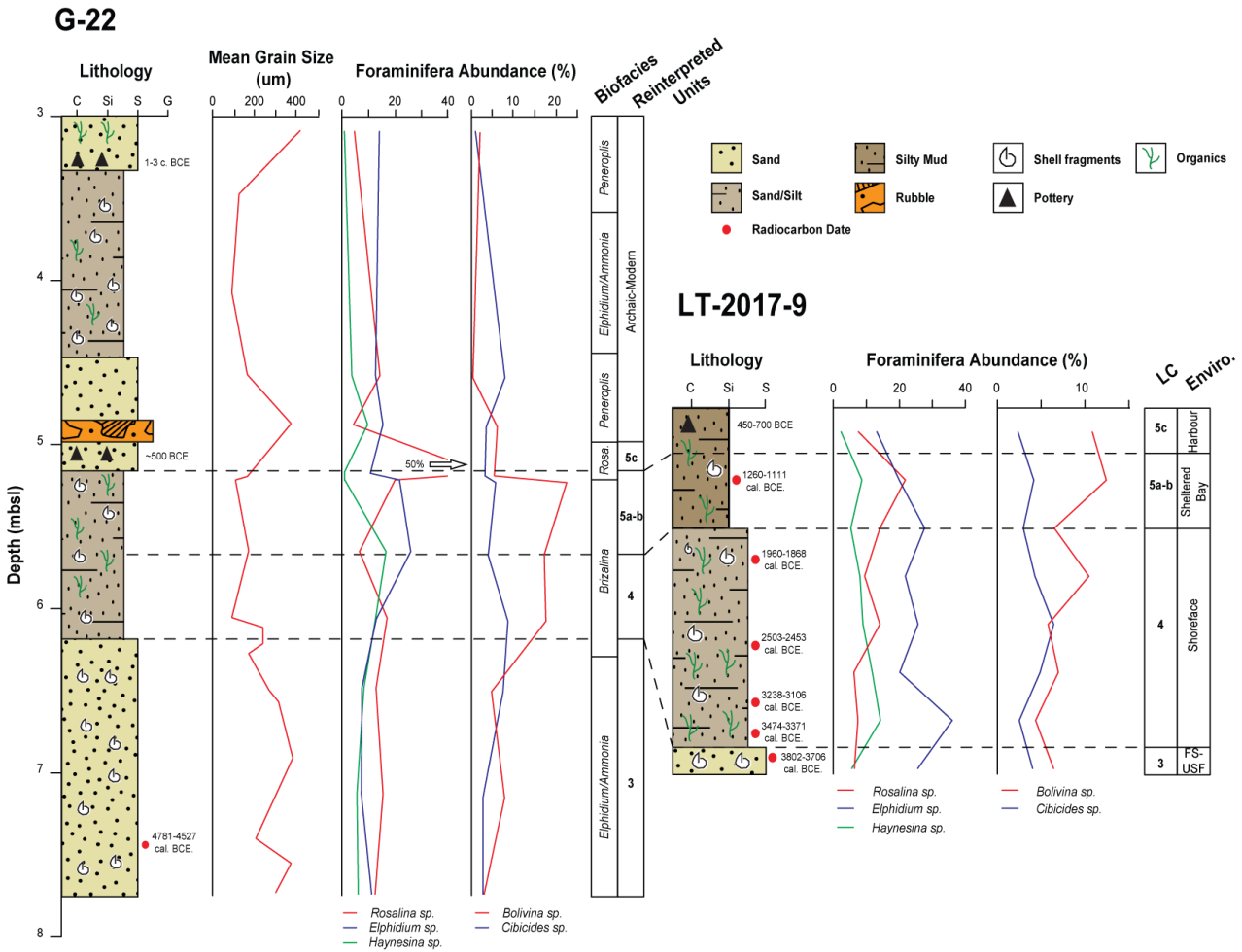

Figure 3.10: Correlation of core 17-9 lithostratigraphy and foraminifera abundances with core G-22 of Goodman et al. (2009). The marine shoreface sands (LC-3, 4) are dominated by *Elphidium* and *Ammonia*. The rise in *Bolivina* and *Cibicides* in LC-4 is interpreted as increasing eutrophication of marine waters at Liman Tepe due to Bronze Age settlement expansion and land clearance. The onset of Archaic harbour construction (ca. 7th c. BCE) in G-22 is indicated by an increase in *Rosalina* in LC-5c, possibly due to proximity to the breakwater.

3.5 Discussion

3.5.1 Coastal Palaeoenvironments and Harbour Phases

The new multiproxy data assembled in this study identifies changes in coastal palaeoenvironments at Clazomenae during the Middle-Late Bronze Age settlement phase and transition from a sheltered embayment (proto-harbour) to an engineered Iron Age (Archaic Period) harbour basin. The changes in the coastal palaeogeography and the harbour development stages are discussed in the following sections and shown in Figure 3.11.

3.5.1.1 Bronze Age Proto-Harbour Phase

On the eastern side of the basin, the transition from LC-4 to LC-5 represents a distinct Middle-Late Bronze Age (1836-1447 cal. BCE in core 17-9) shift from a marine shoreface to a sheltered, low energy environment, as indicated by a switch from *Posidonia* sandy silt to finer-textured, organic-rich mud facies, with elevated Ti/Ca (Figs. 3.8, 3.9). The finer grain size and a decrease in *Posidonia* mattes in LC-5 suggests a shift to a more turbid, low-energy environment that did not support seagrass growth (Pasqualini et al., 1998; Votruba et al., 2016). The Ti/Ca profile shows a distinct upward increase in LC-5 that is a correlatable basin-wide signal in all cores (Fig. 3.9) and indicates increased terrigenous sediment flux to the basin relative to the biogenic carbonate component (Ziegler et al., 2008; Rothwell and Croudace, 2015; Pint et al., 2015; Seki et al., 2019). This is interpreted as a record of increasing soil erosion and runoff, as a result of Middle-Late Bronze settlement expansion and land use impacts. The rise of Bronze Age cultures in the Aegean was associated with increasing agricultural development and other land use impacts (Van Andel et al., 1990; Andreou et al., 1996). The Bronze Age building techniques at Liman Tepe employed mud bricks and clay mined locally from the alluvial plain (Tuncel and Şahoğlu, 2018). The increased terrigenous sediment influx may, in part, record land disturbances due to the mining of clay from river or wetland areas and land clearance and construction activities on the nearby headland (Fig. 3.2).

The distinct shift in the sedimentary facies and element values at the LC-4/LC-5 contact (Fig. 3.9) records the development of a sheltered marine embayment to the west of the Liman Tepe headland, where organic-rich terrestrial mud and silt were accumulating in a low-energy marine environment (Fig. 3.11a). We speculate on two possible causes for this environmental shift:

1) Due to longshore transport of sediment from the east, a natural tombolo formed on the rocky headland to the northwest of Liman Tepe (Figs. 3.6, 3.11a). The tombolo accretion would have limited the westward longshore transport of sandy sediments, promoting the accumulation of Ti-rich muds within the embayment. The decrease in Si in LC-4 (Figs. 3.7, 3.8), is consistent with a decrease in longshore sand supply. The river floodplain to the west of the headland and overland flow from the nearby settlement were potential sources of the terrigenous Ti-rich muds deposited in the embayment (Figs. 3.4, 3.11a). The embayment would have provided a semi-sheltered proto-harbour basin during the LBA period, and a high ground for later construction of the Archaic eastern breakwater (Fig. 3.11a). The tombolo formation may have been initiated by bedrock highs (i.e. Tertiary limestone knolls) to the north of the headland (Goodman et al., 2009). The magnetic high at the end of the eastern breakwater suggests that the volcanic basement here is closer to the surface and might indicate a possible structural control on the bedrock topography and seabed height (Fig. 3.6).

2) The natural sheltered embayment was augmented by construction of a pier or rudimentary breakwater during the Middle-Late Bronze Age (Fig. 3.11a), as suggested by magnetic survey results (Fig. 3.6b). The presence of LBA pottery within the lower part of the breakwater rubble (Goodman, 2006) (core G-24; Fig. 3.9) may indicate the re-use of and modification of a pre-existing Bronze Age structure. A pre-existing bedrock ridge or tombolo (e.g. Fig. 3.11a) may have also been an impetus for augmentation of the natural proto-harbour basin at Liman Tepe. In the Aegean there is currently no evidence for man-made harbour structures prior to the 7th c. BCE (Mauro, 2019). However, at sites on the Levantine coast there are examples of augmentation of natural Middle-Late Bronze Age proto-harbour basins; at Yavne-Yam (Israel) submerged boulder piles were placed to

improve harbouring and at Sidon (Lebanon) there is evidence for reinforcement of sandstone ridges for the same purpose (Marriner et al., 2006).

3.5.1.2 Late Bronze-Iron Age Transition and Archaic Harbour Phase

The Late Bronze-Iron Age transition is recorded in all cores by a decrease in Ti/Ca, which marks the base of LC-5b (Fig. 3.9). The transition is dated to the 13th c. BCE based on the core 17-9 age model (1253-915 cal. BCE; Fig. 3.8). The decline in Ti/Ca is associated with decrease in Br in core 17-9 and Si in core 19-1 (Fig. 3.7). The shift in Ti/Ca and Si is interpreted as a decrease in terrigenous sediment input to the basin, and Br, a decrease in the marine productivity (Rothwell and Croudace, 2015).

The shifts in elemental abundance in LC-5b may signal changes in settlement activity (i.e. reduction in land clearance) or could signal changes in climate or other environmental variables during the early Iron Age. A number of studies have argued for climate impacts of a ~300-year drought period (ca. 13th-11th c. BCE) as a contributing cause for the Late Bronze socioeconomic collapse of eastern Mediterranean cultures (the so-called 'Greek Dark Age' or 3.2 ka event) (Fleitmann et al., 2009; Kaniewski et al., 2013; Finné et al., 2017). At the end of the LBA, urban centres at Mycenae, Troy and Urgarit were destroyed, and settlements were abandoned across a region >6 million km^2 (Knapp and Manning, 2016; Finne et al., 2017). It has been speculated that the regional drought led to a decline in agricultural activity, which resulted in widespread famine, as documented at sites in Syria and Cyprus (Drake, 2012; Kaniewski et al., 2015). To evaluate possible climate impacts at Clazomenae, the Ti/Ca ratio from core 17-9 was compared with several climate proxies from the eastern Mediterranean and the GISP2 temperature record (Fig. 3.12). The Ti/Ca signal is broadly correlated with the Sofular Cave speleothem isotopic record (Black Sea, Turkey), which shows a trend towards lighter $\delta^{18}O$ values during the Late Bronze and a distinct shift to positive values (reduced precipitation) at the beginning of the Dark Age (Fleitmann et al., 2009). The lower resolution records from pollen cultivars (Larnaca) and the Eastern Mediterranean precipitation anomaly show similar broad trends, which indicate a shift to a warmer, drier regional climate after ca. 1200 BCE (Kaniewski

et al., 2013, 2015). The apparent correlations are intriguing and suggest a possible climate driver for the Ti/Ca signals at Liman Tepe, indicating a reduction in precipitation and surface run-off during a drought phase. The reduction in Ti/Ca may record reduced soil erosion due to decreased agricultural activity and reduced land clearance for settlement expansion, which may also be in response to climate changes. Currently, the archaeological record of the Late Bronze-Iron Age transition at Liman Tepe is limited and does not allow for evaluation of possible climate impacts on settlement activity. Drought has been inferred to have been a contributing factor to social upheaval and the disruption of settlements including Liman Tepe, during the Middle Bronze Age (2200-1900 BCE; 4.2 ka event) in western Anatolia (Massa and Sahoglu, 2015).

The onset of the Archaic harbour construction is recorded by a decrease in Ti/Ca (Figs. 3.7-3.9) and a shift in foraminifera biofacies in LC-5c (Fig. 3.10). The decrease in Ti/Ca in LC-5c coincides with the base of Archaic harbour deposits in excavations (~5 mbsl) and the appearance of Archaic pottery (7^{th}-5^{th} c. BCE) in cores 17-9 and G-22 (Fig. 3.9). The age model for core 17-9 yielded an age range for the transition to unit 5c of 1074-616 cal BCE (median age 883 BCE). The decline in Ti/Ca indicates a decrease in terrigenous sediment influx to harbour basin (Fig. 3.8) and is correlated with the onset of the *Rosalina* biofacies in core G-22 (Fig. 3.10). The *Rosalina* biofacies includes *R. bradyi* (>50 %), which prefer rocky or coarse-sand substrates (Avsar and Ergin, 2001; Hayward et al., 2007; Goodman et al., 2009); the large increase in the *Rosalina* following the breakwater construction may record colonization of hardgrounds provided by the rubble mass. A date from Posidonia in sediments immediately below the eastern breakwater provides a *terminus post quem* of 910-807 cal. BCE for the mole construction (Fig. 3.9). However, the abundance of Archaic pottery in the harbour sediments in LC-5c strongly suggests a 7^{th} c. BCE date for the construction of the eastern harbour mole.

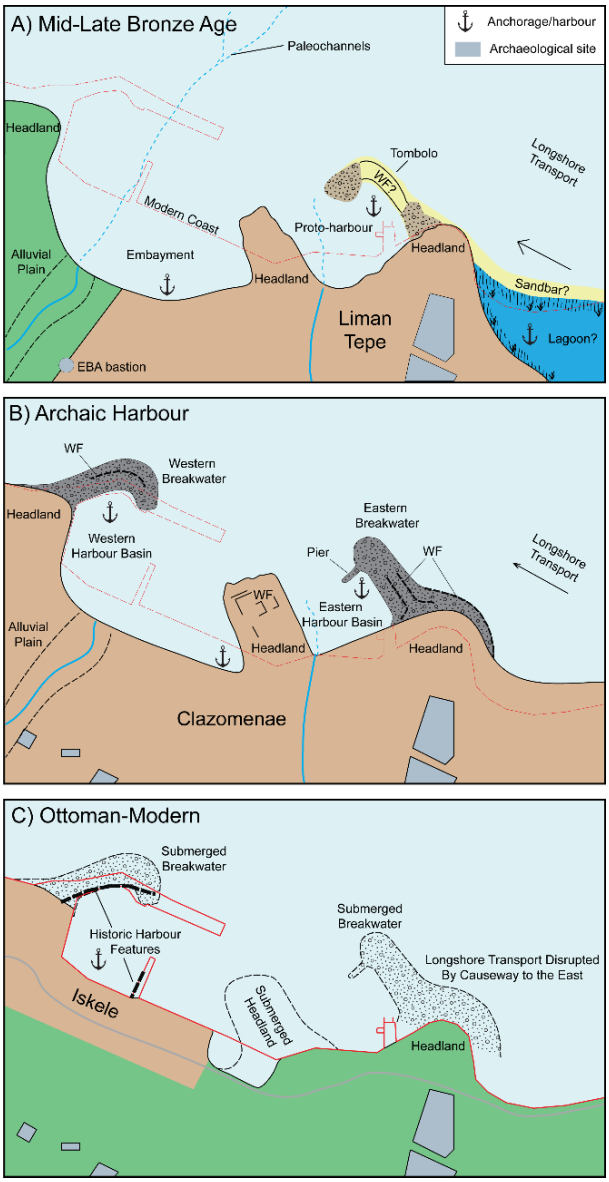

Figure 3.11: Palaeocoastal evolution and harbour development at Clazomenae. A. Middle-Late Bronze Age proto-harbour phase. The fortified citadel of Liman Tepe was situated on a bedrock promontory and marine embayments to east and west of headland would have provided sheltered anchorage areas. A tombolo formed on headland by east-west longshore transport of sand may have enhanced sheltering of western basin, allowing accumulation of muds within basin western (lee) side of headland. Linear magnetic anomaly patterns (Fig. 3.6b) may indicate augmentation of natural tombolo with rubble to form a rudimentary breakwater structure or pier. B. Archaic (ca. 7th c. BCE) harbour phase. Two semi-enclosed harbour basins were formed by construction of rubble breakwater structures on top of existing bedrock structural highs or possible tombolo. The tombolo-shaped western breakwater would have provided a small, sheltered harbour basin protected from the dominant northerly winds. C. Ottoman-modern harbour phase (based on historical photos). Ottoman constructions included two narrow piers the western basin constructed on the remains of the western Archaic breakwater. Photos from the period record dredging in the western harbour basin and backfilling of the shoreline in Iskele harbour.

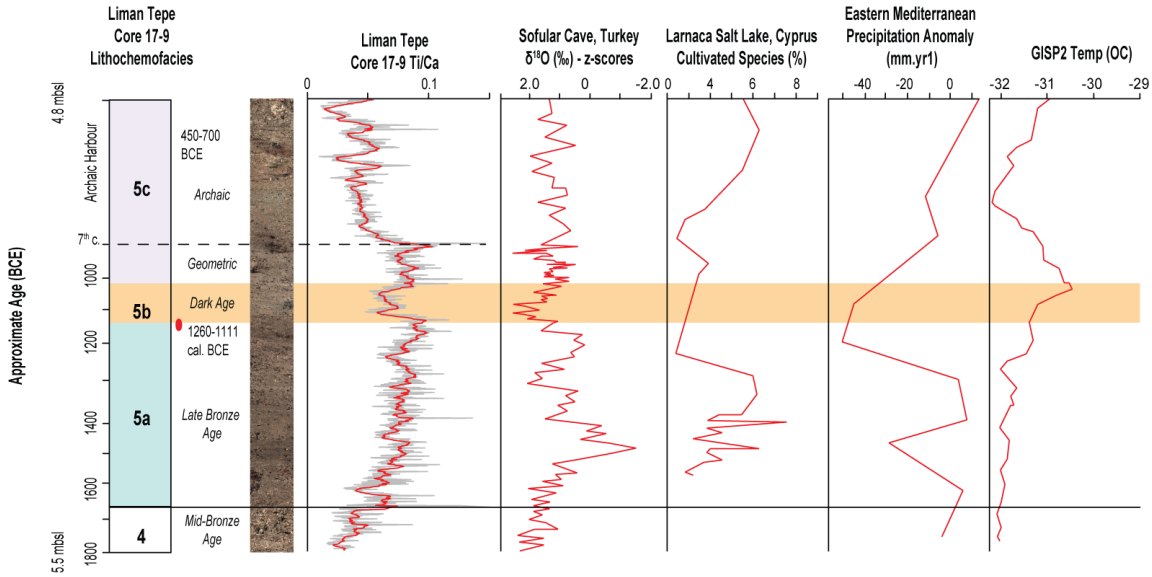

Figure 3.12: Comparison of Ti/Ca record from upper portion of core 17-9 with climate proxies from Sofular Cave (Black Sea, Turkey; Fleitmann et al., 2009), Larnaca Salt Lake (Cyprus; Kaniewski et al., 2013), eastern Mediterranean precipitation (Kaniewski et al., 2013) and GISP2 temperature record (Alley, 2004). The LBA corresponds with a distinct shift to decreased Ti/Ca in LC-5b in all harbour basin cores (Fig. 3.9), indicating a decreased Ti flux to the basin during the dry climate phase. The decrease in the Ti/Ca in LC-5c could be a direct signal of decreased surface runoff (i.e. reduced precipitation) but could also indicate change in human activity at Liman Tepe during the Late Bronze-Iron Age transition.

3.5.2 Archaic Harbour Layout and Construction

Geophysical mapping of the Archaic harbour basin has identified two separate sub-basins with a total harbour area >5 ha (Figs. 3.4, 3.5). This estimate assumes an inner harbour shoreline that was ~30-50 m landward of the modern shoreline (Fig. 3.11b). The western breakwater was constructed as a recurved mole which extended about 150 m eastward of the headland, forming a small, sheltered basin on its lee side that would have been protected from the dominant northerly winds (Fig. 3.11b). The eastern breakwater was built out from the Liman Tepe headland as a rectangular mole structure by the piling of rubble directly onto the sea floor (Figs. 3.5, 3.9). The magnetic survey results suggest that the breakwater was built on top of a pre-existing, arcuate pier structure that lies within the rubble mass (Fig. 3.6b). Using the dimensions of eastern breakwater (35 x 120 m) and the thickness of the rubble core (~4 m; G-24; Fig. 3.8), an estimated 17 x 10^3 m^3 of rubble was required to construct the 120 m long eastern breakwater. Magnetic mapping of the breakwater revealed that the structure is largely composed of limestone rubble, consistent

with excavation work and coring results (Goodman et al., 2009). The western breakwater (Figs. 3.4-3.6) appears to have a similar construction based on side-scan imaging and diver reconnaissance (Tuğcu et al., 2017), which indicates a 4-5 m thick rubble mass composed of boulder- and cobble-sized materials (Fig. 3.5b). Future excavation work will determine the internal structure of the western breakwater.

The wall features on the upper surface of the Archaic eastern breakwater are aligned generally with the rectilinear outline of the mole and likely indicate the foundations of building structures (storehouses, boatsheds?) on the mole surface (Fig. 3.5b). Near the southeastern terminus of the breakwater, other wall features are contiguous with a broad (>3 m wide) wall feature encircling the base of headland that may represent a sea wall or a possibly a city fortification wall (Figs. 3.5b, 3.6b). It is noted that the linear wall structure on the eastern breakwater surface, and the general rectilinear outline of the mole, are not aligned with the arcuate pattern of magnetic anomalies within the eastern breakwater (Figs. 3.5, 3.6b). This further reinforces the interpretation that the magnetic targets are recording the presence of a pre-existing buried structure (LBA?) within the Archaic mole (Fig. 3.6b). Excavations at area D, which penetrated the entire thickness of the rubble mass (>4 m) did not identify a difference in the rubble materials at the base of the breakwater structure and a date of 910-807 cal. BCE was obtained from under the rubble (Fig. 3.9). Further investigations (i.e. geophysics, excavations) will be required to determine the age and origin of the buried structure but we speculate, based on its shape and dimensions, that it represents a narrow pier built out from the headland, perhaps on a pre-existing tombolo attached to the mainland (Goodman et al., 2008). If the buried structure is Late Bronze in age, it is potentially the first example of prehistoric proto-harbour augmentation and engineering work in the Aegean (Mauro, 2019).

To the west of the eastern breakwater, side-scan imaging of the submerged headland shows several linear (wall) features, which may record evidence for architectural features associated with Archaic harbour (Fig. 3.5c). The headland projects from the modern coast about 150 m and during the Archaic would have been close to the same elevation as the

eastern breakwater. The headland divides the Archaic harbour into two separate basins, forming a roughly rectangular eastern harbour basin (EHB) with dimensions ~50 x 100 m (Fig. 3.6a).

3.5.3 Archaic Harbour Depth and Function

The functional depth of the Archaic harbour basin was estimated using the local RSL curve of (Chapter 2) (Figs. 3.9, 3.12). During the early Archaic (ca. 7th c. BCE) sea level was between 1.8-0.9 m lower than present (Fig. 3.13). The lowermost limit of Archaic age sediments in the eastern harbour basin is 5.4 mbsl, which indicates a functional harbour depth of about ~3.6-4.5 m (Fig. 3.9). Based on the current average depth of the rubble mass (ca. 5.7 mbsl), the current breakwater surface would have been at or slightly below (0.8 m) the Archaic sea level. The modern elevation of the eastern breakwater, however, must be considered a minimum estimate of its original height, as it has most likely been reduced by wave erosion and post-emplacement settlement (i.e. sediment compaction) of the rubble mass, which sits on soft compressible sediments. The presence of wall features on the breakwater surface (Fig. 3.5a, b) indicates a superstructure built on top of the breakwater, which would have created a freeboard above sea level. The linear wall features may have functioned as seawalls or possibly as foundations for harbour buildings (e.g. warehouses, ship sheds, quays).

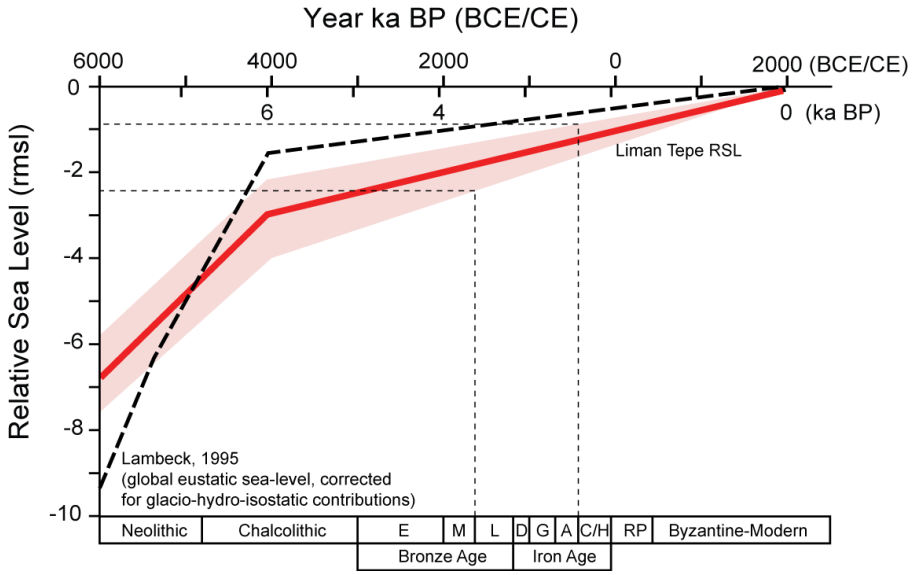

Figure 3.13: Relative sea level (RSL) curve for Clazomenae/Liman Tepe with Lambeck's (1995) eustatic sea level for comparison (modified from Chapter 2). RSL during the Middle-Late Bronze Age was ~1.8 mbsl and had risen by >50 cm by the beginning of the Archaic period. The difference between the local RSL curve and Lambeck's eustatic sea level can be attributed to ongoing tectonic subsidence in the Bay of Izmir. The functional harbour depth is also shown.

The north-east orientation of the eastern breakwater structure suggests that it may have functioned in part to prevent siltation of the harbour basin by interrupting east-west longshore currents (Fig. 3.11b). The western breakwater has a similar surface elevation to its eastern counterpart but is largely obscured by modern harbour constructions, which precludes analysis of the breakwater dimensions and volume. Attached to the eastern breakwater is a possible pier (Sahoglu, 2011; Fig. 3.5b) and there is archaeological evidence for anchoring along the leeward side of the structure (e.g. anchor arm; Votruba et al., 2016).

Clazomenae was an important olive production centre and trading port in the Iron Age and Roman period. As the principal Iron Age port, the Archaic harbour must have served a commercial purpose, which is evident in the wealth of pottery refuse and other cultural materials preserved in the basin. The size of the Archaic harbour basin (>5 ha) is comparable to the Roman Harbour on Karantina Island (Fig. 3.1a), indicating a similar capacity. The division of the harbour into two separate basins (Fig. 3.11b) may indicate

some level of organization of the harbour facilities for both military and commercial purposes.

3.6 Summary

In the Aegean, naturally sheltered coastal environments were used as safe anchorages until the Iron Age, when engineered structures (e.g. breakwaters) were built to enhance natural proto-harbours (Marriner et al., 2010; Mauro, 2019). At Clazomenae, one of the best-preserved early Iron Age harbours in the Aegean, we have documented the transition from a natural proto-harbour embayment to a semi-enclosed engineered harbour using a multi-proxy analysis of cores and geophysical mapping. The Middle-Late Bronze Age transition from a shoreface to naturally sheltered embayment was marked by an increase in Ti/Ca, in a distinctive mud silt facies. The proto-harbour embayment may have been formed in the lee of a tombolo attached to the headland or augmented by construction of a pier or narrow breakwater (Fig. 3.11a). The pattern of linear magnetic anomalies within the core of the eastern breakwater suggests the presence of an earlier (LBA?) man-made structure (Fig. 3.6b).

The Late Bronze to Iron Age transition (ca. 1200 BCE) was marked by a decline in Ti/Ca and a basin-wide lithochemical boundary (Fig. 3.9). The decrease in Ti may record a possible drought phase that has been recognized across the eastern Mediterranean and linked with the LBA socioeconomic collapse (Fleitmann et al., 2009; Drake, 2012; Kaniewski et al., 2013, 2015). The LBA transition occurs over an 8 cm zone (LC-5b), which would be unresolvable with conventional sampling and analytical methods (micropalaeontology, portable XRF, ICPMS, etc.) employing centimetric sample intervals. Using high-resolution μ-XRF-CS with a 500 μm step size, LC-5a was sampled >100 times, allowing it to be identified as a distinct chemofacies, which was correlated across the harbour basin (Fig. 3.9).

The construction of the Clazomenae's Archaic harbour in the 7th c. BCE is recorded by a decrease in Ti/Ca and shift to low energy, eutrophic harbour environment. The harbour

breakwaters were constructed by piling of rubble onto the seabed or by modification and enhancement of a pre-existing breakwater or pier, as suggested by magnetic data. Wall features on the mole surface indicate a harbour superstructure and architectural features. The geoarchaeological and archaeological evidence suggests that the harbour was active during 7th-6th c. BCE and again in the 4th c. BCE and likely served as Clazomenae's principal mainland commercial port.

3.7 References

Alley, R.B., 2004. GISP2 Ice Core Temperature and Accumulation Data. In: Data Contribution Series #2004-013. NOAA/NGDC Palaeoclimatology Program. IGBP PAGES World Data Center for Palaeoclimatology, Boulder CO, USA.

Andreou, S., Fotiadis, M., Kotsakis, K., 1996. Review of Aegean prehistory V: the Neolithic and Bronze Age of northern Greece. American Journal of Archaeology 100(3), 537-597.

Anstee, S., 2001. Removal of range-dependent artifacts from sidescan sonar imagery. Defence Science and Technology organization Victoria (Australia) Aeronautical and Maritime Research Lab.

Artzy, M., 2009. Liman Tepe Underwater Excavations: A Retrospective. Recanati Institute for Maritime Studies News (RIMS News) 35, 11-15.

Avsar, N., Ergin, M., 2001. Spatial distribution of Holocene benthic foraminifera, northeastern Aegean Sea. International Geology Review 43(8), 754-770.

Aytaçlar, N., 2004. The Early Iron Age at Klazomenai. In: Moustaka, A., Skarlatidou, E., Tzannes, M.C., Ersoy, Y. (Eds.), Klazomenai, Teos and Abdera: Metropoleis and Colony. Proceedings of the International Symposium, Abdera, pp. 17-41.

Béthoux, J.P., Copin-Montégut, G., 1986. Biological fixation of atmospheric nitrogen in the Mediterranean Sea. Limnology and Oceanography 31(6), 1353-1358.

Berntsson, A., Rosqvist, G.C., Velle, G., 2014. Late-Holocene temperature and precipitation changes in Vindelfjällen, mid-western Swedish Lapland, inferred from chironomid and geochemical data. The Holocene 24(1), 78-92.

Blaauw, M., Christen J.A., 2011. Flexible paleoclimate age-depth models using an autoregressive gamma process. Bayesian Analysis 6(3), 457-474.

Boyce, J.I., Kresozki, G.M., Erkanal, H., Sahoglu, V., Goodman, B.N., Artzy M., 2007. Shallow water mapping of a submerged Archaic-age harbor at Liman Tepe, Turkey using data-fused magnetic and side-scan data. In 2007 GSA Denver Annual Meeting.

Boyce, J.I., Reinhardt, E.G., Raban, A., Pozza, M.R., 2004. Marine magnetic survey of a submerged Roman harbour, Caesarea Maritima, Israel. International Journal of Nautical Archaeology 33(1), 122-136.

Boyce, J.I., Reinhardt, E.G., Goodman, B.N., 2009. Magnetic detection of ship ballast deposits and anchorage sites in King Herod's Roman harbour, Caesarea Maritima, Israel. Journal of Archaeological Science 36(7), 1516-1526.

Brückner, H., 1997. Coastal changes in western Turkey; rapid delta progradation in historical times. Bulletin-Insitut Oceanographique Monaco-Numero Special, 63-74

Duchêne, H., Fraisse, P., Dalongeville, R., Bernier, P., 2001. Le paysage portuaire de la Délos antique: recherches sur les installations maritimes, commerciales et urbaines, p. 93.

Cervenka, P., De Moustier, C., 1993. Sidescan sonar image processing techniques. IEEE journal of oceanic engineering 18(2), 108-122.

Craigie, N.W., 2018. Principles of elemental chemostratigraphy: A Practical User Guide. Advances in Oil and Gas Exploration & Production. p. 189.

Drake, B. L., 2012. The influence of climatic change on the Late Bronze Age Collapse and the Greek Dark Ages. Journal of Archaeological Science 39(6), 1862-1870.

Erkanal, H., 2008. Liman Tepe: New light on prehistoric Aegean cultures. In: Erkanal, H., Hauptmann, H, Şahoğlu, V. (Eds), The Aegean in the Neolithic, Chalcolithic and the Early Bronze Age. Proceedings of the International Symposium, Urla-Izmir, pp. 179-190.

Erkanal, H., 2014a. Klazomenai/Liman Tepe'nin Limanları. In:, S., Pirson, F., Schmidts, T., (Eds.), Harbors and Harbor Cities in the Eastern Mediterranean. pp. 295-303.

Erkanal, H., 2014b. Liman Tepe in the Late Bronze Age. In Erkanal A. et al. (eds) Batı ve Doğu Akdeniz Geç Tunç Çağı Kültürleri Üzerine Araştırmalar Sempozyumu. Hacettepe Üniversitesi, 2013, Ankara.

Erkanal, H., 2017. Liman Tepe Kazıları. Kazı Sonuçları Toplantısı, 387-406.

Erkanal, H., Aykurt, A., Büyükulusoy, K., Şahoğlu, V, Tuğcu, İ., 2014. Liman Tepe 2012 Yılı Kara ve Sualtı Kazıları, 35. Kazı Sonuçları Toplantısı 3, pp. 499–513.

Erkanal, H., Tuğcu, İ. Şahoğlu, V., 2015. Liman Tepe 2015 underwater excavation campaign. TINA, pp. 82-86.

Ersoy, Y., 2004. Klazomenai: 900-500 B.C. history and settlement evidence. In: Moustaka, A., Skarlatidou, E., Tzannes, M.C., Ersoy, Y. (Eds.), Klazomenai, Teos and Abdera: Metropoleis and Colony. Proceedings of the International Symposium, Abdera, pp. 43-76.

Finkler, C., Baika, K., Rigakou, D., Metallinou, G., Fischer, P., Hadler, H., Emde, K., Vött, A., 2018. Geoarchaeological investigations of a prominent quay wall in ancient Corcyra–implications for harbour development, palaeoenvironmental changes and tectonic geomorphology of Corfu island (Ionian Islands, Greece). Quaternary International 473, 91-111.

Finné, M., Holmgren, K., Shen, C.C., Hu, H.M., Boyd, M., Stocker, S., 2017. Late Bronze Age climate change and the destruction of the Mycenaean Palace of Nestor at Pylos. PloS one 12(12), e0189447.

Fleitmann, D., Cheng, H., Badertscher, S., Edwards, R. L., Mudelsee, M., Göktürk, O. M., Fankhauser, A., Pickering, R., Raible, C.C., Matter, A., Kramers, J., Tüysüz, O., 2009. Timing and climatic impact of Greenland interstadials recorded in stalagmites from northern Turkey. Geophysical Research Letters 36(19).

Flemming, N.C., 1980. Gigantic harbors in the Levant. Archaeology Under Water. In: Muckelroy, K. (Ed), Archaeology under water: an atlas of the world's submerged sites, McGraw-Hill Book Company, p. 168.

Göktaş, F., 2016. Neogene Stratigraphy Of The İzmir-Outer-Bay Islands. Maden Tetkik ve Arama Dergisi 152(152), 1-24.

Goodman, B.N., 2006. The paleogeography of Liman Tepe, Turkey: A multi-proxy geoarchaeological study. Unpublished PhD thesis, McMaster University.

Goodman, B.N., Reinhardt, E.G., Dey, H.W., Boyce, J.I., Schwarcz, H.P., Sahoğlu, V., Erkanal, H., Artzy, M., 2008. Evidence for Holocene marine transgression and shoreline progradation due to barrier development in Iskele, Bay of Izmir, Turkey. Journal of Coastal Research 24(5), 1269-1280.

Goodman, B.N., Reinhardt, E.G., Dey, H.W., Boyce, J.I., Schwarcz, H.P., Sahoğlu, V., Erkanal, H., Artzy, M., 2009. Multi-proxy geoarchaeological study redefines understanding of the paleocoastlines and ancient harbours of Liman Tepe (Iskele, Turkey). Terra Nova 21(2), 97-104.

Greene, E.S., Leidwanger, J., Tuna, N., 2019. Archaeological Investigations in the Harbours of Burgaz, Turkey: 2011–2015 field seasons. International Journal of Nautical Archaeology 48(1), 103-122.

Gregory, B.R., Patterson, R.T., Reinhardt, E.G., Galloway, J.M., Roe, H.M., 2019. An evaluation of methodologies for calibrating Itrax X-ray fluorescence counts with ICP-MS concentration data for discrete sediment samples. Chemical Geology 521, 12-27.

Hadler, H., Vött, A., Fischer, P., Ludwig, S., Heinzelmann, M., Rohn, C., 2015. Temple-complex post-dates tsunami deposits found in the ancient harbour basin of Ostia (Rome, Italy). Journal of Archaeological Science 61, 78-89.

Hadler, H., Vött, A., Koster, B., Mathes-Schmidt, M., Mattern, T., Ntageretzis, K., Reicherter, K., Willershäuser, T., 2013. Multiple late-Holocene tsunami landfall in the eastern Gulf of Corinth recorded in the palaeotsunami geo-archive at Lechaion, harbour of ancient Corinth (Peloponnese, Greece). Zeitschrift für Geomorphologie 57(4), 139-180.

Haggi, A., 2006. Phoenician Atlit and its newly-excavated harbour: a reassessment. Tel Aviv 33(1), 43-60.

Haggi, A., Artzy, M., 2007. The harbor of Atlit in northern Canaanite/Phoenician context. Near Eastern Archaeology 70(2), 75-84.

Hayward, B.W., Grenfell, H.R., Sabaa, A.T., Daymond-King, R., 2007. Biogeography and ecological distribution of shallow-water benthic foraminifera from the Auckland and Campbell Islands, subantarctic southwest Pacific. Journal of Micropalaeontology 26(2), 127-143.

Heisserer, A.J., 1980. Alexander the Great and the Greeks. Norman, Oklahoma: University of Oklahoma Press.

Herodotus, 5th c. BC. The Histories. tr. by A de Selincourt (1996) Penguin Books: New York, p. 622.

Ingram, W.C., Meyers, S.R., Brunner, C.A., Martens, C.S., 2010. Late Pleistocene–Holocene sedimentation surrounding an active seafloor gas-hydrate and cold-seep field on the Northern Gulf of Mexico Slope. Marine Geology 278(1-4), 43-53.

Kaniewski, D., Guiot, J., Van Campo, E., 2015. Drought and societal collapse 3200 years ago in the Eastern Mediterranean: a review. Wiley Interdisciplinary Reviews: Climate Change 6(4), 369-382.

Kaniewski, D., Van Campo, E., Guiot, J., Le Burel, S., Otto, T., Baeteman, C., 2013. Environmental roots of the Late Bronze Age crisis. PloS one 8(8), e71004.

Kaya, O., 1979. Ortadoğu Ege çöküntüsünün (Neojen) stratigrafisive tektoniği. Türkiye Jeoloji Kurumu Bülteni 22(1), 35-58.

Kayan, İ., 1988. Late Holocene sea-level changes on the western Anatolian coast. Palaeogeography, Palaeoclimatology, Palaeoecology 68(2-4), 205-218.

Kayan, İ., Öner, E., Doğan, M., İlhan, R., Vardar, S., 2019. Holocene paleogeography and geoarchaeological interpretations on the Urla-İskele coastal plain. Ege Coğrafya Dergisi 28(1), 11-32.

Knapp, A.B., Manning, S.W., 2016. Crisis in context: The end of the Late Bronze Age in the eastern Mediterranean. American Journal of Archaeology 120(1), 99-149.

Koster, B., Vött, A., Mathes-Schmidt, M., Reicherter, K., 2015. Geoscientific investigations in search of tsunami deposits in the environs of the Agoulinitsa

peatland, Kaiafas Lagoon and Kakovatos (Gulf of Kyparissia, western Peloponnese, Greece). Zeitschrift für Geomorphologie 59, 125-156.

Kraft, J.C., Rapp, G., Kayan, I., Luce, J.V., 2003. Harbor areas at ancient Troy: sedimentology and geomorphology complement Homer's Iliad. Geology 31(2), 163-166.

Krezoski, G., 2008. Paleoenvironmental reconstruction of prehistoric submerged and coastal environments at Liman Tepe/Klazomenai, Turkey. Unpublished Master's thesis, McMaster University.

Krezoski, G.M., Boyce, J.I., Riddick, N.L., Saholgu, V., Erkanal, H., Reinhard, E.G., Goodman-Tchernov, B.N., 2021 (2021, In Prep). Coastal sediment record of the construction of Alexander the Great's causeway at Clazomenae (ca. 4th c. BCE) and its impact on coastal environments (Bay of Izmir, Turkey).

Kylander, M.E., Ampel, L., Wohlfarth, B., Veres, D., 2011. High-resolution X-ray fluorescence core scanning analysis of Les Echets (France) sedimentary sequence: new insights from chemical proxies. Journal of Quaternary Science 26(1), 109-117.

Lambeck, K., 1995. Late Pleistocene and Holocene sea-level change in Greece and south-western Turkey: a separation of eustatic, isostatic and tectonic contributions. Geophysical Journal International 122(3), 1022-1044.

Le Roux, G., Véron, A., Morhange, C., 2005. Lead pollution in the ancient harbours of Marseilles. Méditerranée. Revue géographique des pays méditerranéens/Journal of Mediterranean geography (104), 31-35.

Luyendyk, A.P.J., 1997. Processing of airborne magnetic data. AGSO Journal of Australian Geology and Geophysics 17, 31-38.

Marriner, N., Morhange, C., 2007. Geoscience of ancient Mediterranean harbours. Earth-Science Reviews 80(3-4), 137-194.

Marriner, N., Morhange, C., Boudagher-Fadel, M., Bourcier, M., Carbonel, P., 2005. Geoarchaeology of Tyre's ancient northern harbour, Phoenicia. Journal of Archaeological Science 32(9), 1302-1327.

Marriner, N., Morhange, C., Carayon, N., 2008. Ancient Tyre and its harbours: 5000 years of human-environment interactions. Journal of Archaeological Science 35(5), 1281-1310.

Marriner, N., Morhange, C., Doumet-Serhal, C., 2006. Geoarchaeology of Sidon's ancient harbours, Phoenicia. Journal of Archaeological Science 33(11), 1514-1535.

Marriner, N., Morhange, C., Goiran, J.P., 2010. Coastal and ancient harbour geoarchaeology. Geology Today 26(1), 21-27.

Marriner, N., Morhange, C., Kaniewski, D., Carayon, N., 2014. Ancient harbour infrastructure in the Levant: tracking the birth and rise of new forms of anthropogenic pressure. Scientific Reports 4(1), 1-11.

Marshall, M.H., Lamb, H.F., Huws, D., Davies, S.J., Bates, R., Bloemendal, J., Boyle, J., Leng, M.J., Umer, M., Bryant, C., 2011. Late Pleistocene and Holocene drought events at Lake Tana, the source of the Blue Nile. Global and Planetary Change 78(3-4), 147-161.

Massa, M., Şahoğlu, V., 2015. The 4.2 ka climatic event in west and central Anatolia: combining palaeoclimatic proxies and archaeological data. In: Meller, H., Risch, R., Jung, R., Arz, R.W. (Eds), 2200 BC - A climatic breakdown as a cause for the collapse of the old world? Halle, 61-78.

Mauro, C.M., 2019. Archaic and Classical Harbours of the Greek World: The Aegean and Eastern Ionian Contexts. Archaeopress Publishing Ltd.

Mourtzas, N.D., Kissas, C., Kolaiti, E., 2014. Archaeological and geomorphological indicators of the historical sea level changes and the related palaeogeographical reconstruction of the ancient foreharbour of Lechaion, East Corinth Gulf (Greece). Quaternary International 332, 151-171.

Müller, C., Woelz, S., Ersoy, Y., Boyce, J., Jokisch, T., Wendt, G., Rabbel, W., 2009. Ultra-high-resolution marine 2D–3D seismic investigation of the Liman Tepe/Karantina Island archaeological site (Urla/Turkey). Journal of Applied Geophysics 68(1), 124-134.

Papadopoulos, J.K., 2014. Greece in the early Iron Age: Mobility, commodities, polities, and literacy. In: Knapp, B.A., Van Dommelen, P. (Eds), The Cambridge Prehistory of the Bronze and Iron Age Mediterranean. Cambridge University Press, pp. 178-195.

Pasqualini, V., Pergent-Martini, C., Clabaut, P., Pergent, G., 1998. Mapping ofPosidonia oceanicausing Aerial Photographs and Side Scan Sonar: Application off the Island of Corsica (France). Estuarine, Coastal and Shelf Science 47(3), 359-367.

Pint, A., Seeliger, M., Frenzel, P., Feuser, S., Erkul, E., Berndt, C., Klein, C., Pirson, F., & Brückner, H., 2015. The environs of Elaia's ancient open harbour–a reconstruction based on microfaunal evidence. Journal of Archaeological Science 54, 340-355.

Piva, A., Asioli, A., Schneider, R.R., Trincardi, F., Andersen, N., Colmenero-Hidalgo, E., Dennielou, B., Flores J-A, Vigliotti, L., 2008. Climatic cycles as expressed in sediments of the PROMESS1 borehole PRAD1-2, central Adriatic, for the last 370 ka: 1. Integrated stratigraphy. Geochemistry, Geophysics, Geosystems 9(1).

Rabān, A., (1995). Dor-Yam: maritime and coastal installations at Dor in their geomorphological and stratigraphic context. Excavations at Dor. Final report. Vol. 1., Areas A and C.-A. Introduction and stratigraphy, pp. 285-354.

Ramkumar, M. (2015). Toward standardization of terminologies and recognition of chemostratigraphy as a formal stratigraphic method. In: Chemostratigraphy Elsevier, pp. 1-21.

Reimer, P.J., McCormac, F.G., 2002. Marine radiocarbon reservoir corrections for the Mediterranean and Aegean Seas. Radiocarbon 44(1), 159-166.

Reinhardt, E.G., Goodman, B.N., Boyce, J.I., Lopez, G., van Hengstum, P., Rink, W.J., Mart, Y., Raban, A., 2006. The tsunami of 13 December AD 115 and the destruction of Herod the Great's harbor at Caesarea Maritima, Israel. Geology 34(12), 1061-1064.

Reinhardt, E.G., Raban, A, 1999. Destruction of Herod the Great's harbor at Caesarea Maritima, Israel—geoarchaeological evidence. Geology 27(9), 811-814.

Rothwell, R.G., Croudace, I.W., 2015. Micro-XRF studies of sediment cores: a perspective on capability and application in the environmental sciences. In: Croudace, I.W., Rothwell, R.G. (Eds), Micro-XRF Studies of Sediment Cores, Springer, pp. 1-24

Şahoğlu, V., 2005. The Anatolian trade network and the Izmir region during the Early Bronze Age. Oxford Journal of Archaeology 24(4), 339-361.

Şahoğlu, V., 2010. Ankara University Research Center for Maritime Archaeology (ANKÜSAM) and its role in the Protection of Turkey's Underwater Cultural Heritage. In Congress.

Sayın, E., 2003. Physical features of the Izmir Bay. Continental Shelf Research 23(10), 957-970.

Sayın, E., Eronat, C., 2018. The dynamics of İzmir Bay under the effects of wind and thermohaline forces. Ocean Science 14(2), 285-292.

Scott, D.B., Hermelin, J.O.R., 1993. A device for precision splitting of micropaleontological samples in liquid suspension. Journal of Paleontology 67(1), 151-154.

Seeliger, M., Bartz, M., Erkul, E., Feuser, S., Kelterbaum, D., Klein, C., Pirson, F., Vött, A., Brückner, H., 2013. Taken from the sea, reclaimed by the sea: The fate of the closed harbour of Elaia, the maritime satellite city of Pergamum (Turkey). Quaternary International 312, 70-83.

Seeliger, M., Pint, A., Feuser, S., Riedesel, S., Marriner, N., Frenzel, P., Pirson, F., Bolten, A., Brückner, H., 2019. Elaia, Pergamon's maritime satellite: the rise and fall of an ancient harbour city shaped by shoreline migration. Journal of Quaternary Science 34(3), 228-244.

Seki, A., Tada, R., Kurokawa, S., Murayama, M., 2019. High-resolution Quaternary record of marine organic carbon content in the hemipelagic sediments of the Japan Sea from bromine counts measured by XRF core scanner. Progress in Earth and Planetary Science 6(1), 1-12.

Shalev, A.E., Gilboa, A., Yasur-Landau, A., 2019. The Iron Age Maritime Interface at the South Bay of Tel Dor: results from the 2016 and 2017 excavation seasons. International Journal of Nautical Archaeology 48(2), 439-452.

Shumilovskikh, L. S., Seeliger, M., Feuser, S., Novenko, E., Schlütz, F., Pint, A., Pirson, F., Brückner, H., 2016. The harbour of Elaia: A palynological archive for human environmental interactions during the last 7500 years. Quaternary Science Reviews 149, 167-187.

Sonnenburg, E.P., Boyce, J.I., 2008. Data-fused digital bathymetry and side-scan sonar as a base for archaeological inventory of submerged landscapes in the Rideau Canal, Ontario, Canada. Geoarchaeology 23(5), 654-674.

Stiros, S.C., 2020. Coastal subsidence, destruction layers and earthquakes from an underwater archaeological excavation: Kenchreai, eastern harbour of Roman Corinth, Greece. Mediterranean Geoscience Reviews, 1-15.

Stock, F., Halder, S., Opitz, S., Pint, A., Seren, S., Ladstätter, S., Brückner, H., 2019. Late Holocene coastline and landscape changes to the west of Ephesus, Turkey. Quaternary International 501, 349-363.

Stock, F., Kerschner, M., Kraft, J. C., Pint, A., Frenzel, P., Brückner, H., 2014. The palaeogeographies of Ephesos (Turkey), its harbours, and the Artemision–a geoarchaeological reconstruction for the timespan 1500–300 BC. Zeitschrift für Geomorphologie, Supplementary Issues 58, 33-66.

Stock, F., Knipping, M., Pint, A., Ladstätter, S., Delile, H., Heiss, A.G., Laermanns, H., Mitchell, P.D., Ployer, R., Steskal, M., Thanheiser, U., Urz, R., Wennrich, V., Brückner, H., 2016. Human impact on Holocene sediment dynamics in the Eastern Mediterranean–the example of the Roman harbour of Ephesus. Earth Surface Processes and Landforms 41(7), 980-996.

Stock, F., Pint, A., Horejs, B., Ladstätter, S., Brückner, H., 2013. In search of the harbours: New evidence of Late Roman and Byzantine harbours of Ephesus. Quaternary International 312, 57-69.

Stuiver, M., Reimer, P.J., Reimer, R.W., 2019. CALIB 7.1 [WWW program] at http://calib.org

Tartaron, T.F., 2015. The Settlement at Kalamianos: Bronze Age Small Worlds and the Saronic Coast of the Southeastern Corinthia. Hesperia Supplements 48, 25-38.

Tuğcu, İ., 2017. The preliminary results on the western breakwater of the Liman Tepe/Clazomenae ancient harbour. Journal of the Cukurova University Institute of Social Sciences, 26(1).

Tuncel, R., Şahoğlu, V., 2018. The Chalcolithic of coastal western Anatolia: A view from Liman Tepe, Izmir. In: Dietz, S., Mavridis, F., Tabkosic, Z., Takaoglu, T. (Eds), Communities in transition: The circum-Aegean area during the 5th and 4th millennia BC, Oxbow Books Limited.

Van Andel, T.H., Zangger, E., Demitrack, A., 1990. Land use and soil erosion in prehistoric and historical Greece. Journal of field archaeology 17(4), 379-396.

Votruba, G.F., Artzy, M., Erkanal, H., 2016. A set Archaic anchor arm exposed within P. oceanica matte at Klazomenai/Liman Tepe, Turkey: A contribution for understanding marine stratigraphy. Journal of Field Archaeology 41(6), 671-683.

Wolters, S., Zeiler, M., Bungenstock, F., 2010. Early Holocene environmental history of sunken landscapes: pollen, plant macrofossil and geochemical analyses from the Borkum Riffgrund, southern North Sea. International Journal of Earth Sciences 99(8), 1707-1719.

Young, A., Anstee, S., 2001. A user's guide to Sonarview 1.0: a sidescan sonar post-processing system. Defense Science and Technology Organisation, Victoria (Australia), Aeronautical and Maritime Maritime Research Lab, p. 133.

Ziegler, M., Jilbert, T., de Lange, G.J., Lourens, L.J., Reichart, G.J., 2008. Bromine counts from XRF scanning as an estimate of the marine organic carbon content of sediment cores. Geochemistry, Geophysics, Geosystems 9(5).

CHAPTER 4: Multi-proxy palaeoenvironmental record of coastal tectonic uplift and abandonment (ca. 6th c. CE) of Lechaion's inner harbour, Ancient Corinth (Greece)

Abstract

Lechaion's inner harbour basin was constructed in the 7th-6th c. BCE and served as Corinth's principal port for over a millennium. The harbour decline and abandonment in the 6th c. CE has been attributed to several causes: natural siltation, co-seismic uplift, coastal subsidence, and damage by tsunami impacts. A multi-proxy palaeoenvironmental study was conducted on seven cores from Lechaion's inner harbour to determine changes in the coastal environments and timing and cause of harbour abandonment. Palaeoenvironments were reconstructed using high-resolution micro-XRF core scanning of sedimentary facies and isotopic ($\delta^{18}O$, $\delta^{13}C$) and micropalaeontological analyses (foraminifera, palynomorphs).

The harbour lithostratigraphy consists of an uppermost (~1 m) sequence of laminated mud and marl overlying interbedded pebbly sand and mud containing abundant marine microfossils and Roman pottery refuse. A thin (<12 cm) calcrete layer at the base of the marl defines a basin-wide paraconformity, marking a transition from a marine-estuarine harbour basin to a restricted, evaporitic lake. Basin restriction is recorded by a sharp decline in terrigenous elements (Si, Ti, K, Fe), increased Sr, $\delta^{18}O$, a decline in foraminifera and marine dinoflagellate cysts, and an increase in freshwater algae. The event, constrained by AMS ^{14}C age modelling to the 6th c. CE, is interpreted as a rapid, co-seismic uplift of the harbour floor, most likely during destructive earthquakes of 524 and 551/552 CE. These seismic events have been linked to a ~1.1 m uplift of the nearby Perachora Peninsula and sediment liquefaction structures on-site. No evidence was found for 2nd c. BCE or 6th c. CE tsunami events proposed in previous work. This study represents the most comprehensive geoarchaeological study completed to date in Lechaion's inner harbour and confirms its destruction and abandonment in the 6th c. CE as a result of co-seismic uplift and rapid shoaling of the inner basin.

Keywords: Lechaion, harbour basin, co-seismic uplift, palaeoenvironments, micro-XRF elemental analysis, microfossils

4.1 Introduction

Ancient harbour basins contain important sediment archives of palaeoenvironmental change and human activities and have become a major focus of geoarchaeological studies in the Mediterranean (Marriner et al., 2007, 2010). Multi-disciplinary geoarchaeological studies of harbour sediment have yielded important insights into ancient harbour technology (Reinhardt and Raban, 1999; Boyce et al., 2004, 2009; Marriner et al., 2014; Chapter 3), palaeoecology and stratigraphy (Morhange et al., 2003; Reinhardt et al., 2003), sea level change (Morhange et al., 2001; Goodman et al., 2008; Nixon et al.; 2009; Chapter 2), and long-term records of human modification of natural coastal systems (Marriner at al., 2007, 2014; Goodman et al., 2009; Chapter 3). Harbour sediments can also preserve records of coastal neotectonics, as documented by the uplift or subsidence of harbour structures (Nixon et al., 2009; Stiros and Blackman, 2014; Stiros, 2020), and evidence for earthquake damage and palaeotsunami impacts on coastlines (Reinhardt et al., 1999, 2006; Hadler et al., 2013; 2015). Several recent studies have emphasized the importance of earthquakes and tsunamis in the destruction of ancient harbours and coastal settlements in the eastern Mediterranean (Marriner and Morhange, 2007; Vött et al., 2011, 2018; Hadler et al., 2013, 2015; Goodman-Tchernov and Austin, 2015). However, the identification of tsunamigenic sediments and their differentiation from storm deposits can be problematic when based solely on sedimentary facies or micropalaeontological characteristics (Goff et al., 2004; Tuttle et al., 2004; Kortekaas and Dawson, 2007; Morton et al., 2007; Kolaiti et al., 2017; Costa et al., 2018).

Of the many examples of engineered harbour basins in the ancient world, Lechaion was one of the longest-lived in the Mediterranean (Rothaus, 1995; Stiros et al., 1996; Morhange et al., 2012), serving as Corinth's principal trading port and naval base for over a millennium (Fig. 4.1a). Lechaion's inner harbour (cothon) was constructed in the 7th-6th c. BCE, during the Kypselid Tyranny and underwent several phases of renovations during

the Greek Classical and Roman periods (Rothaus, 1995; Vött et al., 2018). Geoarchaeological evidence indicates that the harbour was abandoned sometime during the 6th c. CE, although settlement at the site continued into the Early Modern period (Rothaus, 1995; Morhange et al., 2012). The decline and abandonment of Lechaion's harbour has been attributed to several causes, including siltation of the basin (Morhange et al., 2012), co-seismic uplift (Mourtzas and Marinos, 1994; Morhange et al., 2012), coastal subsidence (Mourtzas et al., 2014), and damage resulting from tsunami (Hadler et al., 2013; Vött et al., 2018). The role of tsunami impacts at Lechaion is currently debated (Hadler et al., 2011, 2013; Koster et al., 2013; Kolaiti et al., 2017; Vött et al., 2018). Hadler et al. (2013) argued for three tsunami events between the 8th c. BCE to 6th c. CE, based on sedimentary, archaeological, and geophysical lines of evidence. Kolaiti et al. (2017), however, refuted the evidence and attribute the purported tsunamigenic deposits to natural depositional processes.

To better resolve the evolution of Lechaion's inner harbour and the causes and timing of its abandonment, we conducted a detailed, multi-proxy palaeoenvironmental study on seven cores from the inner harbour basin and entrance channel (Fig. 4.1b). The palaeoenvironmental database includes sedimentary facies, micro-XRF element geochemistry, stable isotopes ($\delta^{18}O$, $\delta^{13}C$), and micropalaeontological (foraminifera, palynomorphs) data, representing the most comprehensive geoarchaeological study of Lechaion's inner harbour to date. Our results identify changes in the harbour palaeoenvironments from the onset of Roman occupation (ca. 1st c. BCE) to present.

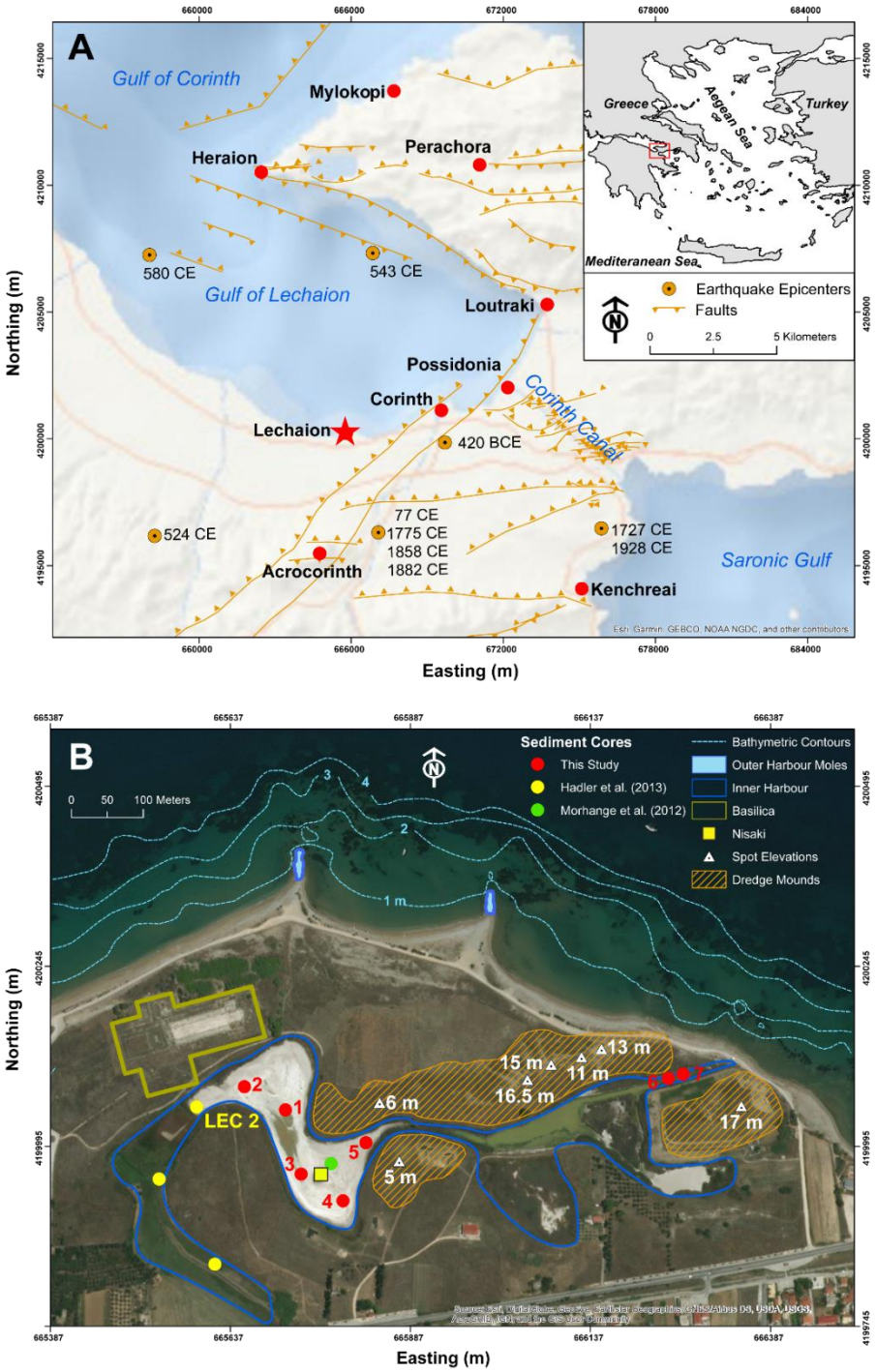

Figure 4.1: A. Map showing location of Lechaion, earthquake epicentres and location of regional faults in the Eastern Gulf of Corinth (modified from Turner et al., 2010, Mourtzas et al., 2014). B. Lechaion's inner and outer harbour basins with core locations, including two previous studies. Nearshore bathymetry (contour interval 1 m) and topographic point elevations (metres relative to mean sea level) modified from Mourtzas et al. (2014). Dredge spoil mounds (up to 17 m) record Classical-Roman age dredging of the harbour basin and entrance channel.

4.2 Study Area

4.2.1 Physical Setting and Geology

Lechaion is located on the eastern Gulf of Corinth, about 3 km north of the ancient city of Corinth (Fig. 4.1a). The port included both excavated inner harbour basins and an outer harbour protected by north-south oriented mole structures (Fig. 4.1b) (Rothaus, 1995; Stiros et al., 1996). The inner harbour basin had a sinuous form in plan, consisting of several smaller, interconnected sub-basins, covering an area of about 10 ha (Fig. 4.1b). The easternmost harbour basin was formerly connected to the sea via a 150-m long and 12-m wide entrance channel (Rothaus, 1995). A topographic depression to the north of the western inner harbour suggests a possible third harbour basin, which may have been connected to the outer harbour. The meandering form of the inner harbour suggests that it was constructed by excavation and widening of a pre-existing river channel or estuary, or perhaps a shallow coastal marsh (Morhange et al., 2012; Kolaiti et al., 2017). The inner harbour is now land-locked and occupied by a low-relief coastal wetland and an ephemeral lake that is flooded during storm events (Fig. 4.1b). The topography around the wetland is defined by several low-relief hills, up to 17 m in height, containing dredge spoils (Rothaus, 1995; Stiros et al., 1996). Noting the large volume of the dredge spoils, Morhange et al. (2012) concluded that the sinuous inner basin was an effective sediment trap, which required continual dredging to maintain a navigable harbour and entrance channels.

The Gulf of Corinth is in an active asymmetric rift zone with one of the highest extensional rates in the world (13-15 mm/year) (Arnijo et al., 1996; Briole et al., 2000; Avallone et al., 2004). The Corinth rift is bounded by west-east trending normal faults that have generated destructive earthquakes (Vita-Finzi and King, 1985) (Fig. 4.1a). Earthquakes with magnitudes up to 7.0 (M_L) have been recorded, with return periods of 20 to 80 years for magnitudes 6.0 and 6.5 respectively (Papadopoulos and Kijko, 1991; Papadopoulos, 2003). Uplift of the rift margins is recorded by preserved marine terraces and wave-cut notches in beachrock (Stiros, 1995; Stiros et al., 1996). Modern Corinth and ancient Corinth are located on uplifted marine terraces (Stiros et al., 1996), composed of

Pleistocene clastic sediments that overlie Plio-Pleistocene marls, limestone, and conglomerates (Keraudren and Sorel, 1987). Co-seismic uplift of the coast has been documented on the nearby Perachora Peninsula (Pirazzoli et al., 1994), Aliki salt pond (Emmanouilidis et al., 2020), and in the Saronic Gulf based on evidence from beachrock and tidal notches (e.g. Kolaiti and Mourtzas, 2016)

4.2.2 Site History and Archaeology

Lechaion's inner harbour was constructed between the 7th-6th c. BCE, during the reign of Periander (Kypselids Period) and a period of Corinthian westward economic expansion (Rothaus, 1995; Stiros et al., 1996; Kolaiti et al., 2017). Lechaion served as a naval base in the early 4th c. BCE during the Corinthian War and in 200 BCE it became a Macedonian naval base. In 146 BCE, the Romans invaded Corinth, and Lechaion was sacked and abandoned. After the Roman re-colonization of Corinth in 44 BCE, Lechaion's harbour was rebuilt and the inner harbour was dredged and the entrance channel re-opened to the sea (Pallas, 1963; Rothaus, 1995; Stiros et al., 1996; Boetto, 2010; Kolaiti et al., 2017). Historical sources record several subsequent phases of harbour renovations during the Roman period (ca. 1st c. CE) and between 353-358 CE (Kent, 1966; Rothaus, 1995). After the 6th c. CE, Lechaion's inner harbour was no longer in use but settlement continued on-site (Rothaus, 1995).

Several archaeological investigations have been conducted at Lechaion, focusing primarily on the Early Christian Basilica (Pallas, 1965; see Rothaus, 1995 for summary). Architectural features exposed at surface include ashlar-constructed quays, retaining walls, and a small (9 x 9 m) rectangular structure located in the centre of the eastern inner harbour basin, known locally as the 'nisaki' (little island) (Fig. 4.1b) (Shaw, 1969; Rothaus, 1995). The nisaki may have served as a base for statuary or as a harbour signaling station (Rothaus, 1995). Geoarchaeological and geophysical investigations at the basilica have identified evidence for buckled floor structures and soil liquefaction features, attributed to 6th c. CE earthquake events, which destroyed the basilica (Apostololopoulos et al., 2015; Minos-Minopoulos et al., 2015). Since in 2014, the Lechaion Harbour Project has conducted

underwater excavations in the outer harbour and geophysical surveys of the inner harbour basins (Kourkoumelis et al., 2017).

4.3 Methods

4.3.1 Coring and Sediment Chronology

Seven sediment cores (70-220 cm length) were extracted along a west-east transect (Fig. 4.1b) using a gas-driven vibracorer with 70 mm galvanized steel tubes (Smith, 1987). Cores were carefully sealed and refrigerated at 4-6 °C to prevent microbial growth and sediment oxidation. Cores were split and one half preserved for micro-XRF core scanning (μ-XRF-CS) and the other half for micropalaeontological and isotopic analyses. Sediment lithofacies, composition and texture (grain size, sorting) were logged in detail and plotted as a west-east core transect (Fig. 4.2). The nearby LEC 2 core of Hadler et al. (2013) was also included in the transect for comparison (Figs. 4.1b, 4.2).

Seven samples of organic matter and shell materials were collected from three cores (2, 3 and 7) for AMS ^{14}C dating (Table 4.1) at Beta Analytic Inc. (Miami, Florida) and calibrated using Calib 7.1 software with the IntCal13 and Marine13 calibration curves (Stuiver et al., 2019). For marine samples, calibration included a marine reservoir correction using a ΔR value of 133 ± 75 (Vött et al., 2018). The radiocarbon chronology was augmented by identification and dating of pottery materials recovered at several intervals in the cores (Fig. 4.2). A Bayesian sediment age-depth model was produced using BACON (Blaauw and Christen, 2011) by combining four AMS ^{14}C dates from core LEC 2 of Hadler et al. (2013) with new dates from core 2 (Fig. 4.3). The LEC 2 core contained the same lithofacies succession as the upper 2 m portion of our core 2 (Fig. 4.2).

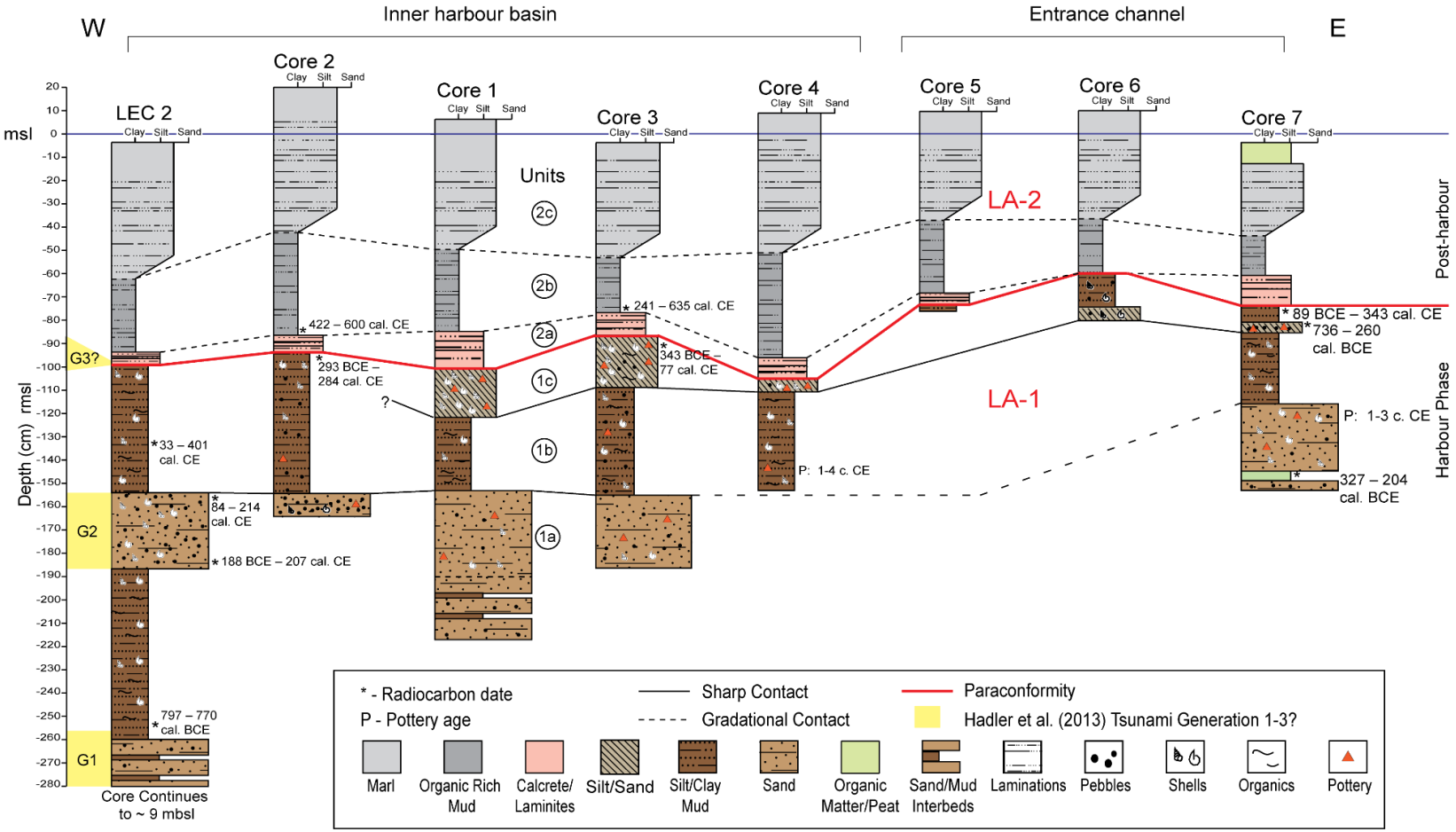

Figure 4.2. West-east lithostratigraphic profile across inner harbour and entrance channel (core locations in Fig. 4.1b). All core depths are relative to mean sea level (rmsl). Core LEC 2 is redrawn from Hadler et al. (2013) showing their proposed tsunamites (G1-G3). Lithofacies assemblages LA-1 and LA-2 are separated by basin-wide paraconformity surface. LA-1 (units 1a-c) comprises interbedded silts, muds, and sands with abundant pottery, deposited in a marine-estuarine harbour environment. LA-2 (units 2a-c) records a shift to a shallow, lacustrine environment dominated by marl deposition. AMS ^{14}C dates compiled in Table 4.1.

Table 4.1: AMS ^{14}C radiocarbon dates calibrated using Calib 7.1 with the IntCal13 and Marine13 calibration curves (Stuiver et al., 2019). Date from core LEC 2 (Hadler et al., 2013) also recalibrated. * Marine reservoir correction ($\Delta R = 133 +/-75$) applied to shell samples (Vött et al., 2018).

Sample Code	Sample #	Material	Elevation (mbsl)	^{14}C Age (BP)	2σ Max and Min Cal. Age		Median Probable Age
Beta-136212	Core2-1	Olive pit	0.84	1540 ± 40	422 CE	600 CE	505 CE
Beta-136213	Core2-2	*Shell	0.95	2510 ± 120	293 BCE	284 CE	64 BCE
Beta-136214	Core3-1	Bulk	0.76	2090 ± 40	241 CE	635 CE	438 CE
Beta-136215	Core3-2	*Shell	0.91	2560 ± 40	343 BCE	77 CE	122 BCE
Beta-136217	Core7-1	*Shell	0.74	2360 ± 40	89 BCE	343 CE	122 CE
Beta-136216	Core7-2	*Shell	0.80	2840 ± 40	736 BCE	260 BCE	484 BCE
Beta-136218	Core7-3	Peat	1.48	2250 ± 40	327 BCE	204 BCE	286 BCE
UCI 73816	LEC 2/6 M	*Shell	1.34	2285 ± 15	33 CE	401 CE	210 CE
UCI 73824	LEC 2/6+ HR	Wood	1.58	1865 ± 15	84 CE	214 CE	138 CE
UCI 73825	LEC 2/7+ PR	Plant fragments	1.86	2455 ± 15	188 BCE	207 CE	7 CE
UCI 73826	LEC 2/9+ PR	Plant fragments	2.54	2565 ± 15	797 BCE	770 BCE	786 BCE

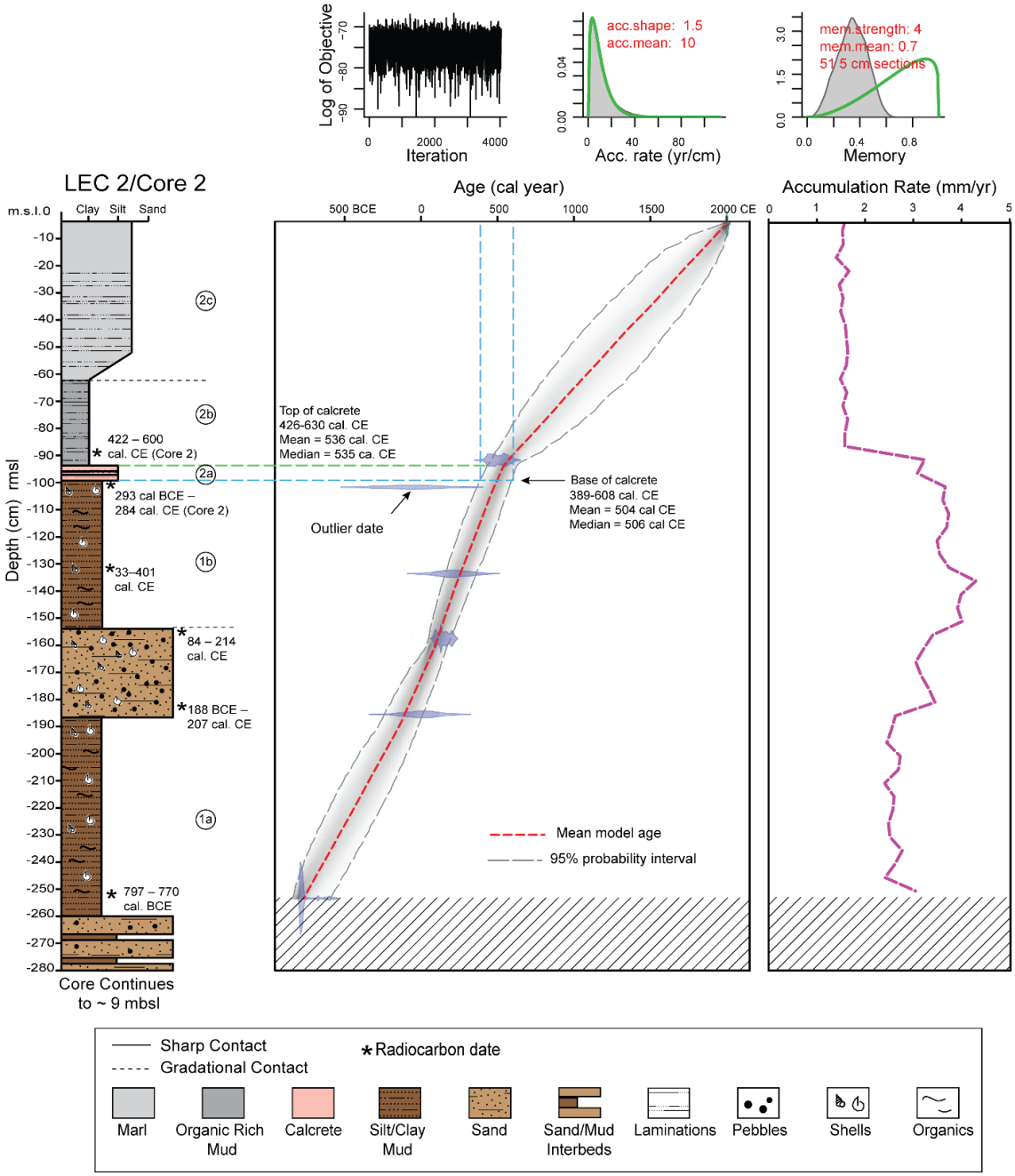

Figure 4.3: Bayesian age-depth model and estimated sediment accumulation rates generated in BACON (Blaauw and Christen, 2011) using combined AMS ^{14}C dates from cores 2 and LEC 2 (Fig. 4.1b). The base of the calcrete (unit 2a, ~99 cm depth), marks transition from a marine-estuarine harbour to a shallow lacustrine environment at 389-608 cal. CE (median = 506 cal. CE). The lowermost date from core 2 intersects the 95% probability envelope but does not lie within it and is likely an outlier, with an apparent age that is too old. The outlier may indicate an erosional hiatus at the top of unit 1b, as the overlying unit 1c is missing in both cores 2 and LEC 2 (Fig. 4.2).

4.3.2 Micro-XRF Core Scanning

Two cores were selected for μ-XRF-CS (ITRAX, Cox Analytical Systems): one from the inner harbour basin (core 1) and one from the entrance channel (core 7) (Fig. 4.1b). Cores were scanned using a Cr tube with a 500 μm step size, 20 s exposure, and 30 kV/25 mA power settings. Core 1 was also scanned using a Mo tube to improve detection of Pb (Croudace et al., 2006; Dulski et al., 2015; Jarvis et al., 2015). XRF spectra were batch analyzed using QSpec^{TM} software and normalized using the ratio of coherent to incoherent scatter to minimize matrix effects produced by changes in sediment porosity, moisture, and organic content (Kylander et al., 2011; Marshall et al., 2011; Berntsson et al., 2014; Gregory et al., 2019).

A Pearson correlation matrix was calculated for the whole cores and for the upper and lower section of each core separately, as the stratigraphy in all cores showed a clear bi-partite subdivision of lithofacies (Fig. 4.2). The elements Si, Ti, K, and Fe were selected as indicators of terrigenous sediment inputs and Ca a proxy for marine biological productivity (Davies et al., 2015; Rothwell and Croudace, 2015). A common contaminant in Roman harbour sediments, Pb was employed as an indicator of anthropogenic pollution (Le Roux et al., 2005; Croudace et al., 2006; Hadler et al., 2013; Stock et al., 2013; Davies et al., 2015). The Ca/Fe ratio was used to determine changes in marine productivity relative to the terrigenous sediment inputs to the harbour basin (Hadler et al., 2013; Rothwell and Croudace, 2015), and Sr to identify phases of high salinity produced by evaporative conditions (Ariztegui et al., 2010; Martín-Puertas et al., 2011; Koutsodendris et al., 2015).

4.3.3 Micropalaeontology

Sediment samples (25 cm^3) were collected from cores 1, 2, 3, and 7 (Fig. 4.1b) for foraminiferal analysis. Samples were disaggregated in water using a Burrel wrist-action shaker and washed through a 63 μm sieve to remove the silt and finer-sized fraction of the sediment. Washed samples were then oven dried at 90 °C and foraminifera isolated by floating the sample in tetrachloroethylene. A dry splitter was used to statistically divide samples for counting (approximately 300) (Fishbein and Patterson 1993; Scott et al., 2007).

Samples containing abundant organic matter were examined wet to preserve delicate agglutinated specimens (e.g. *Trochammina spp.*) and were divided for counting using a wet splitter (Scott and Hermelin, 1993). Species were considered statistically insignificant and removed from further analysis if the standard error was greater than fractional abundance in more than 50 percent of samples (Patterson and Fishbein, 1989). Q-mode cluster analysis was performed to classify biofacies and to assist in environmental interpretations (Fishbein and Patterson, 1993).

For palynological analysis, 5 ml volume samples (determined by liquid displacement) from core 1 were processed using standard palynological techniques for marine sediments (Faegri and Iversen, 1989), modified to avoid harsh oxidation (acetolysis) which has been shown to destroy some non-pollen palynomorphs (NPP) (Marret, 1993; Riddick et al., 2017). Samples were disaggregated in a weak (0.02%) sodium hexametaphosphate solution, treated with HCl (10%) to dissolve carbonates, and HF (48%) to dissolve silicates. A tablet containing a known quantity of *Lycopodium* spores was added during the HCl stage to allow estimation of the absolute abundances of palynomorphs in strew slides examined at 400X magnification.

4.3.4 Isotopic Analysis

For stable isotopic analysis ($\delta^{13}C$, $\delta^{18}O$), taphonomically unaltered specimens of foraminifera, charophytes, ostracods, and undifferentiated mollusk shells were sampled from core 3. Specimens were ultrasonically cleaned in distilled water followed by 0.5 M HCl to remove contaminants. Multiple taxa were analyzed in each sample to provide a measure of the water mass variability within the harbour basin (Reinhardt et al., 2003; Peros et al., 2007). Stable isotope analyses were performed on a VG Autocarb system and OPTIMA isotope-ratio mass spectrometer at McMaster University. Results were reported in standard delta (δ) notation relative to Vienna Pee Dee Belemnite (VPDB). The analytical precision was ± 0.07 ‰ for $\delta^{18}O$ and ± 0.10 ‰ for $\delta^{13}C$.

4.4 Results

4.4.1 Lithostratigraphy and Sediment Chronology

Coring revealed a laterally continuous harbour basin stratigraphy, consisting of two distinct lithofacies assemblages (LA-1, LA-2) separated by a sharp, planar contact. The contact defines a basin-wide paraconformity surface that can be correlated across the inner harbour (0.95-1.05 rmsl) eastward to the entrance channel (0.6-0.7 rmsl) (Fig. 4.2).

4.4.1.1 Lithofacies Assemblage 1

LA-1 consisted of interbedded pebbly sand, mud, and silt (Fig. 4.2). At the base, unit 1a consisted of silty mud intercalated with medium to coarse sand. The sand facies were massive to crudely bedded and contained abundant shell fragments and pottery sherds. In core 7, unit 1a contained a 4-cm thick organic-rich mud and peat layer (1.45-1.49 rmsl). Unit 1b comprised crudely laminated silty mud with disseminated *Posidonia oceanica* seagrass and abundant mollusk shell fragments. Unit 1c (cores 1, 3, 4, 6, 7) consisted of a poorly sorted mixture of granule- to pebble-sized clasts and mollusk shell fragments in a massive to crudely bedded silty to fine sand matrix. Unit 1c lacked primary bedding structures and contained abundant pebbles of Plio-Pleistocene limestone. Roman pottery fragments were abundant in unit 1c, making up 15-20% of the sediment by volume.

Nine radiocarbon dates for LA-1 sediments indicate a broad range of 8th c. BCE to 4th c. CE ages (Fig. 4.2; Table 4.1). In core LEC 2 of Hadler et al. (2013), unit 1a ranged in age from >797-770 cal. BCE to 84-214 cal. CE. The latter date is consistent with the 1st-3rd c. CE age of pottery found at the top of unit 1a in core 7 (1.20-1.30 rmsl) (Fig. 4.2). The peat layer at the bottom of core 7 dated to 327-204 cal. BCE and predates the Roman harbour phase. The peat may record wetland development around the entrance channel prior to the 1st c. BCE harbour renovation (Pallas, 1963; Rothaus, 1995; Stiros et al., 1996). Radiocarbon dates from the overlying units 1b and 1c yielded a wide range of ages and some age inversions, which may indicate sediment disturbance by dredging or dumping of sediments (Morhange and Marriner, 2010; Morhange et al., 2012). For example, unit 1c in

core 7 (0.81-0.84 rmsl) was anomalously old (736-260 cal. BCE) and may represent a dredgate deposit (Fig. 4.2).

LA-1 largely represents harbour basin deposits that accumulated from the ca. 7th c. BCE founding of the harbour through to Roman harbour phase (Figs. 4.2, 4.3). The silt and mud facies record low-energy suspension sedimentation, while sand interbeds, up to 50 cm in thickness, indicate deposition of bedforms (e.g. bars) by traction currents or wave-induced oscillatory currents. The heterogeneous composition of unit 1c, which includes outsized clasts, abundant pottery, and its lack of bedding structure, suggests that it is an anthropogenic deposit; most likely dredge spoils (Rothaus, 1995; Morhange et al., 2012) or ship ballast and refuse. Such coarse-grained admixtures of sediment, pottery, and ballast stones are a common feature of Roman harbour basin fills (Reinhardt and Raban, 1999; Boyce et al., 2009). The marine-estuarine origin of lithofacies assemblage LA-1 is indicated by the presence of *Posidonia* plant fragments, marine mollusk shells and microfossils (see section 4.4.3).

Sediment accumulation rates in LA-1 harbour deposits were between 2-4 mmyr^{-1} and were highest within unit 1b (Fig. 4.3). High sedimentation rates have been recorded in other Roman harbours, for example at Tyre in Lebanon, Marseille in France, and Piraeus in Greece (Marriner and Morhange, 2006, 2007). Sedimentation rate decreased markedly in overlying LA-2 to <1.5 mmyr^{-1} (Fig. 4.3).

4.4.1.2 Lithofacies Assemblage 2

LA-2 consisted of a coarsening-upward laminated mud and silty marl, overlying LA-1 across a sharp, planar contact. Three distinct units were present in LA-2 (Fig. 4.2). At the base of assemblage, unit 2a was defined by a thin (5-12 cm) calcrete (duricrust) layer, composed of indurated and partially cemented calcareous silt with iron-stained laminae, indicating precipitation of iron-oxide minerals (e.g. hematite, limonite). In two locations (cores 2, 3), the calcrete contained a thin zone (< 5 cm) of microbial mats inter-laminated with mud and marl. Carbonate microbial laminites are formed by the

calcification of photosynthetic microbes (cyanobacteria) in a range of environments, including hypersaline lakes, marine lagoons (Arp et al., 1999; Jahnert and Collins, 2013) and freshwater lakes and rivers (Freytet and Plet, 1996; Chen and Lee, 2014; Chagas et al., 2016). Above the calcrete, unit 2b comprised a laminated calcareous mud (marl) that was transitional above with a coarsening upwards sequence of calcareous muddy silt to fine sand (unit 2c). Unit 2c was laminated to crudely bedded at the top the unit and contained abundant seeds, reed fragments and macroscopic Charophyta. In contrast to LA-1, lithofacies assemblage LA-2 contained no visible pottery sherds and was largely devoid of marine mollusk shells and microfossils (see section 4.4.3). Hadler et al. (2013) interpreted similar marl deposits as a semi-terrestrial and 'limnic' environment. Morhange et al. (2012) attributed marl sediments to the progressive land-locking and siltation of the inner harbour basin.

The age of the calcrete (unit 2a) is constrained by four AMS ^{14}C dates (Figs. 4.2, 4.3; Table 4.1). In core 2, a shell below the calcrete dated to 293 cal. BCE to 284 cal. CE and an olive pit, collected above it, to 422-600 cal. CE. In core 3, a shell from below the calcrete dated 343 cal. BCE to 77 cal. CE and a bulk organic sample, collected near it the upper contact, dated 241-635 cal. CE. A fifth sample, collected just below the calcrete in core 7, dated 89 cal. BCE to 343 cal. CE. The Bayesian age model, based on the combined AMS ^{14}C ages from cores LEC 2 and 2, predicts an age of 389-608 cal. CE (median probability 506 cal. CE) for the base of the unit 2a (Fig. 4.3). The AMS ^{14}C age constraints thus point to a probable 6th c. CE date for the paraconformity defining the boundary between LA-1 and LA-2 sediments (Figs. 4.2, 4.3).

The laminated mud and marl sequence of LA-2 and its sharp contact with underlying LA-1 harbour deposits, indicates a marked shift in depositional environments (Fig. 4.2). LA-2 was deposited in a low energy lacustrine environment, which was dominated by calcium carbonate (marl) production, consistent with the abundance of charophytes. The near absence of marine mollusks and microfossils and abundance of lacustrine algae (chlorophytes, charophytes, and peridinioid dinoflagellates) (see section

4.4.3) clearly indicates freshwater conditions in the lake. Marl deposition, as in the modern-day ephemeral lake basin at Lechaion (Fig. 4.1b), occurred during evaporative conditions which would also promote the growth of cyanobacteria mats in a warm, shallow lake, supersaturated with respect to $CaCO_3$ (Chagas et al., 2016). The sharp contact at the base of LA-2, and the partial cementation of the marl to form a duricrust, indicates subaerial exposure and desiccation of marl deposits possibly during dry periods, or due to uplift and emergence of the harbour floor (Stiros, 1995). The notable absence of pottery fragments and ship refuse (e.g. ballast) throughout LA-2 suggests that following the 6th c. CE, the inner harbour was no longer in use.

4.4.2 Micro-XRF Geochemistry

A correlation matrix for LA-1 and LA-2 (core 1) is shown in Figure 4.4 and element profiles in Figures 4.5 and 4.6.

4.4.2.1 Lithofacies Assemblage 1

Terrigenous elements (Si, Ti, K, Fe) were more abundant and highly variable in LA-1 due to the heterogeneity of harbour sediments (Figs. 4.4-4.6). Si varied with sand content and grain-size and Ca values were highly variable and closely tracked Si ($r = 0.63$) (Fig. 4.4a), due to the increased abundance of marine shells and shell fragments within the coarser sand facies of LA-1 (Figs. 4.5, 4.6). In core 7, terrigenous elements and Ca increased in unit 1a above the basal peat layer, which is dated to 327-204 cal. BCE (Fig. 4.6). The peat records a phase of wetland development and possible closure of the inner harbour entrance channel prior to the Roman occupation. Sr and Ca/Fe were relatively invariant and low throughout LA-1 (Figs. 4.5, 4.6). Pb levels show a trend to increasing values in unit 1a, indicating anthropogenic pollution of the harbour basin following the onset of the Roman harbour phase (ca. 1st c. BCE) (Fig. 4.5).

4.4.2.2 Lithofacies Assemblage 2

In LA-2 there was a sharp decrease in the abundance of all terrigenous elements (Si, Ti, K, Fe) at the lower contact of the calcrete (unit 2a) (Figs. 4.5, 4.6). In core 1, the transition from unit 2a to unit 2b, was marked by a sharp increase followed by a decrease

in terrigenous elements over a ~10 cm interval (Fig. 4.5). A similar pattern was observed in unit 2b in core 7 (Fig. 4.6), indicating a renewed input of detrital sediments to the lake basin following the deposition of unit 2a. The Ca profiles in LA-1, showed a slight decline upwards in unit 2b in core 1 (Fig. 4.5) and in unit 2c in core 7 (Fig. 4.6). Ca was positively correlated with the terrigenous elements in LA-2 (Fig. 4.4b), indicating that the $CaCO_3$ in the marl is derived from river and groundwater inputs to the basin. The local geology includes Mesozoic limestone and Plio-Pleistocene marly limestones, which are the likely source of Ca and CO_3 ions in groundwater and surface waters (Keraudren and Sorel, 1987; Pirazzoli et al., 1994; Turner et al., 2010). Several peaks in Ca/Fe in LA-2 (Fig. 4.5, 4.6) are associated with a decrease in terrigenous elements and not elemental Ca, which suggests periods with decreased fluvial and detrital input and increased marl production as opposed to increased marine influence. Sr showed a major increase in abundance within unit 2a and a trend to overall increasing values upwards in LA-2 (Figs. 4.5, 4.6). The sharp increase in Sr is consistent with increased evaporation of brackish lake water within a restricted lagoon or coastal lake environment (Ariztegui et al., 2010; Martín-Puertas et al., 2011; Koutsodendris et al., 2015). Pb values increase sharply within unit 2a and decline at the base of unit 2b, indicating pollution of the lake by urban effluents (Fig. 4.5).

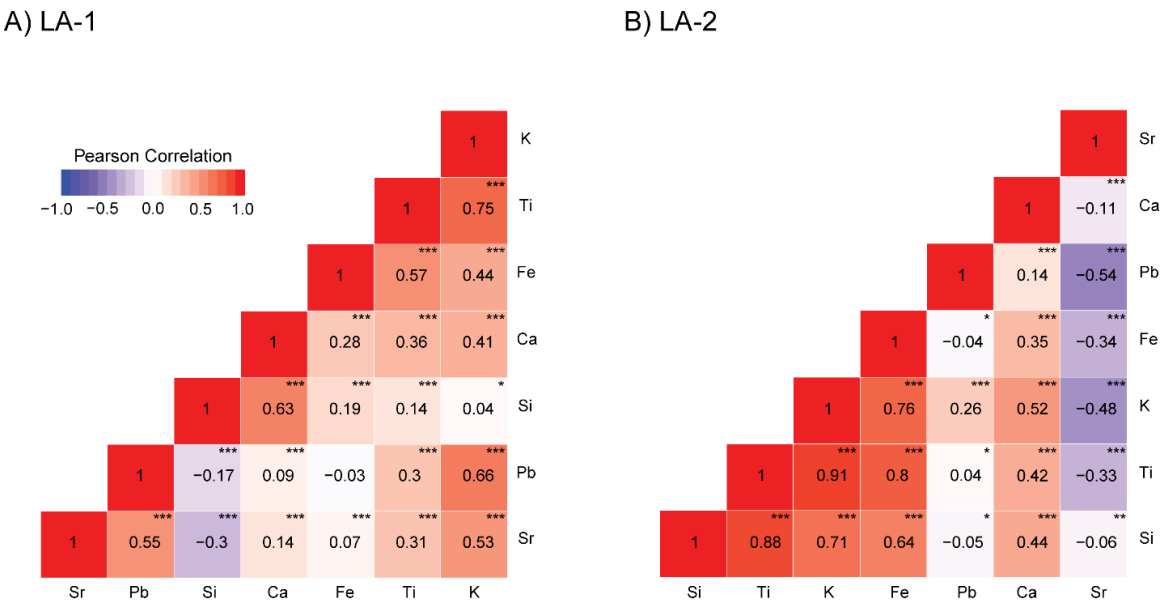

Figure 4.4: Correlation matrices (Pearson's r) for elements selected for analysis from core 1. A. LA-1, B. LA-2. Note strong correlations in LA-2 for detrital elements and relatively weaker correlations in LA-1 due to sedimentary heterogeneity and mix of sediment inputs. P values: *** = <0.001, ** <0.01, * <0.1.

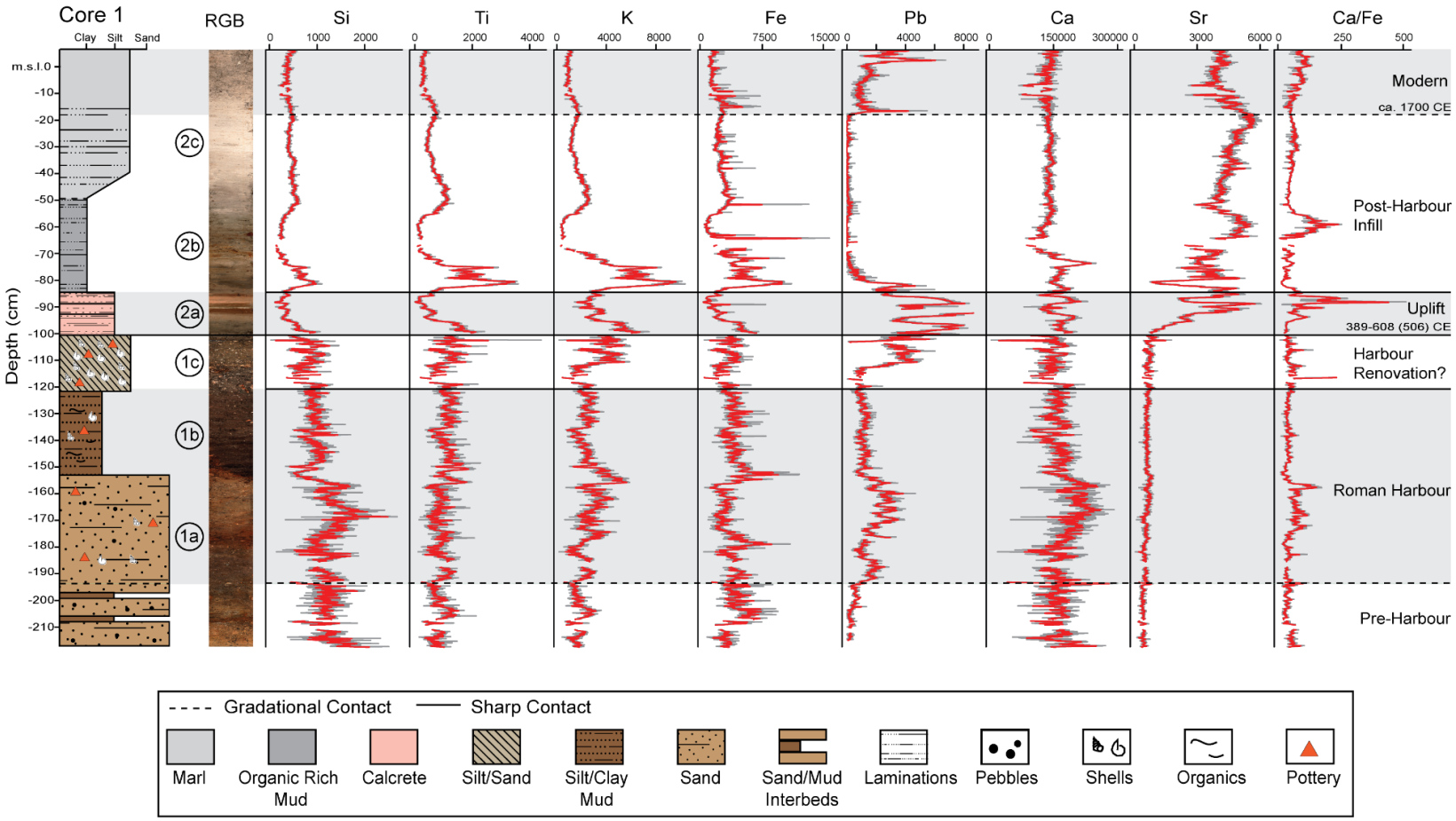

Figure 4.5: Core 1 lithology, RGB image and µ-XRF element profiles. LA-1 had low Sr with highly variable terrigenous elements (Si, K, Ti, Fe), due to the compositional heterogeneity of Roman harbour deposits. Increase in Sr and Ca/Ti in LA-2 marks shift to evaporitic lake environment. Decrease in terrigenous elements in the calcrete (unit 2a) records rapid restriction event recording basin uplift. The re-integration of drainage network and fluvial inputs to the lake is indicated by an increase in terrigenous elements at base of unit 2b. Date of LA-1 to LA-2 transition from BACON age model (Fig. 4.3).

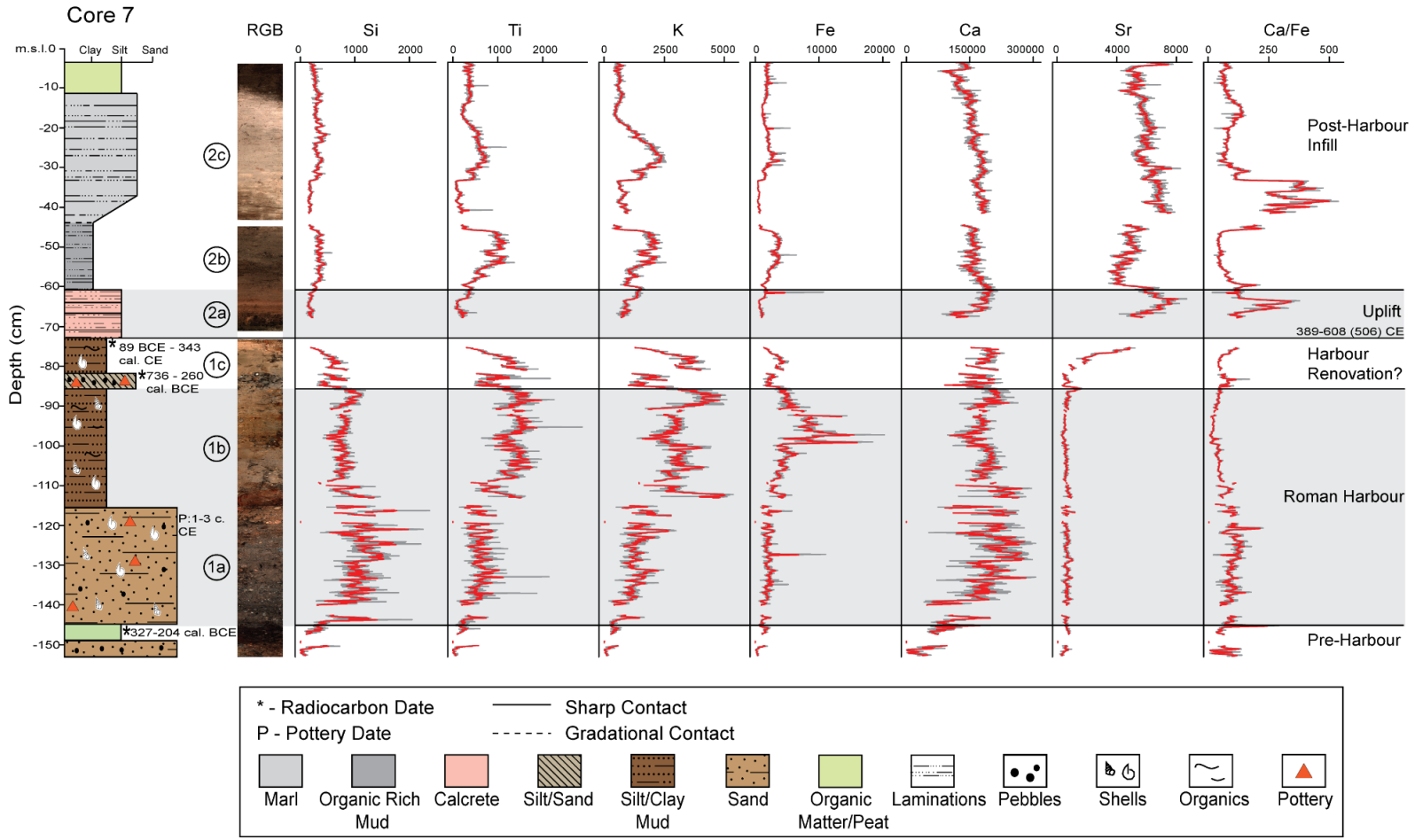

Figure 4.6: Core 7 lithology, RGB image and µ-XRF element profiles. LA-1 had low Sr with highly variable terrigenous elements (Si, K, Ti, Fe), due to the compositional heterogeneity of Roman harbour deposits. The peat layer at base of unit 1a dates to a period of harbour abandonment with possible closure of the entrance channel and wetland development. Increased terrigenous element abundances in unit 1a marks the beginning of the Roman harbour phase. Increase in Sr and Ca/Ti in LA-2 marks shift to evaporitic lake environment. Decrease in terrigenous elements in the calcrete (unit 2a) records rapid restriction event recording basin uplift. The re-integration of drainage network and fluvial inputs to the lake is indicated by an increase in terrigenous elements at base of unit 2b. Date of LA-1 to LA-2 transition from BACON age model (Fig. 4.3).

4.4.3 Micropalaeontology and Stable Isotopes

A total of 75 foraminifera species were identified, of which 45 of were statistically significant and grouped into three distinct biofacies using Q-mode cluster analysis (Fig. 4.7). The distribution of foraminifera, grouped by genera, are shown in Figures 4.8 and 4.9. Samples from LA-1 clustered into Biofacies 1 and 2, while LA-2 was generally devoid of foraminifera, except at the top of cores 2 and 3 (Biofacies 3). Palynomorphs, analysed from core 1 (Fig. 4.10) were abundant in both LA-1 and LA-2, but assemblages differed markedly.

4.4.3.1 Lithofacies Assemblage 1

Biofacies 1 included samples from units 1a and 1b from core 3 (base of core to 1.1 rmsl; Fig. 4.8) and unit 1a from core 7 (Fig. 4.9). The dominant genera (19-22 in total) were *Adelosina spp.* (core 3: 12-23%, core 7: 4-21%) and *Quinqueloculina spp.* (core 3: 20-34%, core 7: 7-26%) and at the base of core 7, *Haynesina spp.* and *Elphidium spp.* were dominant. The higher abundances of porcelaneous taxa (*Adelosina spp.* and *Quinqueloculina spp.*) in Biofacies 1, indicates a marine to hypersaline environment (Murray, 1991). This is consistent with marine values for $\delta^{18}O$ and $\delta^{13}C$ (~0 ‰) (Fig. 4.8) (Reinhardt et al., 2001, 2003; Peros et al., 2007).

Biofacies 2 was identified in core 2 from its base to 0.92 rmsl (units 1a and 1b), core 3 between 1.10-0.88 rmsl (unit 1c; Fig. 4.8) and core 7 between 1.15-0.74 rmsl (units 1b and 1c; Fig. 4.9). The dominant genera (18 in total) in cores 2 and 3 was *Ammonia spp.* (core 2: 16-39%, core 3: 17-28%) and the dominant genera in core 7 were *Bolivinellina spp.* (30-34%) and *Ammonia spp.* (5-23%). In core 7, the abundance of *Adelosina spp.* increased at the top of Biofacies 2. The increased abundance of *Ammonia spp*. In Biofacies 2 indicates basin restriction, while the presence of *Bolivinellina spp.* indicates reduced oxygen levels and a shift to eutrophic conditions in the harbour basin (Murray, 1991; Gupta and Machain-Castillo, 1993). Within Biofacies 2, $\delta^{13}C$ decreased to negative values, indicating increased freshwater input (Peros et al., 2007), while $\delta^{18}O$ fluctuated around 0 ‰ (Fig. 4.8). This is consistent with the foraminiferal assemblages, indicating a restricted,

perhaps more brackish environment.

Palynological samples from LA-1 in core 1 (Fig. 4.10), include cysts of marine dinoflagellates (dinocysts, e.g. *Brigantedinium*, *Spiniferites*, *Lejeunecysta sp.*, *Bitectatodinium tepikiense*, and *Lingulodinium machaerophorum*) and multilocular foraminiferal linings, together with a variety of freshwater algal palynomorphs, including the chlorophytes *Chlorococcum* sp. and *Pediastrum integrum*, the microscopic charophyte desmid *Cosmarium*, cysts/phycomata attributed to the freshwater macrophyte *Chara*, and cysts of *Peridinium* sp. The LA-1 assemblage is interpreted as marine-estuarine conditions. These samples also contained the eggs of the parasitic roundworm *Trichuris*, and abundant fungal spores. Pollen of forbs (asters, cheno-amaranths) and grasses comprise over 25% of the sporomorph assemblage in these samples and various hardwoods (including birch, alder, oak, and willow, as well as grape and olive) recording steppe vegetation, probably with abundant deciduous trees near a humid coast. The presence of pine, TCT (Taxodiaceae/ Cupressaceae/Taxaceae, e.g. cedar) and fir pollen suggest long-distance transport from the mountains.

4.4.3.2 Lithofacies Assemblage 2

No marine macrofossils or shell fragments and few foraminifera were found in the calcrete (unit 2a). Unit 2b marls also contained few foraminifera (Figs. 4.8, 4.9) and abundant ostracods (*Cyprideis torosa*), indicating freshwater to brackish conditions (Pint and Frenzel, 2016; De Deckker and Lord, 2017). The top of unit 2c contained relatively abundant foraminifera (Biofacies 3, dominantly *Ammonia spp.*, in cores 2 and 3; Fig. 4.8) together with abundant seeds and macroscopic charophytes. The reappearance of foraminifera at the top of unit 2c may record periodic overwash and flooding of the lagoon with marine waters during storm surge events. Hadler et al. (2013) recognized a similar 'barren' zone in core LEC 2, interpreted as a shallow limnic environment. In unit 2a, $\delta^{13}C$ values were ~0 ‰, declining to about -5 ‰ at the top of unit 2c, while $\delta^{18}O$ values were 1-2 ‰ in LA-2. These trends suggest a transition from a marine-estuarine environment to an evaporitic lake with increasing freshwater input (Peros et al., 2007). Around 52 cm in core

3, $\delta^{18}O$ values return to near 0 ‰, possibly indicating flooding of the lake by marine overwash (Fig. 4.8).

There were no marine NPP in samples from LA-2 (Fig. 4.10). Unit 2a contained abundant freshwater palynomorphs (~8400/ml, compared to 1800/ml in unit 1c and 3200/ml in unit 1b), including characteristic lacustrine taxa, such as *Botryococcus*, *Tetraedron* and *Scenedesmus* in addition to *Chara* phycomata and cysts of peridinioid dinoflagellates (McCarthy et al., 2021). The rich pollen assemblage (ca. 82000/ml, compared to 47000/ml in unit 1c and 34000/ml in unit 1b) in unit 2a, is associated with a sharp decline in forbs, and an increase in grasses accompanied by sedge pollen, indicative of a freshwater wetland environment and less arid conditions. Fungal palynomorphs were rare. The NPP assemblage in the sample unit 2b is strongly dominated by cysts/phycomata attributed to the freshwater macrophyte *Chara*, which is consistent with lacustrine marl sediments. Again, no marine NPP were found in this sample. The unit 2b sample differs from unit 2a in having a much sparser pollen assemblage, containing a higher relative abundance of conifer pollen.

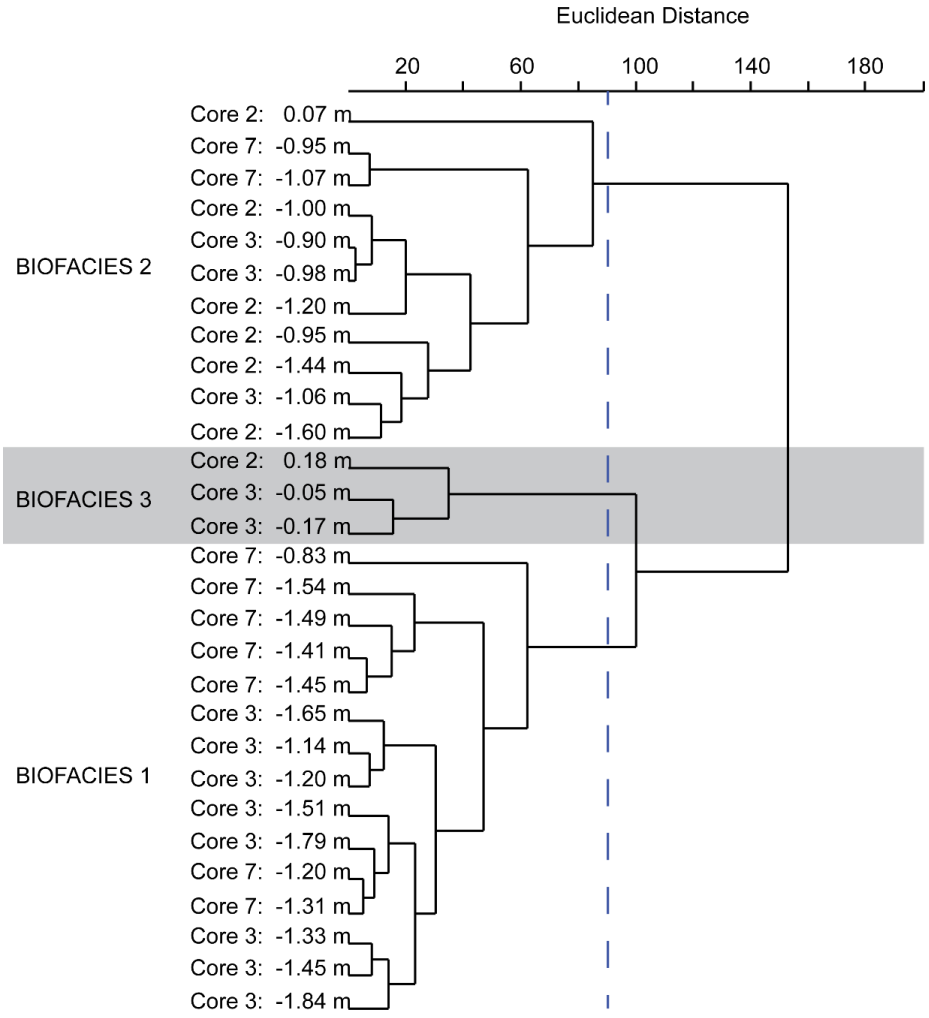

Figure 4.7: Q-mode cluster dendrogram of foraminifera with three identified biofacies.

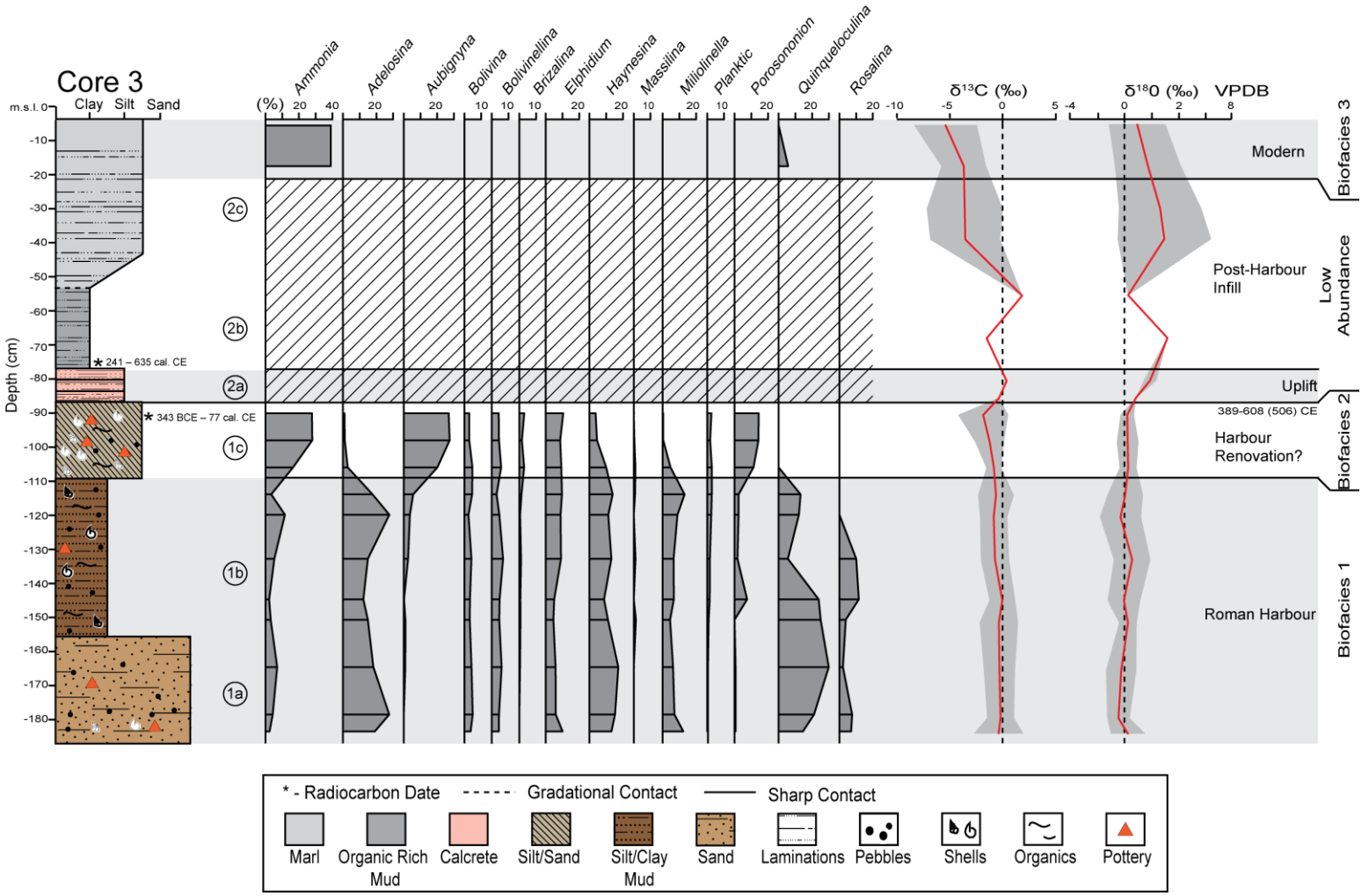

Figure 4.8: Core 3 lithostratigraphy, foraminifera fractional abundances, and stable isotope profiles. Date of LA-1 to LA-2 transition from BACON age model (Fig. 4.3). Biofacies 1 is indicative of marine environment and Biofacies 2 a more restricted, low oxygen, eutrophic environment. Biofacies 3 records marine inputs (e.g. overwash) into the lake. Isotopic values in LA-1 are indicative of normal seawater, and in LA-2, there is a shift to an evaporitic environment, with freshwater inputs.

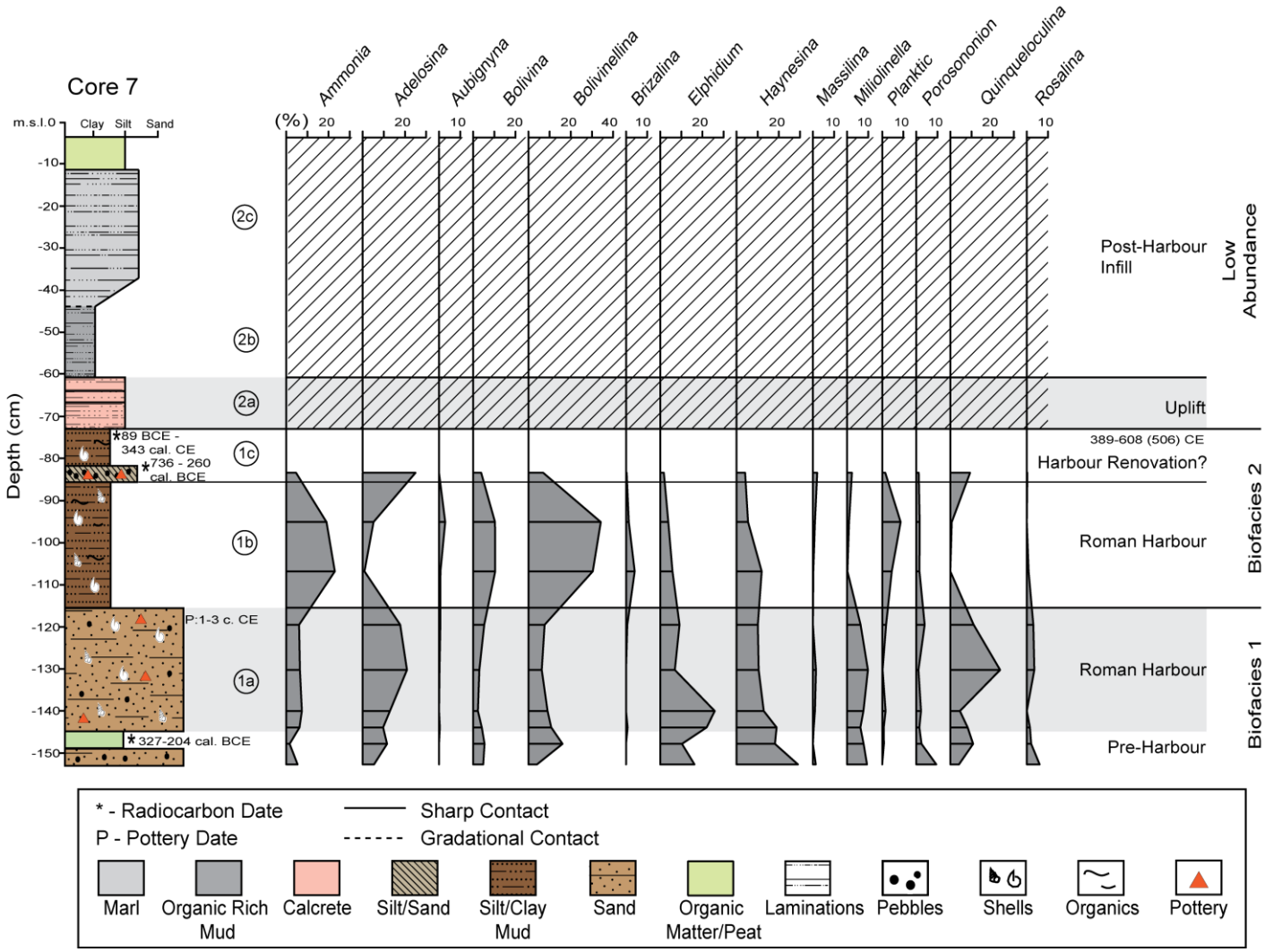

Figure 4.9: Core 7 lithostratigraphy and foraminifera fractional abundances. Date of LA-1 to LA-2 transition from BACON age model (Fig. 4.3). Biofacies 1 is indicative of marine environment and Biofacies 2 a more restricted, low oxygen, eutrophic environment.

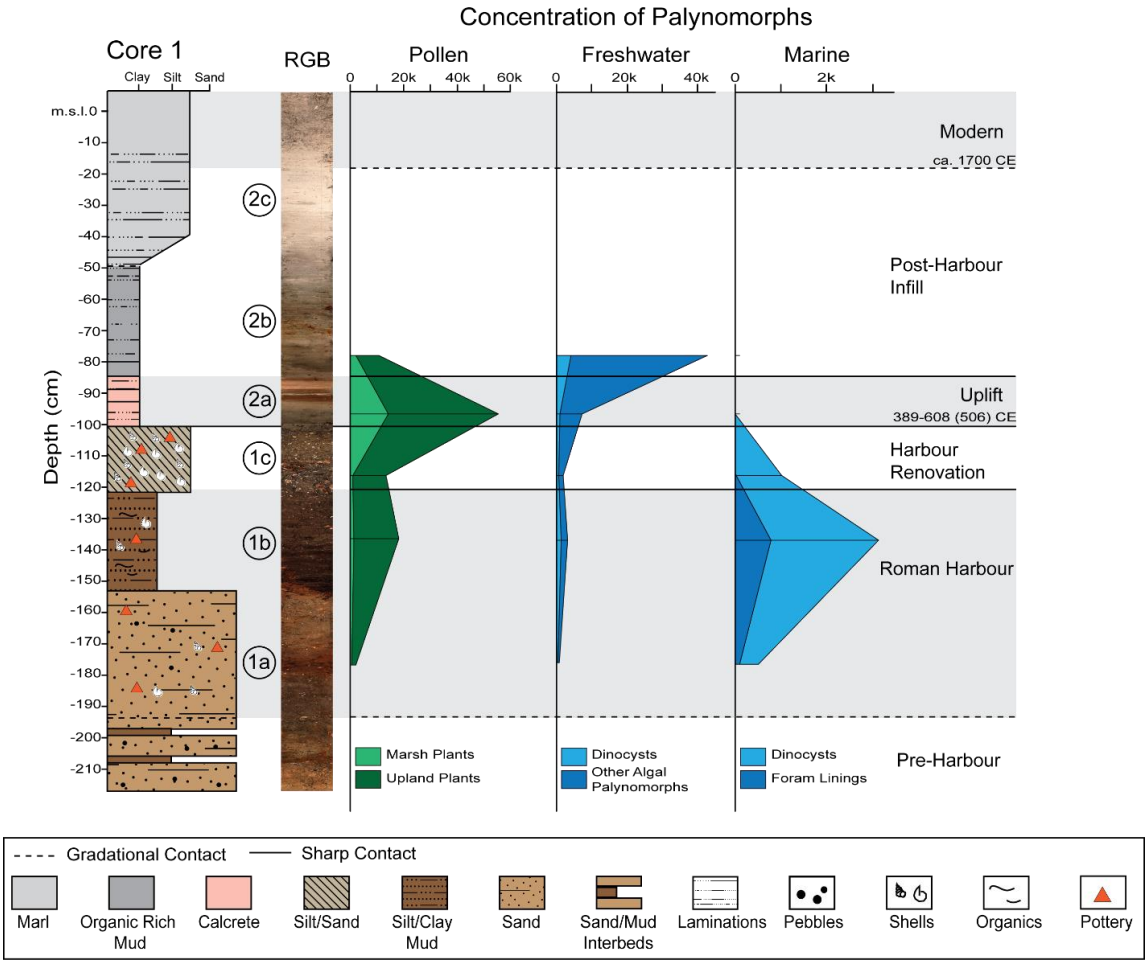

Figure 4.10: Core 1 palynomorphs. Marine palynomorphs are abundant in LA-1 and absent in LA2. Freshwater palynomorphs are abundant in LA-2. Date of LA-1 to LA-2 transition from BACON age model (Fig. 4.3).

4.5 Discussion

4.5.1 Harbour Evolution and Palaeoenvironments

The new multi-proxy dataset identifies changes in Lechaion's inner harbour environments from an active Roman harbour, through the 6th c. CE abandonment, to present day. These changes are discussed in the following sections with reference to Figure 4.11, which summarizes the changes in Lechaion's inner harbour environments.

4.5.1.1 Roman Harbour Phase (1st c. BCE to 6th c. CE)

The Roman harbour phase (Fig. 4.11a) is recorded by the interbedded sand and mud deposits of LA-1. The harbour sediments contained abundant pottery (1st-4th c. CE), rare cultivar pollen (grape and olive), and elevated Pb, all indicating human activity in the harbour and environs. The sediment accumulation rates in LA-1 were between 3-4 $mmyr^{-1}$ (Fig. 4.3), similar to other Roman harbour basins (Marriner and Morhange, 2006, 2007). Sediment accumulation rates declined sharply in the overlying LA-2 marl sequence to <1 mm yr^{-1}. The peat layer within unit 1a (core 7), dated to 327-204 cal. BCE (Figs. 4.2, 4.6), may record the closure of the entrance channel and development of a coastal wetlands prior to the 1st c. BCE Roman harbour renovation (Pallas, 1963; Rothaus, 1995; Stiros et al., 1996; Hadler et al., 2013). The basal interbedded sands and muds in core 1 (within unit 1a) likely correlate with similar facies in LEC 2, which were deposited prior to the initial Archaic harbour construction phase (Fig. 4.2).

The variability in the terrigenous element and Ca profiles in LA-1 (Figs 4.5, 4.6) suggests a mixing of marine and terrestrial sediment inputs in the harbour basin. Terrigenous sediments were likely derived from streams draining the slopes of the Acrocorinth and local surface runoff from the harbour dredge mounds (Fig. 4.1) (Morhange et al., 2012; Kolaiti et al., 2017). The element variability could also represent disturbance ('anthroturbation') due to dredging, dumping of spoils, and anchor scour of bottom sediments (Zalasiewicz et al., 2014; Turner et al., 2015). The increase in Pb, terrigenous elements, and abundant pottery refuse within unit 1c may signal the onset of dredging and harbour renovations (ca. 4th c. BCE; Kent, 1966) (Figs. 4.2, 4.5). Stable isotope values ($\delta^{18}O$ and $\delta^{13}C$; Fig. 4.8) in LA-1 fluctuated around marine values (-0.2- 0.2 ‰) (Reinhardt et al., 2001, 2003; Peros et al., 2007) and foraminiferal and palynological assemblages (Figs. 4.8-4.10) were indicative of a marine-estuarine environment. The increase in *Ammonia spp.* and *Bolivinellina spp.* and the sharp increase in green algal palynomorph abundance in Biofacies 2 indicates reduced oxygen levels and a shift to more eutrophic conditions, possibly due to renovation and restriction of the harbour basin (Murray, 1991; Gupta and Machain-Castillo, 1993).

The significant correlation of Pb with K (r = 0.66; Fig. 4.4a) indicates sorption of Pb to terrigenous clay minerals and transport to the harbour through river inputs or overland runoff. The Pb pollution signal likely records the drainage of urban effluents into the harbour basin containing contaminants from ore smelting industries and other urban sources (Delile et al., 2017). Hadler et al. (2013) previously documented Pb pollutants in the harbour sediments, which Kolaiti et al. (2017) speculated were due to the common use of lead hull sheathing on Roman ships. Delile et al. (2017), however, have argued that hull linings are unlikely sources of Pb contamination in Roman harbour sediments due to the rapid oxidation (passivation) of Pb in seawater, which limits metal leaching. Delile et al. (2017) documented a rise in Pb contamination in harbour sediments at Ostia in the 2nd c. BCE, due to the expansion of Rome's water supply system. The correspondence of Pb with pottery-rich harbour facies (i.e. units 1a, 1c; Fig. 4.5), suggests that Pb might be useful as a proxy for changes in harbour use intensity and perhaps changes in the urban footprint at Lechaion.

4.5.1.2 Harbour Uplift and Abandonment (ca. 6th c. CE)

The paraconformity surface between LA-1 and LA-2 marks a basin-wide shift from a harbour dominated by clastic sediment inputs to an evaporitic lake with mud and marl deposition (Fig. 4.11b). The elevation and basin-wide extent of the calcrete (unit 2a) at the base of LA-2 suggests that the transition occurred synchronously in the inner harbour basin and entrance channel (Fig. 4.2). We interpret this shift as a basin restriction event, which rapidly reduced water levels in the harbour, producing a shallow water, evaporitic lake environment. This rapid, basin-wide facies transition is consistent with uplift of the harbour basin during one or more vertical tectonic displacements of the Lechaion's coastline. The age-depth model constrains the transition to the 6th c. CE (Fig. 4.3), suggesting that it may be linked to one or more co-seismic uplift events that have been identified in the Gulf of Corinth during this period (section 4.5.2).

Rapid basin restriction is also indicated by a shift in all micropalaeontological, isotopic, and geochemical proxies at the base of LA-2 (Figs. 4.5, 4.6, 4.8-4.10).

Foraminifera and marine NPP were abundant in LA-1, but rapidly declined or were absent in LA-2 (also observed by Hadler et al., 2013). The onset of a lacustrine environment is indicated by the appearance of freshwater NPPs, marsh and upland pollen, and the increasing abundance of seeds and macroscopic charophytes in LA-2 (Figs. 4.8-4.10). Elemental profiles record a distinct decline in the abundance of detrital elements within unit 2a and a reduced sediment accumulation rate (<1 mm yr^{-1}), indicating an overall reduction in detrital sediment input to the lake basin (Figs. 4.3, 4.5, 4.6). Increased Sr and $\delta^{18}O$ values (Figs. 4.5, 4.6, 4.8) in LA-2, also record a shift to evaporitic, shallow water environment (Reinhardt et al., 2001, 2003; Peros et al., 2007; Ariztegui et al., 2010; Martín-Puertas et al., 2011; Koutsodendris et al., 2015).

Pb reaches maximum values with several peaks within unit 2a and declines sharply at the base of unit 2b (Fig. 4.5). The Pb inputs suggest continued human activity and effluent runoff into the lake from the Lechaion urban area during the ca. 6^{th} c. CE. The discrete peaks in Pb in unit 2a may record the concentration of heavy metal pollutants in lake sediments during evaporitic phases, or discrete pulses in Pb linked with changes in river inflow and effluent discharge rates (Fig. 4.5). Pb declines to low values within unit 2b, perhaps indicating an overall reduction in urban activity and transport of Pb to the lake from surface sources. An increase in Pb at the top of LA-2 (unit 2c; Fig. 4.5), represents a signal of 'modern' pollution from the 1700's CE onward. Hadler et al. (2013) observed similar trends in Pb at the top of their cores.

As a test for harbour basin uplift, the radiocarbon dates (Table 4.1) were plotted against the Lambeck and Purcell (2005) eustatic sea level curve for the Mediterranean, along with Roman-age dates from previous studies, to estimate the range of harbour water depths. This shows that nearly all radiocarbon samples within the Roman harbour deposits (except LEC 1/11+ HR) lie at a depth of <1 metre below, or up to 0.25 m above, the eustatic sea level curve (Fig. 4.12). Assuming that samples were deposited directly on the harbour floor and buried without later exhumation (i.e. due to dredging), their shallow depths suggest that the harbour floor has been uplifted. Our cores were collected along the axis of

the inner harbour basin and entrance channel where water depths would have been a minimum of 1-2 metres and maintained by dredging (Morhange et al., 2012; Marriner and Morhange, 2006; Boetto, 2010; Salomon et al., 2016).

The large volume of dredge spoils surrounding the inner harbour at Lechaion suggests that dredging was required to maintain a navigable channel and inner harbour basin (Fig. 4.1) (Morhange et al., 2012; Kolaiti et al., 2017). The Roman harbours of Ostia and Portus at their pinnacle (4th c. BCE to 2nd c. BCE and 3rd-5th c. CE, respectively) were navigable by ships with a draught of 4.5 m and by the late 1st c. BCE to early 1st c. CE in Ostia, water depth was approximately 1 m, rendering it unusable to larger ships (Salomon et al., 2016). At Marseilles, dredging was necessary to maintain water depths of at least 1 m (Marriner and Morhange, 2006), while at Lechaion, Boetto (2010) conjectured that the inner harbour was dredged to a depth of 2 m, removing material deposited between the Archaic and Roman harbour phases (Kolaiti et al., 2017). In core 7, the anomalously old radiocarbon age (736-260 cal. BCE) at the top of LA-1 (unit 1c; Fig. 4.2) suggests possible sediment disturbance due to dredging of the harbour entrance. The absence of the calcrete layer at the base of LA-2 in core 6 (Fig. 4.2), may also provide evidence of attempts to re-open the channel following the harbour uplift (Fig. 4.1b).

4.5.1.3 Post-harbour environment (ca. 6th c. CE to present)

Following the harbour uplift, the basin transitioned to a shallow lake environment (Fig. 4.11c), as recorded by the laminated marl and mud deposits of LA-2 and an increase in *Charophyta* and freshwater NPPs (Figs. 4.2, 4.10). The increase in detrital elements (Si, Ti, K, Fe) in unit 2b indicates an increase in terrigenous sediment influx to the basin. This is interpreted as re-establishment of fluvial inputs to the basin, as rivers adjusted to the uplifted base level on the coast. The low abundance of detrital elements in unit 2c, together with decreasing $\delta^{13}C$, elevated Sr and $\delta^{18}O$, low abundances of foraminifera, and the presence of macrophytic charophytes and *Cyprideis torosa* suggests a shoaling, evaporitic lagoon, which was gradually infilling (Figs. 4.5, 4.6, 4.8-4.10). A reversal in $\delta^{18}O$ values, around 52 cm (Fig. 4.8) may indicate increasing marine influence, perhaps due to periodic

overwash and flooding of the lake with marine water. Marine inputs to the lake are also indicated by the reappearance of *Ammonia* and *Quinqueloculina* at the top of the unit 2c (Biofacies 3) (Fig. 4.8).

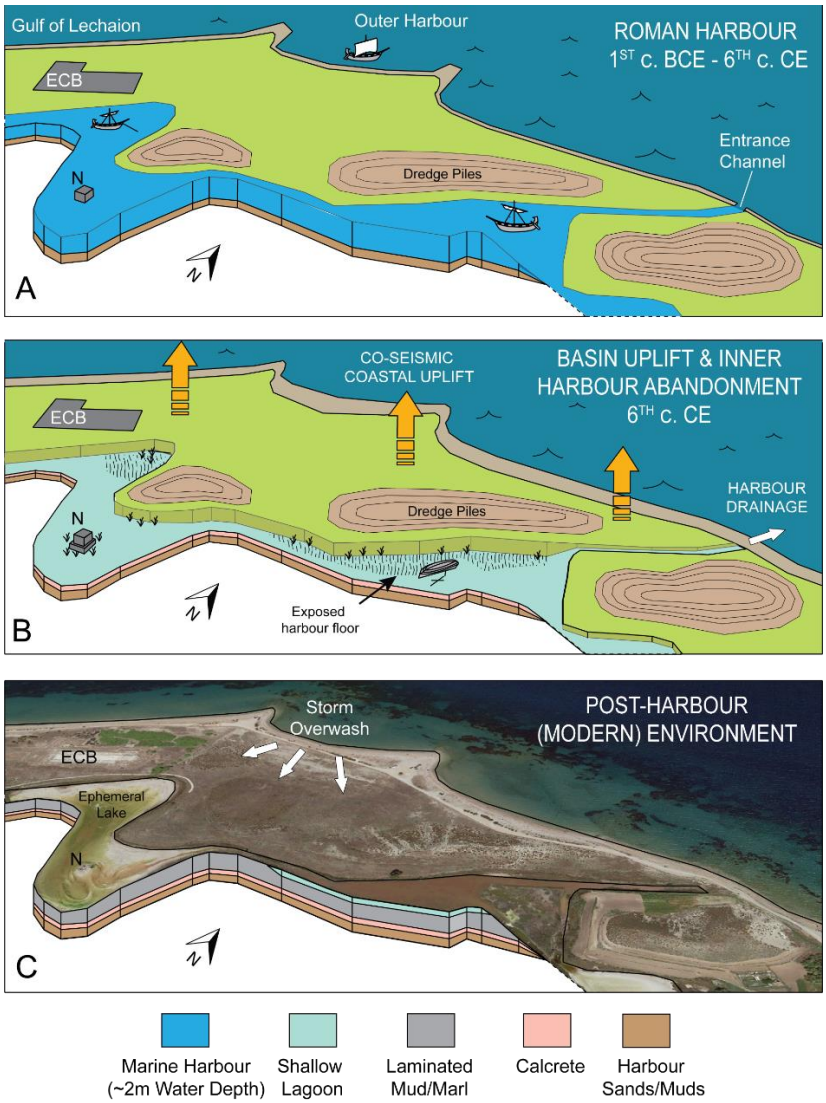

Figure 4.11: Conceptual depositional model for Lechaion's inner harbour basin. A) Roman harbour phase (1st c. BCE to 6th c. CE). Harbour basin mud and sand facies accumulated with inputs from marine, terrestrial/fluvial, anthropogenic sources. B) Coastal uplift and harbour destruction and abandonment (6th c. CE). The harbour basin was rapidly uplifted by more than 1 m, resulting in exposure of the harbour floor and shift to a shallow evaporitic lake or lagoonal environment. The rise in base level resulted in disruption of river inflow and reduction of terrigenous sediment inputs. C) Post-harbour (6^{th} c. to present) environment. Freshwater to brackish coastal lagoon with periodic incursion of marine waters by storm overwash or intermittent reflux into the harbour entrance channel. The modern-day Lechaion inner basin is occupied by ephemeral lake and fringing wetlands. ECB = Early Christian Basilica, N = Nisaki.

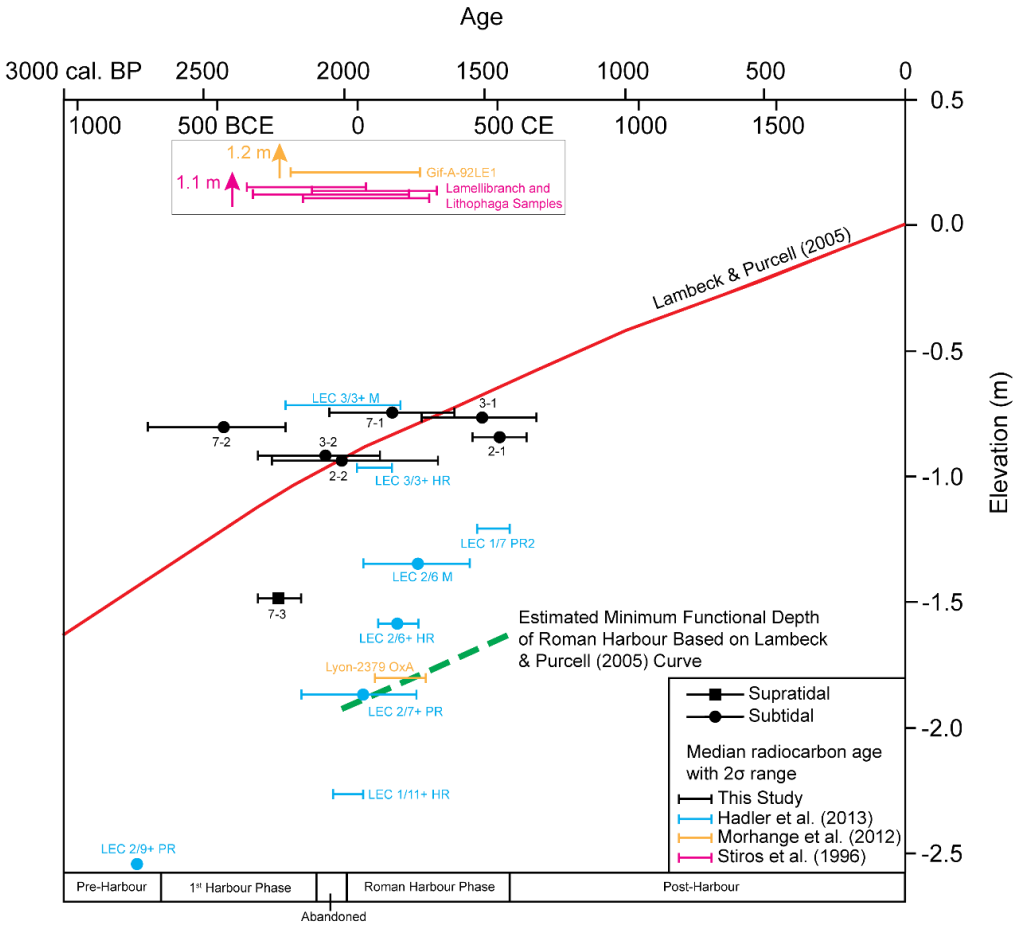

Figure 4.12: Sea level curve of Lambeck and Purcell (2005) plotted with AMS ^{14}C dates from this study and previous work (Stiros et al., 1996; Morhange et al., 2012; Hadler et al., 2013; recalibrated by Vött et al., 2018). The minimum functional harbour depth was estimated as 1 m below the Roman Period sea levels (~0.6-0.9 m below present). The Roman harbour deposits plot above the estimated minimum harbour floor elevation, providing further evidence of coastal uplift.

4.5.2 Timing and Causes of Uplift

Several previous studies have documented evidence for coastal uplift in the eastern Gulf of Corinth. Pirazzoli et al. (1994) documented raised shorelines on the Perachora Peninsula, to the north of Lechaion, and determined four separate uplift events, including ~1.1 m uplift near Heraion, with a recalibrated date of 416-688 cal. CE (Vött et al., 2018). In other recent work, Emmanouilidis et al. (2020) have documented restriction of a lagoonal environment (Aliki salt pond) by uplift of the northeast coast of the Gulf of Corinth (~1 m) between 350-550 cal. CE. The event was recorded by uplifted beachrock and a shift in the microfossil assemblage indicating a hydrologically closed evaporitic lagoon. At Lechaion,

geoarchaeological studies have documented multiple phases of subsidence and uplift (Mourtzas et al., 2014). Stiros et al. (1996) dated uplift of the harbour entrance channel to the 5th-3rd c. BCE using radiocarbon dates on *lithophaga*. Morhange et al., (2012) attributed Lechaion's abandonment to the progressive siltation and land-locking of the harbour basin, followed by a single uplift of 1.2 m in the 4th c. BCE. However, if siltation was the cause, a more gradual change in lithofacies and microfossil assemblages would be expected, as opposed to a basin-wide transition and rapid replacement of marine microfossils by freshwater palynomorphs (Figs. 4.2, 4.8-4.10). Geophysical surveys at the Early Christian Basilica (Apostolopoulos et al., 2015; Minos-Minopoulos et al., 2015) have documented liquefaction features that record damage to the temple by an earthquake in 524 CE (M_L = 6.6) and a second destructive series in 551/552 CE (M_L = 7.2), which caused irreparable damage (Pallas, 1965). According to Procopius, the 524 CE event destroyed the ancient city Corinth and caused widespread damage in the surrounding area (Papazachos and Papazachou, 2003). The 551/552 CE earthquake series caused widespread destruction (MMI = IX) over a large area of the Phokida region and significant damage at Lechaion, including the destruction of the basilica (Minos-Minopoulos et al., 2015).

Our AMS ^{14}C core chronology and age model indicate a likely middle 6th c. CE age for the uplift event (Fig. 4.3). The destructive earthquake series of 524 and 551/552 CE are the most likely candidates and have been identified as the probable cause of soil liquefaction and earthquake damage to the Early Christian Basilica (Minos-Minopoulos et al., 2015). The documented 6th c. CE uplift of the nearby Perachora Peninsula (Pirazzoli et al., 1994; Vött et al., 2018) and Aliki salt pond (Emmanouilidis et al., 2020), if caused by the same events, suggests a potential total uplift of >1 m at Lechaion. We have no way of directly measuring the magnitude of uplift, but the elevations of harbour sediments with respect to the Roman period sea level (0.6-0.9 rmsl) suggests a vertical displacement >1 m to allow for a navigable basin during the pre-uplift period (Fig. 4.12).

4.5.3 Tsunami Impacts?

The role of tsunami impacts at Lechaion has been a topic of recent debate (Kolaiti et al., 2017; Vött et al., 2018). Hadler et al. (2013) proposed three separate tsunami events (Generations 1-3) (Fig. 4.2) identified by coarse-grained sandy gravels and peaks in Ca/Fe interpreted as marine incursion events. The lowermost interbedded sands and muds in their core LEC 2 (4.74-2.56 m), were interpreted as an 8-6th c. BCE event ('Generation 1') and the gravelly sands at mid-core (1.83-1.5 rmsl) as a 1st-2nd c. CE tsunami incursion ('Generation 2') (Fig. 4.2). 'Generation 3' was described as a partly calcified sand and gravel unit with elevated Ca/Fe occurring at the base of lacustrine units in their core LEC3 (Fig. 4.1b). This third event was absent in other cores, which they attributed to dredging (Hadler et al., 2013). Kolaiti et al. (2017) in response, argued that the potential for destructive tsunamis was low in the eastern Gulf of Corinth and that the gravelly sand deposits could have been formed under a range of other natural processes. The lack of geological or historical evidence for destruction of the Early Christian Basilica by a 6th c. CE tsunami event was also cited as an objection.

The proposed 'Generation 2' tsunamite of Hadler et al. (2013) can be correlated with our unit 1a gravelly sand facies based on its stratigraphic position and lithofacies characteristics (Fig. 4.2). Our data do not show a shift in Ca/Fe or foraminifera that might identify an incursion of allochthonous marine sediment in unit 1a. The elemental data instead show an upward increase in terrigenous elements (Si, Ti, K, Fe) and Ca within unit 1a (Figs. 4.5, 4.6) and a corresponding increase in the sediment accumulation rate (2-4 mmyr^{-1}; 190-100 cm) (Fig. 4.3). The significant correlation between Ca and Si ($r = 0.63$; Fig. 4.4a) also suggests a common transport mechanism, and the hydrodynamic sorting of quartz sand and $CaCO_3$ shell materials in unit 1a, as both increase in abundance with increasing grain size. Pb shows a similar upward trend with terrigenous elements (Fig. 4.5), which together suggests an increasingly terrestrial (fluvial?) source for clastic sediments and Pb pollutants in unit 1a.

The composition and elemental geochemistry of the unit 1a (Figs. 4.5, 4.6) suggests mixing of coastal and riverine clastic sediment sources with anthropogenic inputs (e.g. ballast, pottery refuse) and some degree of modification by dredging activities. The coarse-grained texture of sand and gravel facies has been argued as evidence of 'high-energy' tsunami events (Vött et al., 2018) but can also be explained by bottom traction currents due to river inflow, tidal currents, or wave resuspension of sediments in the harbour (Plint, 2010). It can be inferred from the sinuous form of the inner harbour basin (Fig. 4.1b), that the cothon was constructed by the excavation of a pre-existing natural wetland (Morhange et al., 2012), or possibly an estuary or river channel. The harbour basin likely formed part of a wider fluvial drainage network and would have acted as a depocenter receiving stream inflow during seasonal flood events. Given the narrow harbour entrance channel and distance to the coast (~200 m) river discharge events (as opposed to overwash and storm surge) were likely the dominant source of coarse clastic sediments in the harbour infill. The thick, dredgate mounds around the basin margins are also potential local sources of coarse-grained clastic sediments (Fig. 4.1b).

Regarding the 6th c. CE 'Generation 3' tsunami event, we found no evidence for a shell-rich cemented gravels in any of our cores in association with the calcrete or the marl deposits in LA-2 (Fig. 4.2). In cores 1 and 7, a peak in Ca/Fe near the top of the calcrete (unit 2a) records a decrease in Fe and terrigenous input and a relative increase in Ca and Sr, which is clearly indicative of a shift to an evaporative lake environment. The Ca/Fe ratio in LA-2 thus tracks changes in the relative abundance of $CaCO_3$ in the marl relative to the terrigenous clastic sediment inputs and is not a useful proxy for identifying marine incursion events (i.e. tsunamis) in this environment (Figs. 4.5, 4.6).

4.6 Summary

The multi-proxy palaeoenvironmental data presented in this paper confirm the decline and abandonment of Lechaion's inner harbour in the 6th c. CE due to uplift of the harbour floor. Uplift is indicated by a basin-wide paraconformity surface and transition from a marine-estuarine harbour to a freshwater-brackish lacustrine environment. The

transition is recognized in all palaeoenvironmental proxies and the replacement of marine microfossils by abundant freshwater palynomorphs indicates a geologically rapid environmental transition (Figs. 4.5, 4.6, 4.8-4.10).

The uplift event raised the harbour entrance channel above sea level and the inner harbour basin underwent rapid restriction and hydrologic closure. In the post-uplift phase, the basin transitioned from a brackish to freshwater lake environment with periodic influx of marine waters. A decrease in detrital elements (Si, Ti, K, Fe) in the marl facies (LA-2), records a decline in terrestrial/fluvial inputs to the lake, and an associated decrease in the sediment accumulation rate. Basin restriction is also indicated by increased Sr, Ca/Fe, and a shift to positive $\delta^{18}O$ values, consistent with a shallow, evaporitic lagoonal environment. Comparison of the elevations of harbour floor deposits with the eustatic sea-level curve (Fig. 4.10) indicates that they are at too shallow a depth for a functional harbour, providing further evidence for coastal uplift (Fig. 4.12). indicated by the paraconformity at the base of the calcrete layer (Fig. 4.2).

While we cannot rule out tsunami impacts on Lechaion during its long history, our multi-proxy dataset does not provide evidence supporting those described by Hadler et al. (2013) and Vött et al. (2018). The coarse-grained ‘high-energy’ sand and gravel facies purported to be 1^{st}-2^{nd} c. BCE and 6^{th} c. CE tsunami events could have been produced by a range of sedimentary processes, including unidirectional river inflow, tidal currents, and wave-generated oscillatory currents in the harbour basin. Further, we found no evidence for cemented gravels identified as a 6^{th} c. CE tsunami event in our core transect, which spans the entire inner harbour basin and entrance channel (Fig. 4.1b). We have also demonstrated that a peak in Ca/Fe, argued as evidence for tsunami incursions can be explained by a decrease in detrital Fe inputs to the basin following harbour uplift.

4.7 References

Apostolopoulos, G., Minos-Minopoulos, D., Pavlopoulos, K., 2015. Geophysical investigation for the detection of liquefaction phenomena in an archaeological site, Lechaion, Greece. Geophysics 80(4), 105-117.

Ariztegui, D., Anselmetti, F.S., Robbiani, J.M., Bernasconi, S.M., Brati, E., Gilli, A., Lehmann, M. F., 2010. Natural and human-induced environmental change in southern Albania for the last 300 years—Constraints from the Lake Butrint sedimentary record. Global and Planetary Change 71(3-4), 183-192.

Armijo, R., Meyer, B.G.C.P., King, G.C.P., Rigo, A., Papanastassiou, D., 1996. Quaternary evolution of the Corinth Rift and its implications for the Late Cenozoic evolution of the Aegean. Geophysical Journal International 126(1), 11-53.

Arp, G., Reimer, A., Reitner, J., 1999. Calcification in cyanobacterial biofilms of alkaline salt lakes. European Journal of Phycology 34(4), 393-403.

Avallone, A., Briole, P., Agatza-Balodimou, A.M., Billiris, H., Charade, O., Mitsakaki, C., Nercessian, A., Papazissi, K., Paradissis, D., Veis G., 2004. Analysis of eleven years of deformation measured by GPS in the Corinth Rift Laboratory area. Comptes Rendus Geoscience 336(4-5), 301-311.

Berntsson, A., Rosqvist, G.C., Velle, G., 2014. Late-Holocene temperature and precipitation changes in Vindelfjällen, mid-western Swedish Lapland, inferred from chironomid and geochemical data. The Holocene 24(1), 78-92.

Blaauw, M., Christen, J.A., 2011. Flexible paleoclimate age-depth models using an autoregressive gamma process. Bayesian analysis 6(3), 457-474.

Boetto, G., 2010. Le port vu de la mer: l'apport de l'archéologie navale à l'étude des ports antiques. Bolletino Archeol Online, 112-128.

Boyce, J.I., Reinhardt, E.G., Goodman, B.N., 2009. Magnetic detection of ship ballast deposits and anchorage sites in King Herod's Roman harbour, Caesarea Maritima, Israel. Journal of Archaeological Science 36(7), 1516-1526.

Boyce, J.I., Reinhardt, E.G., Raban, A., Pozza, M.R., 2004. Marine magnetic survey of a submerged Roman harbour, Caesarea Maritima, Israel. International Journal of Nautical Archaeology 33(1), 122-136.

Briole, P., Rigo, A., Lyon-Caen, H., Ruegg, J.C., Papazissi, K., Mitsakaki, C., Balodimou, A., Veis, G., Hatzfeld, D., Deschamps, A., 2000. Active deformation of the Corinth rift, Greece: results from repeated Global Positioning System surveys between 1990 and 1995. Journal of Geophysical Research: Solid Earth 105(B11), 25605-25625.

Chagas, A.A., Webb, G.E., Burne, R.V., Southam, G., 2016. Modern lacustrine microbialites: towards a synthesis of aqueous and carbonate geochemistry and mineralogy. Earth-Science Reviews 162, 338-363.

Chen, J., Lee, J.H., 2014. Current progress on the geological record of microbialites and microbial carbonates. Acta Geologica Sinica-English Edition 88(1), 260-275.

Costa, P.J., Gelfenbaum, G., Dawson, S., La Selle, S., Milne, F., Cascalho, J., Ponte Lira, C., Andrade, C., Freitas, M.C., Jaffe B., 2018. The application of microtextural and heavy mineral analysis to discriminate between storm and tsunami deposits. Geological Society, London, Special Publications 456(1), 167-190.

Croudace, I.W., Rindby, A., Rothwell, R.G., 2006. ITRAX: description and evaluation of a new multi-function X-ray core scanner. Geological Society, London, Special Publications 267(1), 51-63.

Davies, S.J., Lamb, H.F., Roberts, S.J., 2015. Micro-XRF core scanning in palaeolimnology: recent developments. In: Croudace, I.W., Rothwell, R.G. (Eds), Micro-XRF Studies of Sediment Cores, Springer, pp. 189-226.

De Deckker, P., Lord, A., 2017. Cyprideis torosa: a model organism for the Ostracoda?. Journal of Micropalaeontology 36(1), 3-6.

Delile, H., Keenan-Jones, D., Blichert-Toft, J., Goiran, J.P., Arnaud-Godet, F., Albarède, F., 2017. Rome's urban history inferred from Pb-contaminated waters trapped in its ancient harbor basins. Proceedings of the National Academy of Sciences 114(38), 10059-10064.

Dulski, P., Brauer, A., Mangili, C., 2015. Combined µ-XRF and microfacies techniques for lake sediment analyses. In: Croudace, I.W., Rothwell, R.G. (Eds), Micro-XRF Studies of Sediment Cores, Springer, pp. 25-102.

Emmanouilidis, A., Unkel, I., Triantaphyllou, M., Avramidis, P., 2020. Late-Holocene coastal depositional environments and climate changes in the Gulf of Corinth, Greece. The Holocene 30(1), 77-89.

Fishbein, E., Patterson, R.T., 1993. Error-weighted maximum likelihood (EWML): a new statistically based method to cluster quantitative micropaleontological data. Journal of Paleontology, 475-486.

Faegri, K., Kaland, P.E., Krzywinski, K., 1989. Textbook of pollen analysis (No. Ed. 4). John Wiley & Sons Ltd.

Freytet, P., Plet, A., 1996. Modern freshwater microbial carbonates: the Phormidium stromatolites (tufa-travertine) of southeastern Burgundy (Paris Basin, France). Facies 34(1), 219-237.

Goff, J., McFadgen, B.G., Chagué-Goff, C., 2004. Sedimentary differences between the 2002 Easter storm and the 15th-century Okoropunga tsunami, southeastern North Island, New Zealand. Marine geology 204(1-2), 235-250.

Goodman, B.N., Reinhardt, E.G., Dey, H.W., Boyce, J.I., Schwarcz, H.P., Sahoğlu, V., Erkanal, H., Artzy, M., 2008. Evidence for Holocene marine transgression and shoreline progradation due to barrier development in Iskele, Bay of Izmir, Turkey. Journal of Coastal Research 24(5), 1269-1280.

Goodman, B.N., Reinhardt, E.G., Dey, H.W., Boyce, J.I., Schwarcz, H.P., Sahoğlu, V., Erkanal, H., Artzy, M., 2009. Multi-proxy geoarchaeological study redefines understanding of the paleocoastlines and ancient harbours of Liman Tepe (Iskele, Turkey). Terra Nova 21(2), 97-104.

Goodman-Tchernov, B.N., Austin Jr, J.A., 2015. Deterioration of Israel's Caesarea Maritima's ancient harbor linked to repeated tsunami events identified in geophysical mapping of offshore stratigraphy. Journal of Archaeological Science: Reports 3, 444-454.

Gregory, B.R., Patterson, R.T., Reinhardt, E.G., Galloway, J.M., Roe, H.M., 2019. An evaluation of methodologies for calibrating Itrax X-ray fluorescence counts with ICP-MS concentration data for discrete sediment samples. Chemical Geology 521, 12-27.

Gupta, B.K.S., Machain-Castillo, M.L., 1993. Benthic foraminifera in oxygen-poor habitats. Marine Micropaleontology 20(3-4), 183-201.

Hadler, H., Vött, A., Koster, B., Mathes-Schmidt, M., Mattern, T., Ntageretzis, K., Reicherter, K., Sakellariou, D., Willershäuser, T., 2011. Lechaion, the ancient harbour of Corinth (Peloponnese, Greece) destroyed by tsunamigenic impact. In Proceedings of the 2nd INQUA-IGCP-467 International Workshop on Active Tectonics, Earthquake Geology, Archaeology and Engineeering, Corinth Greece.

Hadler, H., Vött, A., Koster, B., Mathes-Schmidt, M., Mattern, T., Ntageretzis, K., Reicherter, K., Willershäuser, T., 2013. Multiple late-Holocene tsunami landfall in the eastern Gulf of Corinth recorded in the palaeotsunami geo-archive at Lechaion, harbour of ancient Corinth (Peloponnese, Greece). Zeitschrift für Geomorphologie 57(4), 139-180.

Hadler, H., Vött, A., Fischer, P., Ludwig, S., Heinzelmann, M., Rohn, C., 2015. Temple-complex post-dates tsunami deposits found in the ancient harbour basin of Ostia (Rome, Italy). Journal of Archaeological Science 61, 78-89.

Jahnert, R.J., Collins, L.B., 2013. Controls on microbial activity and tidal flat evolution in Shark Bay, Western Australia. Sedimentology 60(4), 1071-1099.

Jarvis, S., Croudace, I.W., Rothwell, R.G., 2015. Parameter optimisation for the ITRAX core scanner. In: Croudace, I.W., Rothwell, R.G. (Eds), Micro-XRF Studies of Sediment Cores, Springer, pp. 535-562.

Kent, J.H., 1966. The Inscriptions: 1926 –1950. – Amer. School Classic. Stud. Athens, Athens, pp. 64.

Keraudren, B., Sorel, D., 1987. The terraces of Corinth (Greece)—A detailed record of eustatic sea-level variations during the last 500,000 years. Marine Geology 77(1-2), 99-107.

Kolaiti, E., Mourtzas, N.D., 2016. Upper Holocene sea level changes in the west Saronic Gulf, Greece. Quaternary International 401, 71-90.

Kolaiti, E., Papadopoulos, G.A., Morhange, C., Vacchi, M., Triantafyllou, I., Mourtzas, N.D., 2017. Palaeoenvironmental evolution of the ancient harbor of Lechaion (Corinth Gulf, Greece): Were changes driven by human impacts and gradual coastal processes or catastrophic tsunamis? Marine Geology 392, 105-121.

Kortekaas, S., Dawson, A.G., 2007. Distinguishing tsunami and storm deposits: an example from Martinhal, SW Portugal. Sedimentary Geology 200(3-4), 208-221.

Koster, B., Hadler, H., Vött, A., Reicherter, K., 2013. Application of GPR for visualising spatial distribution and internal structures of tsunami deposits–Case studies from Spain and Greece. Zeitschrift für Geomorphologie, Supplementary Issues 57(4), 29-45.

Koutsodendris, A., Brauer, A., Zacharias, I., Putyrskaya, V., Klemt, E., Sangiorgi, F., Pross, J., 2015. Ecosystem response to human-and climate-induced environmental stress on an anoxic coastal lagoon (Etoliko, Greece) since 1930 AD. Journal of Paleolimnology 53(3), 255-270.

Kourkoumelis, D., Lovén, B., Micha, D., Athanasopoulos, P., 2017. Lechaion Harbour Project, 2013-2014", 2nd Sc. Meeting "Archaeological works in Peloponnese", Oct. 2017.

Kylander, M.E., Ampel, L., Wohlfarth, B., Veres, D., 2011. High-resolution X-ray fluorescence core scanning analysis of Les Echets (France) sedimentary sequence: new insights from chemical proxies. Journal of Quaternary Science 26, 109-117.

Lambeck, K., Purcell, A., 2005. Sea-level change in the Mediterranean Sea since the LGM: model predictions for tectonically stable areas. Quaternary Science Reviews 24(18-19), 1969-1988.

Le Roux, G., Véron, A., Morhange, C., 2005. Lead pollution in the ancient harbours of Marseilles. Méditerranée. Revue géographique des pays méditerranéens/Journal of Mediterranean geography (104), 31-35.

Marret, F., 1993. Les effects de l'acétolyse sur les assemblages des kystes de dinoflagellés. Palynosci. 2, 267-272.

Marriner, N., Morhange, C., 2007. Geoscience of ancient Mediterranean harbours. Earth-Science Reviews 80(3-4), 137-194.

Marriner, N., Morhange, C., Doumet-Serhal, C., 2006. Geoarchaeology of Sidon's ancient harbours, Phoenicia. Journal of Archaeological Science 33(11), 1514-1535.

Marriner, N., Morhange, C., Goiran, J.P., 2010. Coastal and ancient harbour geoarchaeology. Geology Today 26(1), 21-27.

Marriner, N., Morhange, C., Kaniewski, D., Carayon, N., 2014. Ancient harbour infrastructure in the Levant: tracking the birth and rise of new forms of anthropogenic pressure. Scientific Reports 4(1), 1-11.

Marshall, M.H., Lamb, H.F., Huws, D., Davies, S.J., Bates, R., Bloemendal, J., Boyle, J., Leng, M.J., Umer, M., Bryant, C., 2011. Late Pleistocene and Holocene drought events at Lake Tana, the source of the Blue Nile. Global and Planetary Change 78(3-4), 147-161.

Martín-Puertas, C., Valero-Garcés, B. L., Mata, M. P., Moreno, A., Giralt, S., Martínez-Ruiz, F., Jiménez-Espejo, F., 2011. Geochemical processes in a Mediterranean Lake: a high-resolution study of the last 4,000 years in Zonar Lake, southern Spain. Journal of Paleolimnology 46(3), 405-421.

McCarthy, F.M.C., Pilkington, P.M., Volik, O., Heyde, A., Cocker, S.L., 2021. Non-pollen palynomorphs in freshwater sediments and their palaeolimnological potential and selected applications. Geological Society, London, Special Publications 511.

Minos-Minopoulos, D., Pavlopoulos, K., Apostolopoulos, G., Lekkas, E., Dominey-Howes, D., 2015. Liquefaction features at an archaeological site: Investigations of past earthquake events at the Early Christian Basilica, Ancient Lechaion Harbour, Corinth, Greece. Tectonophysics 658, 74-90.

Morhange, C., Blanc, F., Schmitt-Mercury, S., Bourcier, M., Carbonel, P., Oberlin, C., Prone, A., Vivent, D., Hesnard, A., 2003. Stratigraphy of late-Holocene deposits

of the ancient harbour of Marseilles, southern France. The Holocene 13(4), 593-604.

Morhange, C., Laborel, J., Hesnard, A., 2001. Changes of relative sea level during the past 5000 years in the ancient harbor of Marseilles, Southern France. Palaeogeography, palaeoclimatology, palaeoecology 166(3-4), 319-329.

Morhange, C., Marriner, N., 2010. Mind the (stratigraphic) gap: Roman dredging in ancient Mediterranean harbours. Bollettino di Archeologia online, 23-32.

Morhange, C., Pirazzoli, P.A., Evelpidou, N., Marriner, N., 2012. Late Holocene Tectonic Uplift and the Silting Up of Lechaion, the Western Harbor of Ancient Corinth, Greece. Geoarchaeology 27(3), 278-283.

Morton, R.A., Gelfenbaum, G., Jaffe, B.E., 2007. Physical criteria for distinguishing sandy tsunami and storm deposits using modern examples. Sedimentary Geology 200(3-4), 184-207.

Mourtzas, N.D., Kissas, C., Kolaiti, E., 2014. Archaeological and geomorphological indicators of the historical sea level changes and the related palaeogeographical reconstruction of the ancient foreharbour of Lechaion, East Corinth Gulf (Greece). Quaternary International 332, 151-171.

Mourtzas, N.D., Marinos, P.G., 1994. Upper Holocene sea-level changes: Paleogeographic evolution and its impact on coastal archaeological sites and monuments. Environmental Geology 23(1), 1-13.

Murray, J.W., 1991. Ecology and distribution of benthic foraminifera. Biology of foraminifera, 221-254.

Nixon, F.C., Reinhardt, E.G., Rothaus, R., 2009. Foraminifera and tidal notches: dating neotectonic events at Korphos, Greece. Marine Geology 257(1-4), 41-53.

Pallas, D.I., 1965. Excavation of the early Christian basilica of Lechaion. Praktika, 1958(PAE 1958), 119-134.

Papadopoulos, G.A., 2003. Tsunami hazard in the Eastern Mediterranean: strong earthquakes and tsunamis in the Corinth Gulf, Central Greece. Natural hazards 29(3), 437-464.

Papadopoulos, G.A., Kijko, A., 1991. Maximum likelihood estimation of earthquake hazard parameters in the Aegean area from mixed data. Tectonophysics 185(3-4), 277-294.

Papazachos, B.C., Papazachou, C., 2003. The earthquakes of Greece. Ziti publications.

Patterson, R.T., Fishbein, E., 1989. Re-examination of the statistical methods used to determine the number of point counts needed for micropaleontological quantitative research. Journal of Paleontology 63, 245-248.

Peros, M.C., Reinhardt, E.G., Schwarcz, H.P., Davis, A.M., 2007. High-resolution paleosalinity reconstruction from Laguna de la Leche, north coastal Cuba, using Sr, O, and C isotopes. Palaeogeography, Palaeoclimatology, Palaeoecology 245(3-4), 535-550.

Pint, A., Frenzel, P., 2017. Ostracod fauna associated with Cyprideis torosa–an overview. Journal of Micropalaeontology 36(1), 113-119.

Pirazzoli, P.A., Stiros, S.C., Arnold, M., Laborel, J., Laborel-Deguen, F., Papageorgiou, S., 1994. Episodic uplift deduced from Holocene shorelines in the Perachora Peninsula, Corinth area, Greece. Tectonophysics 229(3-4), 201-209.

Plint, A.G., James, N.P., Dalrymple, R.W., 2010. Wave-and storm-dominated shoreline and shallow-marine systems. Facies models 4, 167-200.

Reinhardt, E.G., Fitton, R.J., Schwarcz, H.P., 2003. Isotopic (Sr, O, C) indicators of salinity and taphonomy in marginal marine systems. The Journal of Foraminiferal Research 33(3), 262-272.

Reinhardt, E.G., Goodman, B.N., Boyce, J.I., Lopez, G., van Hengstum, P., Rink, W.J., Mart, Y., Raban, A., 2006. The tsunami of 13 December AD 115 and the destruction of Herod the Great's harbor at Caesarea Maritima, Israel. Geology 34(12), 1061-1064.

Reinhardt, E.G., Raban, A., 1999. Destruction of Herod the Great's harbor at Caesarea Maritima, Israel—geoarchaeological evidence. Geology 27(9), 811-814.

Reinhardt, E.G., Stanley, D.J., Schwarcz, H.P., 2001. Human-induced desalinization of Manzala Lagoon, Nile Delta, Egypt: evidence from isotopic analysis of benthic invertebrates. Journal of Coastal Research 17, 431-442.

Riddick, N.L., Volik, O., McCarthy, F.M.G., Danesh, D.C., 2017. The effect of acetolysis on desmids. Palynology, 41(2): 171-179

Rothaus, R., 1995. Lechaion, western port of Corinth: A preliminary archaeology and history. Oxford Journal of archaeology 14(3), 293-306.

Rothwell, R.G., Croudace, I.W., 2015. Micro-XRF studies of sediment cores: a perspective on capability and application in the environmental sciences. In: Croudace, I.W., Rothwell, R.G. (Eds), Micro-XRF Studies of Sediment Cores, Springer, pp. 1-24

Salomon, F., Keay, S., Carayon, N., Goiran, J.P., 2016. The development and characteristics of ancient harbours—applying the PADM chart to the case studies of Ostia and Portus. PLoS One 11(9), e0162587.

Scott, D.B., Hermelin, J.O.R., 1993. A device for precision splitting of micropaleontological samples in liquid suspension. Journal of Paleontology 67(1), 151-154.

Scott, D.B., Medioli, F.S., Schafer, C.T., 2007. Monitoring in coastal environments using foraminifera and thecamoebian indicators. Cambridge University Press.

Shaw, J., 1969. A Foundation in the Inner Harbour at Lechaeum. American Journal of Archaeology 73, 370-372

Smith, D.G., 1987. A mini-vibracoring system. Journal of Sedimentary Research 57(4), 757-758.

Stiros, S.C., 1995. The 1953 seismic surface fault: implications for the modeling of the Sousaki (Corinth area, Greece) geothermal field. Journal of Geodynamics 20(2), 167-180.

Stiros, S.C., 2020. Coastal subsidence, destruction layers and earthquakes from an underwater archaeological excavation: Kenchreai, eastern harbour of Roman Corinth, Greece. Mediterranean Geoscience Reviews, 1-15.

Stiros, S.C., Blackman, D.J., 2014. Seismic coastal uplift and subsidence in Rhodes Island, Aegean Arc: evidence from an uplifted ancient harbour. Tectonophysics 611, 114-120.

Stiros, S., Pirazzoli, P., Rothaus, R., Papageorgiou, S., Laborel, J., Arnold, M., 1996. On the date of construction of Lechaion, western harbor of ancient Corinth, Greece. Geoarchaeology 11(3), 251-263.

Stock, F., Pint, A., Horejs, B., Ladstätter, S., Brückner, H., 2013. In search of the harbours: New evidence of Late Roman and Byzantine harbours of Ephesus. Quaternary International 312, 57-69.

Stuiver, M., Reimer, P.J., Reimer, R.W., 2019. CALIB 7.1 [WWW program] at http://calib.org

Turner, J.N., Jones, A.F., Brewer, P.A., Macklin, M.G., Rassner, S.M., 2015. Micro-XRF applications in fluvial sedimentary environments of Britain and Ireland: progress and prospects. In: Croudace, I.W., Rothwell, R.G. (Eds), Micro-XRF Studies of Sediment Cores, Springer, pp. 227-265.

Turner, J.A., Leeder, M.R., Andrews, J.E., Rowe, P.J., Van Calsteren, P., Thomas, L., 2010. Testing rival tectonic uplift models for the Lechaion Gulf in the Gulf of Corinth rift. Journal of the Geological Society 167(6), 1237-1250.

Tuttle, M.P., Ruffman, A., Anderson, T., Jeter, H., 2004. Distinguishing tsunami from storm deposits in eastern North America: the 1929 Grand Banks tsunami versus the 1991 Halloween storm. Seismological Research Letters 75(1), 117-131.

Vita-Finzi, C., King, G.C.P., 1985. The seismicity, geomorphology and structural evolution of the Corinth area of Greece. Philosophical Transactions of the Royal Society of London. Series A, Mathematical and Physical Sciences 314(1530), 379-407.

Vött, A., Bareth, G., Brückner, H., Lang, F., Sakellariou, D., Hadler, H., Ntageretzis, K., Willershäuser, T., 2011. Olympia's harbour site Pheia (Elis, Western Peloponnese, Greece) destroyed by tsunami impact. Die Erde 142(3), 259-288.

Vött, A., Hadler, H., Koster, B., Matthes-Schmidt, M., Röbke, B. R., Willershäuser, T., Reicherter, K., 2018. Returning to the facts: Response to the refusal of tsunami traces in the ancient harbour of Lechaion (Gulf of Corinth, Greece) by 'non-catastrophists'–Reaffirmed evidence of harbour destruction by. Zeitschrift für Geomorphologie, 275-302.

Zalasiewicz, J., Waters, C.N., Williams, M., 2014. Human bioturbation, and the subterranean landscape of the Anthropocene. Anthropocene 6, 3-9.

CHAPTER 5: Summary

This thesis has documented the results of multi-proxy geoarchaeological investigations at two long-occupied coastal archaeological sites, with the following aims: 1) To investigate Liman Tepe's submerged palaeolandscape, reconstruct changes in coastal palaeoenvironments and palaeogeography, and to identify areas of underwater archaeological potential; 2) To investigate prehistoric proto-harbour development at Liman Tepe-Clazomenae and the transition to the semi-artificial Iron Age harbour; 3) To document the timing and probable causes of abandonment of Lechaion's inner Roman harbour basin.

In Chapter 2, the prehistoric (Neolithic to Bronze Age) coastal palaeogeography and palaeoshoreline positions were reconstructed at Liman Tepe, to identify potential harbouring areas and to predict areas of underwater archaeological potential. The shoreline positions were estimated from the 6700 BCE (middle Neolithic) to the Early Bronze phase of settlement. This paper represents the first *quantitative* palaeoshoreline reconstruction completed at Liman Tepe. Past work had identified the transitions from transgressive to high-stand systems tract and several locations for proto-harbouring were identified based on land core data. This study was the first to reconstruct the Neolithic to Chalcolithic palaeogeography using offshore marine core data. It is also the first in the Aegean to employ a large multi-parameter core and geophysical database and back-stripping methods to estimate palaeoshoreline positions and to reconstruct the coastal palaeogeography. Based on these reconstructions' areas of potential archaeological significance for the Chalcolithic and Neolithic were identified. Importantly, back-stripping was done using both sedimentological and geophysical data, which improves on previous approaches which use the modern coastal topography or a geophysical defined datum (Westley et al., 2014).

The methodology outlined in Chapter 2 can be adapted more broadly in the Mediterranean for palaeoshoreline reconstruction and identification of areas of archaeological potential. The approach is well-suited for investigation of shallow coastal

areas in the Aegean, where former coastal embayments and river valleys (i.e. rias) were rapidly inundated by post-glacial sea level rise. The Bay of Izmir and other rias on the western coast of Turkey are good targets for this approach due to their long settlement history and shallow water depths. This thesis has also demonstrated that micro-XRF core scanning (µ-XRF-CS) can be used as a core correlation tool and for rapid identification of marine transgressive surfaces. Palaeogeographic reconstruction, as demonstrated herein, is an important first step in the identification of submerged early settlement and anchorage sites, which are underrepresented in the archaeological record (Knapp and Demesticha, 2016).

Chapter 3 documented the results of the first comprehensive geoarchaeological investigation of Clazomenae's Archaic harbour. µ-XRF-CS and chemofacies analysis were also evaluated as high-resolution tools for reconstructing harbour palaeoenvironments. The results document the transition from a shoreface environment to sheltered embayment and finally engineered harbour. The sheltered embayment would have been suitable for Middle-Late Bronze Age anchorage, protected by a tombolo and possible early man-made structure. This represents the first known geoarchaeological record of a proto-harbour to engineered harbour transition in the Aegean, and here, evidence for the earliest man-made Aegean harbour structure is presented (additional work required for confirmation). Side-scan imaging of the Archaic harbour revealed linear (wall?) features present on a submerged headland, running parallel to the eastern breakwater, which divided the Archaic harbour into two basins. Using µ-XRF-CS, a distinctive Ti/Ca chemofacies was identified in the harbour sediments, which may record a possible drought event at the Late Bronze Age to Iron Age transition (Greek Dark Age). This adds to the growing body of literature suggesting a climatic component to the social upheaval in the eastern Mediterranean at the end of the Bronze Age (Drake, 2012; Kaniewski et al., 2013, 2015; Finné et al., 2017). Conventional sampling techniques may have missed or misinterpreted this event.

Chapter 4 examined the timing and causes of the decline and abandonment of Lechaion's Roman (cothon) harbour and evaluated geoarchaeological evidence for tectonic

processes on the coast, including proposed tsunami impacts. Using a multi-proxy approach, the transition from an estuarine-marine Roman harbour to a subaerially exposed, brackish-freshwater environment was documented. The environmental change is recorded by a basin-wide paraconformity surface representing a rapid shift in multiple proxies, including microfossils (foraminifera, NPP's), stable isotopes, sedimentary facies, and micro-XRF geochemistry. The cause of this rapid shift was determined to be uplift, coinciding with earthquakes in the 6th c. CE. Prior to this study, the cause of abandonment was widely debated (uplift and siltation, subsidence; Mourtzas and Marinos, 1994; Rothaus, 1995; Morhange et al., 2012; Mourtzas et al., 2014; Kolaiti et al., 2017). The harbour decline had also been attributed to a tsunami (Hadler et al., 2013; Vött et al., 2018), however no evidence of this was observed. The use of µ-XRF-CS and geochemical data was instrumental in this study in identifying the palaeoenvironmental and hydrologic changes caused by the uplift of Lechaion's inner harbour. Unlike previous geoarchaeological studies on this site, this investigation was basin-wide and therefore, able to identify that the environmental shift was both rapid and occurred at roughly the same elevation across the inner harbour, consistent with uplift. The collection of many cores across the study site is important for determining if a facies change is 'localized' or the result of a larger event.

5.1 Future Work

5.1.1 Liman Tepe-Clazomenae

Chapter 2 identified a number of submerged landscape features (e.g. relict river channels, palaeoshorelines) and sites with high archaeological potential that will require future investigation. The thickness of Holocene sediment (>4 m) overlying Neolithic age deposits is a significant challenge for the future investigation of the underwater prehistoric archaeological potential at Liman Tepe. Exploration of palaeoshorelines and other submerged landscapes features (e.g. palaeo-river channels, promontories) will require the use of geophysical survey methods (e.g. magnetics, sub-bottom seismic profiling) and further underwater coring work to locate sites of interest. Once sites have been identified, underwater archaeological excavation and dredging work will be a logistical challenge due

to the water depths (up to 15 m). Exploration for sites on the west side of Karantina Island can be aided by marine geophysical mapping (e.g. magnetic surveys) and sub-bottom profiling of the Holocene sediment thickness. Such work could offer additional insights into the coastal palaeogeography and the location of potential buried archaeological sites. Seismic survey work was not completed as part of this study due to heavy wave conditions on the western side of the island, which prevented seismic surveys using surface towed instruments. Seismic surveys could be optimized using an AUV (autonomous underwater vehicle) equipped with sub-bottom profiling and side-scan sonars that can be deployed under rough sea states (Hrvoic, 2014). Such systems can be programmed to systematically grid map the seabed and sub-bottom stratigraphy with high-resolution imaging capabilities (Missiaen et al., 2017; Batchelor et al., 2020). Diver reconnaissance of the palaeoshoreline and palaeochannel margins (e.g. using diver propulsion systems) could also target areas where active slumping of Holocene deposits may have exposed outcrops and prehistoric cultural materials.

Further investigations in Archaic harbour are required to confirm findings from Chapter 3. Archaeological excavation should continue down to the Middle-Late Bronze Age 'proto-harbour' to confirm it was used for anchorage. Additional coring is required to obtain the southern extent of the basin and to document Archaic-present evolution of the harbour (including abandonment). Further investigation of Archaic harbour architecture is also required to confirm dates of construction and if the magnetic anomalies buried in the eastern breakwater represent an earlier structure.

Few climate records exist for western Anatolia, despite evidence that climate change was a likely cause of prehistoric settlement disruption and abandonment. For example, the 4.2 ka BP megadrought has been linked to disruption of Chalcolithic societies at a number of sites in western Anatolia, including Liman Tepe (Massa and Şahoğlu, 2015). Development of a long-term climate record is needed to determine the role of climate change and resilience of Liman Tepe (Massa and Şahoğlu, 2015), while aiding in interpretation of future climate impacts. Ti/Ca records from the Archaic harbour basin,

suggest the potential for using Ti records as a proxy for tracking changes in settlement activity and land use change. The apparent correlation of Ti/Ca with climate proxies (e.g. Sofular cave stable isotopes; Fleitmann et al., 2009) suggest a possible climate driver for change at Liman Tepe during the Greek Dark Age. Future planned work at Liman Tepe will investigate climate signals in marine harbour sediments and also in terrestrial lacustrine and alluvial deposits that have been identified on land in the areas surrounding the archaeological site. This work will include coring, lithochemofacies analysis (e.g. terrigenous element flux) and pollen studies to investigate the land record of settlement changes and possible climate impacts of the 4.2 ka BP and 3.2 Ka BP drought events. This work will be carried out in tandem with archaeological studies of the Chalcolithic-Bronze Age settlements archaeo-botanical data.

5.1.2 Lechaion

The new multi-proxy results from Lechaion have confirmed the abandonment of the inner harbour basin in the 6th c. CE as a result uplift of the basin (Chapter 4). The magnitude of uplift has been estimated at more than 1 m, which is consistent with the scale of uplift events recorded for Perachora Peninsula (Pirazzoli et al., 1994). Further work is needed at Lechaion to constrain the magnitude of the uplift event and its timing in the mid-6th c. CE. Our available core database indicates some inversion of radiocarbon dates, most likely due to sediment disturbance (e.g. dredging). Further radiocarbon dating of the deposits above and below the paraconformity (i.e. calcrete) will assist in constraining and confirming the 6th c. CE age of the transition.

The large volume of dredge spoils around the inner harbour attests to the dredging activities at Lechaion. Dredgate piles are up to 17 m in thickness and likely contain evidence of dredging over many centuries. Coring and analysis of the sedimentology and pottery contents of the dredge mounds may provide a record of dredging and harbour renovation activities. The dredge spoils also likely contain ship ballast materials, including far-travelled ‘exotic’ lithologies that can be used to reconstruct trade networks (e.g. McManus, 1999; Boyce et al., 2009).

5.2 References

Batchelor, C.L., Montelli, A., Ottesen, D., Evans, J., Dowdeswell, E. K., Christie, F.D., Dowdeswell, J.A., 2020. New insights into the formation of submarine glacial landforms from high-resolution Autonomous Underwater Vehicle data. Geomorphology 370, 107396.

Boyce, J.I., Reinhardt, E.G., Goodman, B.N., 2009. Magnetic detection of ship ballast deposits and anchorage sites in King Herod's Roman harbour, Caesarea Maritima, Israel. Journal of Archaeological Science 36(7), 1516-1526.

Drake, B.L., 2012. The influence of climatic change on the Late Bronze Age Collapse and the Greek Dark Ages. Journal of Archaeological Science 39(6), 1862-1870.

Finné, M., Holmgren, K., Shen, C.C., Hu, H.M., Boyd, M., Stocker, S., 2017. Late Bronze Age climate change and the destruction of the Mycenaean Palace of Nestor at Pylos. PloS one 12(12), e0189447.

Fleitmann, D., Cheng, H., Badertscher, S., Edwards, R.L., Mudelsee, M., Göktürk, O.M., Fankhauser, A., Pickering, R., Raible, C.C., Matter, A., Kramers J., Tüysüz, O. (2009). Timing and climatic impact of Greenland interstadials recorded in stalagmites from northern Turkey. Geophysical Research Letters 36(19).

Hadler, H., Vött, A., Koster, B., Mathes-Schmidt, M., Mattern, T., Ntageretzis, K., Reicherter, K., Willershäuser, T., 2013. Multiple late-Holocene tsunami landfall in the eastern Gulf of Corinth recorded in the palaeotsunami geo-archive at Lechaion, harbour of ancient Corinth (Peloponnese, Greece). Zeitschrift für Geomorphologie 57(4), 139-180.

Hrvoic, D., 2014. High-resolution near-shore geophysical survey using an autonomous underwater vehicle (AUV) with integrated magnetometer and side-scan sonar. Unpublished Master's thesis, McMaster University

Kaniewski, D., Guiot, J., Van Campo, E., 2015. Drought and societal collapse 3200 years ago in the Eastern Mediterranean: a review. Wiley Interdisciplinary Reviews: Climate Change 6(4), 369-382.

Kaniewski, D., Van Campo, E., Guiot, J., Le Burel, S., Otto, T., Baeteman, C., 2013. Environmental roots of the Late Bronze Age crisis. PloS one 8(8), e71004.

Knapp, A.B., Demesticha S., 2016. Mediterranean connections: maritime transport containers and seaborne trade in the Bronze and Early Iron Ages, Taylor & Francis.

Kolaiti, E., Papadopoulos, G.A., Morhange, C., Vacchi, M., Triantafyllou, I., Mourtzas, N.D., 2017. Palaeoenvironmental evolution of the ancient harbor of Lechaion (Corinth Gulf, Greece): Were changes driven by human impacts and gradual coastal processes or catastrophic tsunamis? Marine Geology 392, 105-121.

Massa, M., Şahoğlu, V., 2015. The 4.2 ka climatic event in west and central Anatolia: combining palaeoclimatic proxies and archaeological data. In: Meller, H., Risch, R., Jung, R., Arz, R.W. (Eds), 2200 BC - A climatic breakdown as a cause for the collapse of the old world? Halle, 61-78.

McManus, J., 1999. Coarse estuary mouth ballast gravel deposits: a sourcing case history. Estuarine, Coastal and Shelf Science 48(6), 677-682.

Missiaen, T., Sakellariou, D., Flemming, N.C., 2017. Survey strategies and techniques in underwater geoarchaeological research: An overview with emphasis on prehistoric sites. In: Bailey, G., Harff, J., Sakellariou, D. (Eds), Under the sea: Archaeology and palaeolandscapes of the continental shelf, 21-37.

Morhange, C., Pirazzoli, P.A., Evelpidou, N., Marriner, N., 2012. Late Holocene Tectonic Uplift and the Silting Up of Lechaion, the Western Harbor of Ancient Corinth, Greece. Geoarchaeology 27(3), 278-283.

Mourtzas, N.D., Kissas, C., Kolaiti, E., 2014. Archaeological and geomorphological indicators of the historical sea level changes and the related palaeogeographical reconstruction of the ancient foreharbour of Lechaion, East Corinth Gulf (Greece). Quaternary International 332, 151-171.

Mourtzas, N.D., Marinos, P.G., 1994. Upper Holocene sea-level changes: Paleogeographic evolution and its impact on coastal archaeological sites and monuments. Environmental Geology 23(1), 1-13.

Pirazzoli, P.A., Stiros, S.C., Arnold, M., Laborel, J., Laborel-Deguen, F., Papageorgiou, S., 1994. Episodic uplift deduced from Holocene shorelines in the Perachora Peninsula, Corinth area, Greece. Tectonophysics 229(3-4), 201-209.

Rothaus, R., 1995. Lechaion, western port of Corinth: A preliminary archaeology and history. Oxford Journal of archaeology 14(3), 293-306.

Vött, A., Hadler, H., Koster, B., Matthes-Schmidt, M., Röbke, B. R., Willershäuser, T., Reicherter, K., 2018. Returning to the facts: Response to the refusal of tsunami traces in the ancient harbour of Lechaion (Gulf of Corinth, Greece) by 'non-catastrophists'–Reaffirmed evidence of harbour destruction by. Zeitschrift für Geomorphologie, 275-302.

Westley, K., Plets, R., Quinn, R., 2014. Holocene paleo-geographic reconstructions of the Ramore Head area, Northern Ireland, using geophysical and geotechnical data: Paleo-landscape mapping and archaeological implications. Geoarchaeology 29(6), 411-430.

APPENDIX A: Liman Tepe Chronology

Time Period		Start (c. BCE)	End (c. BCE)
Neolithic		8000	4800
Chalcolithic		4800	3000
Bronze Age	Early	3000	2000
	Middle	2000	1600
	Late	1600	1200
Iron Age	Dark Age	1200	1000
	Geometric	1000	700
	Archaic	700	450
	Classical/Hellenistic	450	114
Roman Period		114	400 CE

Sahoglu, personal communication, September 2017

APPENDIX B: Liman Tepe New Marine Cores

#	Date	UTM (35S)		Water Depth (m)	Tube Length (m)	Stickup (m)	Length (m)	Compaction (m)	Cor. Length (m)
		E	N						
17-2	Aug 2017	480616	4246245	4.53	2.46	0.26	1.666	0.535	2.20
17-3	Aug 2017	480320	4246244	~4.75	3.00	**	1.174	0.280	1.45
17-4	Aug 2017	480142	4246406	7.89	3.00	0.57	1.759	0.672	2.43
17-6	Aug 2017	480480	4246270	4.65	3.00	0.23	1.478	1.292	2.77
17-7	Aug 2017	480597	4246315	5.95	6.00	3.00	2.858	0.142	3.00
17-8	Aug 2017	480314	4246445	7.61	6.00	2.72	2.368	0.913	3.28
17-9	Aug 2017	480329	4246246	~4.8	3.00	1.20	1.520	0.280	1.80
18-2	Oct 2018	480471	4247054	10.81	3.59	0.50	2.122	0.968	3.09
18-3	Oct 2018	480804	4246670	6.91	6.00	3.50	1.876	0.624	2.50
18-4	Oct 2018	481150	4246319	7.02	6.00	1.30	3.646	1.054	4.70
18-5	Oct 2018	480202	4246647	11.05	6.00	2.00	3.108	0.892	4.00
18-6	Oct 2018	480669	4246748	10.84	6.00	1.40	3.353	1.247	4.60
18-7	Oct 2018	480154	4246518	8.67	5.80	1.50	2.745	1.555	4.30
18-8	Oct 2018	480642	4246540	9.37	6.00	1.45	3.261	1.289	4.55
19-1	Aug 2019	480323	4246153	4.50	6.00	2.79	1.949	1.266	3.21
19-2	Aug 2019	480332	4246239	5.08	3.60	1.47	1.835	0.296	2.13
19-3	Aug 2019	480310	4247147	11.77	6.00	2.05	2.600	1.351	3.95
19-4	Aug 2019	480793	4246949	7.99	6.00	1.31	3.570	1.120	4.69
19-5	Aug 2019	480146	4246408	7.95	6.00	1.92	2.870	1.210	4.08
19-6	Aug 2019	480422	4246601	9.89	6.00	1.39	3.470	1.140	4.61

** Core 17-3 compaction assumed similar to 17-9 (based on proximity)

Cores 17-3, 17-9, and 19-1 collected in Trench E/F

APPENDIX C: Liman Tepe Foraminifera Data

LT-2017-9: Foraminifera Abundances

Original Depth (cm):	10	30	50	70	90	110	130	150
Corr. Depth (cm):	12	36	59	83	107	130	154	178
Specimens Counted:	342	266	170	211	156	144	161	125
Specimens /cc:	1094	851	544	675	499	461	258	400
Genera	**Abundances (%)**							
Ammonia	14.0	15.4	10.6	12.3	13.5	20.8	8.7	14.4
Elphidium	13.2	19.9	27.6	21.8	25.6	20.1	36.0	25.6
Haynesina	2.3	8.6	5.3	8.1	9.0	11.8	14.3	5.6
Cibicides	2.3	4.1	2.9	4.3	6.4	4.9	2.5	4.0
Rosalina	7.6	21.8	14.1	9.5	14.1	6.3	7.5	6.4
Adelosina	9.1	1.9	2.9	3.8	3.2	1.4	3.1	4.8
Quinqueloculina	18.4	6.8	16.5	17.1	13.5	13.9	13.0	18.4
Spiroloculina	6.4	1.1	2.4	4.7	0.6	1.4	0.6	0.0
Vertebralina	0.0	1.1	1.8	0.5	1.3	0.7	0.0	2.4
Triloculina	2.0	2.6	1.8	0.9	2.6	2.8	2.5	2.4
Miliolinella	4.7	0.0	1.8	3.3	1.3	2.8	3.7	5.6
Bolivina	10.8	12.4	6.5	10.4	5.8	6.9	4.3	6.4
Bulimina	1.5	0.8	1.8	0.5	1.3	1.4	0.0	0.0
Textularina	0.6	1.1	1.2	0.9	1.3	0.7	1.2	1.6
Planorbulina	3.2	1.5	2.4	0.5	0.6	3.5	2.5	1.6
Peneroplis	0.0	0.8	0.0	0.0	0.0	0.0	0.0	0.0
Ammodiscus	3.8	0.0	0.6	1.4	0.0	0.7	0.0	0.8

Collected by N. Riddick

LT-2019-1: Foraminifera Abundances

Original Depth (cm):	21	50	81	111	126	136	145	153	160	185
Corr. Depth (cm):	35	83	134	184	208	224	239	251	263	305
Specimens Counted:	274	117	155	166	107	135	101	105	0	0
Specimens /cc:	877	374	496	531	342	432	162	84	0	0
Genera	**Abundances (%)**									
Ammonia	18.6	16.2	19.4	15.7	19.6	21.5	19.8	21.0	0.0	0.0
Elphidium	29.9	35.9	28.4	31.9	19.6	23.0	24.8	30.5	0.0	0.0
Haynesina	0.0	7.7	4.5	6.0	14.0	7.4	13.9	11.4	0.0	0.0
Cibicides	0.4	3.4	7.1	4.8	4.7	0.7	0.0	1.9	0.0	0.0
Rosalina	4.4	2.6	10.3	6.6	8.4	12.6	9.9	6.7	0.0	0.0
Adelosina	4.7	7.7	2.6	3.6	1.9	3.7	5.0	3.8	0.0	0.0
Quinqueloculina	25.2	9.4	14.2	15.1	14.0	17.8	14.9	14.3	0.0	0.0
Spiroloculina	1.1	0.9	1.3	0.6	0.9	2.2	1.0	1.0	0.0	0.0
Vertebralina	0.0	0.0	1.3	0.6	0.9	0.0	2.0	0.0	0.0	0.0
Triloculina	2.2	3.4	0.6	3.6	1.9	0.7	0.0	1.0	0.0	0.0
Miliolinella	1.8	1.7	0.6	3.0	2.8	3.0	2.0	1.9	0.0	0.0
Bolivina	9.5	4.3	4.5	4.2	6.5	4.4	5.9	4.8	0.0	0.0
Bulimina	0.0	0.0	0.6	0.6	1.9	0.7	1.0	1.9	0.0	0.0
Textularina	0.4	2.6	1.3	2.4	0.9	0.7	0.0	0.0	0.0	0.0
Planorbulina	0.7	1.7	1.3	0.6	1.9	0.7	0.0	0.0	0.0	0.0
Peneroplis	0.4	1.7	1.3	0.0	0.0	0.0	0.0	0.0	0.0	0.0
Ammodiscus	0.7	0.9	0.6	0.6	0.0	0.7	0.0	0.0	0.0	0.0

Collected by N. Riddick

Foraminifera Abundances

	LT-2018-5				LT-2019-3		LT-2019-4			
Original Depth (cm):	280	290	300	310	225	260	299	311	323	330
Corr. Depth (cm):	361	373	387	399	343	395	421	438	455	465
Specimens Counted:	314	125	3	2	374	0	115	127	114	2
Specimens /cc:	1155	597	619	638	368	406	368	406	122	3
Genera	**Abundances (%)**									
Ammonia	18.2	27.2	0.0	100.0	23.1	0.0	30.4	22.8	27.2	100.0
Elphidium	35.0	53.6	66.7	0.0	37.6	0.0	40.9	29.1	25.4	0.0
Haynesina	10.2	7.2	33.3	0.0	8.5	0.0	8.7	14.2	10.5	0.0
Cibicides	0.0	0.0	0.0	0.0	1.7	0.0	0.9	0.0	0.0	0.0
Rosalina	1.6	1.6	0.0	0.0	0.0	0.0	0.9	5.5	8.8	0.0
Adelosina	5.1	1.6	0.0	0.0	1.7	0.0	1.7	3.1	0.0	0.0
Quinqueloculina	17.8	2.4	0.0	0.0	9.4	0.0	8.7	7.9	11.4	0.0
Spiroloculina	0.6	0.0	0.0	0.0	2.6	0.0	0.9	3.1	1.8	0.0
Vertebralina	0.0	0.0	0.0	0.0	0.0	0.0	0.0	0.0	0.0	0.0
Triloculina	0.0	0.0	0.0	0.0	0.9	0.0	0.9	0.8	1.8	0.0
Miliolinella	1.6	0.8	0.0	0.0	2.6	0.0	0.9	3.1	2.6	0.0
Bolivina	8.6	4.0	0.0	0.0	9.4	0.0	5.2	7.1	8.8	0.0
Bulimina	0.0	0.8	0.0	0.0	0.0	0.0	0.0	0.8	0.0	0.0
Textularina	1.0	0.8	0.0	0.0	0.9	0.0	0.0	1.6	1.8	0.0
Planorbulina	0.0	0.0	0.0	0.0	0.0	0.0	0.0	0.0	0.0	0.0
Peneroplis	0.0	0.0	0.0	0.0	0.0	0.0	0.0	0.0	0.0	0.0
Ammodiscus	0.3	0.0	0.0	0.0	1.7	0.0	0.0	0.8	0.0	0.0

Collected by N. Riddick

G-22: Foraminifera Abundances (Goodman et al., 2009)

Depth (mbsl):	3.1		4.6		4.9		5.2		5.2		5.7		6.1		6.5		7.2		7.8	
Specimens Counted:	388		297		425		888		286		285		296		300		300		292	
Specimens /cc:	621		464		340		496		203		57		631		960		640		156	
Species	**%**	**±**	**%**	**±**	**%**	**±**	**%**	**±**	**%**	**±**	**%**	**±**	**%**	**±**	**%**	**±**	**%**	**±**	**%**	**±**
A. rhomboidalis	0.0	0.0	0.7	0.9	0.0	0.0	0.3	0.4	4.5	2.4	0.0	0.0	1.7	1.5	3.0	1.9	1.7	1.4	1.4	1.3
Adelosina sp B	0.5	0.7	0.3	0.7	0.0	0.0	0.0	0.0	0.0	0.0	0.0	0.0	2.0	1.6	0.3	0.7	0.0	0.0	1.0	1.2
Adelosina sp C	0.0	0.0	0.3	0.7	0.0	0.0	0.3	0.4	0.0	0.0	0.0	0.0	0.0	0.0	0.0	0.0	0.0	0.0	0.0	0.0
Adelosina sp E	0.3	0.5	0.3	0.7	0.0	0.0	0.0	0.0	0.0	0.0	0.0	0.0	0.0	0.0	0.0	0.0	0.0	0.0	0.3	0.7
Adelosina sp F	1.5	1.2	0.0	0.0	0.0	0.0	0.0	0.0	0.0	0.0	0.0	0.0	0.0	0.0	0.0	0.0	0.0	0.0	0.0	0.0
Adelosina sp G	0.0	0.0	0.0	0.0	0.0	0.0	0.0	0.0	0.0	0.0	0.0	0.0	0.0	0.0	1.7	1.4	0.0	0.0	0.3	0.7
A. carinata0striata	0.8	0.9	0.0	0.0	3.5	1.8	0.0	0.0	0.0	0.0	0.0	0.0	0.0	0.0	0.3	0.7	0.0	0.0	0.0	0.0
A. cliarensis	0.0	0.0	0.0	0.0	0.0	0.0	0.1	0.2	0.0	0.0	0.0	0.0	0.0	0.0	0.0	0.0	0.0	0.0	0.0	0.0
A. dubia	0.0	0.0	3.0	1.9	0.0	0.0	0.0	0.0	0.0	0.0	0.0	0.0	0.7	0.9	0.0	0.0	0.3	0.7	0.7	0.9
A. elegans	0.0	0.0	0.7	0.9	0.0	0.0	0.1	0.2	0.7	1.0	0.0	0.0	0.0	0.0	0.0	0.0	0.0	0.0	0.0	0.0
A. jugosa	0.0	0.0	0.7	0.9	0.0	0.0	0.0	0.0	0.0	0.0	0.0	0.0	0.0	0.0	1.7	1.4	2.0	1.6	0.3	0.7
A. mediterranus	0.3	0.5	0.7	0.9	0.0	0.0	1.1	0.7	0.0	0.0	0.0	0.0	1.0	1.1	2.0	1.6	0.3	0.7	2.7	1.9
Affinetra plan	0.8	0.9	1.0	1.1	0.0	0.0	0.0	0.0	0.0	0.0	0.0	0.0	0.0	0.0	0.0	0.0	0.0	0.0	0.3	0.7
Affinetra sp A	0.0	0.0	0.0	0.0	0.0	0.0	0.0	0.0	0.7	1.0	0.0	0.0	0.0	0.0	0.0	0.0	0.0	0.0	0.0	0.0
Ammonia sp A	0.3	0.5	0.0	0.0	1.2	1.0	0.0	0.0	0.0	0.0	0.0	0.0	0.0	0.0	0.0	0.0	0.0	0.0	0.0	0.0
A. convexa	0.0	0.0	0.0	0.0	1.2	1.0	1.4	0.8	0.0	0.0	0.0	0.0	0.3	0.7	0.0	0.0	0.0	0.0	0.0	0.0
A. inflata	0.8	0.9	0.3	0.7	0.0	0.0	0.0	0.0	0.0	0.0	0.0	0.0	0.0	0.0	0.0	0.0	0.0	0.0	0.0	0.0
A. parkinsoniana	5.9	2.3	5.7	2.6	0.0	0.0	2.3	1.0	3.5	2.1	3.2	2.0	2.0	1.6	0.0	0.0	3.7	2.1	2.4	1.8
A. parkinsoniana 'tepida'	0.0	0.0	0.0	0.0	4.7	2.0	0.0	0.0	0.0	0.0	1.8	1.5	0.0	0.0	0.0	0.0	0.0	0.0	0.0	0.0
A. carinata	0.0	0.0	0.0	0.0	0.0	0.0	0.0	0.0	0.0	0.0	0.0	0.0	0.0	0.0	0.0	0.0	0.0	0.0	0.0	0.0
A. mamilla	0.5	0.7	0.7	0.9	0.7	0.8	3.0	1.1	2.8	1.9	4.2	2.3	1.4	1.3	2.0	1.6	0.7	0.9	1.0	1.2
Bolivina sp A	0.0	0.0	0.0	0.0	6.4	2.3	0.0	0.0	0.0	0.0	0.0	0.0	0.0	0.0	0.0	0.0	0.0	0.0	0.0	0.0
B. pseudoplicata	2.1	1.4	0.7	0.9	0.0	0.0	4.4	1.3	11.2	3.7	12.3	3.8	8.8	3.2	0.0	0.0	4.3	2.3	2.1	1.6
B. striatula	0.3	0.5	0.0	0.0	0.0	0.0	1.2	0.7	11.2	3.7	4.9	2.5	8.8	3.2	5.0	2.5	3.7	2.1	1.0	1.2
Buccela sp A	0.5	0.7	0.0	0.0	1.9	1.3	0.3	0.4	0.0	0.0	2.1	1.7	0.0	0.0	9.3	3.3	1.0	1.1	0.3	0.7
Bulimina sp A	0.0	0.0	0.0	0.0	0.0	0.0	0.0	0.0	0.0	0.0	0.7	1.0	0.0	0.0	0.0	0.0	0.0	0.0	0.0	0.0
B. margarit	0.0	0.0	0.0	0.0	0.0	0.0	0.0	0.0	0.0	0.0	0.7	1.0	0.0	0.0	0.0	0.0	0.0	0.0	0.0	0.0
C. polymorpha	0.8	0.9	0.0	0.0	0.0	0.0	0.2	0.3	0.0	0.0	0.0	0.0	0.3	0.7	4.0	2.2	0.0	0.0	2.1	1.6
Cassidella sp A	0.0	0.0	0.0	0.0	1.9	1.3	0.3	0.4	1.4	1.4	0.0	0.0	2.7	1.8	0.7	0.9	1.3	1.3	0.0	0.0
C. constricta silica	0.0	0.0	0.0	0.0	0.0	0.0	0.0	0.0	0.0	0.0	2.1	1.7	0.0	0.0	0.0	0.0	0.0	0.0	0.0	0.0
Cibicidella sp A	0.0	0.0	0.0	0.0	0.0	0.0	0.0	0.0	0.0	0.0	0.0	0.0	0.0	0.0	0.0	0.0	0.0	0.0	0.0	0.0
C. variabilis	1.5	1.2	3.7	2.1	0.0	0.0	1.2	0.7	0.0	0.0	0.0	0.0	0.0	0.0	2.0	1.6	0.0	0.0	1.4	1.3
Cibicides sp A	0.0	0.0	0.3	0.7	0.0	0.0	0.0	0.0	0.0	0.0	0.0	0.0	1.7	1.5	2.0	1.6	0.0	0.0	0.0	0.0
C. advenum	0.0	0.0	0.0	0.0	0.0	0.0	0.0	0.0	0.0	0.0	0.0	0.0	0.0	0.0	2.0	1.6	0.0	0.0	0.0	0.0
C. pseudolobatula	0.0	0.0	2.4	1.7	0.5	0.7	0.3	0.4	0.3	0.7	4.2	2.3	1.0	1.1	1.3	1.3	0.7	0.9	1.0	1.2

G-22: Foraminifera Abundances (Goodman et al., 2009), Cont.

Depth (mbsl):	3.1		4.6		4.9		5.2		5.2		5.7		6.1		6.5		7.2		7.8	
Specimens Counted:	388		297		425		888		286		285		296		300		300		292	
Specimens /cc:	621		464		340		496		203		57		631		960		640		156	
Species	**%**	**±**	**%**	**±**	**%**	**±**	**%**	**±**	**%**	**±**	**%**	**±**	**%**	**±**	**%**	**±**	**%**	**±**	**%**	**±**
C. refulgens	1.0	1.0	2.0	1.6	1.6	1.2	3.0	1.1	5.6	2.7	0.0	0.0	6.1	2.7	2.0	1.6	2.3	1.7	2.1	1.6
C. foliacea	0.3	0.5	3.4	2.1	1.6	1.2	0.1	0.2	0.0	0.0	0.0	0.0	0.0	0.0	0.3	0.7	0.0	0.0	0.0	0.0
Cycloforina sp A	0.0	0.0	0.0	0.0	0.0	0.0	0.0	0.0	0.0	0.0	0.0	0.0	0.0	0.0	0.0	0.0	1.0	1.1	0.7	0.9
Cycloforina sp C	0.0	0.0	0.0	0.0	0.0	0.0	0.0	0.0	0.0	0.0	0.0	0.0	0.7	0.9	0.0	0.0	0.0	0.0	0.0	0.0
Cycloforina sp E	0.5	0.7	0.3	0.7	0.0	0.0	0.1	0.2	0.0	0.0	0.0	0.0	0.0	0.0	0.0	0.0	0.0	0.0	0.0	0.0
C. colomi	0.0	0.0	0.0	0.0	0.0	0.0	0.0	0.0	0.0	0.0	0.0	0.0	0.0	0.0	0.0	0.0	2.0	1.6	3.4	2.1
Cymbaloporetta sp A	0.0	0.0	0.0	0.0	0.0	0.0	0.2	0.3	0.0	0.0	0.0	0.0	0.7	0.9	0.0	0.0	0.0	0.0	0.0	0.0
Elphidium sp A	0.0	0.0	0.0	0.0	0.7	0.8	0.1	0.2	0.0	0.0	1.4	1.4	0.0	0.0	0.0	0.0	0.0	0.0	0.0	0.0
Elphidium sp C	0.0	0.0	0.0	0.0	1.6	1.2	0.0	0.0	0.0	0.0	0.0	0.0	0.0	0.0	0.0	0.0	0.0	0.0	0.0	0.0
Elphidium sp D	0.0	0.0	0.0	0.0	0.5	0.7	0.0	0.0	0.0	0.0	0.0	0.0	0.0	0.0	0.0	0.0	0.0	0.0	0.0	0.0
Elphidium sp F	0.0	0.0	0.0	0.0	2.1	1.4	0.0	0.0	0.0	0.0	0.7	1.0	0.0	0.0	0.0	0.0	0.0	0.0	0.0	0.0
Elphidium sp G	0.0	0.0	0.0	0.0	0.0	0.0	0.0	0.0	0.0	0.0	4.2	2.3	0.0	0.0	0.0	0.0	0.0	0.0	0.0	0.0
E. aculeatum	1.3	1.1	0.0	0.0	0.0	0.0	0.1	0.2	1.4	1.4	1.8	1.5	1.0	1.1	0.0	0.0	1.3	1.3	0.0	0.0
E. advenum	3.6	1.9	4.0	2.2	5.2	2.1	0.3	0.4	1.7	1.5	4.6	2.4	0.0	0.0	2.0	1.6	1.0	1.1	2.4	1.8
E. crispum	0.0	0.0	0.0	0.0	0.0	0.0	0.0	0.0	0.0	0.0	3.2	2.0	1.7	1.5	0.0	0.0	0.0	0.0	0.0	0.0
E. gerthi	0.0	0.0	0.0	0.0	0.5	0.7	0.0	0.0	0.0	0.0	0.0	0.0	0.0	0.0	0.0	0.0	0.0	0.0	0.0	0.0
E. jenseni	1.5	1.2	5.1	2.5	0.0	0.0	3.5	1.2	1.4	1.4	2.1	1.7	6.1	2.7	1.3	1.3	1.0	1.1	2.7	1.9
E. macellum	5.7	2.3	2.4	1.7	3.3	1.7	3.4	1.2	4.9	2.5	4.2	2.3	2.0	1.6	2.0	1.6	2.0	1.6	2.4	1.8
E. translucens	1.8	1.3	1.0	1.1	1.4	1.1	3.0	1.1	12.2	3.8	2.8	1.9	2.0	1.6	1.7	1.4	1.3	1.3	1.7	1.5
E. punctatus	0.0	0.0	0.0	0.0	0.0	0.0	0.0	0.0	0.0	0.0	1.1	1.2	0.0	0.0	0.0	0.0	0.3	0.7	1.7	1.5
Eponides sp A	4.9	2.1	0.7	0.9	4.2	1.9	1.7	0.8	0.3	0.7	0.0	0.0	0.7	0.9	2.3	1.7	3.7	2.1	3.1	2.0
F. scalariformis	0.0	0.0	0.0	0.0	0.0	0.0	0.0	0.0	0.0	0.0	0.0	0.0	0.0	0.0	0.0	0.0	0.0	0.0	0.0	0.0
G. praegeni	0.0	0.0	0.3	0.7	0.0	0.0	0.1	0.2	0.0	0.0	0.0	0.0	1.0	1.1	0.7	0.9	0.0	0.0	1.0	1.2
Globigerina sp A	0.3	0.5	0.0	0.0	0.2	0.5	0.0	0.0	0.0	0.0	0.0	0.0	0.0	0.0	0.0	0.0	0.0	0.0	0.7	0.9
G. lamarckiana	0.0	0.0	0.0	0.0	0.0	0.0	0.0	0.0	0.0	0.0	0.7	1.0	0.0	0.0	0.0	0.0	0.0	0.0	0.0	0.0
Haynesina sp A	0.0	0.0	1.3	1.3	6.1	2.3	0.0	0.0	0.0	0.0	0.0	0.0	0.0	0.0	0.0	0.0	0.0	0.0	0.0	0.0
Haynesina sp B	0.0	0.0	0.7	0.9	0.0	0.0	0.0	0.0	0.7	1.0	0.0	0.0	6.8	2.9	0.7	0.9	0.0	0.0	1.7	1.5
Haynesina sp C	0.0	0.0	0.0	0.0	0.0	0.0	0.0	0.0	0.0	0.0	0.0	0.0	0.0	0.0	4.0	2.2	0.0	0.0	0.0	0.0
Haynesina sp E	0.5	0.7	0.0	0.0	0.0	0.0	0.6	0.5	0.0	0.0	0.0	0.0	0.0	0.0	0.0	0.0	3.0	1.9	2.1	1.6
Haynesina sp F	0.0	0.0	0.0	0.0	0.0	0.0	0.0	0.0	0.0	0.0	0.0	0.0	0.0	0.0	0.0	0.0	0.0	0.0	0.0	0.0
H. depressula	0.0	0.0	1.3	1.3	3.3	1.7	0.0	0.0	0.0	0.0	16.5	4.3	5.7	2.7	3.3	2.0	2.3	1.7	2.1	1.6
L. bicornis	0.0	0.0	0.3	0.7	0.0	0.0	0.0	0.0	0.0	0.0	0.0	0.0	0.7	0.9	1.0	1.1	0.0	0.0	1.0	1.2
L. lobatula	0.0	0.0	0.0	0.0	0.2	0.5	0.3	0.4	0.0	0.0	0.0	0.0	0.7	0.9	0.0	0.0	0.0	0.0	0.0	0.0
M. gualtieriana	1.8	1.3	0.0	0.0	0.0	0.0	0.0	0.0	0.0	0.0	0.0	0.0	0.0	0.0	1.3	1.3	2.0	1.6	0.0	0.0
Miliolinella sp B	0.3	0.5	7.1	2.9	4.9	2.1	2.1	1.0	2.4	1.8	0.0	0.0	2.7	1.8	5.7	2.6	9.3	3.3	8.2	3.2

G-22: Foraminifera Abundances (Goodman et al., 2009), Cont.

Depth (mbsl):	3.1		4.6		4.9		5.2		5.2		5.7		6.1		6.5		7.2		7.8	
Specimens Counted:	388		297		425		888		286		285		296		300		300		292	
Specimens /cc:	621		464		340		496		203		57		631		960		640		156	
Species	**%**	**±**	**%**	**±**	**%**	**±**	**%**	**±**	**%**	**±**	**%**	**±**	**%**	**±**	**%**	**±**	**%**	**±**	**%**	**±**
Miliolinella sp E	0.0	0.0	0.0	0.0	0.0	0.0	0.0	0.0	0.0	0.0	0.0	0.0	0.0	0.0	0.0	0.0	0.3	0.7	0.0	0.0
M. dilatata	0.0	0.0	0.0	0.0	0.0	0.0	0.0	0.0	0.0	0.0	0.0	0.0	0.0	0.0	0.0	0.0	2.3	1.7	1.4	1.3
M. elongata	0.3	0.5	0.0	0.0	0.0	0.0	0.0	0.0	0.0	0.0	0.0	0.0	0.0	0.0	0.0	0.0	0.0	0.0	0.0	0.0
M. subrotunda	3.4	1.8	0.3	0.7	3.3	1.7	0.0	0.0	0.0	0.0	0.0	0.0	0.0	0.0	0.0	0.0	0.3	0.7	0.0	0.0
Nonionella sp	1.3	1.1	0.0	0.0	0.0	0.0	0.5	0.4	0.0	0.0	1.1	1.2	0.3	0.7	1.0	1.1	0.0	0.0	0.0	0.0
P. pertusus	19.3	3.9	0.7	0.9	9.4	2.8	0.1	0.2	0.0	0.0	0.0	0.0	0.0	0.0	0.0	0.0	0.0	0.0	0.0	0.0
P. planatus	7.5	2.6	0.0	0.0	0.5	0.7	0.0	0.0	0.0	0.0	0.0	0.0	0.0	0.0	0.0	0.0	0.0	0.0	0.0	0.0
P. mediterranensis	0.0	0.0	1.0	1.1	1.2	1.0	0.0	0.0	0.3	0.7	0.0	0.0	0.0	0.0	0.0	0.0	0.0	0.0	0.0	0.0
P. retinaculata	0.0	0.0	0.0	0.0	1.2	1.0	0.0	0.0	0.0	0.0	0.0	0.0	0.0	0.0	0.0	0.0	0.0	0.0	0.0	0.0
Polymorphina sp A	0.0	0.0	0.0	0.0	0.0	0.0	0.0	0.0	0.0	0.0	0.0	0.0	0.0	0.0	0.0	0.0	0.0	0.0	0.3	0.7
P. granosum	0.0	0.0	0.0	0.0	0.0	0.0	0.0	0.0	0.0	0.0	1.8	1.5	0.0	0.0	0.0	0.0	0.3	0.7	0.0	0.0
Pseudotriloculina sp A	0.0	0.0	2.7	1.8	0.0	0.0	0.0	0.0	1.0	1.2	0.0	0.0	0.0	0.0	0.7	0.9	1.7	1.4	0.0	0.0
Pseudotriloculina sp B	0.0	0.0	0.0	0.0	0.0	0.0	0.0	0.0	0.0	0.0	0.0	0.0	0.0	0.0	0.0	0.0	1.0	1.1	1.4	1.3
Pseudotriloculina sp C	0.0	0.0	3.0	1.9	0.0	0.0	0.0	0.0	0.0	0.0	0.0	0.0	0.7	0.9	0.0	0.0	0.0	0.0	0.0	0.0
Pseudotriloculina sp D	0.0	0.0	0.0	0.0	0.0	0.0	0.6	0.5	0.0	0.0	0.0	0.0	0.0	0.0	0.0	0.0	0.0	0.0	0.0	0.0
P. cuneata	0.8	0.9	1.0	1.1	0.0	0.0	0.1	0.2	0.3	0.7	0.0	0.0	0.7	0.9	3.7	2.1	5.0	2.5	5.5	2.6
P. laevigata	1.0	1.0	5.4	2.6	4.2	1.9	1.8	0.9	1.0	1.2	0.0	0.0	0.7	0.9	2.0	1.6	3.0	1.9	1.7	1.5
P. oblonga	0.0	0.0	0.7	0.9	0.0	0.0	0.1	0.2	0.0	0.0	0.0	0.0	0.0	0.0	0.0	0.0	0.0	0.0	0.0	0.0
P. rotunda	1.8	1.3	0.7	0.9	0.0	0.0	0.7	0.5	2.1	1.7	0.0	0.0	0.7	0.9	0.3	0.7	0.0	0.0	1.7	1.5
P. subrotunda	0.0	0.0	0.0	0.0	0.0	0.0	0.0	0.0	0.0	0.0	0.0	0.0	0.3	0.7	0.0	0.0	1.0	1.1	0.0	0.0
Pyrgo sp A	0.3	0.5	0.3	0.7	0.0	0.0	0.0	0.0	0.0	0.0	0.0	0.0	0.7	0.9	0.0	0.0	0.0	0.0	0.0	0.0
Quinqueloculina sp C	0.5	0.7	1.3	1.3	0.0	0.0	0.2	0.3	1.0	1.2	0.0	0.0	1.0	1.1	1.7	1.4	5.7	2.6	4.8	2.5
Quinqueloculina sp D	0.5	0.7	0.0	0.0	0.0	0.0	0.0	0.0	0.0	0.0	0.0	0.0	0.7	0.9	0.0	0.0	0.0	0.0	0.0	0.0
Quinqueloculina sp E	0.5	0.7	0.3	0.7	0.0	0.0	0.0	0.0	0.0	0.0	0.0	0.0	0.0	0.0	0.0	0.0	0.0	0.0	0.0	0.0
Quinqueloculina sp G	0.0	0.0	0.3	0.7	0.0	0.0	0.0	0.0	0.0	0.0	0.0	0.0	0.3	0.7	0.0	0.0	0.0	0.0	1.0	1.2
Quinqueloculina sp H	0.0	0.0	0.0	0.0	0.0	0.0	0.0	0.0	0.3	0.7	0.0	0.0	0.0	0.0	0.0	0.0	0.0	0.0	0.0	0.0
Quinqueloculina sp I	0.0	0.0	0.0	0.0	0.0	0.0	0.1	0.2	0.0	0.0	0.0	0.0	0.0	0.0	0.0	0.0	0.0	0.0	0.0	0.0
Quinqueloculina sp J	0.5	0.7	0.0	0.0	0.0	0.0	0.0	0.0	0.0	0.0	0.0	0.0	0.0	0.0	0.0	0.0	0.0	0.0	0.0	0.0
Quinqueloculina sp K	0.0	0.0	0.3	0.7	0.0	0.0	0.0	0.0	0.3	0.7	0.0	0.0	0.0	0.0	0.0	0.0	0.0	0.0	0.0	0.0
Q. annectens	0.0	0.0	0.0	0.0	0.0	0.0	0.0	0.0	0.0	0.0	0.0	0.0	0.0	0.0	0.0	0.0	0.0	0.0	0.0	0.0
Q. auberiana	1.3	1.1	0.7	0.9	0.0	0.0	0.7	0.5	0.0	0.0	0.0	0.0	0.0	0.0	0.7	0.9	1.7	1.4	0.0	0.0
Q. bertheloticana	1.0	1.0	1.7	1.5	0.2	0.5	0.8	0.6	0.7	1.0	0.0	0.0	0.7	0.9	0.3	0.7	1.0	1.1	1.0	1.2
Q. bosciana	0.0	0.0	0.3	0.7	0.0	0.0	0.0	0.0	0.0	0.0	0.0	0.0	0.0	0.0	0.0	0.0	0.0	0.0	0.0	0.0
Q. disparilis	0.0	0.0	0.0	0.0	0.0	0.0	0.0	0.0	0.0	0.0	0.0	0.0	0.0	0.0	0.7	0.9	0.0	0.0	0.0	0.0
Q. laevigata	0.0	0.0	1.3	1.3	0.0	0.0	0.0	0.0	0.0	0.0	0.0	0.0	2.0	1.6	1.3	1.3	0.7	0.9	1.4	1.3

G-22: Foraminifera Abundances (Goodman et al., 2009), Cont.

Depth (mbsl):	3.1		4.6		4.9		5.2		5.2		5.7		6.1		6.5		7.2		7.8	
Specimens Counted:	388		297		425		888		286		285		296		300		300		292	
Specimens /cc:	621		464		340		496		203		57		631		960		640		156	
Species	**%**	**±**	**%**	**±**	**%**	**±**	**%**	**±**	**%**	**±**	**%**	**±**	**%**	**±**	**%**	**±**	**%**	**±**	**%**	**±**
Q. parvulaa	1.5	1.2	0.0	0.0	0.0	0.0	0.0	0.0	0.0	0.0	0.0	0.0	0.3	0.7	0.0	0.0	0.3	0.7	0.0	0.0
Q. patagonica	1.8	1.3	1.3	1.3	0.0	0.0	1.7	0.8	2.8	1.9	0.0	0.0	0.7	0.9	1.7	1.4	1.3	1.3	5.1	2.5
Q. ungeriana	0.0	0.0	0.3	0.7	0.2	0.5	0.0	0.0	0.0	0.0	0.0	0.0	0.0	0.0	0.0	0.0	0.0	0.0	0.0	0.0
Reusselasp A	0.0	0.0	0.0	0.0	0.2	0.5	0.2	0.3	0.7	1.0	0.0	0.0	0.0	0.0	1.7	1.4	0.0	0.0	0.0	0.0
Rosalina sp A	0.0	0.0	0.0	0.0	0.0	0.0	0.1	0.2	0.0	0.0	0.0	0.0	0.0	0.0	0.0	0.0	0.3	0.7	0.0	0.0
Rosalina sp B	0.3	0.5	0.3	0.7	0.0	0.0	0.1	0.2	0.0	0.0	0.0	0.0	0.0	0.0	0.0	0.0	0.0	0.0	0.0	0.0
Rosalina bradyi	2.3	1.5	7.1	2.9	0.7	0.8	50.7	3.3	7.7	3.1	6.3	2.8	10.1	3.4	0.0	0.0	11.7	3.6	5.1	2.5
R. floridensis	0.0	0.0	6.7	2.9	0.7	0.8	2.8	1.1	11.2	3.7	0.0	0.0	6.8	2.9	5.3	2.5	0.0	0.0	7.2	3.0
R. macropora	0.5	0.7	0.0	0.0	1.4	1.1	0.5	0.4	1.0	1.2	0.0	0.0	0.0	0.0	0.0	0.0	0.0	0.0	0.0	0.0
R. orientalis	1.3	1.1	0.0	0.0	1.2	1.0	0.0	0.0	0.0	0.0	0.0	0.0	0.0	0.0	7.3	2.9	3.3	2.0	0.0	0.0
S. costata	1.3	1.1	4.4	2.3	4.5	2.0	1.5	0.8	0.0	0.0	0.0	0.0	0.3	0.7	1.0	1.1	1.7	1.4	2.7	1.9
S. grata	0.0	0.0	0.0	0.0	0.5	0.7	0.0	0.0	0.0	0.0	0.0	0.0	0.0	0.0	0.0	0.0	0.0	0.0	0.0	0.0
Siphonaperta sp A	1.0	1.0	0.0	0.0	0.0	0.0	0.0	0.0	0.0	0.0	0.0	0.0	0.0	0.0	0.0	0.0	0.0	0.0	0.0	0.0
S. aspera	0.0	0.0	3.4	2.1	0.0	0.0	0.0	0.0	0.0	0.0	0.0	0.0	0.7	0.9	0.0	0.0	0.3	0.7	0.0	0.0
Siphonvigerina sp A	0.0	0.0	0.0	0.0	0.0	0.0	0.0	0.0	0.0	0.0	2.5	1.8	0.0	0.0	0.0	0.0	0.0	0.0	0.0	0.0
Spiriloculina sp A	0.0	0.0	0.0	0.0	0.5	0.7	0.0	0.0	0.0	0.0	0.0	0.0	0.3	0.7	0.0	0.0	0.3	0.7	1.7	1.5
Spiriloculina sp B	1.3	1.1	0.0	0.0	0.0	0.0	0.1	0.2	0.0	0.0	0.0	0.0	0.0	0.0	0.0	0.0	0.0	0.0	0.0	0.0
Spiriloculina sp C	0.0	0.0	0.7	0.9	0.0	0.0	0.0	0.0	0.0	0.0	0.0	0.0	0.0	0.0	0.0	0.0	0.0	0.0	0.0	0.0
Spiroloculina sp D	0.0	0.0	0.0	0.0	1.9	1.3	0.0	0.0	0.0	0.0	0.0	0.0	0.0	0.0	0.0	0.0	0.0	0.0	0.0	0.0
Stomatorbina concentrica	0.0	0.0	0.0	0.0	0.0	0.0	0.0	0.0	0.0	0.0	1.8	1.5	0.0	0.0	0.0	0.0	0.0	0.0	0.0	0.0
Tetromphalus bulloides	0.0	0.0	0.0	0.0	2.4	1.4	0.0	0.0	0.0	0.0	0.0	0.0	0.0	0.0	0.0	0.0	0.0	0.0	0.0	0.0
Textularia sp A	0.0	0.0	0.0	0.0	0.0	0.0	0.0	0.0	0.0	0.0	0.4	0.7	0.0	0.0	0.0	0.0	0.0	0.0	0.0	0.0
T .marioni	2.8	1.7	0.7	0.9	2.4	1.4	0.7	0.5	1.7	1.5	0.0	0.0	1.0	1.1	1.7	1.4	4.0	2.2	2.4	1.8
T. ornata	1.3	1.1	0.0	0.0	0.0	0.0	0.0	0.0	0.0	0.0	0.0	0.0	0.0	0.0	0.0	0.0	0.0	0.0	0.0	0.0
T. plicata	0.0	0.0	1.3	1.3	0.0	0.0	0.0	0.0	0.3	0.7	0.0	0.0	0.0	0.0	1.3	1.3	0.0	0.0	0.0	0.0
T. schreiberiana	0.0	0.0	0.0	0.0	0.0	0.0	0.0	0.0	0.0	0.0	0.0	0.0	0.0	0.0	2.0	1.6	0.0	0.0	0.0	0.0
T. subgranosum	0.0	0.0	0.0	0.0	0.0	0.0	0.5	0.4	0.0	0.0	0.0	0.0	0.0	0.0	0.0	0.0	0.0	0.0	0.0	0.0
T. inflata	0.0	0.0	0.0	0.0	1.9	1.3	0.0	0.0	0.0	0.0	7.0	3.0	0.0	0.0	0.0	0.0	0.0	0.0	0.0	0.0
Vertebralina striatula	4.4	2.0	0.0	0.0	2.1	1.4	0.0	0.0	0.0	0.0	0.0	0.0	0.0	0.0	0.0	0.0	0.3	0.7	0.0	0.0

APPENDIX D: Lechaion Foraminifera Data

Core 2: Statistically Significant Species Abundance

Sample:	2-1A	2-1B	2-4A	2-4B	2-4C	2-4D	2-4E
Depth from MSL (m):	0.18	0.07	-0.95	-1.00	-1.20	-1.44	-1.60
Specimens Counted:	67	10	168	190	818	127	53
Genera	**Abundances (%)**						
Adelosina dubia	-	-	1.2	0.5	0.7	5.5	-
Adelosina sp. 3	-	-	19.6	4.2	1.2	1.6	-
Ammonia beccarii "parkinsoniana"	28.4	71.4	19.1	21.6	38.8	20.5	12.0
Ammonia beccarii "tepida"	1.5	28.6	4.2	2.6	-	6.3	4.0
Aubignyna planidorso	-	-	9.5	21.6	14.1	15.0	10.0
Bolivina pseudoplicata	-	-	1.8	-	1.7	-	2.0
Bolivina varabilis	-	-	1.2	1.1	0.4	2.4	-
Bolivinellina sp. 1	-	-	3.0	3.2	4.2	1.6	10.0
Brizalina dilatata	-	-	-	2.1	0.7	0.8	-
Brizalina striatula	-	-	-	0.5	0.4	2.4	2.0
Elphidium limbatum	-	-	5.4	9.5	5.5	6.3	14.0
Floresina sp. 1	-	-	-	-	0.7	-	2.0
Fursenkoina acuta	-	-	-	0.5	-	-	-
Haynesina depressula	-	-	-	4.2	3.2	3.2	4.0
Massilina gualtierana	-	-	9.5	4.7	-	2.4	4.0
Miliolinella semicostata	-	-	3.0	0.5	2.8	11.0	10.0
Neoconorbina terquemi	-	-	-	-	0.1	-	2.0
Plancktic sp.	-	-	2.4	5.3	3.6	0.8	8.0
Porosononion granosum	-	-	6.6	13.2	19.3	4.7	12.0
Quinqueloculina laevigata	1.5	-	-	-	0.1	-	-
Quinqueloculina sp. 1	31.3	-	3.6	1.1	-	3.9	-
Quinqueloculina sp. 3	-	-	0.6	-	-	-	2.0
Quinqueloculina sp. 7	32.8	-	8.9	2.6	2.1	8.7	-
Quinqueloculina ungeriana	4.5	-	-	-	-	-	2.0
Spirophthalmidium acutimargo	-	-	-	-	0.1	-	-
Uvigerina mediterrana	-	-	0.6	0.5	0.2	-	-

Collected by K. Chomicki

Core 3: Statistically Significant Species Abundance

Sample:	3-1A	3-1B	3-4A	3-4B	3-4C	3-5A	3-6A	3-6B	3-6C	3-7A	3-7B	3-7C	3-8A
Depth from MSL (m):	-0.05	-0.17	-0.90	-0.98	-1.06	-1.14	-1.20	-1.33	-1.45	-1.51	-1.65	-1.79	-1.84
Specimens Counted:	181	458	648	541	697	1011	453	581	487	605	528	369	357
Genera	Abundances (%)												
**Ammonia beccarii 'type'*	-	-	-	-	-	-	-	-	1.6	-	-	-	-
Adelosina carinata-striata	-	-	-	-	-	-	2.6	1.0	1.2	0.7	1.1	1.9	2.5
Adelosina dubia	-	-	0.5	0.6	1.4	8.8	11.3	6.4	4.9	6.8	8.0	11.9	7.0
Adelosina sp. 1	-	-	-	-	-	2.4	1.1	1.9	-	-	-	-	-
Adelosina sp. 3	-	-	1.7	2.4	1.7	3.4	4.1	5.7	5.7	15.2	5.7	6.2	2.2
Ammonia beccarii "parkinsoniana"	5.2	14.6	22.7	25.2	14.8	3.3	11.7	5.4	2.2	3.1	7.0	4.3	2.5
Ammonia beccarii "tepida"	33.9	23.6	5.1	2.8	1.7	0.2	-	-	-	-	-	-	-
Aubignyna planidorso	-	-	26.9	27.4	20.1	5.7	3.7	2.6	0.2	1.0	1.0	-	-
Bolivina pseudoplicata	-	-	1.5	1.5	1.7	3.3	1.3	2.6	2.0	3.1	4.0	4.9	3.6
Bolivina varabilis	-	-	1.2	1.3	3.0	1.3	1.1	1.6	1.2	-	0.2	-	-
Bolivinellina sp. 1	-	-	4.2	4.3	5.6	2.9	4.6	6.7	4.7	4.5	5.9	4.3	4.2
Brizalina dilatata	-	-	1.4	0.4	0.7	0.4	0.2	1.0	0.4	0.3	0.2	-	-
Brizalina striatula	-	-	1.5	1.1	2.2	0.9	0.2	-	0.2	0.3	0.2	-	-
Bulimina marginata	-	-	-	-	0.7	0.1	-	-	-	0.3	-	-	-
Elphidium limbatum	-	-	10.5	8.7	9.3	9.7	8.9	9.2	5.1	4.6	5.9	4.6	7.6
Elphidium translecens	-	-	-	-	-	-	-	-	-	-	-	1.4	2.5
Floresina sp. 1	-	-	0.2	0.6	0.9	0.7	0.2	-	1.8	0.7	0.4	0.8	-
Fursenkoina acuta	-	-	-	-	-	-	0.4	0.5	-	1.5	0.4	-	0.6
Haynesina depressula	-	-	3.7	4.5	10.0	13.9	11.3	13.1	8.7	11.1	17.2	14.4	13.2
Massilina gualtierana	-	-	0.2	0.4	1.0	0.8	-	1.0	-	1.3	0.2	-	-
Miliolinella semicostata	-	-	0.3	0.4	4.7	13.0	8.9	6.6	6.7	4.5	6.3	7.1	12.3
Miliolinella sp. 2	-	-	-	-	-	0.1	-	-	-	-	-	-	-
Neoconorbina terquemi	-	-	0.2	-	0.3	0.6	1.5	0.7	-	2.3	1.3	-	-
Planciktic sp.	-	-	2.5	1.7	2.7	2.7	2.4	1.6	1.4	0.8	0.4	0.5	0.6
Porosononion granosum	-	-	14.4	14.3	11.3	2.4	2.4	1.7	4.3	-	0.6	0.5	0.6
Porosononion sp. 1	-	-	-	-	-	-	-	-	3.3	-	-	-	-
Quinqueloculina auberiana	-	-	-	-	-	-	3.5	2.8	3.9	2.5	1.3	0.5	1.1
Quinqueloculina laevigata	-	-	-	-	-	4.2	2.6	-	-	2.8	6.8	-	-
Quinqueloculina patagonica	-	-	-	-	-	2.0	-	-	6.5	3.6	4.0	10.0	6.2
Quinqueloculina sp. 1	17.2	9.4	0.2	0.2	0.7	1.7	-	1.6	4.5	2.8	1.5	0.5	0.8
Quinqueloculina sp. 3	-	-	-	0.2	-	0.3	0.7	0.7	2.4	1.5	1.9	2.2	1.1
Quinqueloculina sp. 4	-	1.1	-	-	-	-	3.0	2.6	-	-	-	-	-
Quinqueloculina sp. 5	-	2.4	-	-	0.4	0.2	1.5	1.6	-	-	-	-	-
Quinqueloculina sp. 7	29.9	45.0	1.1	0.9	4.0	11.6	10.4	10.9	14.0	17.0	13.3	14.4	22.1
Quinqueloculina ungeriana	-	2.8	-	-	-	0.4	-	-	-	3.6	2.8	-	-
Rosalina sp. 1	-	-	-	-	-	-	-	10.0	11.6	3.8	2.1	7.6	7.0
Spiroloculina angulosa	-	-	-	-	-	0.4	-	-	-	-	-	-	-
Spirophthalmidium acutimargo	-	-	-	0.2	0.1	0.6	0.7	0.4	0.2	0.2	0.2	0.8	1.4
Triloculina marioni	-	-	-	-	0.7	1.4	-	-	-	-	-	-	-
Uvigerina mediterrana	-	-	-	0.8	-	-	-	0.2	-	-	-	0.5	0.6

Collected by K. Chomicki

Core 7: Statistically Significant Species Abundance

Sample:	7-5A	7-5B	7-5C	7-6A	7-6B	7-6C	7-7A	7-8A	7-9A
Depth from MSL (m):	-0.83	-0.95	-1.07	-1.20	-1.31	-1.41	-1.45	-1.49	-1.54
Specimens Counted:	344	311	461	327	477	310	270	242	148
Genera	**Abundances (%)**								
Adelosina carinata-striata	-	-	-	-	0.2	0.3	-	0.4	-
Adelosina dubia	12.5	2.6	0.4	8.9	10.3	6.1	4.8	5.4	2.7
Adelosina sp. 1	-	-	-	1.2	1.7	-	-	0.4	-
Adelosina sp. 3	43.9	4.5	2.0	9.8	9.0	5.2	4.1	2.9	1.4
Ammonia beccarii "parkinsoniana"	4.7	19.0	23.0	6.1	6.5	7.4	6.3	1.7	5.4
Aubignyna planidorso	-	2.9	0.7	0.6	0.2	-	0.4	-	-
Bolivina pseudoplicata	3.2	6.8	8.2	4.0	2.1	1.3	3.7	5.4	2.0
Bolivina varabilis	0.6	3.6	2.2	1.2	0.8	1.0	0.4	-	2.7
Bolivinellina sp. 1	7.0	34.2	30.4	7.7	6.3	9.0	10.8	16.1	4.1
Brizalina dilatata	-	1.3	2.2	-	-	-	-	-	-
Brizalina striatula	0.3	-	2.0	0.6	-	-	0.7	-	-
Elphidium limbatum	1.7	3.9	5.9	9.2	6.9	25.8	21.9	10.3	16.2
Floresina sp. 1	1.2	0.7	1.1	0.3	-	0.7	-	-	-
Fursenkoina acuta	0.3	0.3	0.9	-	0.2	-	-	-	0.7
Haynesina depressula	4.1	5.5	11.9	10.1	10.5	12.9	19.0	18.2	29.1
Massilina gualtierana	2.0	1.0	0.2	-	1.5	1.0	0.4	-	1.4
Miliolinella semicostata	2.3	1.0	0.2	6.4	9.9	7.7	6.3	7.9	9.5
Neoconorbina terquemi	-	-	-	1.8	1.9	1.9	1.5	-	1.4
Planciktic sp.	1.5	8.7	4.6	1.8	0.2	1.6	0.7	0.8	-
Porosononion granosum	1.2	1.6	1.5	4.0	1.1	2.3	1.5	2.5	9.5
Quinqueloculina auberiana	-	-	-	0.3	0.6	-	-	-	-
Quinqueloculina laevigata	0.9	-	-	-	-	-	0.7	-	-
Quinqueloculina patagonica	2.9	0.3	-	5.2	8.6	2.3	3.4	5.4	2.0
Quinqueloculina sp. 1	0.9	-	-	1.2	1.5	1.0	1.1	0.4	-
Quinqueloculina sp. 3	1.5	-	-	1.8	1.7	-	-	-	-
Quinqueloculina sp. 4	-	-	-	-	-	1.0	-	4.1	1.4
Quinqueloculina sp. 5	-	-	0.2	0.9	-	-	-	-	-
Quinqueloculina sp. 7	6.4	1.6	1.1	12.5	11.1	11.6	8.6	13.6	4.1
Quinqueloculina ungeriana	0.9	-	-	-	2.5	-	-	-	-
Rosalina sp. 1	0.3	-	0.9	3.1	3.6	-	1.5	2.1	6.1
Spirophthalmidium acutimargo	-	-	-	0.9	0.4	-	-	0.4	-
Uvigerina mediterrana	-	0.3	0.7	0.3	0.2	-	1.1	1.7	-

Collected by K. Chomicki

APPENDIX E: Lechaion Core 3 Isotopic Data

Depth from MSL (m)	Sample	$d^{13}C$ (‰)	$d^{18}0$ (‰)
-0.174	Shell fragments	-1.147	3.422
-0.299	Shell fragments	-7.685	1.724
-0.389	Shell fragments	-6.848	2.368
-0.804	Shell fragments	0.320	2.201
-0.854	Shell fragments	-0.367	0.853
-0.904	Shell fragments	-4.832	-0.501
-0.984	Shell	-2.720	1.617
-1.059	Shell	-0.834	0.149
-1.139	Shell	0.910	1.732
-1.203	Shell	0.153	2.742
-1.328	Shell	-0.097	2.650
-1.448	Shell	1.334	1.913
-1.513	Shell	1.673	1.072
-1.653	Shell	1.997	1.167
-1.793	Shell	1.599	0.347
-1.838	Shell	1.121	0.804
-0.054	Quinqueloculina sp. 7	1.121	0.915
-0.174	Quinqueloculina sp. 7	1.121	0.293
-0.904	Quinqueloculina sp. 7	1.121	-0.073
-1.139	Quinqueloculina sp. 7	1.121	-1.438
-1.203	Quinqueloculina sp. 7	1.121	-1.764
-1.328	Quinqueloculina sp. 7	1.121	-1.125
-1.448	Quinqueloculina sp. 7	1.121	-1.482
-1.513	Quinqueloculina sp. 7	1.121	-0.846
-1.653	Quinqueloculina sp. 7	1.121	-2.212
-1.793	Quinqueloculina sp. 7	1.121	-1.453
-1.838	Quinqueloculina sp. 7	1.121	-1.193
-0.904	oyster Shell	1.121	0.353
-0.054	Ostracod	1.121	-0.105
-0.174	Ostracod	1.121	1.208
-0.299	Ostracod	1.121	0.166
-0.389	Ostracod	1.121	-0.166
-0.554	Ostracod	1.121	0.264
-0.679	Ostracod	1.121	3.169
-0.804	Ostracod	1.121	1.568
-0.904	Ostracod	1.121	0.653
-0.984	Ostracod	1.121	0.458
-1.059	Ostracod	1.121	-0.271
-1.139	Ostracod	1.121	1.367
-1.203	Ostracod	1.121	-0.124
-1.328	Ostracod	1.121	0.381
-1.448	Ostracod	1.121	0.822
-1.513	Ostracod	1.121	0.540
-1.653	Ostracod	1.121	0.284
-1.793	Ostracod	1.121	0.046
-1.838	Ostracod	1.121	1.843
-1.059	Miliolinella semicostata	1.121	-0.783
-1.139	Miliolinella semicostata	1.121	-1.413
-1.328	Miliolinella semicostata	1.121	-0.059
-1.448	Miliolinella semicostata	1.121	-1.158
-1.513	Miliolinella semicostata	1.121	0.101
-1.653	Miliolinella semicostata	1.121	-1.087
-1.793	Miliolinella semicostata	1.121	-1.188
-1.838	Miliolinella semicostata	1.121	-0.835
-0.984	Haynesina depressula	1.121	-0.001
-1.059	Haynesina depressula	1.121	0.716
-1.328	Haynesina depressula	1.121	-0.211
-1.653	Haynesina depressula	1.121	-0.373
-1.793	Haynesina depressula	1.121	0.471
-0.904	Elphidium limbatum	1.121	0.576
-0.984	Elphidium limbatum	1.121	0.273
-1.059	Elphidium limbatum	1.121	0.565
-1.139	Elphidium limbatum	1.121	0.915
-1.203	Elphidium limbatum	1.121	-0.915
-1.328	Elphidium limbatum	1.121	0.194
-1.448	Elphidium limbatum	1.121	-0.646
-1.513	Elphidium limbatum	1.121	0.382
-1.653	Elphidium limbatum	1.121	0.267
-0.054	Charophyte	1.121	3.857
-0.174	Charophyte	1.121	4.855
-0.299	Charophyte	1.121	6.013
-0.389	Charophyte	1.121	6.630
-0.904	Aubignyna planidorso	1.121	1.191
-0.984	Aubignyna planidorso	1.121	0.504
-1.059	Aubignyna planidorso	1.121	0.918
-1.203	Aubignyna planidorso	1.121	-0.453
-1.448	Aubignyna planidorso	1.121	-0.174
-0.054	Ammonia beccarii 'tepida'	1.121	-0.892
-0.174	Ammonia beccarii 'tepida'	1.121	-1.172
-0.984	Adelosina sp. 3	1.121	-0.931
-1.139	Adelosina sp. 3	1.121	-0.400
-1.203	Adelosina sp. 3	1.121	-1.594
-1.793	Adelosina sp. 3	1.121	-1.231
-0.904	AB parkinsoniana	1.121	0.700
-0.984	AB parkinsoniana	1.121	-0.301
-1.059	AB parkinsoniana	1.121	0.564
-1.139	AB parkinsoniana	1.121	-0.433
-1.203	AB parkinsoniana	1.121	0.039
-1.328	AB parkinsoniana	1.121	2.095
-1.448	AB parkinsoniana	1.121	0.439
-1.513	AB parkinsoniana	1.121	0.266
-1.653	AB parkinsoniana	1.121	0.222
-1.793	AB parkinsoniana	1.121	-0.129
-1.838	AB parkinsoniana	1.121	0.646

Collected by K. Chomicki

APPENDIX F: Lechaion Core 1 Palynomorph Data

NPP	Depth (cm):	78	96	116	136	156	176
	Lycopodium spike:	12	11	21	11	2	59
Chlorophytes	Botryococcus braunii	1	2			1	
	Chlorococcum	1		3	1		
	Pediastrum			1		1	2
	Scenedesmus		1				
	Tetraedron		1				
	indet coccal	18					16
	Total	20	4	4	1	2	18
Charophytes	Zygnema	18					1
	Spirogyra						
	INDET cysts/ phycomata	175	29	10	7		
	Cosmarium	2			1		2
	Euastrum lacustre/ E. denticulatum						
	Total	195	29	10	8	0	3
Coprophilous	Trichuris eggs			2	2		
	Fungi			Many	Many		
Marine	Brigantedinium cyst		0		8	1	1
	Lejeunecysta cyst		0		1		1
	Lingulodinium machaerophorum cyst		0	1			
	Bitectatodinium tepikiense cyst			1	1		
	Spiniferites cyst		0	6	2	4	10
	indet marine cyst			2			1
	Total	0	0	10	12	5	13
	Foraminifer linings	0	0	0	4	1	1

Collected by F.M.G. McCarthy

Pollen/Spores	Depth (cm):	78	96	116	136	156	176
	Lycopodium spike:	12	11	21	11	2	59
Tree pollen	Pinus	8.5	32	6.5	8		7
	Abies		3	0	1		1
	Picea	1					
	TCT		3	3	1		1
	Alnus		9	1	0		3
	Betula	2	5	11	3		1
	Ostrya	1	12	1	3		2
	Corylus		1		0		
	Fraxinus nigra-type			1	0		
	Quercus	1		3	1		1
	Salix			7			
	Ulmus		2		0		
Other	indet pollen	26	120	52	51		
	Ericaceae		4	3	1	1	
	Asteraceae	1	5	6	1		2
	Artemisia		11	9	3		1
	Chenopodiaceae	7	3	16	13		5
	Poaceae	10	59	5	7		
	Cyperaceae	2	10	4	0		8
	aquatics		3				
	Dryopteris-type spore		0	1	0		
	trilete spore		1	0	0		

Collected by F.M.G. McCarthy